
MECHANISMS OF NEURONAL PATHOLOGY IN A MODEL OF GREY MATTER INFLAMMATION

Emily Melisa Ullrich Gavilanes



Graduate School of
Systemic Neurosciences
LMU Munich

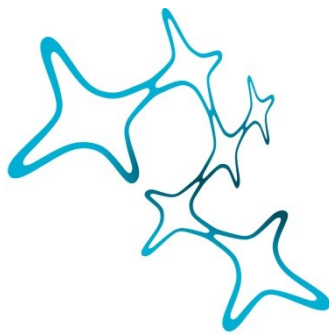


Dissertation der
Graduate School of Systemic Neurosciences der
Ludwig-Maximilians-Universität München

22nd of June, 2023

MECHANISMS OF NEURONAL PATHOLOGY IN A MODEL OF GREY MATTER INFLAMMATION

Emily Melisa Ullrich Gavilanes



Graduate School of
Systemic Neurosciences

LMU Munich



Dissertation der
Graduate School of Systemic Neurosciences der
Ludwig-Maximilians-Universität München

22nd of June, 2023

Supervisor

Prof. Dr. Martin Kerschensteiner

Institute of Clinical Neuroimmunology

University Hospital and Biomedical Center of the

Ludwig-Maximilians Universität München

First Reviewer: Prof. Dr. Martin Kerschensteiner

Second Reviewer: Prof. Dr. med. Veit Rothhammer

External Reviewer Prof. Dr. Dr. Anna-Sophia Wahl

Date of Submission: 22.06.2023

Date of Defense : 23.10.2023

To Pia and Jorge,
I miss you every day

“Hay que luchar por todos bonitamente, equitativamente, honradamente y racionalmente”

- Tránsito Amaguaña

Contents

List of abbreviations.....	10
Abstract	13
Zusammenfassung	15
Chapter I: Introduction.....	17
I.1 Multiple sclerosis	17
I.1.1 Epidemiology	17
I.1.2 Pathology	18
I.1.2.1 White matter	18
I.1.2.2 Grey matter.....	20
I.1.3 Clinical course	21
I.1.4 Age as a risk factor for MS progression	22
I.1.5 Treatments.....	23
I.1.6 MS animal models	25
I.2. Synapse loss as a neuropathological hallmark	27
I.2.1 Synapse loss in neuroinflammation	28
I.2.1.1 Cellular mechanisms of synapse loss	29
I.2.1.2 Molecular mechanisms of synapse loss	30
I.3 Imaging techniques to visualize neuropathology in the inflamed CNS.....	31
I.3.1 MRI.....	32
I.3.2 PET scanning	33
I.4 Molecular techniques to analyse and manipulate neuropathology in the inflamed CNS	34
I.4.1 snRNA-seq.....	35
I.4.2 CRISPR/Cas.....	35
Chapter II: Aim of the study.....	38
Chapter III: Materials and methods.....	40
III.1 Materials	40
III.1.1 Surgery Materials.....	40
III.1.2 Induction of systemic and cortical EAE (cMS model)	42
III.1.3 Perfusion and immunohistochemistry.....	42
III.1.4 Viral labelling	44
III.1.5 Imaging.....	44
III.1.6 Single nuclei RNA sequencing	45
III.1.7 3'-Bulk RNA sequencing.....	47

III.1.8 CRISPR/Cas9	47
III.1.8.1 sgRNA design and testing <i>in vitro</i>	47
III.1.8.2 Viral labelling for <i>in vivo</i> use	50
III.1.9 PET scanning	52
III.1.10 CSF1R inhibitor and BTK inhibitor treatment.....	52
III.1.11 Software	52
III.2 Methods	53
III.2.1 Experimental Animals	53
III.2.2 c-MS Induction	54
III.2.3 Cranial window surgery	54
III.2.4 Two-photon <i>in vivo</i> microscopy	55
III.2.5 Immunofluorescence/ Immunohistochemistry.....	55
III.2.6 Confocal microscopy.....	57
III.2.7 Nuclei isolation and FACS sorting.....	58
III.2.8 sgRNA and plasmid cloning	59
III.2.9 Virus production	61
III.2.10 <i>In vitro</i> retroviral infection of HoxB8 cells.....	63
III.2.11 TIDE sequencing	63
III.2.12 AAV-induced CRISPR/Cas9 KO <i>in vivo</i>	64
III.2.13 3' bulk mRNA sequencing.....	65
III.2.14 Treatment with inhibitors of microglial activation	65
III.2.15 PET/CT imaging	65
III.2.16 Bioinformatic Analysis.....	66
III.2.17 Image analysis	67
Chapter IV: Results	71
IV.1 A mouse model of grey matter inflammation.....	71
IV.2 A mouse model of chronic grey matter inflammation.....	78
IV.3 Understanding neuronal pathology in MS: transcriptomics changes in the cMS model mapped together with MS patients	82
IV.4 Mechanistic dissection and therapeutic targeting of neuronal pathology in the cMS model ..	87
IV.4.1 CRISPR/Cas9 KO of candidates obtained from transcriptomic analysis	89
IV.4.2 Inhibiting microglial activation to prevent synapse loss in the cMS model.....	97
IV.5 PET/CT tracing of synapse loss	99
Chapter V: Discussion.....	103
V.1 Disease modeling of cortical MS pathology, advances and challenges	103

V.2 Mapping of patients' data sets and models as a potential bridge for better mechanistic understanding and therapeutic targeting	105
V.3 CRISPR/Cas9 KO as a method to understand candidates, mechanisms and determine therapeutic potential of candidate genes	107
V.4 Microglia phagocytosis blocking and its potentials in neuroinflammation.....	110
V.5 PET tracing as means to track MS progression but also to define good therapeutic administration time points.....	111
V.6 Concluding remarks	113
Chapter VI: References	114
Supplementary Data.....	130
Acknowledgements	138
List of publications	140
Curriculum vitae	141
Eidesstatliche Versicherung / Affidavit	143
Author contributions.....	144
Copyrights and Permissions	147

List of abbreviations

AD	Alzheimer's Disease
APC	Antigen Presenting Cell
BSA	Bovine Serum Albumin
c-MS	cortical MS
Cas	CRISPR-associated endonuclease
CFA	Complete Freund's Adjuvant
CIS	Clinically Isolated Syndrome
CNS	Central Nervous System
CRISPR	Clustered Regularly Interspaced Short Palindromic Repeats
crRNA	CRISPR RNA
CSF	Cerebrospinal fluid
CT	Computed tomography
DEGs	Differentially Expressed Genes
DIS	Dissemination in Space
DIT	Dissemination in Time
DMT	Disease Modifying Treatment
EAE	Experimental Autoimmune Encephalomyelitis
EBV	Epstein-Barr Virus
eCFP	Enhanced Cyan Fluorescent Protein
eGFP	Enhanced Green Fluorescent Protein
FACS	Fluorescence Activated Cell Sorting
FC	Fold change
GABA	γ -Aminobutyric Acid
i.c.	Intracerebral
Ifngr1	Interferon Gamma Receptor 1
IFN γ	Interferon- γ
KO	Knockout
KOFP	Kusabira Orange Fluorescent Protein
MBP	Myelin Basic Protein
MMF	Medetomidine-Midazolam-Fentanyl

MOG	Myelin Oligodendrocyte Glycoprotein
MRI	Magnetic Resonance Imaging
MS	Multiple Sclerosis
NAGM	Normal Appearing Grey Matter
NAWM	Normal Appearing White Matter
NFAT	Nuclear Factor of Activated T-cells
NGF	Nerve Growth Factor
NK	Natural Killer (cells)
NO	Nitric Oxide
Nrf2	nuclear factor erythroid-derived 2-like
NT	Non-targetted
PAM	Protospacer Adjacent Motif
PAFR	Platelet Activating Factor Receptor
PBS	Phosphate Buffered Saline
PBS-T	Triton X-100 in PBS
PCA	Principal Component Analysis
PET	Positron Emission Tomography
PLP	Proteolipid Protein
PNS	Peripheral Nervous System
PPMS	Primary Progressive Multiple Sclerosis
PSAP	Prosaposin
ROI	Region of Interest
ROS	Reactive Oxygen Species
ROSMAP	Religious Order Study
RRMS	Relapsing-Remitting Multiple Sclerosis
RyanR	Ryanodine Receptor
SCH	Spinal Cord Homogenate
sgRNA	Single-Guide RNA
snRNA-seq	Single Nucleus RNA sequencing
SPMS	Secondary Progressive Multiple Sclerosis
SUV	Standardized uptake values
SV2a	Synaptic Vesicle Glycorotein 2a

TIDE	Tracking of Indels by Decomposition
TNF α	Tumor Necrosis Factor α
tracrRNA	Trans Activating crRNA
UMAP	Uniform Manifold Approximation and Projection
VOI	Volume of Interest

Abstract

Multiple sclerosis (MS) is a chronic, inflammatory, and demyelinating disease of the central nervous system (CNS). It is characterized by formation of lesions both in white and grey matter. Upon disease evolution into progressive stages, grey matter pathology plays a larger role and permanent disability ensues.

Grey matter pathology of MS has been widely characterized through histopathological studies in terms of demyelination, neuronal pathology, and inflammation. However, the mechanisms that play a role in pathology development and progression are not fully understood. Furthermore, treatment options for progressive stages of MS are limited and we have no way of effectively blocking ongoing cortical neurodegeneration. Thus, my PhD project focused on modeling, visualizing, understanding, and therapeutic targeting of cortical grey matter pathology. To address these questions, I used a combination of confocal microscopy, multiphoton *in vivo* microscopy, bioinformatic transcriptomic analysis, CRISPR/Cas9 gene editing, and PET imaging.

The first part of my thesis aimed to establish a mouse model of grey matter pathology that resembled cortical pathology in MS. This model was induced in BiozziABH mice, which is a strain characterized by high antibody response and susceptibility to chronic CNS inflammation. Mice were immunized with MOG, followed by an intracerebral injection of pro-inflammatory cytokines to induce cortical lesions. Results suggest that our mouse model indeed presents with cortical grey matter demyelination, synapse loss and inflammatory lesions, which in turn, resembles previously described grey matter pathology in MS. Moreover, an age effect was observed in pathology resolution, with older mice displaying a more sustained neuroinflammatory response while younger mice spontaneously resolved inflammation. Further analysis of grey matter lesions revealed a potential role of synaptic calcium accumulation and phagocyte engulfment in neuronal pathology.

In the second part of the thesis, the focus was on investigating pathways and mechanisms underlying neuronal pathology in grey matter of MS. For this purpose, we utilized single nuclei transcriptomic analysis of our mouse model, which was further mapped together with data sets from MS patients. We aimed at determining a MS specific gene signature that was present both in our model as well as in patients with MS. To ensure MS specificity, we further analysed the enrichment of our cortical MS-related gene signature in an Alzheimer's disease patient data set. Our results demonstrated a species conservation of a cortical MS-related gene signature with five genes that are highly upregulated in neurons in the inflamed cortex of mice and humans that are interesting targets for further mechanistic analysis.

We subsequently aimed to establish a CRISPR/Cas9 system for neuron-specific gene knockout which could then be used for investigation of mechanisms and pathways by which our candidate genes might play a role in MS pathology. Using two of the target genes, we demonstrated that the CRISPR/Cas9 system was successful in knocking out genes in neurons. However, we were up to now not able to conclusively resolve the role our selected genes played in MS grey matter pathology.

In the next part of my thesis, we aimed to test different therapeutic strategies in our mouse model to determine if they would inhibit neuronal pathology in the inflamed grey matter or could rescue existing pathology. We tested immunomodulatory therapies targeting microglia

activation as a strategy to limit the induction of neuronal pathology and could show that CSF1R inhibition can prevent synapse loss in the cortical MS model.

Finally, we investigated imaging based approaches that could be used to track synaptic pathology in MS. For this purpose we performed a preclinical study with a SV2a specific PET tracer in our cortical MS model. PET imaging of mice demonstrated that the PET tracer was able to sensitively detect synapse loss in our model with the reduction in tracer uptake corresponding to the synaptic density decrease that was observed by histological examinations *in situ*.

Overall, the results obtained of my thesis provide new insights into the pathomechanisms underlying neuronal pathology in the grey matter, the therapeutic strategies that can be used to prevent it and the imaging strategies that can be used to track it in MS patients.

Zusammenfassung

Die Multiple Sklerose (MS) ist eine chronische, entzündliche und demyelinisierende Erkrankung des zentralen Nervensystems (ZNS), die durch die Bildung entzündlicher demyelinisierender Läsionen sowohl in der weißen als auch in der grauen Substanz gekennzeichnet ist. Dabei spielt bei fortgeschrittenem Krankheitsstadium die Pathologie der grauen Substanz eine größere Rolle und trägt wesentlich zur bleibenden Behinderung der Patienten.

Die Pathologie der grauen Substanz bei MS ist durch histopathologische Studien im Hinblick auf Demyelinisierung, neuronale Pathologie und Entzündung ausgiebig charakterisiert worden. Die Mechanismen, die bei der Entwicklung und dem Fortschreiten der Pathologie eine Rolle spielen, sind jedoch noch nicht vollständig geklärt. Darüber hinaus sind die Behandlungsmöglichkeiten für die fortgeschrittenen Stadien der Multiplen Sklerose begrenzt. Daher fokussierte sich meine Promotion auf die Visualisierung, das Verständnis und die Suche nach therapeutischen Strategien für die Pathologie der kortikalen grauen Substanz. Um diese Fragen zu klären, habe ich eine Kombination aus konfokaler und in vivo Multiphotonenmikroskopie, Einzelzell Transkriptomanalyse, CRISPR/Cas9-Gene Editing, und PET-Bildgebung eingesetzt.

Der erste Teil meiner Arbeit zielte darauf ab, ein Mausmodell mit MS ähnlicher Pathologie der kortikalen grauen Substanz zu entwickeln. Dieses Modell wurde in BiozziABH-Mäusen etabliert, einem Mausstamm, der sich durch eine hohe Antikörperreaktion und einen Krankheitsverlauf auszeichnet, der dem schubförmig-remittierenden Verlauf der MS ähnelt. Die Mäuse wurden mit MOG immunisiert, gefolgt von einer intrazerebralen Injektion von proinflammatorischen Zytokinen, um kortikale Läsionen zu induzieren. Die Ergebnisse deuten darauf hin, dass unser Mausmodell tatsächlich Läsionen der kortikalen grauen Substanz aufweist, die wiederum der zuvor beschriebenen Pathologie der grauen Substanz bei MS ähneln. Darüber hinaus wurde ein Alterseffekt auf den Zeitverlauf der Pathologie beobachtet, wobei ältere Mäuse eine länger anhaltende neuroinflammatorische Reaktion zeigten, während bei jüngeren Mäusen die Entzündung spontan abklang. Weitere Analysen der Läsionen der grauen Substanz ergaben eine zentrale Rolle der Phagozyten vermittelten Synapsenentfernung bei der neuronalen Pathologie in der entzündeten grauen Substanz.

Im zweiten Teil meiner Arbeit lag der Schwerpunkt auf der Untersuchung der Mechanismen, die der neuronalen Pathologie in der grauen Substanz zugrunde liegen. Zu diesem Zweck nutzten wir Einzelzell-Transkriptomanalysen aus unserem kortikalen MS Modell, die wir vergleichend mit entsprechenden Datensätzen aus MS-Patienten untersucht haben. Unser Ziel war es, eine MS-spezifische Gensignatur zu finden, die in unserem Modell vorhanden ist und gleichzeitig relevant für MS Patienten ist. Um die MS-Spezifität zu gewährleisten, haben wir zur Kontrolle die von uns identifizierte Gensignatur auch in einem Datensatz von Alzheimer-Patienten untersucht, in dem wir keine vergleichbare differentielle Regulation feststellen konnten.

Anschließend haben wir begonnen ein CRISPR/Cas9 System für einen Neuronen spezifischen Genknockout zu etablieren, um so besser untersuchen zu können, wie unsere Kandidatengene die neuronale Pathologie in der grauen Substanz beeinflussen können. Wir konnten bei zwei Zielgenen nachweisen, dass unser CRISPR/Cas9 System im Prinzip in der

Lage ist Gene in Neuronen ausschaltet, allerdings konnten wir die genaue Rolle dieser Gene in der Pathologie von MS bisher nicht abschliessend definieren.

Im nächsten Teil meiner Arbeit wollten wir verschiedene therapeutische Strategien in unserem Mausmodell testen, um zu ermitteln, ob diese die Entstehung der Pathologie der grauen Substanz verhindern können oder die bestehende Pathologie retten können. Wir testeten immunomodulatorische Therapien, die auf die Aktivierung von Mikroglia abzielen, und konnten zeigen, dass eine Inhibierung des CSF1R den Synapsenverlust im kortikalen MS Modell verhindern kann.

Schließlich wollten wir untersuchen, wie wir die synaptische Pathologie in MS Patienten sichtbar machen können. Dazu führten wir eine präklinische Studie mit einem SV2a spezifischen PET-Tracer in unserem kortikalen MS Modell durch. Die PET-Bildgebung zeigte dabei eine hohe Spezifität des PET-Tracers zur Bestimmung des Synapsenverlusts, der in seinem Umfang der *in situ* beobachteten Abnahme der synaptischen Dichte entsprach.

Zusammenfassend tragen die Resultate meiner Dissertation dazu bei unser Verständnis der Pathologie der grauen Substanz bei MS Patienten zu erweitern und zeigen Ansätze auf, die die Therapie und Diagnostik der neuronalen Pathologie verbessern können.

Chapter I: Introduction

I.1 Multiple sclerosis

Described over a hundred years ago by Charcot, Carswell, Cruveilhier and others, multiple sclerosis (MS) is as a chronic immune-mediated demyelinating and neurodegenerative disease of the central nervous system (CNS). MS is a heterogenous multi-factorial inflammatory disease, which is caused by complex interactions between genetic and environmental factors. In MS, demyelinating lesions are formed in the white and grey matter of the brain and spinal cord, which in time lead to axonal loss and neurological deficits (Carswell, 1838, Pearce, 2005, Filippi et al., 2018). Beginning in early adulthood, MS is the most common non-traumatic cause of disability in young adults, with 50% of the patients needing help walking after 10-15 years of disease onset (Kamm et al., 2014, Noseworthy et al., 2000, Weinshenker et al., 1989). The cause for MS has not yet been elucidated, which makes treatments for MS focus on modifying the disease rather than targeting the cause to eradicate or alleviate disease symptoms.

I.1.1 Epidemiology

MS is one of the most intensely studied diseases in terms of epidemiology. In MS, both genetics and environmental factors play a role. Disease onset starts at 20 to 35 years of age for relapsing-remitting MS (RRMS), while primary progressive MS (PPMS) has a disease onset at around 40 years of age. However, up to 10% of patients with RRMS had their initial demyelination event before the age of 18 (Filippi et al., 2018, Yeshokumar et al., 2017). Following MS onset, patients are expected to survive approximately ~20-45 years. MS patients have a reduced life expectancy of 6-10 years compared to the general population (Bronnum-Hansen et al., 2004, Kamm et al., 2014, Leray et al., 2016).

The ratio of MS incidence between females and males has increased over time, with it being 3:1 currently. This relationship is observed specifically for RRMS, which might be caused by altered female responses to environmental factors. However, males are more likely to have a progressive disease, brain atrophy, accumulation of disability and worse recovery from initial attacks (Bove and Chitnis, 2013, Bove and Chitnis, 2014).

MS has a heterogenous geographic distribution. It is more prevalent in North America and Europe and least frequent in East Asia and sub-Saharan Africa. In Europe, prevalence has a North-South gradient, with Scandinavian countries and the United Kingdom having a greater MS predominance than more Mediterranean countries like Italy, Greece and Spain (Leray et al., 2016).

Due to the geographic distribution of MS and as the world has become more globalized, migration studies started to be conducted to determine its effects in MS onset. Early studies showed that migration of Northern Europeans to Israel or South Africa, particularly under the age of 15, would decrease their risk of developing MS compared to the risk in their native countries. However, if migration occurred after the age of 15, they would maintain the risk seen in their native countries (Alter et al., 1966, Dean and Kurtzke, 1971). Later studies showed that MS risk decreased upon migration from the United Kingdom and Ireland to Australia, regardless of age of migration (Hammond et al., 2000). A recent study suggests that region of origin of migrants rather than age of migration plays a role, suggesting that migrants from Middle Eastern countries have a higher risk of developing MS and that longer

residence in Canada was associated with higher risk independently of the age of migration. These studies suggest that environmental factors contribute to MS risk (Rotstein et al., 2019).

Even though the cause of MS is not known, several genetic and environmental factors have been shown to increase the risk of MS. Environmental factors which increase the risk of MS include smoking, low vitamin D levels, lack of sun exposure, obesity during adolescence and Epstein-Barr virus (EBV) infection. In fact, a recent study suggests that infection with EBV increases the risk of MS by 32-fold, which is not the case for other viral infections. Furthermore, this study shows that nearly all subjects who developed MS had previously been infected with EBV (Bjornevik et al., 2022, Filippi et al., 2018, Kamm et al., 2014, Olsson et al., 2017). Genetic factors can also confer risk of MS in a heritably polygenic manner, meaning risk increases upon polymorphisms in several different genes which all confer a small risk increase. Genome-wide association studies have identified over 200 genes that can pose as risk variants, many of which are part of the HLA locus. Genetic polymorphisms in genes involved in T-cell proliferation and activation (IL2, IL7R) as well as genes in other components of adaptive and innate immunity like TNF associated and modulatory genes have also been observed to increase the risk of MS (Baranzini and Oksenberg, 2017, Filippi et al., 2018, Olsson et al., 2017). Although many factors have been identified to increase MS risk, no genetic or environmental factor per se can be determined as a disease cause.

I.1.2 Pathology

The key pathological hallmark of MS are inflammatory demyelinating lesions in the CNS. Within the lesions, a marked area of myelin loss can be observed as well as axonal injury and a glial scar. Lesions usually surround one or several vessels and have inflammatory cells that are perivascular but can also infiltrate the parenchyma. The inflammatory cell types around lesions vary depending on whether lesions are active or inactive (Lassmann et al., 2001, Noseworthy et al., 2000, Ontaneda et al., 2017). During the early stages of the disease in the RRMS form, pathology is dominated by focal inflammatory lesions, however as disease progresses diffuse lesions in the grey matter and white matter are accompanied by microglial activation and neurodegeneration (Figure 1) (Kamm et al., 2014, Lucchinetti et al., 2011, Ontaneda et al., 2017). White and grey matter pathology in MS is thought to be relatively independent from each other and can therefore be studied separately as they might be guided by different underlying mechanisms (Calabrese et al., 2012, Trapp et al., 2018).

I.1.2.1 White matter

MS has long been considered a disease of the white matter. During the early stages of the disease (clinically isolated syndrome or RRMS) focal active demyelinating lesions can contain dense macrophage and lymphocyte (particularly CD8+ T-cells) infiltration, activated microglia and sometimes reactive astrocytes (Filippi et al., 2018, Schumacher, 2017). Active plaques can be usually distinguished by their dense infiltration of macrophages, which contain myelin degradation products (Frischer et al., 2015). As the disease progresses, slowly expanding plaques can be recognized by some axonal transection and their inactive core, with little macrophages, surrounded by activated microglia. In progressive stages of the disease, diffuse white matter pathology with inactive lesions and shadow plaques have been observed. Inactive lesions have well defined demyelination, decreased axonal density, reactive gliosis and some microglia activation in the peripheral white matter. Shadow plaques refer to lesion sites where remyelination and reparative processes have taken place. The

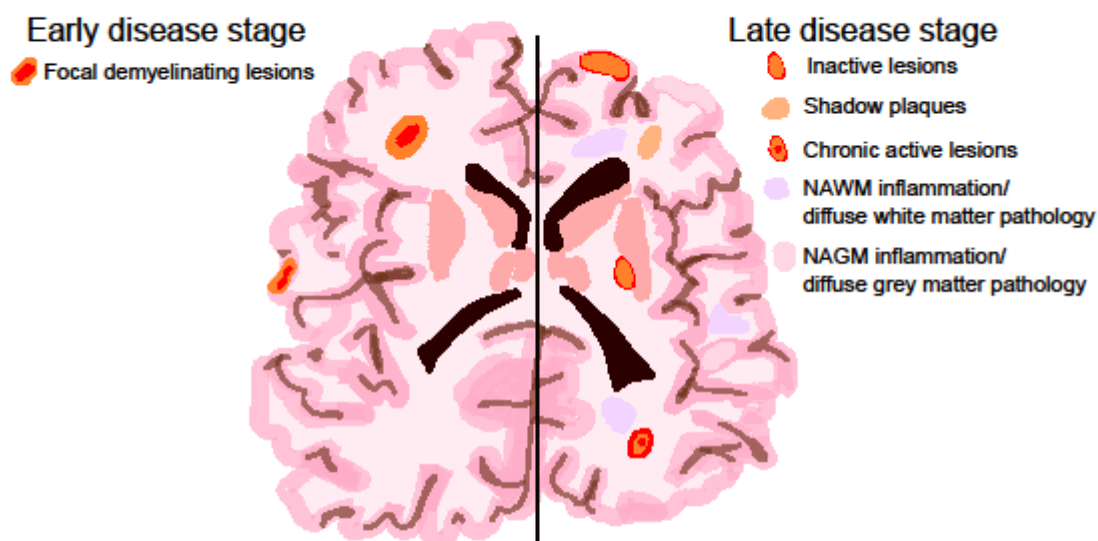


Figure 1: Pathology of early and late Multiple Sclerosis. In early stages of the disease (left), focal demyelinating lesions in the white and grey matter can be observed. In later stages of the disease (right), pathology becomes more complex with a mixture of inactive lesions, chronic active lesions, shadow plaques, as well as diffuse white and grey matter lesions being found. Figure created by Emily Melisa Ullrich Gavilanes.

remyelination efficiency of the plaques varies greatly among patients and locations within the CNS and therefore provides the appearance of a ‘shadow’ at a previously active lesion site. Chronic active plaques can also contain macrophages at the edge of the lesion and some at the lesion core (Filippi et al., 2018, Frischer et al., 2015, Schumacher, 2017). Inflammatory activity continues with disease progression and in progressive MS patients, inflammatory markers can be encountered in normal appearing white matter (NAWM) which is not observed in controls. In NAWM there is an influx of inflammatory cells, microglia activation and neuronal damage. Swelling and fragmented axons are found in the NAWM to an extent that is not correlated to white matter lesions (Kutzelnigg et al., 2005).

Peripheral immune cell activation and infiltration is an important part in lesion formation in MS. The CNS is an immune-privileged site, meaning that after development it is sealed off and separated by the blood brain barrier (BBB), which then restricts and can tightly regulate trafficking of molecules and cells into the CNS (Pachter et al., 2003). In MS, however, the BBB becomes permeable in both lesioned and periventricular NAWM. Patients with recent relapses showed a more permeable BBB than patients whose relapses were further removed in time (Cramer et al., 2014). This permeability is caused by differential expression of pro-inflammatory cytokines, chemokine receptors and integrins e.g. by infiltrating TH-17 lymphocytes which allows the subsequent infiltration of macrophages and plasma cells. CNS resident immune cells can also secrete inflammatory mediators that recruit inflammatory cells. This pro-inflammatory environment created can be sensed by immune cells and CNS

resident cells, which then altogether contribute to the axonal and neuronal damage observed in MS pathology (Filippi et al., 2018, Frischer et al., 2009, Reboldi et al., 2009).

I.1.2.2 Grey matter

While white matter changes are an important factor in the manifestation of MS, grey matter pathology is what determines the prognosis and the cognitive symptoms of a patient (Calabrese et al., 2012, Kutzelnigg and Lassmann, 2006). During the early stages of the disease, clinically isolated syndrome (CIS) or RRMS, focal demyelinated lesions occur in the grey matter where they can affect the cortex, frequently are located in the sulci, but can be distributed anywhere in the brain such as the thalamus, basal ganglia or hippocampus. These lesions are small intracortical and perivenous lesions (Geurts et al., 2007, Haider et al., 2016, Kutzelnigg and Lassmann, 2006, Lucchinetti et al., 2011). During the progressive stages of the disease, brain atrophy and neuronal degeneration have been observed. At this stage patients have more band-like subpial demyelinating lesions which affect the cortical gyrus or can extend to multiple adjacent gyri. These lesions affect the basis of cortical sulci, especially deep infoldings of the brain surface like the insular cortex. Furthermore, subpial lesions in progressive MS can have different cortical depths with some of them affecting three to four layers of the cortex, while larger lesions affect the entire cortical layering. Subpial demyelination also is associated with meningeal immune cell infiltration including macrophages, plasma cells, T- and B-lymphocytes (Kutzelnigg and Lassmann, 2006, Lucchinetti et al., 2011, Schumacher, 2017). A third type of lesion in the grey matter are leukocortical lesions, located at the interface between grey and white matter. These lesions are the easiest to identify in patients with the use magnetic resonance imaging (MRI) and can help predict cognitive deficits (Dutta and Trapp, 2007, Forslin et al., 2018).

Two different patterns of neurodegeneration have been observed in the cortex of MS patients: retrograde degeneration due to axonal injury in the white matter, and oxidative injury in cortical neurons. It has been proposed, that particularly in the progressive stages of MS, demyelination and neurodegeneration, including axon and dendrite damage, are driven by microglial activation, production of reactive oxygen species (ROS) and oxidative damage (Fischer et al., 2013, Haider et al., 2016). In progressive stages of MS, diffuse grey matter neurodegeneration with pronounced dendritic synaptic loss in both demyelinated but also normal appearing grey matter (NAGM) has been observed (Jurgens et al., 2016). CUX2 projection neurons in the upper layers of the cortex have been found to be vulnerable and lost in MS, when surrounded by meningeal inflammation, and express an upregulation of stress pathways. In the rims of MS plaques, reactive astrocytes, stressed oligodendrocytes and activated microglia could be observed (Schirmer et al., 2019). Although cortical lesions in patients, contain less inflammation than white matter lesions, significant neuronal injury occurs in them. Many neurofilament positive swellings could be noted along dendrites and axons, in the presence of activated microglia, suggesting microglial association with neuronal pathology. Microglia cells would extend processes to neuronal cell bodies and contact dendrites and axons, however they did not associate with transected neurites in cortical lesions (Dutta and Trapp, 2007).

Cortical inflammatory lesions in MS and its associated neuronal damage are more correlated to physical and cognitive disability progression in MS. As such, grey matter lesions contribute

to the disease burden of MS and are thereby critical to be further studied (Calabrese et al., 2012, Dutta and Trapp, 2007).

I.1.3 Clinical course

Diagnosis of MS is usually done through a combination of clinical criteria with input from imaging and other paraclinical studies. Four subtypes of MS have been defined based on the clinical course of the disease (Figure 2). The initial stages of MS begin with clinical manifestations of usually reversible episodes of neurological deficits. These episodes can last days or weeks and usually will be defined as CIS, if single, or if recurring, as part of RRMS where every episode qualifies as a relapse. In time, for about 70% of patients, some neurological deficits become permanent. A progression of clinical disability is common after 10-15 years, marking the disease progression into secondary progressive MS (SPMS). For about 15% of patients the progressive nature of the disease starts at onset leading to what is known as PPMS (Filippi et al., 2018, Lublin et al., 2014, Ontaneda et al., 2017).

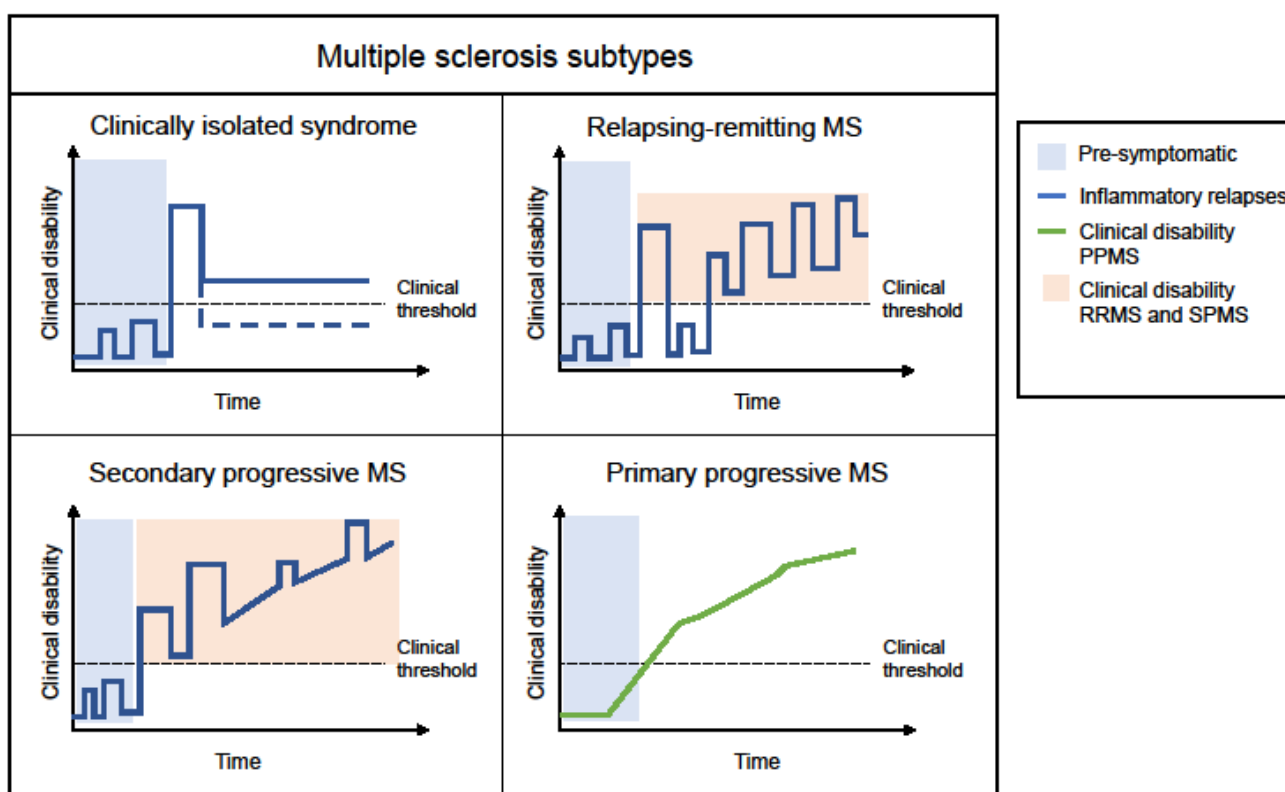


Figure 2: Clinical disease subtypes of Multiple Sclerosis. Multiple sclerosis has been defined to have 4 clinical subtypes: Clinically isolated syndrome (CIS) with partial (solid-line) or full remission (dashed line) of symptoms (top left). Relapsing Remitting MS (RRMS) with relapses with partial or full remissions interspersed with periods of stability (top right). Secondary progressive MS (SPMS) with an initial relapsing and remitting phase followed by continuous symptom worsening and increasing disability (bottom left). Primary progressive MS (PPMS) an aggressive disease course with continuous symptom worsening and disability accrual from disease onset (bottom right). Figure inspired and modified from nationalmssociety.org (Lublin et al., 2014)

The different subtypes of MS can be classified as active or inactive based on clinical assessment of relapse or on MRI activity. MRI has a high-sensitivity for detecting disease-associated demyelinating lesions and is therefore helpful for diagnosis of MS but also to track disease progression. Critical factors in MS diagnosis and progression are demyelinating lesion dissemination in time (DIT) and dissemination in space (DIS), which can be tracked using MRI. CIS is the first clinical presentation of a disease with demyelinating lesions that can resemble MS. Coupled with MRI lesions, CIS has a high risk to meet criteria to diagnose the disease as MS. In MS, gadolinium-enhancing lesions or enlarging T2 lesions can be observed in MRI and coupled with clinical symptoms can result to the diagnosis of RRMS, SPMS or PPMS. Patients who show gadolinium-enhancing lesions within a year with lesion DIT or DIS are considered to have an active disease course, while inactive lesions without clinical symptoms can be considered as non-progressing disease (Filippi et al., 2018, Lublin et al., 2014). Although different disease subtypes have been denoted for MS, the distinction between them is not well defined, particularly between RRMS and SPMS where a transition time cannot be easily pinpointed. Thereby, MS could also be considered a dynamic disease where some clinical symptoms overlap with different disease sub-types which would consider clinical variability observed in different patients (Krieger et al., 2016).

I.1.4 Age as a risk factor for MS progression

Ageing is one of the biggest risk factors for many neurodegenerative diseases (Ganz et al., 2018, Hou et al., 2019, Wyss-Coray, 2016). While most neurodegenerative diseases are diagnosed in aged individuals, MS is most commonly diagnosed in individuals aged 20 to 40 (Malecka et al., 2021). Age of diagnosis, however, plays a role in MS as disease onset in older individuals is associated with shorter times to disability (Scalfari et al., 2011, Confavreux et al., 2003). MS onset in middle-aged individuals, between 40 and 50, can duplicate or even triple the risks of developing secondary progressive MS compared to individuals with onset at age 20. Moreover, with increasing age at diagnosis, there is a higher proportion of patients that develop primary progressive MS (Scalfari et al., 2011). Age also influences transition from RRMS to progressive phases in MS, as this happens more often in the fifth decade. Even though clinical disease activity decreases with age, so does the potential of recovery following relapses as well as the efficacy of disease modifying treatments (Zeydan and Kantarci, 2020).

The disease course of MS can be affected by senescence associated mechanisms taking place in patients during ageing processes. Changes in immune activation with age, for example, can limit immunomodulation in the CNS and lead to worse recovery from relapses. MS itself has been observed to cause alterations to the immune system, leading to premature senescence, possibly as a result of recurrent antigen exposure and chronic immune stimulation. Moreover, middle-age associated changes in microglia function have been observed leading to altered responses to CNS demyelination, which can contribute to neurodegeneration (Zeydan and Kantarci, 2020, Klein et al., 2018). Furthermore, CNS integrity and structural reserves decrease with age. Decline in white matter integrity can play a role in the transition to the progressive MS phase, as well as to limitations in recovery (Tutuncu et al., 2013, Zeydan and Kantarci, 2020). Aging, therefore, should be considered an important target in MS research in order to improve recovery, prevent disease progression and disability accrual.

I.1.5 Treatments

Despite extensive research in MS, no established cause or cure for the disease has been found. Treatment of MS has focused on immunomodulating, and immune-suppressive agents meant to dampen the inflammation caused in MS. Many treatments that are disease modifying can also delay the progression of the disease (Gholamzad et al., 2019). Although progressive MS has potential for higher disease burden and cognitive decline, most existing MS treatments are meant to target the relapsing remitting state of the disease and are much less efficient in targeting the progressive stages of the disease (Ontaneda et al., 2017).

Initial first line injectable disease modifying treatments (DMTs) for RRMS were developed in the 1990s with interferon-beta1b showing a reduction in relapse frequency for one third of patients and decreasing the risk of disease progression. Interferon-beta 1 among others downregulates the expression of proinflammatory cytokines while increasing the expression of anti-inflammatory cytokines. It can further reduce the trafficking of inflammatory cells across the BBB and increase nerve growth factor (NGF) production (1993, Kieseier, 2011, Paty and Li, 1993). Within a couple of years, glatiramer acetate, an analog of myelin basic protein (MBP), was tested as well and showed a decrease in relapse rate in patients. However, no effect was found on disease progression (Johnson et al., 1995, Johnson et al., 1998, Tselis et al., 2007). Following these two therapies, mitoxantrone, a second-line therapy, was developed and used for patients who had more aggressive forms of RRMS or SPMS and use of first line therapy was unsuccessful. As a cytotoxic immunosuppressive therapy, mitoxantrone causes the inhibition of DNA synthesis and repair. Therefore, it inhibits T-cell activation, T- and B-cell proliferation and antibody production (Hartung et al., 2002).

Several oral therapies were subsequently introduced for RRMS treatment. Fingolimod, the first, is a functional antagonist of the sphingosine-1-phosphate type 1 receptor and allows its internalization in lymphocytes. This leads to lymphocyte sequestration in the lymph nodes. Fingolimod patients showed significant decrease in relapse rates and a decrease in disability progression (Kappos et al., 2010). Teriflunomide, a reversible inhibitor of the mitochondrial enzyme dihydroorotate dehydrogenase, reduced T- and B-cell activation, proliferation, and response to autoantigens. Moreover, Teriflunomide reduced relapse rates, MRI evidence of disease activity, and in some cases disability progression in patients when compared to placebo (O'Connor et al., 2011). Dimethyl fumarate, an antioxidant which activates the nuclear factor erythroid-derived 2-like (Nrf2) pathway thereby creating an anti-inflammatory effect, provides a significant decrease in relapse rate as well as disease activity measured by MRI (Gold et al., 2012). Oral medications, while safe and well tolerated also come with adverse effects for example in the gastrointestinal tract (Craddock and Markovic-Plese, 2015).

Therapeutic focused research subsequently moved towards using monoclonal antibodies to target RRMS due to their selectivity and higher efficiency as potential second-line therapies. Natalizumab, a humanized monoclonal antibody that targets alpha4 integrin in the antigen-4 adhesion molecule, prevents migration of leukocytes through the BBB. A reduced risk of sustained disability progression and reduced relapses in RRMS patients was observed upon Natalizumab treatment. However, Natalizumab treatment has been associated with multifocal leukoencephalopathy, a CNS infection caused by a pathogenic form of the JC virus. As Natalizumab treatment causes reactivation of the virus, an assay to detect if a patient is a

carrier of the JC virus should be performed before considering Natalizumab treatment (Polman et al., 2006, Sorensen et al., 2012). Alemtuzumab is a humanized monoclonal antibody directed against CD52 which leads to the depletion of T- and B- lymphocytes in an antibody dependent cell mediated cytolysis. Alemtuzumab was more effective than interferon-beta in patients with early RRMS, leading to reduced relapses, decreased disability accumulation and improvement in the disability score (Freedman et al., 2013, Investigators et al., 2008). Rituximab, a chimeric anti-CD20 monoclonal antibody causing B cell depletion, showed significant reduction in relapses and in MS lesion activity. The success of Rituximab in targeting RRMS further establishes a role of B-cells in RRMS. Despite promising results, the manufacturers of Rituximab decided to not continue to seek FDA approval for MS treatment (Craddock and Markovic-Plese, 2015, Hauser et al., 2008). Ocrelizumab, a humanized anti-CD20 monoclonal antibody, was pursued instead of Rituximab, as it was less immunogenic and associated with more antibody dependent depletion of B-cells rather than the complement dependent depletion used by Rituximab. Ocrelizumab was observed to have a pronounced depletion of relapses and MRI activity also compared to Interferon-beta1a (Kappos et al., 2011). Ofatumumab, another anti-CD20 monoclonal antibody also resulted in a strong decrease in MRI observed lesions in patients with MS. Ofatumumab, in contrast to other anti-CD20 antibodies, provided the benefit of being administrated subcutaneously and therefore can be self-administered by patients (Kang and Blair, 2022, Sorensen et al., 2014). Ublituximab, a recently tested anti-CD20 antibody, has an enhanced affinity for CD16A and activates natural killer (NK) cells thereby promoting antibody-dependent NK cell-mediated cytolysis of B-cells. Ublituximab treatment, resulted in lower relapse rates and decreased MRI detected lesions in patients with RRMS than those treated with teriflunomide (Steinman et al., 2022). Multiple monoclonal antibodies are still being studied and currently tested for treatment of MS with some having positive effects and thereby showing promise for therapeutic approval in the coming years.

As was previously described, therapeutic progress in MS has mostly been achieved in RRMS with varying degrees of success being obtained in progressive disease stages. Drugs previously established for RRMS have been tested for their effects in progressive MS. Interferon beta-1 therapies showed mixed results: while some had positive results (1998, Cohen et al., 2002), others presented negative results (Andersen et al., 2004, Panitch et al., 2004). Glatiramer acetate therapy in patients with PPMS also showed negative results (Wolinsky et al., 2007). Similarly, while Fingolimod showed reduction in MRI lesions, it did not inhibit disease progression (Lublin et al., 2016). Natalizumab treatment of SPMS patients, had mixed results. Even though it did not have an effect in worsening of disability, a benefit was observed on the progression of the upper-limb disease component (Kapoor et al., 2018). Rituximab treatment in PPMS patients showed no effect in confirmed disease progression, however upon subgroup analysis, it was promising in younger patients under 50 years of age (Hawker et al., 2009). A subsequent study using Ocrelizumab in young PPMS patients with higher inflammatory lesions, showed a decrease in MRI activity and disease progression. Age might therefore be an important factor to consider for the successful treatment of progressive MS (Montalban et al., 2017).

Due to the limited success of anti-inflammatory drugs in progressive MS, other therapeutic approaches might need to be developed. Neuroprotective strategies, for example, have demonstrated some promising results when it comes to disability progression and brain

atrophy. Simvastatin, a drug which has immunomodulatory and neuroprotective properties, reduced the brain atrophy in SPMS patients (Chataway et al., 2014). Biotin, at high doses has been suggested to enhance cellular energy production leading to decreased neurodegeneration, improved axonal function and promotes remyelination. Treatment with Biotin, lead to a reversal and reduction in disability in some MS patients (Sedel et al., 2016, Tourbah et al., 2016), however a subsequent trial showed no association of high-dose biotin with disability improvement (Couloume et al., 2020). Further treatment strategies that are being studied include repair promoting therapeutics that stimulate remyelination, the transplantation of stem cells which can then act as tissue protective, and therapies that focus on targeting known mechanisms of progressive MS (Ontaneda et al., 2017). Therapies for progressive MS are still not well defined nor successful in preventing progress of disability for patients. Therefore, more studies that elucidate the pathomechanisms taking place in these stages of the disease are important to help targeting of said mechanisms and development of better therapeutic strategies for progressive MS.

Based on the number of available drugs and treatments for MS and their different impact on patients, the American Academy of Neurology (Rae-Grant et al., 2018), and the European Committee of Treatment and Research in Multiple Sclerosis (Montalban et al., 2018) published American and European guidelines for the treatment of MS patients. In this way, they aimed to create a standard of recommendations for physicians to follow that would take into account all disease-modifying drugs and would make suggestions when to use a specific therapy. These guidelines have allowed for homogenous treatment of MS across America and Europe and are meant to continuously get updated to reflect the current status of drug development for MS.

I.1.6 MS animal models

Animal models of MS have played an important role in helping to understand the pathogenesis and mechanisms that are at play during the onset and progression of the disease. MS is a complex disease, and as such, no single animal model is able to reproduce all of its characteristics. However, they serve as tools to study disease development, the pathogenic mechanisms of the disease and developing therapeutic approaches (Procaccini et al., 2015). Most animal models are rodent models, but also zebrafish and marmoset models of MS are used to study the disease (Burrows et al., 2019, Hart et al., 2000).

The most commonly used MS animal model is the experimental autoimmune encephalomyelitis (EAE) rodent model. EAE is an induced model, in which the interaction of immune and neuropathological mechanisms leads to a disease that shares the key pathological features of MS including inflammation, demyelination, gliosis and axonal loss. The mechanisms of remyelination and the resolution of inflammation observed in some MS lesions can also be noted in the EAE model, making it a good model for these characteristics as well (Constantinescu et al., 2011). There are two main methods of EAE induction: immunization with CNS peptides and adoptive transfer of encephalitogenic T-cells. CNS peptides commonly used are the myelin oligodendrocyte glycoprotein (MOG), myelin basic protein, proteolipid protein (PLP), and spinal cord homogenate (SCH). For immunization, the peptide used is usually emulsified in complete Freund's adjuvant (CFA), containing *mycobacterium* to increase induction efficiency (Burrows et al., 2019, Constantinescu et al., 2011). Pertussis toxin is sometimes also used to help disrupt BBB integrity, thereby

increasing immunization efficiency (Linthicum et al., 1982). Immunization induces activation of myelin antigen specific T-cells, their proliferation and differentiation into effector T-cells. Effector T-cells cross the BBB and get re-activated in the CNS by resident myelin antigen presenting cells (APCs) (Kawakami et al., 2004). Effector T-cells then release pro-inflammatory cytokines like Interferon- γ (IFN γ), tumor necrosis factor- α (TNF α), and IL-17, which in turn recruits further immune cells like macrophages and neutrophils into the CNS and leads to the destruction of the myelin sheaths (Burrows et al., 2019, Lees et al., 2008). Destruction of myelin sheaths causes ascending paralysis in the animals starting at the tail, then progressing to the hindlimbs and finally the upper limbs (Johnson et al., 2010). A further method to induce EAE is adoptive transfer of T-cells. Initially performed in rats, in this method antigen-specific T-cells are isolated or generated, proliferated *in vitro* and subsequently intravenously injected into a naive animal. This transfer of T-cells is enough to cause an EAE disease course. The T-cell transfer model has been used to study antigen specificity and T-cell patterns during EAE (Ben-Nun et al., 1981, Lohse et al., 1989).

EAE induced by immunization has been used to generate mouse models, rat models and non-human primate models. Although the rodent models are among the most used, the marmoset, a non-human primate, EAE model has been used as a last step for treatment testing in MS due to the higher degree of similarity between primates and humans. The marmoset model is induced in a very similar manner to the rodent models, develops in nearly 100% of immunized animals and shows clinical signs similar to RRMS or PPMS which can be followed via MRI. Despite the advantages of using marmosets, due to ethical, availability and cost considerations, this model is not used for preclinical studies but rather for testing of therapeutic efficiency and dosage of new drugs targeting MS (Burrows et al., 2019, Hart et al., 2000).

Besides the EAE model for MS, different models exist to study particular phenotypes such as demyelination and remyelination. Toxin models of demyelination are used to study the processes and mechanisms taking place during de- and remyelination and are induced commonly by cuprizone or lysolecithin (Procaccini et al., 2015). Cuprizone-induced demyelination, initially described in the 1960s, causes microscopic lesions in the cerebellar cortex as well as non-inflammatory demyelination (Carlton, 1966). Cuprizone, a copper chelator, causes specific oligodendrocyte dystrophy and death, followed by demyelination. Subsequently, axonal pathology can be observed, even two weeks after cuprizone removal from diet, in addition to remyelination (Burrows et al., 2019, Stidworthy et al., 2003). Lysolecithin is a phospholipase A2 activator which induces demyelination in specific areas when injected to the spinal cord. A week after lysolecithin injection, small amounts of extracellular myelin debris were observed as remyelination processes began, which then advanced rapidly (Jeffery and Blakemore, 1995). Demyelination occurs due to primary toxic effects of the solution on the myelin sheaths. The compact myelin sheaths start splitting following the injection of lysolecithin and then degrade around the undamaged axons (Hall, 1972). Toxin induced demyelination, although good to study the mechanisms that are involved in de and re-myelination, does not replicate more of the disease pathology and the complex interplay of cells that is involved in MS (Procaccini et al., 2015).

Even though EAE is a good model for MS, its primary site of lesion induction is in the spinal cord white matter tracks while the cerebral cortex remains mostly intact (Lassmann and Bradl, 2017). In order to study cortical grey matter pathology, different models have been developed

and explored. A Lewis rat model of T-cell transfer, using T-cells directed against β -synuclein, a neuronal specific protein, resulted in grey matter inflammation which included gliosis neuronal destruction and brain atrophy (Lodygin et al., 2019). Other models, however, have focused on mimicking the pro-inflammatory cytokine milieu that exists in grey matter pathology. To recreate this milieu in a mouse model, pro-inflammatory cytokines were injected, TNF α and IFN γ , into the right motor cortex of rMOG₁₋₁₂₅ immunized Th/+ mice which have a B-cell receptor transgenic for a MOG-specific demyelinating antibody. Subpial and cortical demyelination was most pronounced at day 5 following the pro-inflammatory cytokine injection (Lagumersindez-Denis et al., 2017). A model in rats uses a stereotactic injection of IFN γ and TNF α into the cortex of Lewis rats which were previously sub clinically immunized with a MOG-CFA emulsion. Following the stereotactic intracortical injection, the rats would present cortical lesions similar to those in MS patients, as well as intracortical and subpial demyelination, infiltration of immune cells, acute axon damage and neuron death (Merkler et al., 2006). This rat model was adapted by our group into a mouse model using MOG immunized mice with a *BiozziABH/ C57BL6J* background and cortically injecting them with pro-inflammatory cytokines TNF α and IFN γ , and its characterization is part of the work in this thesis.

1.2. Synapse loss as a neuropathological hallmark

Following injury or an inflammatory insult, pathological processes occur in neurons leading to their dysfunction and possible degeneration such as axonal pathology including axon degeneration, synapse loss and neuron cell death (Figure 3). While these features all lead to neuropathology, here we will focus on synapse loss.

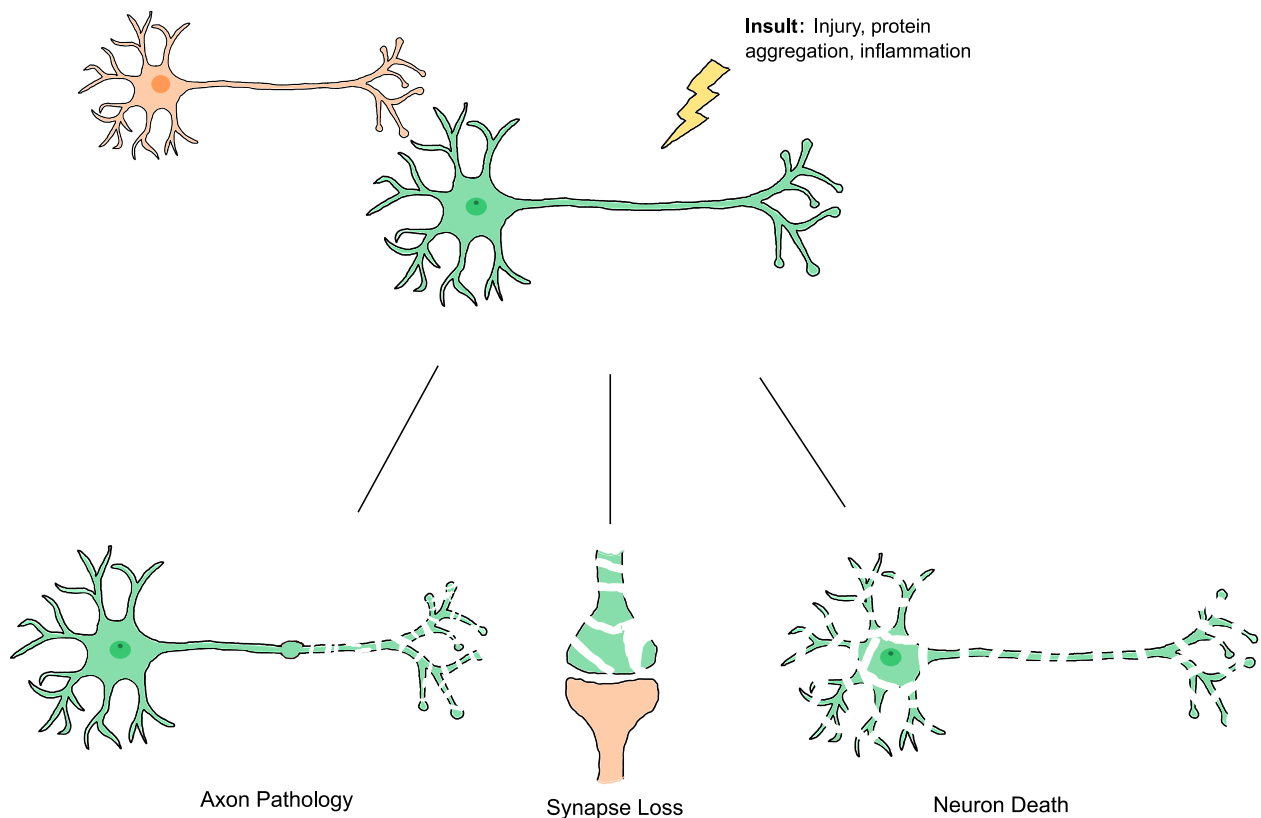


Figure 3: Types of neuropathology include axon pathology, synapse loss and neuron death.

Upon insult into neurons, it being an injury, pathogenic protein aggregation or neuroinflammation, neurons can undergo pathological mechanisms leading to degeneration and swelling of axons, loss of dendritic spines or axonal boutons, or neuronal death. Figure created by Emily Melisa Ullrich Gavilanes.

Synapse loss is a process that has been extensively studied due to its role in both physiological and neuropathological processes.

In the early stages of development, a high density of synapses is observed when compared to adult brains. These synapses, however, have a different morphology, more consistent with immature synapses. During development, synapses undergo a process of activity-based selection, which leads to the pruning of excess synapses. Selective elimination of overproduced synapses during childhood, adolescence, and sometimes even early adulthood, allows for maturation and maintenance of active synaptic spines as well as the stabilization of synapses during adulthood (Changeux and Danchin, 1976, Huttenlocher, 1979, Petanjek et al., 2011). A correct balance in synapse formation and elimination is necessary to ensure proper brain development and function, as changes in these dynamics can lead to neuropathological processes and cognitive impairment (Cardozo et al., 2019, Feinberg, 1982, Geinisman et al., 1986, McWilliams and Lynch, 1984). Increased synapse loss has been described in multiple psychiatric disorders (Cagnoli et al., 2012, Feinberg, 1982, Glantz and Lewis, 2000, Sellgren et al., 2019), neurodegenerative diseases (Dauer and Przedborski, 2003, Lui et al., 2016, Murmu et al., 2015), and in the context of brain neuroinflammation (Eccles et al., 1966, Mock et al., 2021, Terry et al., 1991).

1.2.1 Synapse loss in neuroinflammation

Synapse loss was described as a consequence of ischemia as early as 1966 in the cat spinal cord (Eccles et al., 1966). Synapse loss can contribute to disability observed in patients after stroke, thus the recovery of lost synaptic contacts has been proposed as a therapy to help functional recovery of stroke patients (Hasbani, 2000). This potential therapeutic effect has lately led to the development of positron emission tomography (PET) tracers that can help track synaptic numbers in patients of stroke (Lyu et al., 2020).

In AD synaptic loss has been a thoroughly studied topic due to its high correlation with cognitive impairments observed in patients. This correlation was much stronger than that observed with plaque deposition or the presence of neurofibrillary tangles, and thus led to in depth studies of synapse loss in the neuroinflammatory conditions observed (DeKosky et al., 1996, Terry et al., 1991).

An increasing number of studies have also been conducted on synapse loss in MS as this phenomenon has been widely observed not only in patients, but also in the mouse EAE model used to mimic the disease pathology of MS (Jurgens et al., 2016, Petrova et al., 2020, Ziehn et al., 2010, Zoupi et al., 2021). Post-mortem studies of MS patients' tissue have revealed that 58-96% of synapses are lost throughout the spinal cord of patients in demyelinating lesions (Petrova et al., 2020). In the brain grey matter, studies have shown significant dendritic spines loss in the demyelinated cortex and in NAGM of the insular and

frontotemporal lobe (Jurgens et al., 2016); loss of synapses in neocortical lesions of the superior frontal gyrus, the precentral and the post central gyrus (Wegner et al., 2006); and loss of presynaptic input of glutamatergic and GABAergic synapses in lesioned grey matter, NAGM in cortical regions and in layer V cortical regions of the inferior frontal sulcus and the superior temporal sulcus (Vercellino et al., 2022). Furthermore, synapse loss has also been identified in the hippocampus (Dutta et al., 2011, Michailidou et al., 2015, Papadopoulos et al., 2009), cerebellum (Albert et al., 2017), and thalamus (Werneburg et al., 2020). Synapse loss can be considered an important part of the pathology of MS, as well as of multiple neuroinflammatory conditions and thus could play an important role as a target for therapies meant to reduce neuroinflammation and the damages associated with it.

I.2.1.1 Cellular mechanisms of synapse loss

Synapse loss affects neurons and their connectivity. However, they are not the only cells involved in this process. Multiple glial cells have been associated to synapse loss, in particular microglia, astrocytes and infiltrating phagocytes (Figure 4).

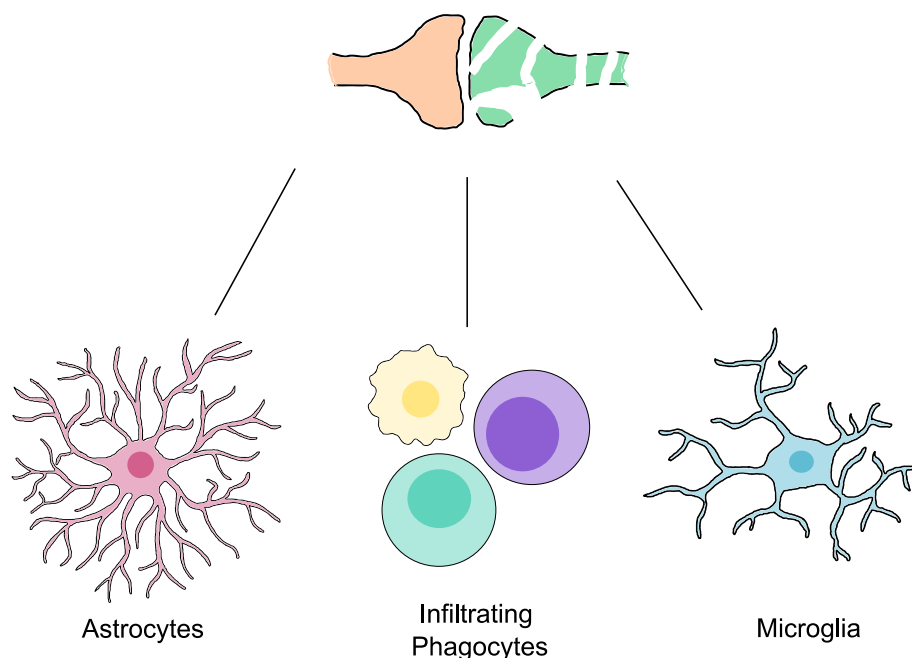


Figure 4: Cells involved in synaptic engulfment leading to synapse loss. Astrocytes, infiltrating phagocytes and microglia have been described to play a role in synaptic engulfment in several neurodegenerative diseases and neuroinflammatory conditions. Figure created by Emily Melisa Ullrich Gavilanes.

Microglia have been linked to synapse loss in studies concerning neuroinflammation. Following ischemia microglia become activated, increase the duration of contacts with synapses, and can mediate synapse engulfment (Shi et al., 2021, Wake et al., 2009). In mouse models of early AD, microglia are thought to phagocytose synapses as synaptic puncta can be observed within microglial cells (Hong et al., 2016). Finally, microglia have also been considered a key mediator in synapse engulfment during MS with synaptic material being detected within microglial lysosomes in MS patients, in addition to mouse and marmoset models of EAE (Werneburg et al., 2020).

Astrocytes, like microglia, have also been associated with synapse engulfment in ischemia. In neuroinflammatory conditions, astrocytes become reactive and can act as phagocytes for synapses (Morizawa et al., 2017, Shi et al., 2021).

Furthermore, peripheral phagocytes that infiltrate the brain in neuroinflammatory conditions have also been discovered to take part in synaptic phagocytosis. In Rasmussen's encephalitis and in a déjà vu mouse model of encephalitis, CD8+ T-cells and peripheral phagocytes invade the CNS and take part in the engulfment of synapses, with STAT1- JAK2 pathway and CCL2 playing a critical role in the interaction between neurons and phagocytes for synaptic uptake (Di Liberto et al., 2018).

1.2.1.2 Molecular mechanisms of synapse loss

Even though synapse loss is widely observed during development, adulthood and in pathological conditions, the exact mechanism by which it occurs is not known and different options have been proposed. Several mechanisms proposed overlap between development and neuroinflammatory conditions, thus this section will focus mainly on those described for neuroinflammation.

In ischemic neuroinflammatory conditions, astrocytes and microglia have been observed to play a role in the phagocytosis of synapses. The ABCA1 pathway plays a critical role in reactive astrocytes' switch to a phagocytic phenotype in a spatiotemporally restricted pattern, usually further from the ischemic core region. ABCA1 is upregulated in astrocytes, which in turn upregulates its pathway molecules MEGF10 and GULP1 and would lead to increase astrocytic phagocytosis (Morizawa et al., 2017). Furthermore, MEGF10 and MERTK were shown to be involved in microglial and astrocytic phagocytosis following ischemic and haemorrhagic stroke. Microglia and astrocytes were observed to engulf pre- and post-synaptic material after stroke, with microglia engulfing more synapses than astrocytes. Both microglia and astrocytes seemed to upregulate MEGF10 and MERTK, which together with their downstream pathways are thought to play a role in the engulfment of synapses in models of more severe stroke (Shi et al., 2021). The complement system has also been suspected to play a role in synaptic uptake in a different study with stroke models. At an acute time point in stroke, C3 complement deposition, activation, and microgliosis could be observed leading to synapse uptake by microglia that persisted for up to 30 days poststroke and limited cognitive recovery of mice (Alawieh et al., 2020). The different mechanisms described, could all play roles following stroke, as complement could act as an initial method of uptake followed by MEGF10 and MERTK upregulation. The mechanisms could also work simultaneously in different spatial patterns, or they could be relevant to different stroke types. It would be important to carry out subsequent studies to find out if there is an interplay between these mechanisms and whether other mechanisms could play a role in the synapse loss observed in stroke.

In Alzheimer's disease multiple studies have focused on the complement system as a mechanism of synapse loss, but recent studies have also proposed different mechanisms involved in this process. Complement proteins C1q and C3 have been observed to have increased deposition in AD and have been noted to play a role in synapse loss during AD progression. In the presence of oligomeric A β , C1q activates C3 and subsequently microglia interact with deposited C3 through their C3 receptor, thereby facilitating phagocytosis of

synapses tagged by complement deposition (Fonseca et al., 2004, Hong et al., 2016, Shi et al., 2017). Increased nitric oxide (NO) production leads to a noncanonical S-transnitrosylation in AD, which can subsequently cause synapse loss. Enzymes with aberrant catalytic activities, from different biochemical pathways, form an alternative network with a transnitrosylation cascade resulting in SNO-Drp1 protein production which causes mitochondrial fragmentation, bioenergetic compromise and synapse loss (Nakamura et al., 2021). Fibrinogen, a blood protein, has also been described in promoting synapse elimination in AD. Fibrinogen deposits in the brain can act as an additive mechanism in synapse loss by activating pro-oxidant ROS pathways and by inducing microglia activation by binding to the CD11b-CD18 receptor (Merlini et al., 2019). Similar to ischemic neuroinflammatory conditions, the proposed mechanisms in AD could act in a synergistic manner and not be mutually exclusive, thereby leading to the great synapse loss that has been observed in AD patients. It would be interesting to see if further mechanisms of synapse loss may play a role in AD and whether these mechanisms provide an additive effect or might have a spatiotemporal segregation to those already outlined.

In MS, less mechanisms have been proposed for the synaptic loss that is observed in grey matter of patients. Increased C3 protein deposition and synapse loss in the retinogeniculate system was observed in MS patients' brains, in a preclinical non-human primate model of MS as well as in two mouse models of demyelination. C3 but not C1q was enriched close to synapses of the visual thalamus and led to reactive microglial engulfment of synapses (Werneburg et al., 2020). In addition, platelet activating factor receptor (PAFR) signalling has been identified as playing a role in microglial engulfment of hippocampal excitatory post-synapses in an EAE mouse model of MS. It is suggested that upon microglial activation, PAFR signaling can lead to neuronal excitotoxicity and subsequent microglial uptake of synapses (Bellizzi et al., 2016). Although these proposed mechanisms help to gather insight into synapse loss in specific brain regions during MS, further insights into possible mechanisms are needed to explain the synapse loss observed in other grey matter areas and cortical regions in MS patients.

Besides the different mechanisms proposed to cause synapse loss in neuroinflammatory conditions, calcium dysregulation has also been linked to synapse loss in several studies. In AD, it is proposed that soluble A β oligomers can activate Calcineurin, a calcium dependent phosphatase, which can subsequently activate the transcription factor nuclear factor of activated T-cells (NFAT) leading to dystrophic neurites, dendritic simplification and spine loss (Wu et al., 2010). Also in AD, Ryanodine receptor (RyanRs) channels, which release calcium from the ER, are upregulated and in older AD neurons RyanR3 has been observed to increase network excitability, amyloid plaque load, spontaneous seizures and mushroom spine loss (Liu et al., 2014). All in all, calcium seems to be an important molecule to consider when investigating mechanisms involved in synapse loss, although a more comprehensive explanation to whether the synapses are removed or collapse on their own is needed.

I.3 Imaging techniques to visualize neuropathology in the inflamed CNS

Recognition of neuroinflammation and neuropathology is a crucial step in the diagnosis of many neuronal diseases. Neuropathology occurs in many disorders before clinical signs of the disease are observed in patients. Imaging techniques can therefore be helpful to determine time points for disease prevention and treatment (Hampel et al., 2020). Detecting

neuroinflammation in vivo can be a challenging task due to the isolation of the CNS from other systems and the poor accessibility that exists to the CNS itself. To solve this problem, approaches have been made to do non-invasive neuroimaging techniques like MRI which can allow to track in real time some of the changes taking place in the brain.

Different methods have been used to study neuropathology in the inflamed CNS throughout time. In the past two decades, MRI has grown as a method for diagnosis and disease monitoring. During the past few years, other imaging techniques like PET have been emerging to image different disease components (Tommasin et al., 2019). More imaging techniques have been increasingly used in MS to investigate disease pathology. For instance, magnetic resonance spectroscopy, which can detect metabolite patterns and concentrations, has been used to look at inflammatory signals and microglia activation (Fleischer et al., 2016).

I.3.1 MRI

MRI is an imaging technique which is based on the principle of magnetic moment that exists in atomic nuclei of certain elements such as hydrogen. This magnetic moment induces a dipolar magnet with mechanics similar to that of spinning objects. Upon application of an external magnetic field, the nucleus is aligned either parallel or perpendicularly to the external field. However, due to its rotation it will rotate around the external magnetic field axis. The nuclei, possessing spin, can be excited within the external magnetic field through the application of a second magnetic field, applied in short pulses, perpendicular to the original one. The nucleus will then absorb energy and can subsequently transition from higher to lower energy levels by emitting energy. This emitted energy can, in turn, be detected, amplified and displayed. During MRI, multiple pulses are applied to obtain multiple decay from energy levels which are subsequently averaged to improve the signal to noise ratio. The averaged signal decays will then provide a time-domain signal which is made from contributions of different nuclei within the studied environment. Energy decay from different environments can then be processed via Fourier transformation into an MRI image which will detect, for example, free water or hydrogen bound to tissue (Grover et al., 2015).

MRI scanners use cryogenic superconducting magnets, which were initially conducted at a field strength of 1.5 Teslas. Currently 3 Tesla systems are used due to their improved signal-to-noise ratio, higher spatial and temporal resolution, and improved quantification. MRI imaging can further be classified into T1 and T2-weighted based on the types of relaxation, longitudinal or transverse respectively, that is detected from the nuclear spin. MRI has limitations, as it is sensitive to motion artifacts and has a limitation on imaging speed. These limitations, however, have been improved over the last decades as MRI is a powerful tool with many benefits. Due to its lack of radiation, MRI has become very important for non-invasive diagnostics, to study different functional applications, and for disease tracking (Grover et al., 2015, Stoja et al., 2021).

Neuroimaging techniques have been used for the past couple of decades consistently for diagnosis and monitoring of several neuroinflammatory diseases. In AD, structural and functional MRI provide support for clinical diagnosis by identifying characteristic patterns or structural and functional brain alterations consistent with the disease. MRI also plays an important role in ischemic stroke where it determines patients in immediate need of treatment,

but different variables of MRI can also provide information about the ischemic penumbra (Gonzalez, 2012).

For MS, MRI is the most sensitive, non-invasive imaging technique which allows to monitor inflammation. In the early phase of MS and during diagnosis, MRI can detect new lesions in the CNS and these lesions are later on used as confirmation for MS diagnosis (Traboulsee and Li, 2006). In fact, MRI protocols were incorporated into the international panel guidelines for diagnosis of MS in 2001 (McDonald et al., 2001). Clinically routine MRIs are performed in MS patients allowing for sensitive qualitative and quantitative assessment of demyelinating lesions in the CNS, as well as tissue atrophy. Moreover, MRI has become a key supportive outcome measured in clinical trials to evaluate disease progression and lesion formation. However, MRI is frequently incapable to determine ongoing pathological processes taking place in NAWM and NAGM, an important component in disease progression. For this reason, advanced MRI techniques or the combination of MRI with other imaging techniques has taken place in recent years (Hemond and Bakshi, 2018).

I.3.2 PET scanning

PET is an imaging system, which as its name implies relies on the emission of a positron from a neutron-deficient radioisotope. Due to the instability of the radioisotope, it will decay to a stable state and release a positron, transforming itself into a neutron. The released positron will then travel a small distance and will interact with an electron in an annihilation reaction. This produces two high-energy photons which travel in a straight line in opposite directions and can be detected by a PET scanner outside the body. The PET scanner has detectors made of scintillator crystals which are coupled to photomultipliers. PET imaging has various limitations, the first one being the noise, which is reliant on the amount of radioisotope injected into the patient, as well as the detector scintillator density and the capabilities of the scanner. A second large limitation is the spatial resolution PET provides, which is based on the estimation of the annihilation reaction by the photon detector and in turn by the detector fidelity. In order for the estimation of location to be possible, both photons need to arrive to the detector within 1-10 ns to call it a true coincidence as scattering or random coincidences could also take place, introducing noise (Vaquero and Kinahan, 2015).

In order to improve the spatial resolution of PET, PET can be carried out together with MRI or computed tomography (CT). PET-CT combines the tracer metabolic ability of PET with the high anatomic resolution of CT, to provide a PET image that is better spatially resolved. PET-CT has become the standard approach in the past couple decades, in many fields such as oncology, due to the benefits they offer over stand-alone PET (Beyer et al., 2000, Vaquero and Kinahan, 2015). PET-MRI has gained interest in the past years despite their slow development and the challenges that occur from technically combining both modalities. PET-MRI has better soft tissue imaging capabilities than CT as well as a wider variety of imaging types that can be performed. Unlike PET-CT, PET-MRI can be imaged simultaneously and can be integrated into one machine providing imaging data that is comparable to that of PET-CT (Al-Nabhani et al., 2014, Vaquero and Kinahan, 2015). Multimodal imaging with PET and CT or MRI has provided a revolutionary way to approach diagnosis due to the potential that exists by looking at physiological and morphological changes simultaneously.

Various isotopes have been used for labelling in PET, however the most common is ^{18}F due to its longer half-life. Radiotracers injected into patients are meant to label biologically active compounds with the radioisotopes. The radiotracer would then accumulate in locations where the compound is metabolized (Vaquero and Kinahan, 2015). Development of new radiotracers has increased in recent years with specific tracers for specific diseases and pathologies, gaining interest due to their potential for disease differentiation. PET combined with MRI has been used to map structural and metabolic features of various tracers such as TSPO, a tracer used to monitor glial activation or peripheral benzodiazepine receptor that correlates with microglial activation (Debruyne et al., 2003, Oh et al., 2011). In the same way, amyloid and tau tracers have been used to study brain pathology and disease properties in AD (Johnson et al., 2012, Steward et al., 2022). Synapse loss has also been monitored through PET tracers, previously used in stroke models (Lyu et al., 2020). PET tracers and PET scanning are versatile tools that can be used to monitor and diagnose multiple diseases based on the development of radiotracers linked to biomarkers of specific diseases. As such, PET scanning can become an invaluable tool in analysing different pathologies associated with diseases and in tracking the progress of said pathologies in conditions such as neuroinflammation. Neuroimaging techniques continuously improve and become better at recognizing neuroinflammatory disease pathology, thus making them incredibly useful tools in disease diagnosis and monitoring.

I.4 Molecular techniques to analyse and manipulate neuropathology in the inflamed CNS

In order to gain a deeper understanding of neuropathology development and mechanisms at play in the inflamed CNS, molecular techniques are needed to help analyse and manipulate specific pathways. This manipulation would in turn elucidate the role specific pathways or molecules play in neuropathological conditions. Lately, single-cell multiomics analyses have provided a very valuable tool to advance knowledge in mechanisms involved in neuroinflammatory processes and could become very valuable in the coming years in clinical settings and personalized treatment (Ingelfinger et al., 2022). Recently discovered methods have also proved to be efficient in developing treatment strategies for neuroinflammation. For example, the CRISPR-Cas9 gene editing system has been helpful in testing the effects of knockout (KO) of target pathways and proteins and determining their potential as therapeutic targets (Luo et al., 2019). Research methods are consistently changing and developing, providing new opportunities to study neuroinflammation and neuropathology.

Multiomics refers to the integration of several omics methods, which have become the gold standard for the study of differential cell processes and components and have been adapted to the single cell resolution. Advances in multiomics have provided multiple tools that can be applied to study different cellular properties involved in diverse networks during neuroinflammation (Ingelfinger et al., 2022). One can for instance obtain the proteome, transcriptome and epigenome in single cells and thus analyze the interconnection that exists between them and predict the influence they have on each other (Swanson et al., 2021). While some analyses have been performed and helped to elucidate previously unknown mechanisms or interactions, the rapid development of omics technology will allow for a larger combination of techniques and a broader understanding of neuroinflammation in the future (Ingelfinger et al., 2022).

Gene modification has been one of the main ways to study pathways and especially the proteins and genes involved in these pathways for a long time. Gene targeting is a process that has revolutionized biomedical research and allows scientists to study pathways through animal models with conditional, inducible, and even some time multi-gene knockouts. By using gene modification techniques like knockouts, research can be performed on the *in vivo* functions and expression of specific genes. This in turn has allowed for the study of the role many genes and proteins play in particular pathologies. Following CRISPR/Cas discovery, gene targeting became easier and more accessible to researchers, providing an important tool for understanding of specific proteins in pathologies and diseases (Eisener-Dorman et al., 2009, Thyagarajan et al., 2003, Jinek et al., 2013).

I.4.1 snRNA-seq

Single-cell RNA sequencing has emerged as an important tool to understand processes taking place in cells. Introduced as a variation of single-cell RNA sequencing, single nucleus RNA sequencing (snRNA-seq) provides benefits compared to single-cell: it provides a less biased cellular coverage and works better when it comes to isolation from tissues where intact cell isolation is complex, like the CNS. The dissociation of the tissue is quite easy and does not require protease digestion or heating, making it less likely to have aberrant transcription. snRNA-seq can provide further insight into regulatory mechanisms that are happening in the nucleus all while having a great gene coverage, high reproducibility and a similar gene-expression variation as single-cell RNA sequencing (Grindberg et al., 2013, Lacar et al., 2016).

Different methods are available to perform snRNA-seq, some of which are high throughput but also low throughput methods exist. Low throughput methods like Smart-seq2 sequencing, sort nuclei into a well of a multi-well plate, where the cDNA is generated (Picelli et al., 2013). High throughput methods like 10x genomics are bead-based methods which can distribute nuclei into droplets containing reagents and barcoded beads which then interact with the nuclei to get a single nucleus per bead, marking the cDNA generated from said nucleus (Zheng et al., 2017). Low throughput methods usually have a higher sequencing depth and can detect more genes than high throughput methods. In comparison, high-throughput methods are more consistent with their results and less time consuming (Ding et al., 2020). Whenever performing snRNA-seq it is recommended to use both exon and intron reads, as nuclear transcripts might contain more unspliced transcripts, this would provide a higher sequencing depth and detect more genes (Bakken et al., 2018). All in all, snRNA-seq is a very useful tool when studying tissues that cannot be readily dissociated or from frozen samples, while still providing high sensitivity and good detection (Ding et al., 2020).

I.4.2 CRISPR/Cas

Initially discovered by Charpentier and Doudna in 2012, CRISPR/Cas9 technology received the Nobel Prize in Chemistry in 2020. Clustered regularly interspaced short palindromic repeats (CRISPR)/ CRISPR-associated endonuclease (Cas), is a genome editing technique discovered upon the investigation of *Streptococcus Pyogenes* (Deltcheva et al., 2011). CRISPR/Cas systems are part of the immune system that protect bacteria against phages and plasmids. In bacteria, the CRISPR/Cas system integrates the phage or plasmid DNA derived spacers into the CRISPR locus. Then, the bacteria expresses short guide CRISPR

RNAs (crRNAs) that are composed of single repeat spacer unit. Finally, interference with the foreign genomes occurs with the help of Cas endonucleases. Cas9 needs two short RNAs to facilitate its activity (Deltcheva et al., 2011). crRNA and trans-activating crRNA (tracrRNA) form a two RNA structure that directs Cas9 to introduce double stranded breaks into target DNA complementary to the crRNA. Both RNA molecules can be engineered into a single RNA molecule which can also lead to sequence specific Cas9 double strand cleavage (Jinek et al., 2012). The engineering step of both RNA molecules into one, as well as the observation that Cas9 can be reprogrammed to target specific DNA sequences, is what allowed the CRISPR/ Cas9 system to be usable for genome editing in different cell types. Hybrid engineered RNAs, renamed to single-guide RNAs (sgRNAs) could be introduced into human cells and would lead to double strand DNA breaks at the genomic DNA site complementary to the guide RNA sequence. For DNA cleavage both the guide RNA and Cas9 expression are necessary (Jinek et al., 2013).

Once the CRISPR/ Cas system was shown to work in eukaryotic cells, it offered a vast possibility of modifications to improve its efficiency or to provide more genome editing opportunities. The first step was to look inside the existing system and to optimize both Cas9 and the guide RNAs (Jinek et al., 2013). Then, modification ensued to get higher efficiency with less off-target cutting from Cas9, which led to the observation, that a protospacer adjacent motif (PAM) sequence downstream of the target DNA is needed to ensure correct activity of the nuclease (Lee et al., 2016). Furthermore, the system could be used to knock out proteins by using the cell's non homologous end joining DNA repair system or to induce targeted DNA repair by introducing a sequence together with the Cas9 that could then be used for homologous end joining and precise DNA modifications (Lee et al., 2016). Further variations were then created to use Cas9 not as an endonuclease, but in a catalytically defective manner and as a guiding molecule, which could direct other specific enzymes such as base editors to the desired DNA target (Komor et al., 2016). In the same way, using a catalytically deficient Cas9 in a complex with other enzymes, targeting of the epigenome to modulate gene expression has been possible (Pulecio et al., 2017). Cas proteins have also been used for RNA targeting: an engineered RNA-targeting Cas9 has been able to eliminate toxic RNA foci, reverse abnormal mRNA splicing (Batra et al., 2017), while RNA-targeting Cas13 enzyme has been used for knockdown generation (Abudayyeh et al., 2017). The versatility of the CRISPR/ Cas system is continuously being explored to find new modifications, which can be beneficial for basic research but also for therapeutic approaches.

CRISPR/ Cas systems have great potential for disease therapeutics. The CRISPR/Cas9 technology has enabled fast creation of many animal models previously non-existent for certain diseases, resembling their pathology and allowing scientists to better study them. It has also been used as a first step to investigate genes of interest from genomic and transcriptomic analyses to see their effect in disease pathology. Furthermore, CRISPR/ Cas9 has helped with the removal or correction of pathogenic mutations or the insertion of protective mutations by using directed repair (Cox et al., 2015). The catalytically deficient Cas9 systems could be very useful to target disorders with point mutations (Antoniou et al., 2021), alterations in the patterns of genetic modifications, or where gene activation and repression are not functioning properly like in cancer (Liu et al., 2018, Pulecio et al., 2017). Moreover, RNA-targeting Cas9 has great potential in eliminating repeat expansion RNA seen in some polyglutamine diseases such as Huntington's disease (Batra et al., 2017). CRISPR/

Cas gene editing based therapeutics is a rapidly evolving field with the number of clinical trials increasing every year and showing higher potential in targeting many diseases (Innovative Genomics Institute, 2022).

Chapter II: Aim of the study

Neuroinflammation is a crucial component of multiple sclerosis. Inflammatory procedures in CNS tissue lead to differential types of white and grey matter pathology. Grey matter pathology is a key pathological process that correlates with disability during MS progression. Studies into mechanisms leading to grey matter pathology as well as treatments for progressive disability have been scarce and therefore these pathomechanisms are not yet fully understood. Thus, the overall aim of my PhD project was to investigate the mechanisms taking place in grey matter neuroinflammation leading to neuronal pathology, such as synapse loss, while also looking for ways to monitor this pathology *in vivo* and to test therapeutic strategies that could improve neuronal disease-related phenotypes.

In the first part of my project, my focus was to characterize mouse models of cortical grey matter inflammation resembling MS, particularly in terms of neuropathology of synapse loss. This part aimed to answer the following questions:

- Can the cortical MS model replicate key pathological features of grey matter inflammation in MS?
- What effect does age have on evolution of pathology in the cortical MS mouse model?

The results observed in the first part laid the groundwork for the next parts of the project. In the second part of the project, the pathways underlying neuron pathology in grey matter were investigated through single nuclei transcriptomics analysis of cortical MS mice and were compared to MS patients. Candidate genes obtained from the transcriptomic analysis were then tested in a CRISPR/Cas9 system that we aimed to develop. In this part the following questions were aimed to be answered:

- What molecular signature is induced in neurons during the formation and recovery phase of the cortical MS model?
- Which aspects of the molecular signature observed in the neurons in the cortical MS model are also present in the cortical neurons of MS patients?
- Which of these differentially regulated genes could be good targets for further mechanistic studies and therapeutic strategies?
- Can we develop a CRISPR/Cas9 KO system that works in the brain?
- How does the knock-out of gene targets from the snRNA seq influence the pathology observed in the cortical MS model?

Finally, in the last part of the project the aim was to test therapeutic strategies to reduce neuron pathology in the cortical MS model, as well as finding diagnostic strategies to see components of neuron pathology *in vivo* through PET imaging. This part aimed to answer the following questions:

- What effect would blocking microglial activation have in the neuron pathology of cortical MS?
- What part of neuron pathology could be targeted *in vivo* during PET imaging? Would this tracing method be a good potential approach for MS patients?

Overall, this project aimed to characterize, understand and target mechanisms of neuropathology in a translatable approach that could make results relevant for MS patients suffering from grey matter neuroinflammation.

Some results of the first part of the project are published in Jafari, Schumacher, Snaidero, **Ullrich Gavilanes**, [...], Merkler, Misgeld & Kerschensteiner, *Nature Neuroscience*, 2021; and on Mezydlo, Treiber, **Ullrich Gavilanes**, [...], Misgeld & Kerschensteiner. *Neuron*. 2023.

Chapter III: Materials and methods

III.1 Materials

III.1.1 Surgery Materials

Medications and Reagents		
Kx Anesthesia	Ketamine 10% (Ketamine Hydrochloride) Xylazin 20mg (Xylazine)	CP-pharma GmbH, Burgdorf, Germany Bela-Pharm GmbH, Vechta, Germany
Iso Anesthesia	Isofluran CP (Isoflurane)	CP-pharma GmbH, Burgdorf, Germany
MMF Anesthesia	Fentanyl 0.05mg Dormicum 5mg (Midazolam) Dormilan 1mg/mL (Medetomidine hydrochloride)	B.Braun AG, Melsungen, Germany Cheplapharm Arzneimittel GmbH, Greifswald, Germany Alfabet Tierarzneimittel GmbH, Neumünster, Germany
Anesthesia Antagonist	Atipazole 5mg (Atipamezole hydrochloride) Flumazenil 0.1 mg Naloxone 0.4 mg (Naloxone hydrochloride)	Prodivet Pharmaceuticals S.A., Raeren, Belgium Hameln GmbH, Hameln, Germany B.Braun AG, Melsungen, Germany
Analgesia	Temgesic 0,324 mg (Buprenorphine hydrochloride) Xylocain 2% (Lidocaine hydrochloride) Metamizol 500 mg (Metamizol-Sodium)	Reckitt Benckiser GmbH, Heidelberg, Germany Aspen GmbH, Munich, Germany WDT- Werner Dosiertechnik GmbH, Wertingen, Germany
Sterile artificial mouse cerebrospinal fluid (aCSF) (Solution A and B in 1:1 ratio)	Solution A: 8.66 g NaCl 0.224 g KCl 0.206 g CaCl ₂ · 2H ₂ O 0.163 g MgCl ₂ · 6H ₂ O Solution B: 0.214 g Na ₂ HPO ₄ · 7H ₂ O 0.027 g NaH ₂ PO ₄ · H ₂ O dH ₂ O ad 500 mL	Merck Millipore, Darmstadt, Germany Sigma-Aldrich Chemie GmbH, Taufkirchen, Germany Merck Millipore, Darmstadt, Germany
Hydration solution	Ringerlösung Fresenius (Ringer's solution) Glucose 5% Saline (NaCl 0.9%)	B. Braun AG, Melsungen, Germany
Skin and eye protection/ disinfection	Bepanthen Augen- und Nasensalbe 5g (eye ointment) Cutasept Lösung 250 ml (antiseptic spray) Braunovidon Salbe 10% (Povidon iod) Ethanol 70%	Bayer AG, Leverkusen, Germany Bode Chemie GmbH & Co, Hamburg, Germany B. Braun AG, Melsungen, Germany CLN GmbH, Niederhummel, Germany
Cranial window	Paladur (Dental cement set)	Kulzer GmbH, Hanau, Germany

	Histoacryl (Topical skin adhesive)	B.Braun AG, Melsungen, Germany
--	------------------------------------	--------------------------------

Tools and Materials		
Syringes and needles	Syringe 3pc 3 and 5ml Omnifix luer slip BD Plastipak Hypodermic luer slip syringe 1ml Hypodermic Needles BD Microlance 3 30 Gauge (0.3 mm, yellow)	B. Braun AG, Melsungen, Germany Becton, Dickinson & Co, Franklin Lakes, USA
Tissue exposure tools	Feather blade, surgical scalpel Noyes Spring Scissors (big) Vannas-Tübingen Spring Scissors (small) Dumont Mini Forceps Inox Style 3 (big) Dumont Mini Forceps Inox Style 5 (small)	Pfm medical AG, Cologne, Germany FST GmbH, Heidelberg, Germany
Wound closure	Ethicon Ethilon monofil 6-0 size (skin) AutoClip system	Johnson & Johnson Medical GmbH, Norderstedt, Germany FST GmbH, Heidelberg, Germany
Cranial Window	4mm Ø coverslip for cranial window Metal head bar 0.4 mm and 0.5 mm stainless steel drill head	Warner Instruments, Hamden, USA Hager&Meisinger GmbH, Neuss, Germany Meisinger, Neuss, Germany
Other	Blaubrand intraMark micropipettes (Ultrathin pulled glass pipette) Sugi	Brand GmbH & Co KG, Wertheim, Germany Kettenbach GmbH&Co KG, Eschenburg, Germany

Devices		
Microscope	Olympus KL 1500 LCD (light source for stereomicroscopy) Olympus Stereo Microscope SZ51	Olympus Deutschland GmbH, Hamburg, Germany (Headquarters in Japan)
Sterilizer	FST 250 Hot Bead Sterilizer	FST GmbH, Heidelberg, Germany
Other	T/Pump Heating Pad Hammer MicroMotor Kit 0-25000 Stereotaxic Frame MouseOx system	Gaymar Industries, NY, USA Foredom Electric Co. Connecticut, USA Stoelting CO, Wood dale, USA Starr Life Science Corp, Oakmont, USA

III.1.2 Induction of systemic and cortical EAE (cMS model)

Reagents		
MOG emulsion	Purified recombinant MOG (N1-125, from E. Coli) Mycobacterium Tuberculosis H37 RA Incomplete Freund's adjuvant (IFA) Pertussis toxin from Bordetella pertussis, inactivated Acetate buffer 20mM pH3.0	Stock solution, produced by the laboratory of Doron Merkler (University of Geneva) and by laboratory of Martin Kerschensteiner Sigma-Aldrich Chemie GmbH, Taufkirchen, Germany
Cortical EAE	TNF-alpha IFN-gamma Bovine Albumin Serum (BSA) Fraction V	R&D System, Minneapolis, USA Peptotech GmbH, Hamburg, Germany Sigma-Aldrich Chemie GmbH, Taufkirchen, Germany

Tools and Materials		
Syringes and Needles	Hamilton 1 ml syringes Hypodermic Needles BD Microlance 3 23 Gauge (0-6 mm, blue)	Hamilton, Bonaduz, Switzerland Becton, Dickinson & Co, Franklin Lakes, USA

III.1.3 Perfusion and immunohistochemistry

Reagents		
Perfusion	PFA 4% (paraformaldehyde) in phosphate buffer pH 7.4 ready-to-use; stored in 4°C for max 2 weeks Heparin-Natrium 25.000IE (Heparin sodium)	Morphisto GmbH, Frankfurt a.M, Germany Ratiopharm GmbH, Ulm, Germany
Microdissection	Sodium azide 0.1% in 1x PBS Sucrose 30%	Sigma-Aldrich Chemie GmbH, Taufkirchen, Germany Sigma-Aldrich Chemie GmbH, Taufkirchen, Germany
ICH/ IF	PBS 10x (Phosphate buffered saline) pH7.4 Triton X-100 Gibco goat Serum, donkey serum Tissue-Tek O.C.T (Cryoprotection) Vectashield Mounting Medium	Sigma-Aldrich Chemie GmbH, Taufkirchen, Germany Invitrogen GmbH, Darmstadt, Germany Sakura Fintek Ltd, Tokyo, Japan Vector Laboratories Inc., Burlingame, USA

	Agarose 3%	Sigma-Aldrich Chemie GmbH, Taufkirchen, Germany
--	------------	--

Antibodies, dyes and tracers		
Primary antibodies	Anti-Synapsin-1 polyclonal rabbit A21244 Anti-LAMP1 monoclonal rat #121601 Anti-PSD95 polyclonal rabbit #51-6900 Anti-Homer-1 polyclonal guinea pig #160004 Anti-NeuN polyclonal rabbit SAB4300883 Anti-MBP polyclonal rabbit A0623 Anti-Iba-1 polyclonal rabbit 019-19741 Anti-I-A/I-E (MHCII) monoclonal rat 556999	Merck Millipore, Darmstadt, Germany Biolegend, San Diego, USA Invitrogen GmbH, Darmstadt, Germany Synaptic Systems, Göttingen, Germany Sigma-Aldrich Chemie GmbH, Taufkirchen, Germany DAKO, Santa Clara, USA FUJIFILM Wako, Osaka, Japan BD Pharmingen, San Diego, USA
Secondary antibodies	Goat anti-rabbit AlexaFluor 647 Goat anti-rat AlexaFluor 594 Goat anti-rat AlexaFluor 488 Donkey anti-guinea pig AlexaFluor 647 Goat anti-rabbit AlexaFluor 405 Goat anti-rabbit AlexaFluor 488 Goat anti-rabbit AlexaFluor 594 Goat anti-rat AlexaFluor647	Invitrogen GmbH, Darmstadt, Germany
Dyes/ Tracers	DAPI NeuroTrace 640/660 fluorescent Nissl NeuroTrace 435/455 fluorescent Nissl	Invitrogen GmbH, Darmstadt, Germany

Tools and Materials		
Perfusion	Noyes Spring Scissors (big) Dumont Mini Forceps Inox Style 3 (big) Safety-Multifly 21 G 20 mm	FST GmbH, Heidelberg, Germany Sarstedt AG & Co, Nümbrecht, Germany
IHC/ IF	Microscope slides 76x26 mm Microscope cover slips 24x60 mm 24-well cell culture plate 15 and 50 ml centrifuge tubes Pipettes, pipette tips and tubes (0.5, 1.5, 2 ml)	Gerhard Menzel Glasbearbeitungswerk GmbH, Braunschweig, Germany Becton, Dickinson and Company, Franklin Lakes, USA Sarstedt AG & Co, Nümbrecht, Germany Eppendorf AG, Hamburg, Germany

Devices		
Perfusion	Ismatec IP high precision multichannel pump	ISMATEC SA, Labortechnik-Analytik, Glattbrugg, Switzerland
IHC/ IF	Leica CM1950 (cryostat) Leica VT1000 S (Vibratome) Vortex-Genie 2 (vortex) Polymax 1040 (shaker)	Leica Microsystem GmbH, Wetzlar, Germany Scientific Industries Inc., Bohemia, USA Heidolph Instruments GmbH, Schwabach, Germany

III.1.4 Viral labelling

Viruses		
AAV	AAV1.hSyn1.Twitch2b.WPRE.SV40 #100040-AAV1	Addgene, Watertown, USA

* For CRISPR related viruses please look at section 1.7

III.1.5 Imaging

Devices		
Microscopes and Objectives	<p><u>Leica TCS SP8 upright with DMI6000 confocal microscope</u> <i>Equipped with a HCX PL Fluotar 5x/0.15, a HC PL Apo 63x/1.40 oil immersion objectives, a PL Apo 20x/0.75 immersion correction CS2 objective and an HC PL Apo 40x/1.30 oil immersion objective</i></p> <p><u>Leica SP8X WLL upright confocal microscope on a DM6 stand</u> <i>Equipped with an HPCL Fluotar 10x/0.30 objective, a HC PL APO 20x/0.75 CS2 objective, an HC PL APO 20x/0.75 Immersion correction CS2 objective, a HC PL APO 40x/1.30 Oil immersion CS2 objective, an HC PL APO 63x/1.30 glycerol correction CS2 objective, and an HC PL APO 63x/1.40 oil immersion CS2 objective</i></p> <p><u>Leica SP8 Falcon upright DM8 system with one and two photon excitation (DIVE)</u> <i>Equipped with an HC PL Fluotar 5x/0.15 objective, an HC PL Fluotar 10x/0.3 objective, an HC PL APO 20x/0.75 immersion correction CS2 objective, an HC</i></p>	Leica Microsystem GmbH, Wetzlar, Germany

	<p><i>PL APO 40x/1.30 oil immersion CS2 objective, a HC PL APO 63x/1.40 oil immersion CS2 objective, and an HC PL APO 63x/1.30 glycerol correction CS2 objective.</i></p> <p><u><i>Olympus FV1000 confocal system mounted on an upright BX61 microscope</i></u> <i>Equipped with 10x/0.4 water immersion objective, a 20x/0.85 oil immersion objective and 60x/1.42 oil immersion objective</i></p> <p><u><i>Olympus FV 1200 MPE/ Olympus MPE-RS multiphoton microscope</i></u> <i>Equipped with X25/1.05 water immersion objective; femtosecond-pulsed Ti:Sapphire laser (Mai Tai HP-DS or Insight DeepSee, Newport/ Spectra Physics) and opto-electrical intensity regulation</i></p>	<p>Olympus Deutschland GmbH, Hamburg, Germany (Headquarter in Japan)</p>
Clamping devices	Head-fix device	Narishige Inc., NY, USA

III.1.6 Single nuclei RNA sequencing

Reagents		
Nuclei Isolation	<p>Nuclei EZ Lysis buffer</p> <p>Dulbeccos Phosphate buffer saline modified without calcium chloride and magnesium chloride</p> <p>Bovine Serum Albumin solution, 10% in DPBS, low endotoxin, fatty acid free, suitable for cell culture, sterile-filtered Protector RNase Inhibitor (10000U)</p> <p>Nuclear Pierce DAPI</p> <p>Anti-NeuN monoclonal rabbit recombinant AlexaFluor 647 antibody</p> <p>TotalSeq-A0456 anti-Nuclear Pore Complex Proteins Hashtag 1 antibody</p>	<p>Sigma-Aldrich Chemie GmbH, Taufkirchen, Germany</p> <p>Merck Millipore, Darmstadt, Germany</p> <p>Thermo-Fisher Scientific, Planegg, Germany</p> <p>Abcam, Cambridge, UK</p> <p>Biologend, San Diego, USA</p>

	<p>TotalSeq-A0456 anti-Nuclear Pore Complex Proteins Hashtag 2 antibody</p> <p>TotalSeq-A0456 anti-Nuclear Pore Complex Proteins Hashtag 3 antibody</p> <p>TotalSeq-A0456 anti-Nuclear Pore Complex Proteins Hashtag 4 antibody</p> <p>TotalSeq-A0456 anti-Nuclear Pore Complex Proteins Hashtag 5 antibody</p> <p>TotalSeq-A0456 anti-Nuclear Pore Complex Proteins Hashtag 6 antibody</p> <p>Mouse BD Fc block</p>	BD Pharmingen, San Diego, USA
10x snRNA sequencing	<p>Chromium Next GEM Single Cell 3' GEM, Library & Gel Bead Kit v3.1</p> <p>3' Feature Barcode Kit</p> <p>Chromium Next GEM Chip G Single Cell Kit</p> <p>Single Index Kit T set A</p>	10x Genomics, Pleasanton, USA

Tools and Materials		
Cortex and Nuclei Isolation	<p>50 mL syringe with Luer-lock</p> <p>Noyes Spring Scissors (big)</p> <p>Vannas-Tübingen Spring Scissors (small)</p> <p>Disposal Safety Scalpels</p> <p>MACS SmartStrainers 30µm</p> <p>MACS SmartStrainers 70µm</p> <p>Pestle for microtubes 1,5/2,0 ml</p> <p>Pipettes, pipette tips and tubes (0.5, 1.5, 2 ml)</p> <p>FACS tube 5 mL 75 mm x 12 mm PS 125</p> <p>5mL Polystyren Round-bottom tube with cell-strainer cap</p>	<p>Becton, Dickinson & Co, Franklin Lakes, USA</p> <p>FST GmbH, Heidelberg, Germany</p> <p>Aesculap AG, Tuttlingen, Germany</p> <p>Miltenyi Biotec, Begisch Gladbach, Germany</p> <p>A. Hartenstein GmbH, Würzburg, Germany</p> <p>Eppendorf AG, Hamburg, Germany</p> <p>VWR, Ismaning, Germany</p> <p>Becton, Dickinson & Co, Franklin Lakes, USA</p>

Devices		
Nuclei Isolation	Eppendorf Centrifuge 5417R	Eppendorf AG, Hamburg, Germany
FACS sorting	<p><u>BD FACSAriaFusion</u></p> <p><i>Equipped with 4 lasers (405, 488, 561, 640nm)</i></p> <p><u>BD FACSAriaIIIu</u></p>	Becton, Dickinson & Co, Franklin Lakes, USA

	<i>Equipped with 4 lasers (405, 488, 561, 633nm)</i>	
10x snRNA-seq	10x Chromium controller 10x Vortex Adapter 10x Gasket 10x Magnetic separator Chromium Next GEM Secondary Holder	10x Genomics, Pleasanton, USA

III.1.7 3'-Bulk RNA sequencing

Reagents		
Library preparation and RNA quality	RNeasy Plus Micro Kit Collibri™ 3' mRNA Library Prep Kit for Illumina Molecular BioProducts™ RNase™ AWAY Agilent DNA 1000 Kit SPRIselect Reagent	Qiagen, Hilden, Germany Thermo Fisher Scientific, Planegg, Germany Agilent Technologies, Waldbronn, Germany Beckman Coulter, Brea, USA

Devices		
RNA quality	Agilent 2100 Bioanalyzer	Agilent Technologies, Waldbronn, Germany

III.1.8 CRISPR/Cas9

III.1.8.1 sgRNA design and testing *in vitro*

Reagents		
sgRNA cloning into retroviral vector	FastDigest Bpil Fast AP FastDigest Bufer (10X) Nuclease-free Water QIAquick Gel Extraction Kit T4 DNA Ligase Reaction Buffer T4 DNA Ligase T4 Polynucleotide Kinase Quick Ligation Kit	Thermo Fisher Scientific, Planegg, Germany Qiagen, Hilden, Germany New England Biolabs, Frankfurt am Main, Germany
Bacterial transformation and plasmid growth	NEB Stable Competent cells S.O.C medium Agar-agar Ampicillin Sodium Salt Biochemica Rattler Plating Beads (4.5 mm) sterile <u>LB medium:</u> Yeast extract	New England Biolabs, Frankfurt am Main, Germany Invitrogen GmbH, Darmstadt, Germany Merck, Darmstadt, Germany PanReac AppliChem, Darmstadt, Germany Zymo Research, Freiburg im Breisgau, Germany Sigma-Aldrich Chemie GmbH, Taufkirchen, Germany

	Sodium chloride Peptone from Casein (Tryptone)	Merck, Darmstadt, Germany
Plasmid isolation and Sequencing preparation	QIAprep Spin Miniprep Kit EB buffer	Qiagen, Hilden, Germany
Retrovirus generation	<u>HEK cell medium:</u> DMEM, low glucose, GlutaMAX Penicillin Streptomycin (10,000 U/mL) FBS SUPERIOR Stabil TransIT-LT1 Transfection Reagent Trypsin-EDTA (0.25%), phenol red	Thermo Fisher Scientific, Planegg, Germany Bio&SELL, Feucht, Germany MoBiTec GmbH, Göttingen, Germany Thermo Fisher Scientific, Planegg, Germany
Retrovirus infection of HoxB8 cells	<u>HoxB8 cell medium:</u> RPMI-GlutaMAX Recombinant murine IL-3 Recombinant murine IL-6 B-estradiol Puromycin Dihydrochloride 2-Mercaptoethanol	Sigma-Aldrich Chemie GmbH, Taufkirchen, Germany Peprotech GmbH, Hamburg, Germany Sigma-Aldrich Chemie GmbH, Taufkirchen, Germany Thermo Fisher Scientific, Planegg, Germany
gDNA isolation and PCR amplification	DNeasy Blood & Tissue Kit MinElute PCR Purification Kit Q5 reaction buffer pack Q5 High-Fidelity DNA polymerase Quick-Load® 1 kb Plus DNA ladder Deoxynucleotide Solution Mix Agarose 1% DNA Gel Loading Dye peqGreen DNA/RNA Dye <u>Tris-Acetate-EDTA buffer</u> TrisBase Acetic acid EDTA	Qiagen, Hilden, Germany New England Biolabs, Frankfurt am Main, Germany Sigma-Aldrich Chemie GmbH, Taufkirchen, Germany Thermo Fisher Scientific, Planegg, Germany Peqlab Biotechnologie GmbH, Erlangen, Germany Sigma-Aldrich Chemie GmbH, Taufkirchen, Germany

Tools and Materials		
Cell culture	12-well cell culture plate 6-well cell culture plate 5 mL, 10 mL, 25 mL, 50 mL Corning® Costar® Stripette® serological pipettes, individually paper/plastic wrapped	Becton, Dickinson and Company, Franklin Lakes, USA Sigma-Aldrich Chemie GmbH, Taufkirchen, Germany

Gel excision	X-TRACTA Generation II	Biozym Scientific GmbH, Oldendorf, Germany
--------------	------------------------	---

Cells and plasmids		
Cells	HEK293T cells Cas9-expressing HoxB8-FL Flt3L-producing B16 melanoma cell line	ATCC, Manassas, USA Provided by Seren Baygün from Prof. Dr. Marc Schmidt- Supprian's lab
Competent cells	Stellar Competent Cells	Clontech, Mountain View, USA
Plasmids	MSCV-pU6-(BbsI)-CcdB-(BbsI)- Pgk-Puro-T2A-BFP MSCV-pklv2-U6-(sgNon- Targeting)-Pgk-Puro-T2A- tdTomato pCL-Eco	Addgene, Watertown, USA In house cloning Provided by PD. Dr. Naoto Kawakami

sgRNA and Primers		
sgRNA	<u><i>Ifngr1</i></u> : 3. TTCAGGGTCAAATACGAGGA <u><i>NeuN</i></u> : TCGGGGTCCCTGAACCGGA (Platt et al., 2014) <u><i>PSAP</i></u> : 1. CTACGTGGACCAGTATTCCG 2. TCTGGCATAAAATCACATTG 3. AAAGTGTGTCACCGAAGCT 4. TCAACCACCTCCTTGCACG 6. TGAGTCCAACAAGATCCCGG	Metabion, Planegg, Germany
Primers	<u><i>Hu6 primer</i></u> : GAGGGCCTATTTCCCATGATT <u><i>Ifngr1 sgRNA specific</i></u> : 3F: CGAGGCAGAGTGTAGGTAAG 3R: CTTAATTGCCAACACTGGCC <u><i>NeuN sgRNA specific</i></u> : F: GTCTGCAGGACTACCTTACAAC R:GCTGGGCTGTTCTCTTT <u><i>PSAP sgRNA specific</i></u> : 1F: GGGACACTTCGATCTATTCTGG 1R: CGCAATGCTCCTTCCTATACA 2F: GGTACCTTCTGTTGCTGTTCTC 2R: AGTCCAGAGTTGGGTGCTAT 3F: CACTCACCTTGTGGCTAACT 3R: AGCCTATATGTATGACCTGGAAAG 4F: TTTACCCATCGGTGTGTGG 4R: CAAGGAGCCCTATGAAGAAGAG 6F: CCTGGTGTGCAACTTCCTAA 6R: CATCAGACACCAGCTTCATACA	Metabion, Planegg, Germany

Devices		
Cloning and PCR	Biometra Trio Thermal Cycler Nanodrop 2000C/2000	Analytik Jena, Jena, Germany Thermo Fisher Scientific, Planegg, Germany
Agarose Gel Electrophoresis and gel extraction	PerfectBlue Gel system Power Pac 200 High Performance Ultraviolet Transilluminator Quantum Vilber Lourmat	Peqlab Biotechnologie GmbH, Erlangen, Germany Bio Rad, Feldkirchen, Germany UVP, Jena, Germany Vilber, Eberhardzell, Germany

III.1.8.2 Viral labelling for *in vivo* use

Reagents		
AAV plasmid cloning	BsrGI enzyme HindIII enzyme KpnI enzyme EcoRI enzyme NcoI enzyme NheI enzyme CutSmart buffer Gibson Assembly Master Mix	New England Biolabs, Frankfurt am Main, Germany
sgRNA cloning into AAV vector	SapI enzyme	New England Biolabs, Frankfurt am Main, Germany
Plasmid isolation and Sequencing preparation	QIAGEN Plasmid Maxi Kit	Qiagen, Hilden, Germany
AAV production generation	Poly-Lysine Opti-MEM PEI MAX DNase I, RNASE-free, recombinant SYBR mix Polyethylene Glycol (PEG) 8000 Magnesium chloride, anhydrous Potassium chloride, powder, BioReagent Trizma hydrochloride solution Benzonase Phenol red solution Pluronic F-68 Non-ionic Surfactant OptiPrep™	Thermo Fisher Scientific, Planegg, Germany Polysciences, Hirschberg an der Bergstraße, Germany Roche, Basel, Switzerland Bio Rad, Feldkirchen, Germany Selleck Chemicals, Houston, USA Sigma-Aldrich Chemie GmbH, Taufkirchen, Germany Thermo Fisher Scientific, Planegg, Germany Serumwerk Bernburg AG, Oslo, Norway
gDNA isolation and PCR amplification	QIAamp DNA Micro Kit	Qiagen, Hilden, Germany

Tools and Materials		
Cell culture	Greiner CELLSTAR 14.5 cm diameter dish T75 flasks	Greiner Bio-One, Frickenhausen, Germany Thermo Fisher Scientific, Planegg, Germany
Virus production	0.45 µm filters 100 kDA Amicon filters Stainless steel 316 syringe needle, pipetting blunt 90° tip 20 mL syringes (Luer lock) qPCR plates qPCR closing film Cell scraper Quick-Seal Centrifuge Tubes	Merck Millipore, Darmstadt, Germany Becton, Dickinson & Co, Franklin Lakes, USA Bio Rad, Feldkirchen, Germany Techno Plastic Products, Trasadingen, Switzerland Beckman Coulter Biomedical GmbH, Munich, Germany

Devices		
Plasmid isolation	Avanti JXN-26 Centrifuge	Beckman Coulter Biomedical GmbH, Munich, Germany
Virus production	CFX Connect Real-Time PCR Optima™ L-90K Ultracentrifuge Water bath WB-4MS	Bio Rad, Feldkirchen, Germany Beckman Coulter Biomedical GmbH, Munich, Germany BioSan, Riga, Latvia

Cells and plasmids		
Cells	HEK293T cells	ATCC, Manassas, USA
Plasmids	pAdDeltaF6 packaging helper plasmid pUCmini-iCAP-PHP.eB capsid pAAV2/9n capsid pAAV-u6-sgRNA-hsyn-Cre-2a-eGFP-KASH-WPRE pAAV-u6-sgRNA-hsyn-mCherry-KASH-WPRE pAAV-u6-sgRNA-hsyn-eGFP-KASH-WPRE pAAV-u6-NeuNsgRNA-Cbh-mCherry-WPRE pAAV-u6-sgRNA-Cbh-eGFP-WPRE pAAV-u6-sgRNA-hsyn-Cre-2a-eCFP-WPRE pAAV-u6-sgRNA-hsyn-Cre-2a-KusabiraOrangeFP-WPRE	Addgene, Watertown, USA In house cloning

	pAAV-u6-sgRNA-hsyn-eGFP-2a-eCFP-WPRE pAAV-u6-sgRNA-hsyn-eGFP-2a-KusabiraOrangeFP-WPRE	
--	--	--

sgRNA refers to backbone here specific RNA described in the text were cloned

sgRNA and Primers		
Primers	<p><u>WPRE reverse primer</u> CATACGGTAAAAGGAGCAAC</p> <p><u>Titer determination</u> F- GGA ACC CCT AGT GAT GGA GTT R- CGG CCT CAG TGA GCG A</p> <p><u>Cloning of KASH plasmids</u> mCherry-KASH specific primers: F- AAGGTACCACCGGTGCCACCATGG R- GATATCGAATTCCTAGGTGGGAGG</p> <p>eGFP-KASH specific primers: F-GGGCCATGGT GAGCAAGGGCGAGGAG R- GATATCGAATTCCTAGGTGGGAGG</p> <p><u>Cloning of double FP plasmids</u> eGFP amplification F-GCAGTCGAGAAGGTACTCGCCACCATGGTGAGCA R- CCCTCTCCACTGCCGCTAGCCTTGACAGCTCGTCCATGCC</p>	Metabion, Planegg, Germany

III.1.9 PET scanning

III.1.10 CSF1R inhibitor and BTK inhibitor treatment

Reagents		
CSF1R inhibitor	CSF-1R inhibitor compound Vehicle	Sanofi, Boston, USA
BTK inhibitor	BTK inhibitor PEG 200	Sanofi, Boston, USA Merck Millipore, Darmstadt, Germany

III.1.11 Software

Data analysis		
snSeq analysis	Jupyter Lab- R console version 3.6.1 <u>RStudio, R</u> Seurat (Satja lab)	Open source, modified BSD license www.jupyter.org RStudio: Integrated Development for R, Boston, USA
Bulk RNA seq analysis	<u>Galaxy platform</u> RNA star (Dobin et al., 2013) HTseq count (Anders et al., 2015) DESeq2 (Love et al., 2014)	Open source, Penn State University, Johns Hopkins University, Oregon Health and Science University, USA

Image analysis	Adobe Creative Suite CS6 (Photoshop, Illustrator) ImageJ Huygens Essentials NeuronStudio software VIAS software Imaris	Adobe Systems Inc., San Jose, California, USA General Public License http://rsbweb.nih.gov Huygens SVI, Hilversum, Netherlands Developed by Wearne lab, Mount Sinai School of Medicine, New York, USA Oxford Instruments, Oxfordshire, England
----------------	---	---

sgRNA , primer design and TIDE analysis		
sgRNA design	Broad Institute GPP Web Portal sgRNA Designer	Broad Institute of MIT and Harvard, Cambridge, USA
Primer design	Benchling IDT primer quest tool	Benchling Inc., San Francisco, USA Integrated DNA Technologies, San Diego, USA

PET imaging		
PET scan reconstruction	PMOD V3.5	PMOD TecnoLogies, Basel, Switzerland

III.2 Methods

III.2.1 Experimental Animals

Experiments were performed on two animal age groups: for our young c-MS model at 8-14 weeks, and for our middle-aged model at 10-12 months old. Both male and female animals were used for all experiments and were equally distributed into control and experimental groups. Mice were randomly allocated to groups in all experiments. All animals were bred in our animal facility at the BMC, Planegg, Germany and housed under standard conditions (12h light/dark cycle, maximum 5 mice per cage, autoclaved food and water supplied *ad libitum*). The cages were provided with enrichment consisting of play tunnels, nesting material, and a red plastic mouse house. For PET experiments, animals were transferred 2-3 weeks pre-experimental start to the animal facility of the Nuclear Medicine Department of Klinikum Großhadern, Munich, Germany, and housed under standard conditions with the above described enrichment. Mice were weaned at postnatal day 21. Animals with F1 and F2 background of *C57Bl/6J* strain (Jackson Laboratory) and of *BiozziABH* (designated as *BiozziABH/RijHsd*, Harlan laboratories) were crossbred in our facility and used for all experiments. To assess spine density and dendritic pathology in c-MS *in situ*, as well as for PET imaging we used *Thy1-GFP-Mx BiozziABH* mice (derived from *Tg(Thy1-EGFP)MJrs/J*, which were provided as a gift from J. Sanes and J. Lichtman, Harvard University). To evaluate phagocyte activation, infiltration and synaptic engulfment, we used *CCR2^{RFP}x Biozzi ABH*

mice (derived from *B6.129(Cg)-Ccr2tm2.1lfc/J*, Jackson Laboratory) and *CX₃CR-1^{GFP} x BiozziABH* mice (derived from *B6.129P-Cx₃cr-1tm1Litt/J*, Jackson Laboratory). For viral labeling used for calcium analysis in dendrites and synapses, either *CCR2^{RFP} x Biozzi ABH* or *C57Bl6Jx BiozziABH* mice were used. For nuclei isolation and subsequent snRNA-seq *C57Bl6Jx BiozziABH* mice were used. For CRISPR/Cas9 knockout experiments, *R26-Cas9 x BiozziABH* (derived from *Gt(ROSA)26Sor^{tm1.1(CAG-cas9*,-EGFP)Fezh/J}*, Jackson Laboratory) mice were used.

All animal experiments were performed in accordance with regulations of the relevant animal welfare acts and protocols approved by the local animal ethics committee of the state of Bavaria (Regierung von Oberbayern) in accordance with European guidelines.

III.2.2 c-MS Induction

The c-MS model was induced in young mice (8-14 weeks) and middle-aged (10-12 months) mice as follows: young mice were anesthetized with ketamine-xylazine anesthesia (87 mg/kg + 3 mg/kg) while middle-aged mice were anesthetized with a combination of medetomidine-midazolam-fentanyl (MMF, 0.5 mg/kg + 5 mg/kg + 0.05 mg/kg). Anesthetized mice were subsequently immunized subcutaneously with 200 µl of an emulsion containing 30 µg of purified recombinant rat MOG (N1-125, expressed in *E. coli*) and complete Freund's adjuvant, consisting of incomplete Freund's adjuvant and 10 mg/ml of *Mycobacterium tuberculosis* H37 Ra. Pertussis toxin (75-200 ng) was administered intraperitoneally on day 0 and day 1 after immunization. The immunization procedure was repeated 1 week after the first.

At 21- 28 days following initial MOG immunization, animals were anesthetized with MMF and intracortically injected with 2 µl of a cytokine mix of 0.25 µg/µl of recombinant mouse TNFα and 750 U/µl of recombinant murine IFNγ in phosphate buffered saline (PBS)/ 0.1% bovine serum albumin (BSA) at coordinates 1.2 mm lateral, 0.6 mm caudal to bregma, depth 0.8 mm, to evoke cortical lesions. Surgery was performed with the use of a 0.4 mm stainless drill head to open a fine hole into the skull, where a 25 µm in diameter glass capillary was used to inject the cytokines over 15-30 minutes. A 1:2 dilution of cytokines was used for Round 2 of the PET imaging experiment. Middle-aged mice were treated with 200 mg/kg Metamizole prior to surgery start. Skull skin was sutured, and animals were injected with AFN antagonist as well as buprenorphine (0.05-0.1 mg/kg), which was used as analgesia post-surgery and for the days following up the surgery.

Animals were weighed daily and classified based on an EAE scoring system developed to assess neurological and locomotor deficits: 0- no detectable clinical signs, 0.5- partial tail weakness, 1- complete tail paralysis, 1.5- gait instability, 2- hind limb paresis, 2.5- hind limb paresis with partial dragging, 3- complete hind limb paralysis, 3.5- complete hind limb paralysis and fore limb paresis, 4- hind and fore limb paralysis, 5- death. A score of 3.5 or higher would result in immediate sacrifice of the animal.

III.2.3 Cranial window surgery

To assess *in vivo* calcium levels in spines and dendrites upon cortical neuroinflammation, we performed a craniotomy and implanted a cranial window over the somatosensory cortex of animals as previously described (Holtmaat et al., 2009). In short, animals were anesthetized with MMF and head-fixed in the stereotaxic frame. Using a 0.5 mm stainless steel drill head,

craniotomy was performed. A 4 mm diameter cover slip was placed above the somatosensory cortex before being sealed using histoacryl glue and dental cement, as well as placing a head bar for imaging purposes. In order to image baseline calcium levels of dendrites and spines, 10 days before imaging, 0.5 μ l of 1×10^{12} viral particles of AAV1.hSyn1.Twitch2b.WPRE.SV40 were injected 0.3 mm deep into the somatosensory cortex and analgesia was performed with buprenorphine post-surgery and on the days following the surgery. On the imaging day, an acute cranial window was implanted as described above.

III.2.4 Two-photon in vivo microscopy

For acute in vivo imaging of calcium accumulation in dendrites and spines, animals were anesthetized with MMF intraperitoneally and an acute cranial window was implanted as described above. 30 minutes after window implantation, to allow for dental cement drying, in vivo microscopy was performed using an Olympus FV1200-MPE or an Olympus MPE-RS two-photon microscopy system, equipped with a femto-second pulsed Ti:Sapphire laser (Mai Tai HP-DS or Insight DeepSee, Spectra-Physics) and laser power was attenuated by acousto-optical modulators. Emission was detected with non-descanned gallium arsenide phosphide (GaAsP) detectors. We used a two-photon wavelength of 840 nm to excite both proteins on the calcium indicator Twitch2b, mCerulean3 and cpVenusCD. Fluorescence of mCerulean3 was collected in a cyan channel (referred to as "CFP") while fluorescence of cpVenusCD was collected on the yellow channel (referred to as "YFP"), using emission barrier filter pairs with 455-490 and 526-557 nm respectively. Images were acquired with a 25x/1.05 dipping cone water-immersion objective, at 12-bit, pixel size of 124 nm/pixel, dwell time of 2.0 μ s/pixel and a laser power of 30-50mW measured in the back focal plane. A z-spacing of 1 μ m was used to capture volume stacks of 30-60 μ m of depth into the cortical layer I from the surface. Imaging of spine calcium activity over time was done under isoflurane anesthesia with a resonant scanner system at 15 Hz (Olympus MPE-RS) and continuous monitoring through a MouseOx system equipped with a thigh sensor for small animals. Images were acquired using a 25x/1.05 dipping cone water-immersion objective, with a zoom of 4x and a pixel size of 249 nm/pixel using averaging to increase the signal to noise ratio. Fluorescence of Twitch2b proteins was collected in the cyan and yellow channels as described above using the same barrier filter pairs. No signs of photodamage were observed over the imaging period in animals. No obvious difference could be noticed in the fraction of spines with elevated calcium levels between MMF and isoflurane anesthetized animals. Two-photon in vivo microscopy was performed together with Adrian-Minh Schumacher.

III.2.5 Immunofluorescence/ Immunohistochemistry

Mice were lethally anesthetized with isoflurane and transcardially perfused with 4% (wt/vol) paraformaldehyde in PBS using a peristaltic pump (velocity 6 mL/min) and brains were post-fixed at 4°C in 4% PFA.

For synaptic pathology and spine density measurement, brains were post-fixed overnight, dissected from the skull and cut into 80-100 μ m thick coronal sections using a Leica vibratome. Sections were stained with the free-floating method. Sections were washed with 1x PBS and 0.1% (vol/vol) Triton X-100 in PBS (PBS-T) and incubated for 20 minutes with NeuroTrace 640/660 fluorescent Nissl dye (1:500, Invitrogen). Sections were then washed with 0.1% PBS-T and 1x PBS and mounted into slides with Vectashield (Vector laboratories).

For evaluation of myelin length, brains were post-fixed for 12-24 hours in 4% PFA, isolated and cryoprotected in 30% sucrose for 72 hours. The samples were embedded in Tissue-Tek (Sakura), frozen down to -20°C and cut in 50 µm thick coronal sections on a Leica cryostat. Sections were stained with the free-floating method. First, sections were rinsed with 1xPBS and treated with methanol for crisp MBP staining. Methanol treatment meant incubating samples in cold methanol for 20 minutes at -20°C followed by rinsing with 1xPBS before blocking with 10% goat serum in 0.5% PBS-T for 1 hour at room temperature. Sections were incubated overnight with rabbit anti-MBP antibody (1:200, DAKO) in 1% goat serum in 0.5% PBS-T. Sections were washed with 1xPBS and incubated at 4°C overnight with AlexaFluor-conjugated goat anti-rabbit 594 antibody (1:1000, Invitrogen) in 1% goat serum in 0.5% PBS-T before being counterstained with DAPI (1:10,000, Invitrogen) and mounted with Vectashield (Vector laboratories).

For evaluation of phagocyte activation and infiltration brains were post-fixed for 12-24 hours with 4% PFA, isolated and cut in 80-100 µm thick coronal sections in a Leica vibratome. Sections were stained in the free-floating method. Sections were washed with 1xPBS and blocked with 10% goat serum in 0.5% PBS-T for 1 hour at room temperature. Subsequently, the sections were incubated overnight with rabbit anti-Iba-1 (1:300, FUJIFILM Wako) and/or rat anti-MHC II (I-A/I-E) (1:300, BD Pharmingen) antibodies in 1% goat serum in 0.5% PBS-T at 4°C. They were then washed with 1xPBS and incubated overnight at 4°C with AlexaFluor-conjugated goat anti-rabbit 647 (1:500, Invitrogen) and/or AlexaFluor-conjugated goat anti-rat 594 (1:500, Invitrogen) antibodies in 1% goat serum in 0.5% PBS-T before being counterstained with DAPI (1:10,000, Invitrogen) or NeuroTrace 435/455 fluorescent Nissl dye (1:500, Invitrogen) and mounted with Vectashield (Vector laboratories).

To evaluate presynaptic engulfment, brains were post-fixed for 4-6 hours in 4% PFA, isolated and cut in 40 µm thick coronal sections using a Leica vibratome. The sections were stained in the free-floating method. They were washed with 1xPBS and blocked with 10% goat serum in 0.1% PBS-T for 1 hour at room temperature and then incubated overnight at room temperature with rabbit anti-Synapsin-1 (1:500, Millipore) and rat anti-LAMP1 (1:300, Biolegend) antibodies in 1% goat serum in 0.1% PBS-T. The sections were then washed with 1xPBS and incubated overnight at 4°C with AlexaFluor-conjugated goat anti-rabbit 647 (1:500, Invitrogen) and AlexaFluor-conjugated goat anti-rat 594 (1:500, Invitrogen) or AlexaFluor-conjugated goat anti-rat 488 (1:500, Invitrogen) antibodies in 1% goat serum in 0.1% PBS-T, before being counterstained with DAPI (1:10,000, Invitrogen) and mounted with Vectashield (Vector laboratories).

To evaluate postsynaptic engulfment, brains were post-fixed for 4-6 hours in 4% PFA, isolated and cryoprotected in 30% sucrose for 72 hours. The samples were embedded in Tissue-Tek medium (Sakura) and cut in 40 µm thick coronal sections using a Leica cryostat. Sections were stained in the free-floating method. Sections were washed with 1xPBS and blocked with 20% goat serum in 1x PBS for 1 hour at room temperature before being incubated at 4°C overnight with rabbit anti-PSD95 (1:200, Invitrogen) and rat anti-LAMP1 (1:300, Biolegend) or for 36 hours with guinea pig anti-Homer-1 antiserum (1:500, Synaptic Systems) and rat anti-LAMP1 antibody (1:300, Biolegend) in 10% goat serum in 0.3% PBS-T. They were washed with 1xPBS and incubated for 4 hours at room temperature with AlexaFluor-conjugated goat anti-rabbit 647 (1:500, Invitrogen) and AlexaFluor-conjugated goat anti-rat 594 (1:500, Invitrogen) or AlexaFluor-conjugated goat anti-rat 488 (1:500,

Invitrogen) antibodies in 1% goat serum in 0.1% PBS-T. Sections were counterstained with DAPI (1:10,000, Invitrogen) and mounted with Vectashield (Vector laboratories).

For determination of NeuN CRISPR/Cas9 KO, brains were post-fixed for 6 hours in 4% PFA, isolated and cryoprotected in 30% sucrose for 72 hours. Brains were embedded in Tissue-Tek medium (Sakura) and cut in 60 µm thick coronal sections using a Leica cryostat and collected in PBS for free-floating staining. Sections were washed with 1xPBS and blocked with 10% goat serum in 0.5% PBS-T before being incubated overnight at 4°C with rabbit anti-NeuN (1:400, Sigma Aldrich) in 1% goat serum in 0.5% PBS-T. Afterwards, sections were washed with 1xPBS and incubated for 4 hours at room temperature with AlexaFluor-conjugated goat anti-rabbit 405 (1:500, Invitrogen) in 1% goat serum in 0.5% PBS-T. Sections were then mounted with Vectashield (Vector laboratories).

III.2.6 Confocal microscopy

To image transgenic fluorescence or immunofluorescence-stained tissue, we used upright confocal laser-scanning microscopes FV1000 (Olympus), SP8 (Leica) equipped with a standard set and fixed laser lines or an SP8 (Leica) equipped with a UV and white light laser, or an SP8 Falcon upright DM8 system with one and two photon excitation (DIVE) (Leica) equipped with a UV laser and white light laser.

For imaging of spine density in young mice and in PET scan tissue, myelin length, microglia number and activation and infiltrating phagocyte quantification, an upright FV1000 Olympus with standard filter sets and laser lines was used. To reconstruct apical dendrites in *GFP-M x BiozziABH* mice for characterization of young animals, a 60x/1.42 NA oil immersion objective (Olympus) was used with a digital zoom of 3.5, a z-spacing of 200 nm and a pixel resolution of 75 nm per pixel in order to image the 100 µm coronal brain sections. The Kalman method was used for averaging of two images. For imaging of PET scanned tissue to measure spine density, the 60x/1.42 NA oil immersion objective (Olympus) was used with a digital zoom of 2.4, a z-spacing of 200 nm and a pixel resolution of 43 nm per pixel. To acquire images to quantify microglia numbers, their activation based on MHCII staining, microglia nodules, infiltrating phagocytes based on Iba-1 staining and *Ccr2^{RFP}* expression, coronal brain sections of *CX3CR1 x BiozziABH* as well as *CCR2 x BiozziABH* mice were imaged with a 20x/0.85 NA oil immersion objective (Olympus) at z-spacing of 1.5 µm and pixel resolution of 2.5 µm per pixel. To image myelin status, overviews were taken with 20x/0.85 NA oil immersion objective (Olympus) at z-spacing of 1.5 µm and pixel resolution of 2.5 µm per pixel while myelin length was quantified with higher magnification images taken with a 60x/1.42 NA oil objective, z-spacing of 0.33 µm and pixel resolution of 0.27µm per pixel. All imaging in the Olympus FV1000 was recorded in PMT detectors.

For synapse phagocytosis in c-MS and in CSF1R inhibitor treatment, spine density analysis in middle-aged mice and in CSF1R-inhibitor treated mice as well as NeuN CRISPR/Cas9 KO, an upright LeicaSP8 confocal microscope equipped with a standard filter set and laser lines was used. To evaluate synapse phagocytosis, 40 µm thick coronal sections were imaged with an 40x/1.30 NA oil immersion objective (Leica) with a zoom of 3.0, z-spacing of 200 nm and a pixel resolution of 79 nm per pixel. The synaptic staining as well as the phagocyte labelling and LAMP1 were recorded with hybrid photo detectors (HyDs). For spine density analysis, 100 µm thick coronal sections were imaged with a 63x/1.40 NA oil immersion

objective (Leica), an overview was taken at zoom of 1.0 in a single plane and a pixel resolution of 0.48 μm per pixel in tile scan mode. Images of dendrites for further analysis were taken only in the eGFP channel with a zoom of 2.4, z-spacing of 200 nm and a pixel resolution of 42 nm per pixel. Both eGFP and NeuroTracer 640/660 signal was recorded with hybrid photo detectors (HyDs). To image the NeuN CRISPR/Cas9 KO, 60 μm thick coronal sections were imaged with a 63x/1.40 NA oil immersion objective (Leica) a zoom of 1, on a single plane and with a pixel resolution of 0.18 μm per pixel. Both NeuN and mCherry signal from the virus were recorded using hybrid photo detectors (HyDs).

For spine density quantification in BTK-inhibitor and in *lfngr1* CRISPR/Cas9 KO, imaging was performed in an upright Leica SP8X WLL confocal microscope, equipped with a 405 nm laser, WLL2 laser (470-670 nm) and acusto-optical beam splitter. To investigate spine density upon BTK-inhibitor treatment, 100 μm coronal sections were imaged with a 63x/1.40 NA oil immersion objective (Leica). An overview was taken at zoom 0.75 in a single plane and a pixel resolution of 0.17 μm per pixel in tile scan mode. Images of dendrites for further analysis were taken only in the eGFP channel with a zoom of 2.4, z-spacing of 200 nm and a pixel resolution of 36 nm per pixel. Both eGFP from the transgenic labelling and NeuroTracer 640/660 signal was recorded with hybrid photo detectors (HyDs). For spine density quantification of *lfngr1* CRISPR/Cas9 KO imaging was performed with a 63x/1.40 NA oil immersion objective (Leica). An overview was taken at zoom 1 in a single plane and a pixel resolution of 0.48 μm per pixel in tile scan mode. Images of dendrites for further analysis were taken without the NeuroTracer 640/660 channel with a zoom of 2.4, z-spacing of 200 nm and a pixel resolution of 36 nm per pixel. The eCFP from the virus was detected by a photo multiplier tube (PMT) detector, eGFP, Kusabira Orange FP signal from the viruses as well as the NeuroTracer 640/660 signals were detected with hybrid photo detectors (HyDs).

III.2.7 Nuclei isolation and FACS sorting

To sort nuclei for snRNA-seq and for CRISPR/Cas9 evaluation, mice were first transcardially perfused with PBS. The right hemisphere cortex was isolated (ipsilateral to cytokine and virus injection) and was put into an Eppendorf tube containing Nuclei EZ lysis Buffer. Cortex was homogenized on ice with a pestle and the tube was filled with Nuclei EZ lysis buffer and incubated for 5 minutes. Cortex homogenate was subsequently filtered through a 70 μm cell strainer and transferred to a new tube, where nuclei were centrifuged at 500xg for 5 minutes at 4°C (all centrifugation steps were carried on this conditions). Supernatant was decanted, and nuclei were once again resuspended in Nuclei EZ lysis buffer. Following a 5-minute incubation on ice, nuclei were centrifuged. Supernatant was once again decanted and 500 μl of Buffer 1 (1x DPBS, 1.0% BSA and 0.2 U/ μl RNase inhibitor) were added for 5 minutes without resuspension to allow for buffer exchange. The tube was subsequently filled with Buffer 1 and nuclei were resuspended, then centrifuged. Supernatant was decanted and nuclei were incubated for 5 minutes with 1:1000 Fc block. Each sample was subsequently incubated for 10 minutes on ice in the dark with 1:500 of Alexa Fluor conjugated rabbit anti-mouse NeuN and with 1:200 Hashtag antibody. A different hashtag was used per sample to label nuclei for snRNA-seq, while no Hashtag antibodies were used during CRISPR/Cas9 related nuclei isolation. Following incubation time, samples were washed with Buffer 1 and centrifuged. The washing step was repeated once again and nuclei were resuspended in Buffer 2 (1x DPBS, 1.0% BSA, 0.2 U/ μl RNase Inhibitor, 10 μm /mL DAPI). For snRNA-seq samples, all samples were pooled during Buffer 2 resuspension in a total volume of 1 mL

Buffer 2. For CRISPR/Cas9 samples, each sample was resuspended in 500 μ l Buffer 2. Nuclei were filtered through a 30 μ m cell strainer and were FACS sorted.

Nuclei were FACS sorted in the Core Facility Flow Cytometry BMC together with Dr. Arek Kendirli, Clara de la Rosa del Val, and Eduardo Beltrán in BD FACSAriaFusion and BD FACSAriaIIIu machines. Each FACS machine is equipped with 4 lasers: 405, 488, 561 and 640 nm for the FACSAriaFusion and 405, 488, 561 and 633 nm for the FACSAriaIIIu. Nuclei for snRNA-seq were sorted with a gating strategy first based on granularity and size to obtain nuclei and remove debris, doublets were then removed, DAPI and NeuN staining allowed for selection of nuclei and to allow us to assess the number of approximate neurons per sample. In this case, all DAPI positive nuclei were sorted. In total 20,000 nuclei were sorted of which, 10,000 were set into a mixture containing gel beads, cell-mastermix and partitioning oil, which altogether would generate GEMs. GEMs could then be used for reverse transcription and chip loading in the Chromium Next GEM Single Cell 3' GEM, Library & Gel Bead Kit v3.1. For snRNA-seq, this kit was subsequently followed together with the 3' Feature Barcode Kit and samples were sent for sequencing.

Nuclei for CRISPR/Cas9 evaluation were sorted with a gating strategy as follows: first gating was based on granularity and size to obtain the nuclei and remove debris; then based on size of the samples, single nuclei were selected removing doublets, DAPI and NeuN staining allowed for selection of neuronal specific nuclei, and from there, infected cells with target sgRNA could be selected based on the fluorophore used for their sorting (eGFP for NeuN and NT sgRNA sorting, mCherry for PSAP and *lfng1* sgRNA sorting). Nuclei were then kept at 4°C and used for TIDE sequencing or 3' bulk mRNA sequencing.

III.2.8 sgRNA and plasmid cloning

In order to perform CRISPR/Cas9 knockout of target genes, sgRNAs for those genes were designed using the Broad Institute GPP sgRNA Designer tool (<https://portals.broadinstitute.org/gpp/public/analysis-tools/sgrna-design>). Selected sgRNAs were ordered as oligos with the sgRNA sequence and the reverse complement sequence, which had to be modified to increase their cloning efficiency into retroviral and AAV plasmids, needed for testing and evaluation of knockout effect, by adding a G at the 5' end of the sgRNA if it did not already start with one. Additional modification required were adding CACC (for retro virus sgRNA) or ACC (for AAV sgRNA) overhangs to the forward sequence and AAAC (for retro virus sgRNA) or AAC (for AAV sgRNA) to the reverse sequence. These oligos were ordered from Metabion and were cloned into the desired plasmids. For cloning into retroviral plasmids, MSCV-pU6-sgRNA-Pgk-Puro-T2A-BFP had to be digested with *BS*I, while AAV plasmids had to be digested with *Sap*I in order to allow sgRNA cloning into the sgRNA backbone. Plasmids were digested for 1-24 hours at 37°C with CutSmart buffer and were ran in a 1% agarose gell with 1 μ l Peq Green in TAE buffer for 30 minutes. The band at the digested plasmid size was gel excised and purified using the QIAquick gel extraction kit following manufacturer's instructions and was used for sgRNA cloning. Complementary oligos were phosphorylated with T4 PNK in 10X T4 Ligation Buffer and annealed by using a thermocycler protocol of 1 minute at 95°C followed by a temperature decrease of 5°C per minute until 25°C were reached. Annealed Oligos were then ligated to the digested retrovirus or AAV plasmid using Quick ligase for 5 minutes at room temperature. Ligated plasmid was transformed into Stellar Competent cells by heat shock at 42°C for 55 seconds. Transformed

bacteria were grown overnight at 37°C on an agar plate with Ampicillin. The next day single colonies could be selected and grown overnight in LB media containing Ampicillin in a bacteria shaker at 37°C and 400 RPM. Plasmid DNA could subsequently be isolated with the QIAprep Spin Miniprep Kit following manufacturer's instructions and the plasmid could be sent for Sanger sequencing using the hU6 primer. A glycerol stock was created for correctly sequenced plasmids which could then be used for virus production.

For AAV viruses, several plasmids were cloned in house to obtain the desired sequence, under the guidance and with the help of Dr. Arek Kendirli. For generation of pAAV-u6-sgRNA-hSyn-eGFP-KASH-WPRE and pAAV-u6-sgRNA-hSyn-mCherry-KASH-WPRE which were used as backbones for introduction of sgRNA used for TIDE sequencing and bulk RNA-seq in vivo, Snapgene was used as a method to design these plasmids based on the AAV-u6-sgRNA-hSyn-Cre-2a-eGFP-KASH-WPRE plasmid (Addgene). To generate the mCherry-KASH variant, a two-step cloning had to be performed. First, generation of a pAAV-u6-sgRNA-Cbh-mCherry-KASH-WPRE plasmid was performed by digesting a pAAV-u6-sgRNA-Cbh-mCherry-WPRE that was kindly provided by Almir Aljovic (and is used for the NeuN knockout) and the AAV-u6-sgRNA-hSyn-Cre-2a-eGFP-KASH-WPRE with BsrGI and HindIII. The KASH fragment was inserted into the Cbh-mCherry-WPRE backbone through a ligation to obtain the resulting pAAV-u6-sgRNA-Cbh-mCherry-KASH-WPRE. In the second step, the generated plasmid was used for PCR amplification of the mCherry-KASH sequence with the specific primers described in materials section III.1.8.2. The amplified PCR product was run on a 1% agarose gel, where the right amplicon size could be gel extracted and purified with the QIAquick gel extraction kit and the DNA concentration could be measured in the Nanodrop. Both the mCherry-KASH product and the AAV-u6-sgRNA-hSyn-Cre-2a-eGFP-KASH-WPRE were subsequently digested with KpnI and EcoRI and were ligated using 75 ng of the restricted backbone and 50 ng of the digested insert. Ligation was performed at room temperature for 5 minutes and the ligated plasmid was transformed into Stellar competent cells through heat shock at 42°C for 55 seconds. Bacteria were grown overnight in agar plates with ampicillin. Single colonies could be selected and following growth in LB media with ampicillin could be prepped with the QIAprep Spin Miniprep Kit. To confirm the sequence of the ligation product the plasmid was Sanger sequenced using the hU6 primer and a reverse WPRE primer. To generate the pAAV-u6-sgRNA-hSyn-eGFP-KASH-WPRE plasmid, the generated pAAV-u6-sgRNA-hSyn-mCherry-KASH-WPRE plasmid was digested with NcoI and EcoRI. eGFP-KASH was amplified with PCR from the AAV-u6-sgRNA-hSyn-Cre-2a-eGFP-KASH-WPRE using eGFP-KASH specific primers described in materials section III.1.8.2 and was purified as described above. The purified fragment was likewise digested with NcoI and EcoRI. The digested eGFP-KASH fragment (42 ng) and digested pAAV-u6-sgRNA-hSyn-mCherry-KASH-WPRE plasmid (75 ng) were ligated with quick ligase at room temperature for 5 minutes. The ligated plasmid was transformed into Stellar competent cells as described above and colonies were selected that could be used for Sanger sequencing to determine correct ligation via hU6 primer and WPRE reverse plasmid.

Further generation of plasmids pAAV-u6-sgRNA-hsyn-eGFP-2a-eCFP-WPRE and pAAV-u6-sgRNA-hsyn-eGFP-2a-KusabiraOrangeFP-WPRE was performed as follows with the help of Dr. Arek Kendirli. In a first step, the pAAV-u6-sgRNA-Cbh-mCherry-WPRE plasmid kindly provided by Almir Aljovic was digested with AgeI and HindIII. An eGFP fragment was PCR amplified from an eGFP-Ires-Cre plasmid kindly provided by Yi-Heng Tai. The eGFP

fragment was then inserted into the digested pAAV-u6-sgRNA-Cbh-mCherry-WPRE via Gibson Assembly. For the second step, previously generated pAAV-u6-sgRNA-hSyn-Cre-2a-eCFP-WPRE and pAAV-u6-sgRNA-hSyn-Cre-2a-KusabiraOrangeFP-WPRE plasmids kindly provided by Paula Sanchez and Adinda Wens were used. These plasmids were digested with KpnI and NheI. From the generated pAAV-u6-sgRNA-Cbh-eGFP-WPRE plasmid, eGFP was PCR amplified using the eGFP specific primers described in methods part III.1.8.2. Following purification of digested plasmid and of the fragment as described above, the insert was added into the digested plasmids via a Gibson assembly. Assembled plasmids were then transformed into Stellar competent cells via heat shock as described above and following single colony selection, primer sequence could be confirmed via Sanger sequencing using the Hu6 and the WPRE reverse primer.

III.2.9 Virus production

To perform gene editing through the CRISPR/Cas9 system both *in vitro* and *in vivo*, viruses had to be produced to deliver the sgRNA into cells. For *in vitro* infection of Cas9-expressing HoxB8-FL cells, retroviruses were produced as follows: approximately 750,000 HEK cells were seeded per well in a 6-well plate (1 sgRNA for each retrovirus was used per well) in antibiotic free media. 1.2-1.5 µg of MSCV-pU6-sgRNA-Pgk-Puro-T2A-BFP (where sgRNA was specific for every targeted sgRNA cloned as described above) or MSCV-pklv2-U6-(sgNon-Targeting)-Pgk-Puro-T2A-tdTomato plasmid, 1.2-1.5 µg Pcl-Eco and 7.5 µl TransIT were added in 500µl RPMI media, vortexed and incubated at room temperature for 30 minutes. Following incubation, the mix was added dropwise to the seeded HEK cells. The day after transfection, media of the wells was changed to HoxB8 cell media (RPMI GlutaMAX supplemented with 0.1% 2-Mercaptoethanol, 1 µM β-estradiol and supernatant from Flt3L-producing B16 melanoma cell line with a final concentration of 35 ng/ml). 48 hours after transfection, media was collected from HEK cells and was centrifuged at 3000 rpm for 5 minutes. Retrovirus could then proceed to be used for infection of HoxB8 cells.

For *in vivo* infection in *R26-Cas9x BiozziABH mice*, AAV viruses were produced through two different purification methods. In the first method, which was used for the production of the php.eb AAV-u6-lfng1sgRNA-hSyn-eGFP-2a-KusabiraOrangeFP-WPRE and php.eb AAV-u6-NTsgRNA-hSyn-eGFP-2a-eCFP-WPRE viruses, 2 x 10⁶ HEK cells were seeded in 15 cm plates coated with poly-lysine 24 hours before transfection and kept at 37°C with 5% CO₂. The following day, cells were transfected with 16 µg plasmid DNA, 10 µg of php.eb capsid plasmid, 20 µg pAdDeltaF6 packaging helper plasmid and 100 µg Polyethylenimine (PEI) in 4 ml Opti-MEM per plate (usually 4 plates were needed per virus). The mix was allowed to rest for 20-30 minutes at room temperature prior to transfection to allow PEI:DNA complex formation. Once the incubation was finished, the cells were transfected dropwise with 4 ml mixture per dish. 24 hours after transfection, cells were checked under the fluorescence microscope for transfection efficiency and their media was changed to media without FBS. 72 hours after transfection, a first harvest of the supernatant was performed, and HEK media without FBS was once again added to the HEK cells. Harvested supernatant was spun down at 1500 RPM, 5 minutes, 4°C and was subsequently filtered through a 0.45 µm filter into a bottle that was kept at 4°C. 72 hours following first harvest, a second harvest was performed and supernatant was again spun down and filtered. Combined supernatant from both harvests could be used for concentration. For concentration, a 100 kDa AMICON filter was equilibrated by adding 15 ml PBS and spinning it at 4200 RPM for 2 minutes at 4°C. The

harvested virus was then added and spun at 4200 RPM for 30 minutes at 4°C. The spinning step was repeated until the desired volume (200-300 µl) was reached and the virus could be tittered and aliquoted for storage at -80°C.

The second method was used for production of php.eb. AAV-u6-PSAPsgRNA-hSyn-mCherry-KASH-WPRE, php.eb AAV-u6-NTsgRNA-hSyn-eGFP-KASH-WPRE, php.eb AAV-u6-NeuNsgRNA-hSyn-eGFP-KASH-WPRE, AAV9 pAAV-u6-NeuNsgRNA-Cbh-mCherry-WPRE, php.eb AAV-u6-NeuNsgRNA-hSyn-eGFP-KASH-WPRE, and php.eb AAV-u6-NTsgRNA-hSyn-eGFP-KASH-WPRE. In this method, HEK cells were seeded 24 hours prior to transfection in 15 cm plates and kept in a humidified incubator at 37°C with 5% CO₂. The following day, cells were transfected with 16 µg plasmid DNA, 10 µg of php.eb capsid plasmid, 20 µg pAdDeltaF6 packaging helper plasmid and 100 µg Polyethylenimine (PEI) in 4 ml Opti-MEM per plate (usually 4 plates were needed per virus). The mix was allowed to rest for 20-30 minutes at room temperature prior to transfection to allow PEI:DNA complex formation. Once the incubation was finished, the cells were transfected dropwise with 4 ml mixture per dish. 24 hours after transfection, cells were checked under the fluorescence microscope for transfection efficiency and their media was changed. 72 hours after transfection the supernatant was harvested as well as the HEK cells and virus purification was started. For every 80 ml of harvested supernatant (usually a whole virus coming from 4 plates), 20 ml of Polyethyleneglycol were added and the mixture was placed on a horizontal roll shaker for 1 hour at 4°C before it was moved to an upright position without shaking for 3 hours, to allow virus precipitation. Samples were then centrifuged at 2818xg for 15 minutes at 4°C and the virus pellet was carefully resuspended in 1 ml 1xPBS/ 0.001% pluronic F68/ 200 mM NaCl and kept at 4°C while purification from HEK cells was taking place. To harvest cells, 5 ml PBS was added to each plate and cells were detached with the use of a cell scraper. Cells were collected from each plate with the same virus and pooled into one 50 ml Falcon tube. Cells were centrifuged at 1500 rpm for 5 minutes at 4°C and the pellet was resuspended in lysis buffer. Lysed cells then underwent 3 freeze/thaw cycles by freezing 10 minutes in liquid nitrogen followed by 10 minutes thawing at 55°C. Following the 3 cycles, cells were equilibrated to 37°C, where they were incubated for 45 minutes with 50 µM Benzonase. Cells were centrifuged at 4200 RPM for 10 minutes at 4°C and were also kept at 4°C until Iodixanol gradient was prepared. An iodixanol gradient of 4 layers capped by the lysed cell virus supernatant and the virus pellet from the harvested supernatant. The 4 layers were prepared and overlaid as follows:

- Layer 1: 15% iodixanol - prepared by adding 4.5 ml 60% iodixanol in 13.5 ml 1M NaCl/PBS-MK buffer ((26,3g MgCl₂, 14.91 KCl in 1x PBS in a total volume of 100ml, sterilize and pass through 0.22-µm filter)
- Layer 2: 25% iodixanol - prepared by adding 5 ml of 60% iodixanol in 7 ml of 1M NaCl/PBS-MK buffer and 30 µl phenol red
- Layer 3: 40% iodixanol - prepared by adding 6.7 ml of 60% iodixanol in 3.3 ml of 1M NaCl/ PBS-MK buffer
- Layer 4: 60% iodixanol - prepared by adding 10 ml of 60% iodixanol and 45 µl phenol red

Layers were overlaid with the use of a Stainless steel 316 syringe with a blunt 90° tip always added the new layer at the bottom of the QuickSeal tube. Lysed cell virus supernatant and the virus pellet from the harvested supernatant were layered at the top of the gradient. PBS

was used to top off the tube, which was then sealed. QuickSeal tubes loaded with the gradient and the virus were ultracentrifuged in a T70i rotor at 200,000xg for 2 hours at 18°C. Following centrifugation, QuickSeal tubes were removed from the rotor taking care to not disturb the gradient and were punctured at the 40%-60% interface with an 18 G needle. The layer containing the virus obtained from the gradient puncturing was then used for virus concentration. For virus concentration a 100 kDa AMICON filter was equilibrated by covering it in 0.1% Pluronic F68 in 1x PBS and incubating it at room temperature for 10 minutes. The solution was removed, 0.01% Pluronic F68 in 1xPBS was added and the AMICON filter was centrifuged at 3000 RPM for 5 minutes at 4°C. The filter membrane was next covered in 0.001% Pluronic F68 in 1x PBS and was once again centrifuged at 3000 RPM for 5 minutes at 4°C. The AMICON filter was loaded with the virus obtained from the QuickSeal tube puncturing which was topped with 0.001% Pluronic F68 in 1xPBS and was centrifuged at 4200 RPM for 20 minutes at 4°C. 0.001% Pluronic F68 in 1x PBS was then added and the AMICON filter was centrifuged at 4200 RPM for 20 minutes at 4°C. This last step was repeated until the virus inside was AMICON filter was clean of iodixanol and the desired concentration was achieved. The virus could at this point be titered and aliquoted for storage at -80°C.

Virus titration was performed following the addgene titration protocol using SYBR green technology found in <https://www.addgene.org/protocols/aav-titration-qpcr-using-sybr-green-technology/>. qPCR was ran on the Bio-Rad CFX Maestro software and final titer was calculated for each virus from the standard curve and the different dilutions.

III.2.10 *In vitro* retroviral infection of HoxB8 cells

In order to assess the efficiency of diverse sgRNAs for CRISPR/Cas9 knockout, these were initially tested *in vitro* in Cas9-expressing HoxB8-FL cells kindly provided by Seren Baygün from Prof. Dr. Marc Schmidt-Supprian's lab and maintained in culture by Dr. Arek Kendirli and Clara de la Rosa del Val in our laboratory. Retroviruses previously produced as described above and collected from HEK cell media were each pipetted in a 1:1 volume ratio with HoxB8 cells in media (around 200,000 cells) in a well of a 12-well plate. The plate with cells and retrovirus was centrifuged at 1200xg for 45 minutes with acceleration 4 and brake 4 at room temperature. Following centrifugation, retroviral spin infected HoxB8 cells were kept in a humidified incubator at 37°C with 5% CO₂. The day following retroviral infection, HoxB8 cells were checked under the microscope for expression of fluorescent proteins (BFP, tdTomato) and were transferred into media containing 5 µg/mL Puromycine used for selection of cells. Following selection and growth of sgRNA infected HoxB8 cells for around 7 days, the cells were used for TIDE sequencing.

III.2.11 TIDE sequencing

To evaluate the efficiency and frequency of sgRNA in generating indel mutations at the genomic level, TIDE sequencing was performed at the *in vitro* level with HoxB8 cells retrovirally infected with targeted and not targeted sgRNA, as well as at the *in vivo* level with nuclei sorted from *R26-Cas9x BiozziABH* mice infected with AAVs containing the target and not targeted sgRNA.

For HoxB8 cells TIDE sequencing, HoxB8 were collected and spun down at 300xg for 5 minutes at room temperature and resuspended in PBS. Genomic DNA was isolated using the DNeasy Blood and Tissue Kit following the manufacturer's instructions.

For nuclei sorted as described above coming from in vivo CRISPR/Cas9 knockout in mice, nuclei were spun down at 500xg for 5 minutes at room temperature and resuspended in 500 μ l PBS. Genomic DNA was isolated using the QIAamp DNA Micro Kit following the manufacturer's instructions.

Once genomic DNA was obtained from HoxB8 cells or from nuclei, PCR amplification of sgRNA targeted regions was performed with primers specific for each sgRNA (see materials section 1.8.1 sgRNA and primers table). PCR was performed with 10 μ l 5x Q5 buffer, 0.5 μ l Q5 High-Fidelity DNA Polymerase, 1 μ l dNTPs, 100-200ng gDNA in a total volume of 50 μ l. The PCR program was run as follows: 30sec - 98°C, 10 sec - 98°C, 20 sec - 62°C, 30 sec - 72°C and 2 min - 72°C. PCR amplification products were run on a 1% agarose gel with 1 μ l Peq Green in TAE buffer for 30 minutes. The bands at the expected amplicon size were gel excised and purified using the QIAquick gel extraction kit following manufacturer's instructions, followed by clean up of extracted products using the MinElute PCR Purification Kit. Genomic DNA was quantified in the Nanodrop, and 50 ng DNA was sent for Sanger sequencing with the PCR specific primers. Once sequencing results were obtained, knockout efficiency was evaluated using webtools Inference of CRISPR Editing v2 (ICE) (Conant et al., 2022) or tracking of indels by decomposition tool (TIDE) (Brinkman et al., 2014) where the target sgRNA samples were compared to non-targeted control samples.

III.2.12 AAV-induced CRISPR/Cas9 KO *in vivo*

To perform a CRISPR/Cas9 KO in cortical neurons of mice, we performed a local neuronal i.c. AAV virus injection into the right brain cortex hemisphere of *Cas9x BiozziABH mice*. Animals were anesthetized with MMF and head-fixed in the stereotaxic frame. Using a 0.5 mm stainless steel drill head, a fine hole was opened in the skull, where a 25 μ m in diameter glass capillary was used to inject 0.5 μ l of AAV virus at coordinates 1.2 mm lateral, 0.6 mm caudal to bregma and a depth of 0.8 mm, just like with cytokine injections. Skull skin was subsequently sutured and animals were injected with AFN antagonist as well as buprenorphine which was used as analgesia for the days following up the surgery.

Virus injection was performed 21 days prior to first immunization in c-MS induction for PSAP KO and the respective control NT animals with 1×10^{12} viral particles of php.eb. AAV-u6-PSAPsgRNA-hSyn-mCherry-KASH-WPRE or php.eb. AAV-u6-NTsgRNA-hSyn-eGFP-KASH-WPRE respectively for PSAP and NT animals.

For NeuN knockout, virus injection was performed 21 days prior to nuclei isolation in healthy mice with 1×10^{12} viral particles of php.eb AAV-u6-NeuNsgRNA-hSyn-eGFP-KASH-WPRE or php.eb AAV-u6-NTsgRNA-hSyn-eGFP-KASH-WPRE for TIDE analysis. For verification of NeuN knockout virus injection was performed 21 days prior to perfusion and PFA fixation in healthy mice with 1×10^{12} viral particles of AAV9 pAAV-u6-NeuNsgRNA-Cbh-mCherry-WPRE.

For *Ifngr1* knockout, virus injection was performed 21 days prior to nuclei isolation in healthy mice with 1×10^{12} viral particles of php.eb AAV-u6-NeuNsgRNA-hSyn-eGFP-KASH-WPRE

or php.eb AAV-u6-NTsgRNA-hSyn-eGFP-KASH-WPRE for TIDE analysis. For phenotypic analysis, virus co-injection was performed on the day of first immunization for c-MS mice and matched healthy controls, with 1×10^{12} viral particles of both php.eb AAV-u6-Ifngr1sgRNA-hSyn-eGFP-2a-KusabiraOrangeFP-WPRE and php.eb AAV-u6-NTsgRNA-hSyn-eGFP-2a-eCFP-WPRE. Viruses were injected directly adjacent to each other, within 0.1 mm distance in the lateral axis.

III.2.13 3' bulk mRNA sequencing

To assess the effects of CRISPR/Cas9 derived PSAP KO at the RNA level, cortical nuclei samples isolated from PSAP sgRNA and NT sgRNA i.c. injected c-MS mice were used for 3' bulk mRNA sequencing. In short, following FACS sorting, cortical nuclei were centrifuged at 500xg, for 5 minutes at room temperature. Supernatant was removed and RNA isolation was performed with the RNeasy Plus Micro kit as per the manufacturer's instructions. Resulting RNA was stored at -80°C until library preparation performed by Veronika Pfaffenstaller and Dr. Arek Kendirli. For library preparation, samples were thawed and calibrated to room temperature. The library was prepared using the Invitrogen Collibri 3' mRNA Library Prep Kit for Illumina system as per manufacturer's instructions. Library quality was subsequently checked on the DNA 1000 Chip with Agilent Bioanalyzer. Good quality samples were submitted to the laboratory of functional genome analysis (LAFUGA, Gene Center Munich) sequencing service for single-end 50 bp sequencing on HiSeq 1500.

III.2.14 Treatment with inhibitors of microglial activation

To determine the effect of therapeutic inhibition of microglia activation in c-MS mice, the c-MS model was induced as described above and animals were treated daily from the day of cytokine injection until perfusion at c-MS day 3 (four days in total) with 25 mg/kg intraperitoneal injection of the CSF1R-inhibitor compound (Sanofi) or vehicle. In the same way, c-MS induced mice were treated daily from the day of cytokine injection until perfusion (four days) with 15 mg/kg through an oral gavage of the BTK-inhibitor compound (Sanofi) or vehicle (100% PEG 200).

III.2.15 PET/CT imaging

Small animal positron emission tomography (PET) procedures followed an established standardized protocol for radiochemistry, acquisition, and post-processing (Brendel et al., 2016, Overhoff et al., 2016) and were performed by Laura Bartos. In $n=8$ c-MS mice and $n=4$ sham mice, SV2A small-animal PET/CT was performed 1 day prior to perfusion and a baseline scan was performed one week before immunization. After induction of anesthesia with isoflurane (1.5%; delivery 2.0 L/min) and topical application of an eye ointment (Bepanthen), a micro-catheter (30G needle, 14 cm plastic tube, 30G attachment) was inserted into the lateral tail vein. Starting with the injection of $[^{18}\text{F}]\text{UCB-H}$ (14.6 ± 0.8 MBq in 200 μl isotonic saline solution), PET emission data were acquired for 60 min post injection (p.i.) to measure cerebral SV2A expression using a small animal Mediso PET/CT system (Mediso, Muenster, Germany). An x-ray computed tomography (CT) scan was performed prior to the PET scan. All small-animal PET experiments were performed with isoflurane anesthesia (1.5%; delivery 1.5 L/min). A total of four animals were measured simultaneously and image data was generated from head to tail. Body temperature, heart and respiratory functions were monitored during the whole measurement.

The PET reconstruction procedure was an Ordered Subsets Expectation Maximization (OSEM-3D) algorithm with decay correction, scatter correction, attenuation correction, dead time correction, and sensitivity normalization. The CT scan enabled attenuation correction. The resulting PET images had $212 \times 212 \times 235$ voxels of $0.4 \times 0.4 \times 0.4$ mm³. Data were binned to a total of 28 frames, consisting of 6×10 s, 6×30 s, 6×60 s, and 10×300 s. The resulting CT images had $972 \times 972 \times 930$ voxels of $0.12 \times 0.12 \times 0.12$ mm³. PET reconstruction was performed by Laura Bartos.

III.2.16 Bioinformatic Analysis

Bioinformatic analysis throughout this thesis was performed in several different steps and manners for the different sections and can be described as follows:

a. Single nuclear RNA sequencing, c-MS data processing and data mapping

Following nuclei isolation and preparation of the 10X genomics Chromium libraries as described above, resulting sequencing files for c-MS data (n=5 Healthy control, n=4 c-MS day 3, n=4 c-MS day 14) were demultiplexed using Cell Ranger software from 10X Genomics to obtain an expression matrix containing a unique molecular identifier (UMI) per gene reads. Subsequently, files were analyzed by Eduardo Beltrán with the use of the Seurat pipeline (Butler et al., 2018, Hao et al., 2021, Satija et al., 2015, Stuart et al., 2019) in Jupyter lab (Kluyver et al., 2016) to barcode based on hashtags, create a Seurat object, run a quality control of the data, normalize it, scale it, perform linear dimensional reduction, determine dimensionality, cluster cells, visualize them using UMAPs, and assign initial cell type identity to the clusters. Following cell type determination, neuronal clusters were selected and a subset from the data was created for further analysis. The subset was then used for data mapping to the Allen Institute Human Brain Motor Cortex atlas (Bakken et al., 2021) together with data sets obtained from our collaborator Prof. Doron Merkler (University of Geneva), Schirmer et al., 2019 data set and the Religious Order Study (ROSMAP) AD (Mathys et al., 2019) data sets which were open access data sets. Mapping of data sets was performed by Klara Eglseer. Gene conversion in the c-MS data set had to be first performed to humanize the mouse genes and find gene orthologs using the Biomart “getLDS” function from Bioconductor (Durinck et al., 2009). The MS patient data set obtained from Prof. Doron Merkler (n=3 healthy controls, n=6 MS patients) was obtained using SMARTSeq technology, while all other data sets were obtained using 10X Chromium technology. The data set from Schirmer et al., 2019 comprised of human post mortem tissue samples separated into chronic active and chronic inactive lesions (n=9 healthy controls, n=12 MS patients) and was obtained open source from the National Center of Biotechnology Information (NCBI) from the sequence Read archive (accession number PRHNA544731). The Mathys et al., 2019 data set, obtained from the Synapse portal, was part of the ROSMAP study where frozen postmortem brain tissue (n=24 no pathology, n=24 Alzheimer’s disease pathology) was analyzed to profile ageing and dementia. Data sets were mapped to the Allen brain atlas Human Brain Motor Cortex Atlas (Bakken et al., 2021) using the Symphony algorithm (Kang et al., 2021). Mapped data yielded different cell types from which once again only the neuronal population was extracted for subsequent analyses performed by Veronika Pfaffenstaller. Differential gene expression was calculated using the “FindMarker” function in Seurat where the log fold change threshold and the “min.pct” argument were manually set to 0.

b. 3' bulk mRNA-seq of PSAP-KO

Following nuclei isolation and preparation of the 3' mRNA libraries as described above, resulting sequencing files for PSAP-KO and NT controls (n=5, n=4, respectively) were first analyzed with the Galaxy platform (Galaxy, 2022). Here we utilized the reference genome mm.10.3.ensGene.gtf, openly available, to help us process our raw count data files. FastQ files obtained from LAFUGA sequencing service of the LMU were first processed with RNA Star version 6 (Dobin et al., 2013), where files would be aligned to the reference genome. Alignment was considered successful, and samples were used, if the quality of alignment exceeded 60%. Aligned samples, in Bam files, were next processed using the HTSeq V06.1p1 (Anders et al., 2015) function under default parameters to generate HTSeq count files. HTSeq count files were then used for DESeq2 (Love et al., 2014) and resulting files were annotated using the Mus.musculus.GRCm39.104.gtf file to obtain gene names rather than Ensembl IDs as well as concatenated with an internal header file. DESeq2 results included PCA analysis as well as normalization of counts based on KO vs NT. Samples showing a diverging PCA were excluded. DESeq2 files were then moved to RStudio for plotting purposes and were further analyzed by Veronika Pfaffenstaller.

c. Statistical analysis

Statistical methods for sequencing data were carried out in R by Veronika Pfaffenstaller. Normal distribution of data was checked using a Shapiro-Wilk test using 5000 random values from each data set as the sample size exceeded the limit of values. Correlation was determined with Pearson's correlation. Comparisons between two groups were made with a student's t-test for normally distributed data, regarding average expression of ferroptosis in the acute mouse model, both MS patient data sets and the AD data set.

For fixed tissue analysis, statistical significance was calculated with Graphpad Prism V6.0 and V7.0. Normality was tested for every group with the Shapiro-Wilk test. ANOVA and t-tests were used for groups with normal distribution while Kruskal-Wallis and Mann-Whitney U tests were used upon determination of non-normal distribution. For PET imaging analysis a t-test was used together with Cohens d calculation. Data is expressed as mean \pm standard error of the mean. P-values obtained were corrected for multiple comparisons with Bonferroni's multiple comparison test and in all analyses $p < 0.05$ was considered statistically significant. Statistical test details are further described in the figure legends as well as p-values stated as significant levels.

III.2.17 Image analysis

a. Image processing and analysis

Post-processing of confocal imaging was performed with open-source image analysis software ImageJ (Schneider et al., 2012) and Adobe Photoshop.

b. Reconstruction of pyramidal neurons

The confocal images taken for analyzing spine density were deconvoluted using Huygens Essential version 16.05, 21.10 (Huygens SVI), in the GFP channel only, using 40 iterations and the classical MLE algorithm with a signal-to-noise ratio and background value calculated for every specific new experiment with different imaging parameters. Cortical pyramidal neurons were reconstructed with the Volume Integration and Alignment System (VIAS)

software (Rodriguez et al., 2003) and semi-automatic tracing of the apical dendrite and spines was performed with NeuronStudio software (Rodriguez et al., 2003, Wearne et al., 2005). To analyze spine density over prolonged time points, and to evaluate the effects of the CSF1R inhibitor, BTK-inhibitor, *lfng1* KO in c-MS, and PET scanned tissue, dendritic stretches were selected that were located at layers II-IV with a dendrite radius of 0.55 to 1.2 μm coming from pyramidal layer V neurons. These neurons in *GFP-Mx BiozziABH* animals were located 1000 to 2000 μm from the midline, contralateral to the injection site, unless stated as ipsilaterally and in a distance of maximum 600 μm caudal or frontally to the injection site. For PET experiments both ipsi- and contralateral sides were analyzed in the same range. For *lfng1*-KO dendrites on the ipsilateral side to both virus and cytokine injection were selected based on their infection by either NT or *lfng1* sgRNA noticed by their co-expression of eCFP or Kusabira Orange FP, respectively. Selected dendrites were 0.5 to 1.2 μm radius and were located at layers II-IV coming from pyramidal layer V neurons. All spine density graphs were presented as mean \pm SEM.

c. Myelin length analysis

Myelin length analysis was performed in ImageJ (Fiji) using the 'freehand line tracing tool' to mark and measure length of internodes (MBP) positioned within three squares defined with the 'grid' plugin (area per point 5000 μm^2 , 33% of the total area, tracing every 15 frames of stacks with around 120-130 frames).

d. Phagocyte activation and infiltration

Overview images were split into cortical layers based on the nucleic acid (NeuroTrace or DAPI) staining and were analyzed in regions of interest (ROI) that were 1000-2000 μm laterally to the midline. The cell counter plugin (ImageJ) was used to count the number of $\text{CX}_3\text{CR1}^{\text{GFP}}$ cells as well as their co-labelling with MHCII immunofluorescence signal. The same plugin was used to determine the number of Ccr2^{RFP} positive cells or *Iba1* positive $\text{CX}_3\text{CR1}^{\text{GFP}}$ negative cells. Cell number was reported as a percentage of cells or as number of cells per volume. To assess the effect of CSF1R inhibitor compound, three counting frames of 200 x 200 μm per section and six sections per animal were selected in layers III-IV, at 1000-2000 μm contralateral to the cytokine injection. Microglia nodules were quantified within the cortex area including the border to the corpus callosum of 1000-2000 μm ipsilateral to the cytokine injection. A nodule was defined as a group of more than 4 cells with a distance of not more than 15 μm from soma to soma in which cells were $\text{CX}_3\text{CR1}^{\text{GFP}}$ and MHCII positive. Number of nodules was quantified per volume, while nodule size was measured by obtaining the diameter of a circle that would surround the entirety of the nodule.

e. Dendritic and spine calcium levels

To analyze the Ca^{2+} levels in dendrites and spines using the Twitch2b sensor signal, both CFP and YFP channels were visualized individually in greyscale to determine ROIs. Fluorescence intensities of the spine head and of 5 regions of the dendritic shaft were measured in the CFP and in the YFP channels, respectively, with background correction performed with non-neurite areas nearby. Crosstalk from the CFP to the YFP channel was encountered, therefore the YFP signal was corrected by subtraction of the measured crosstalk-fraction of CFP signal. Background and crosstalk corrected YFP/CFP ratios were interpreted as representative of Ca^{2+} concentration based on the previously established FRET-based calcium sensor. Spines with a signal-to-noise ratio of <5.2 measured in the YFP channel were excluded from further analysis. Ca^{2+} high spines were defined as those with YFP/CFP ratios greater than mean plus 3 standard deviations of the ratios measured when imaging healthy control animals. If two different microscopes were used to measure a single

data set, data was normalized to the control mean measured on each microscope. Population analysis of dendritic and spine Ca^{2+} as well as analysis of CSF1R inhibitor treatment experiments were performed by an investigator blinded to treatment status. For dynamic analysis of spine fate, 10 dendrites were selected per region of analysis and all spines were identified in time points 0 hours, 2 hours and measured. Data was stratified and grouped using a custom R script as follows: calcium decrease if Ca^{2+} concentration at 2 hours was less than Ca^{2+} concentration at 0 hours; calcium increase if Ca^{2+} concentration at 2 hours was larger than 2 times the Ca^{2+} concentration at 0 hours; and spine loss if it was not detectable at 2 hours.

Ratiometric images presented were processed in ImageJ by creating intensity projections of 3D stack sections from the CFP and YFP channels individually. A binary thresholded mask of dendritic outlines was generated with the image channel that presented the higher signal-to-noise ratio after application of pixel outlier filters. The projection images were each then multiplied by the binary mask and divided in the YFP/CFP manner. Resulting images were pseudo-colored with a custom look-up table spanning from low calcium in blue, via red, to high calcium in yellow hues. Images were exported as RGB images to Photoshop and greyscale images were despeckled. Dendritic and spine calcium level analysis was performed together with Adrian-Minh Schumacher.

f. Analysis of synapse engulfment

A minimum of 10 individual $\text{CX}_3\text{CR1}^{\text{GFP}}$ or Ccr2^{RFP} positive cells per animal were reconstructed by Imaris software (Oxford Instruments) automatically in a stack of $5.14\ \mu\text{m}$. A mask was then created with the rendered surface on the Synapsin-1, PSD95, Homer-1 channels and the spots function was used to identify spheres representing positive signals. Average intensity of five ROIs in non-positive background were used to define the threshold in each channel needed for visual confirmation of spheres. Spheres that were not visually confirmed or fully engulfed by the cell were manually removed. The LAMP1 channel was used for assessment of sphere colocalization. Furthermore, the LAMP1 channel was masked by the cell surface and volume was reconstructed within the cell to determine LAMP1 volume per cell. In the $\text{CX}_3\text{CR1}^{\text{GFP}}$ cells Δ in quantification refers to the subtraction of average volume of healthy controls from CSF1R or vehicle treated c-MS mice.

g. PET/CT image analysis

All small animal PET imaging analyses were performed by Laura Bartos by PMOD (V3.5, PMOD Technologies, Basel, Switzerland) using CT for spatial normalization (Brendel et al., 2016). A 40-60 min frame was analyzed, and normalization of activity was performed by standardized uptake values (SUV). Non-linear PET coregistration of SUV normalized images of the brain was performed via the CT to a brain CT template, with spatial normalization parameters equal to previously described PET template coregistration (Overhoff et al., 2016). The PET lesion volume of interest in c-MS mice was defined on a T1 MRI template (aligned to the CT template space) as described below. An ellipsoid sphere ($10\ \text{mm}^3$) was placed in the neocortex of the lesion site as a target volume-of-interest (VOI) and served for assessment of SV2A PET tracer uptake. Additionally, the VOI was mirrored to the contralateral hemisphere to obtain SV2A expression in non-affected tissue, which later also served to test for suitability of simplified normalization (lesion site to contralateral hemisphere ratio). The subtraction of group average PET images of sham and c-MS mice served for voxel-wise visualization of SV2A tracer signal reduction throughout the whole brain of c-MS mice.

Chapter IV: Results

IV.1 A mouse model of grey matter inflammation

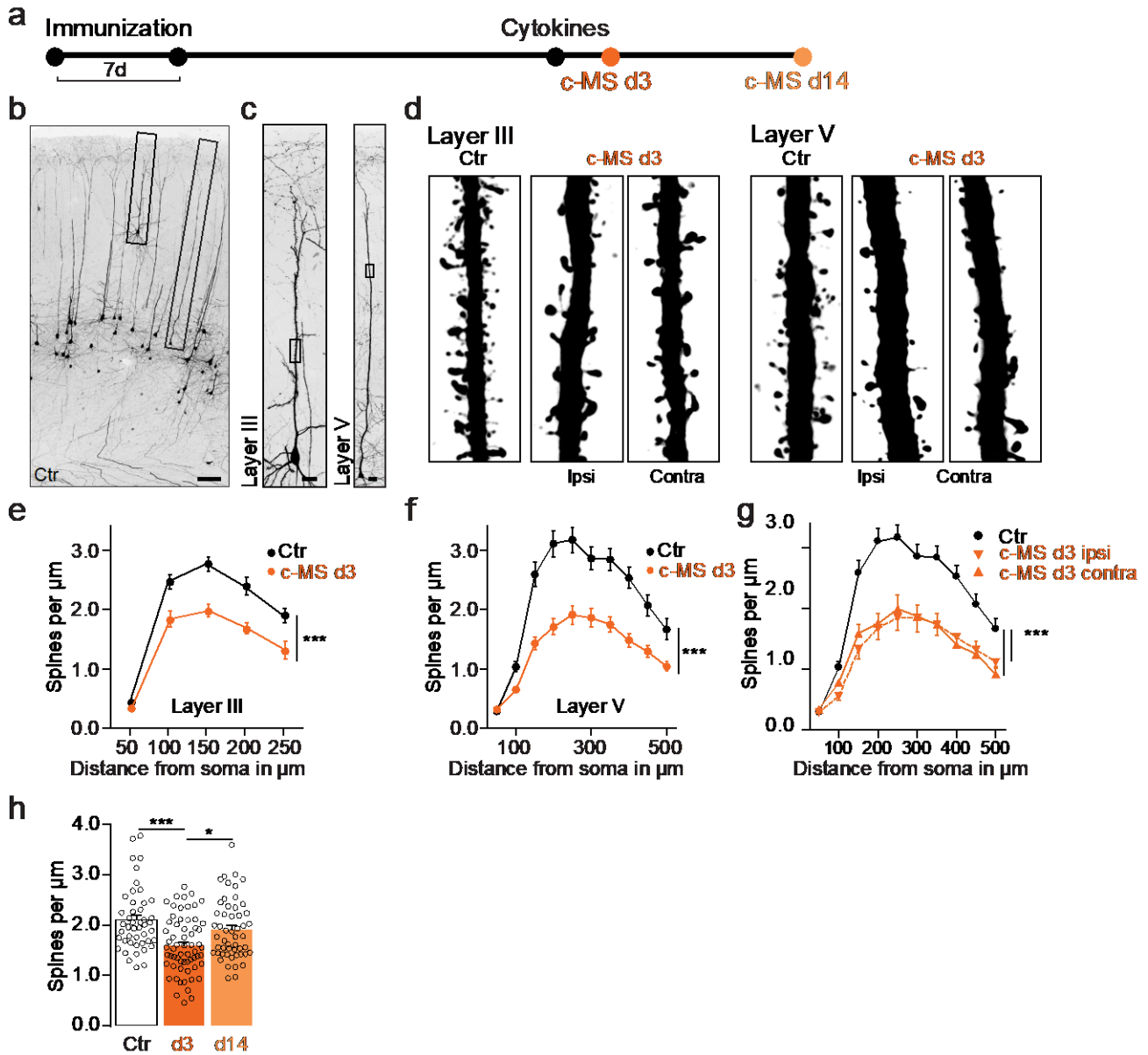


Figure 5: Projection neurons lose synaptic input in a cortical model of Multiple Sclerosis.

a) Schematic of experimental design to measure spine density in our c-MS model at c-MS day 3 (perfusion 3 days following cytokine injection) and c-MS day 14 (perfusion 14 days following cytokine injection). **b**) Overview of cortex projection neuron labelling in a *Thy1-GFP-M x BiozziABH* mouse. **c**) Reconstruction of boxes in (b) of a confocal image of a layer III (left) and layer V (right) pyramidal neuron. **d**) Apical dendrite segments of locations typically found in boxes in (c) following deconvolution in control and c-MS mice layer III (left) and layer V (right) neurons. **e**, **f**) Spine density in apical dendrites as function of distance from soma of **e**) layer III neurons ($n=13$ Ctr and $n=15$ c-MS d3 neurons from $n=6$ mice per group; mean \pm SEM; two-way RM ANOVA) and **f**) layer V neurons ($n=21$ Ctr and $n=28$ c-MS d3 neurons from $n=7$ and $n=8$ mice respectively; mean \pm SEM; two-way RM ANOVA). **g**) Spine density in apical dendrites as function of distance from soma in ipsi- and contra-lateral sides to cytokine injection site in layer V neurons at c-MS d3 ($n=21$ Ctr, $n=17$ ipsilateral, $n=11$ contralateral neurons from $n=7$ Ctr mice and $n=8$ c-MS d3 mice; mean \pm

SEM; two-way RM ANOVA followed by Bonferroni's multiple comparisons test. h) Spine density of layer V contralateral dendrites over c-MS course (n=46 Ctr, n=62 c-MS d3 and n=52 c-MS d14 dendritic stretches from n=7 Ctr, n=8 c-MS d3 and n=9 c-MS d14 mice; mean \pm SEM; one-way ANOVA followed by Bonferroni's multiple comparisons test). Scale bars in b: 100 μ m; c: 20 μ m; d: 1 μ m. Display range is adjusted for images in panels b-d uniformly in each panel. Deconvoluted images are used in panel d. Abbreviations: Ctr: control; c-MS: cortical MS model; d3: perfused at day 3; d14: perfused at day 14; Ipsi: ipsilateral to cytokine injection; Contra: Contralateral to cytokine injection. *** $p < 0.001$, ** $p < 0.01$, * $p < 0.05$. Figure modified from Figure 1 and Supplementary Figure 2 of Jafari et al., *Nature Neuroscience* 2021 paper.

As previously described, grey matter pathology of MS is crucial for disease progression. The most commonly used mouse models to mimic MS pathology, such as the EAE model, focus on the white matter pathology of the disease (introduction I.1.5), leaving a lack of grey matter pathology studies. During the first part of my thesis, we characterized a mouse model adapted in our lab by Dr. Mehrnoosh Jafari from a rat model for cortical grey matter inflammation that was established by Tanja Jürgens (Merkler et al., 2006). The cortical pathology in this model was induced by using MOG immunized mice on a *BiozziABH/ C57BL6J* background and injecting the pro-inflammatory cytokines TNF α and IFN γ into the somatosensory cortex (Figure 5a). This cytokine injection resulted in cortical lesions which were subsequently characterized in terms of synaptic pathology (Figure 5), demyelination, and inflammation (Figure 6). This part was performed in collaboration with Dr. Mehrnoosh Jafari, Dr. Adrian-Minh Schumacher, Dr. Aleksandra Mezydło, Tradite Neziraj and Virag Kocsis-Jutka. Dr. Jafari, Dr. Schumacher, Dr. Mezydło, Tradite Neziraj and I generated the c-MS model as well as collected and analyzed data. Dr. Jafari analyzed synaptic pathology, inflammation, as well as part of the synaptic punctae phagocytosis. Dr. Schumacher analyzed data for inflammation and calcium imaging. Dr. Mezydło generated the c-MS model, collected, and analyzed data for the demyelination. Tradite Neziraj collected and analyzed data related to the inflammation in c-MS. Virag Kocsis-Jutka performed analysis for the calcium imaging in dendrites. I analyzed data for the calcium imaging, synaptic punctae phagocytosis. The results from this section are published in Jafari, Schumacher, Snaidero, **Ullrich Gavilanes**, [...], Merkle, Misgeld & Kerschensteiner, *Nature Neuroscience*, 2021 and the demyelination analysis is published in Mezydło, Treiber, **Ullrich Gavilanes**, [...], Misgeld & Kerschensteiner. *Neuron*. 2023.

Synaptic loss is a pathogenic process that has been observed in the cortex of MS patients (Jurgens et al., 2016, Vercellino et al., 2022, Wegner et al., 2006). As such, Dr. Jafari investigated whether our cortical MS (c-MS) model would reproduce this widespread phenotype observed in progressive MS. For this purpose, she reconstructed the dendrites of sparsely labelled cortical projection neurons from layer III and layer V of *Thy1-GFP-M x BiozziABH* mice (Figure 5b-d). Dr. Jafari observed that there was a significant reduction in spine density in both layer III (Figure 5e) and layer V (Figure 5f) neurons, irrespectively of distance from the soma, at day 3 post cytokine injection (d3), which marks the peak of acute pathology in our c-MS model. This spine loss was observed both ipsilaterally and contralaterally to cytokine injection (Figure 5g). When investigating longer time points, however, we observed that the spine pathology recovered, and spine density reverted back to healthy control levels spontaneously by day 14 post cytokine injection (d14) (Figure 5h). Overall, we could observe synaptic pathology in our mouse model, resembling widespread synaptic loss in progressive MS both in the lesion site (ipsilateral) and in NAGM (contralateral

to injection site) (Jurgens et al., 2016). This in turn shows the value of our mouse model to further study neuronal pathology in grey matter neuroinflammatory conditions.

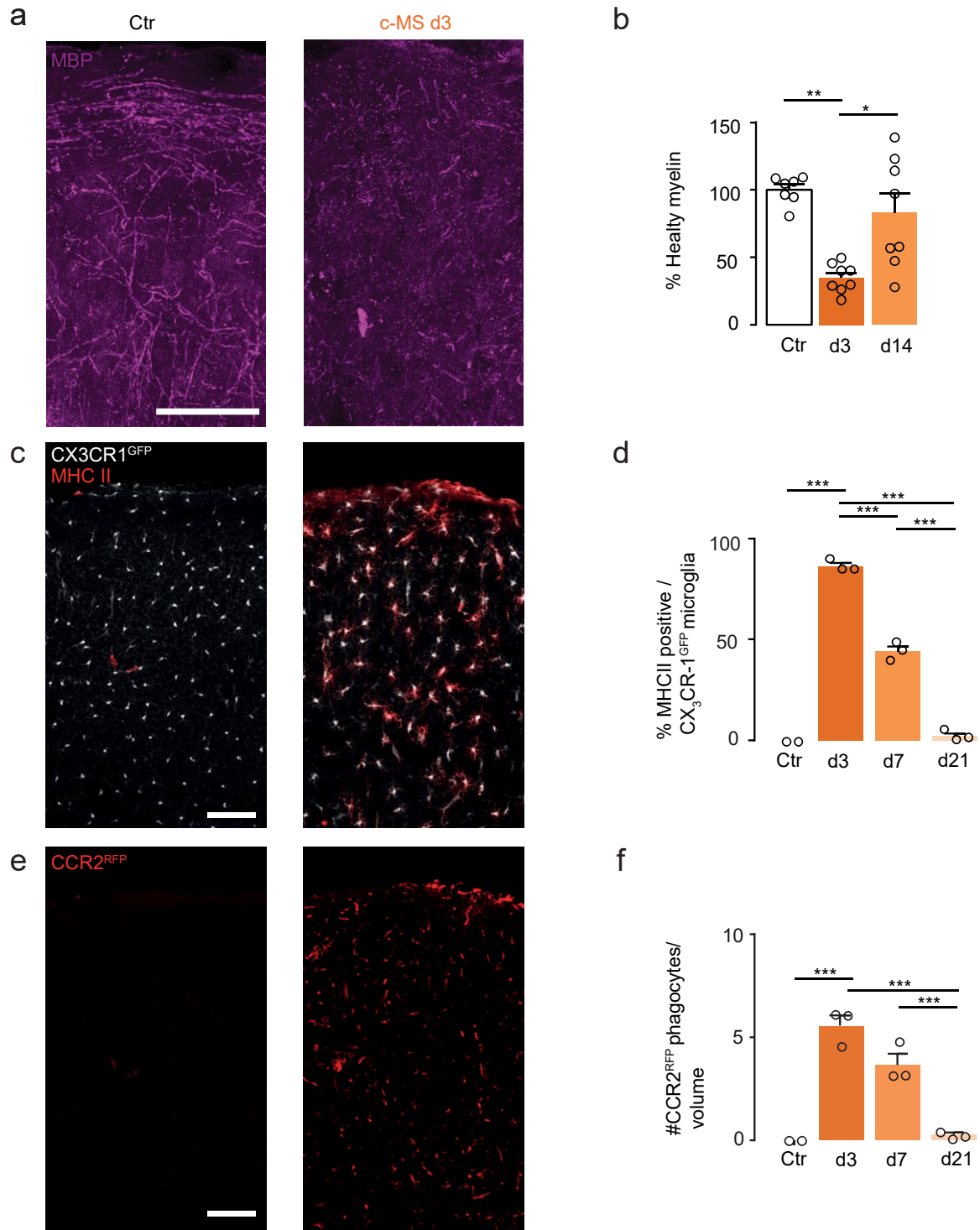


Figure 6: Histopathological characterization in a mouse model of cortical Multiple Sclerosis. **a)** Confocal representative images of internodes (MBP, magenta) in the somatosensory cortex of c-MS mice following cytokine injection. Left: healthy control; right: c-MS d3. **b)** Internode density of cortex lesion sites along c-MS course (n=7 Ctr, n=8 c-MS d3, n=8 c-MS d14 mice; mean \pm SEM; Kruskal-Wallis test followed by Dunn's multiple comparisons test). **c)** Confocal representative images of microglial cells (CX3CR1^{GFP}, grey) activation based on MHCII (red) expression. Left: healthy control; right: c-MS d3. **d)** Percentages of activated microglia (% MHCII positive/ all CX₃CR-1^{GFP} cells) along c-MS course (n=2 Ctr, n=3 c-MS d3, n=3 c-MS d7, n=3 c-MS d21 mice; mean \pm SEM; one-way ANOVA followed by Bonferroni's multiple comparisons test). **e)** Confocal representative images of infiltrating Ccr2^{RFP} (red) phagocytes. Left: healthy control; right: c-MS d3. **f)** Number of infiltrating Ccr2^{RFP} positive phagocytes along c-MS course (n=2 Ctr, n=3 c-MS d3, n=3 c-MS d7, n=3 c-MS d21 mice; mean \pm SEM; one-way ANOVA followed by Bonferroni's multiple comparisons test). Scale bars in a, c and e: 100 μ m. Abbreviations: Ctr: control; c-MS: cortical MS model; dX: perfused at day X. ***p<0.001, ** p<0.01, *p<0.05. Figure modified from Figure 1 Mezydlo et al., Neuron, 2023 and Supplementary Figure 7 of Jafari et al., Nature Neuroscience 2021 papers.

In following steps to characterize our mouse model and to investigate the extent to which it mimics MS pathology, Dr. Mezydlo, Dr. Schumacher and Tradite Neziraj assessed demyelination and inflammation, both pathological hallmarks thoroughly described in MS (Carswell, 1838, Filippi et al., 2018, Kamm et al., 2014, Lucchinetti et al., 2011, Ontaneda et al., 2017, Pearce, 2005). They studied these phenotypes by staining *C57BL6J x BiozziABH* mice with MBP for demyelination, while for microglia inflammation *CX₃CR-1^{GFP} x BiozziABH* mice with GFP labelled microglia stained for MHCII marker were used. Finally, for phagocyte infiltration, cells in *CCR2^{RFP} x BiozziABH* mice which are RFP labelled infiltrating macrophages were quantified. At c-MS day 3, subpial lesions forming in the cortex could be observed with wide demyelination (Figure 6a-b). Moreover, just like with the synaptic pathology, the myelin levels recovered and by c-MS day 14 went back to almost control levels (Figure 6b). Further investigation into the c-MS mouse model showed that cortical lesions elicited by cytokine injection had MS characteristic microglia activation (Figure 6c-d) and peripheral phagocyte infiltration (Figure 6e-f). Just like with demyelination and spine pathology, however, the microglia activation and phagocyte infiltration spontaneously resolved and 21 days after cytokine injection, these inflammatory hallmarks could almost no longer be observed (Figure 6d, f). These results, once again show the value of our mouse model in mimicking different characteristics of grey matter MS pathology, while also revealing spontaneous resolution of inflammation in our model.

Based on our findings of synaptic pathology and inflammation, Dr. Schumacher and I, with the help of Virag Kocsis-Jutka, wanted to further explore the mechanisms that may play a role in the observed neuroinflammatory pathology. In a first step, we explored whether synaptic loss specifically targets a subset of spines without affecting the dendrite and neighbouring spines. In order to do this, we focused on the study of calcium changes in dendrites and spines. Dysregulation of calcium homeostasis has been previously described to play a role in synapse loss in other neuroinflammatory diseases (Liu et al., 2014, Wu et al., 2010). Thus, we used labelling of a subset of cortical neurons through rAAV-mediated expression of the ratiometric calcium sensor Twitch-2b (Thestrup et al., 2014) as a method

to study calcium changes in our c-MS model combined with *in vivo* two photon imaging. We

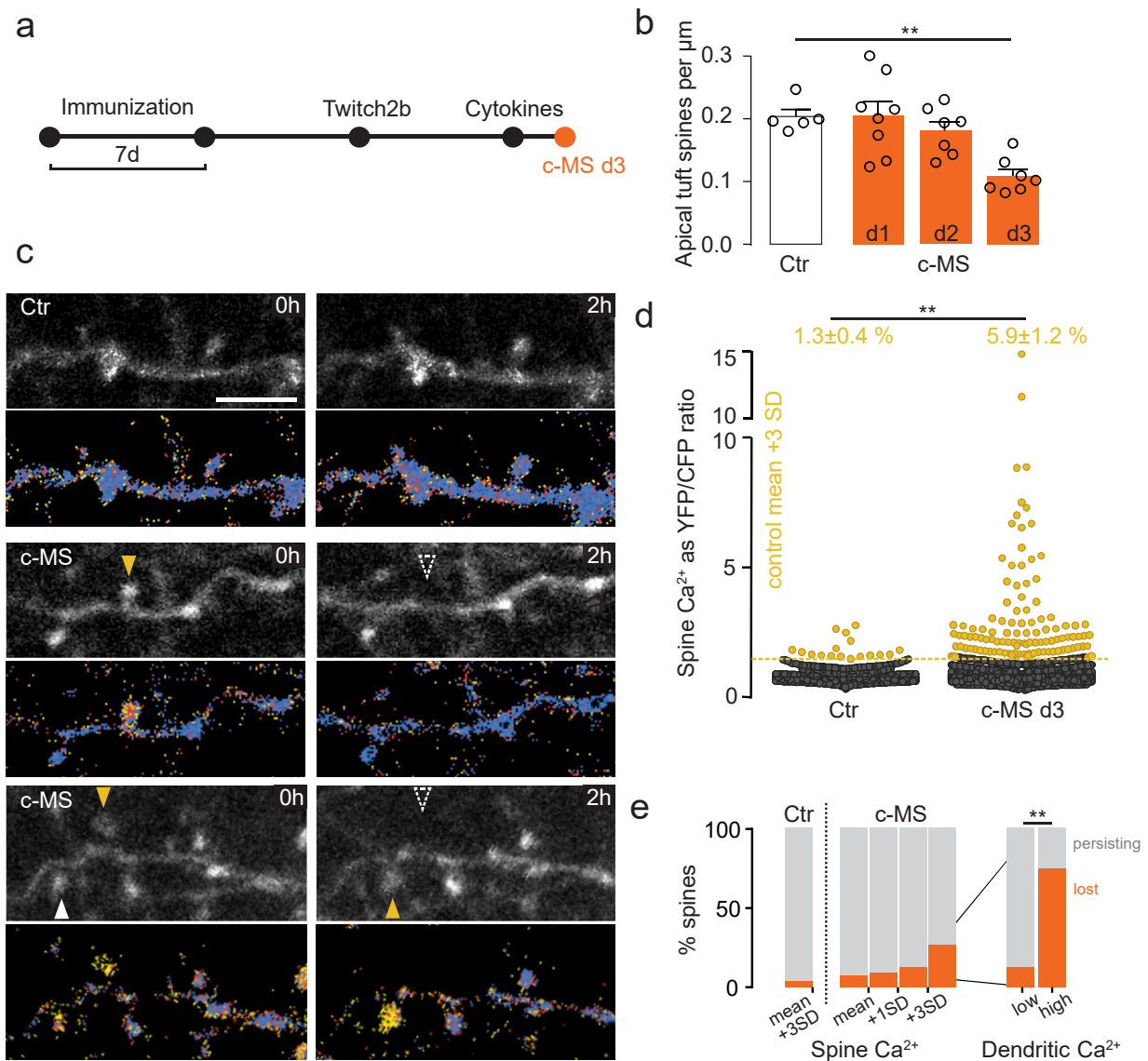


Figure 7: Localized spine calcium accumulations primes spines for removal. **a)** Schematic of experimental design for *in vivo* imaging of Ca^{2+} levels in the c-MS model with the use of a genetically encoded FRET-based calcium indicator Twitch2b delivered via local viral gene transfer in an AAV. **b)** Spine density in apical tuft dendrites of *Thy1-GFP-M x BiozziABH* mice quantified *in situ* along c-MS course (n=5 Ctr, n=8 c-MS d1, n=7 c-MS d2, n=7 c-MS d3 mice; mean \pm SEM; one-way ANOVA followed by Bonferroni's multiple comparisons test). **c)** Multiphoton time-lapse images in healthy control (top) and c-MS mice (d2, middle; d3, bottom) represented as greyscale images of the YFP channel and as ratiometric (YFP/CFP) images color coded and masked for cytoplasmic Ca^{2+} levels. Yellow arrowhead depicts high Ca^{2+} spine White arrowhead depicts low Ca^{2+} spines with Ca^{2+} changes over 2 hours. Dashed arrowhead depicts a spine that has

disappeared following high Ca^{2+} accumulation. Gamma was 1.2 for greyscale images. **d)** Ca^{2+} concentrations plotted as YFP/CFP ratios of single spines in Ctr and cMS- d3 mice. Dashed line represents threshold of 3x SD above control mean for high Ca^{2+} . Top values are the percentage of spines per animal with high Ca^{2+} showed as mean \pm SEM. (n= 8 Ctr, n=17 c-MS d3 mice; Mann-Whitney U test). **e)** Spine fate over a 2-hour imaging time course according to baseline Ca^{2+} concentration at t=0h (shown as mean + X times SD of healthy controls) in Ctrl mice (left) and c-MS mice (middle). The percentage of high Ca^{2+} spines (3x SD above control mean) lost within 2 hours was further divided based on their individual peri-spine dendritic Ca^{2+} concentrations (low vs high defined as 3xSDabove mean calcium levels in control dendrites) (right). (n=24 spines with low dendrite calcium, n= 8 spines with high dendrite calcium; Fisher's exact test). Abbreviations: Ctr: control; c-MS: cortical MS model; dX: perfused at day X.; SD: standard deviation. Scale bars in c: 5 μm . ** p<0.01. Figure modified from Figure 4 of Jafari et al., Nature Neuroscience 2021 paper.

could record calcium levels in spines of the apical dendritic tufts of cortical neurons, after cytokine injection, at different time points up to c-MS day 3 (Figure 7a). At this time, the lowest spine density was observed at the apical tuft (Figure 7b). Around 5% of spines showed a localized increased calcium accumulation, measured as calcium levels above the mean +3 standard deviations of control spine calcium levels in c-MS mice at peak of inflammation compared to control mice (Figure 7d). Subsequently, we used our ratiometric calcium imaging system to track the fate of high calcium spines over time (Figure 7c). We could observe that in c-MS mice some high calcium spines would be lost over time, while some lower calcium spines would become high calcium spines (Figure 7c). Furthermore, Dr. Schumacher determined that the probability of spines to be lost would increase with higher calcium concentrations within them and was at its highest when higher calcium spines were located in a dendrite which itself also had calcium accumulation (Figure 7e). The loss of high calcium spines together with the observation of lower calcium spines becoming calcium high suggests a dynamic process of calcium accumulation in spines which leads to their removal and synaptic loss.

To further understand the process by which the synaptic loss observed occurs, Dr. Jafari and I assessed whether phagocytic cells are responsible for synaptic removal at the acute stage of our model. We analyzed the role microglia and infiltrating phagocytes play in synapse uptake by quantifying the number of phagocytosed synaptic punctae within microglia or infiltrating cells through 3D reconstruction of cortex tissue from mice genetically labelled for microglia (*CX₃CR-1^{GFP} x BiozziABH* mice) or infiltrating macrophages (*CCR2^{RFP} x Biozzi ABH* mice) (Figure 8). Pre-synaptic engulfment was evaluated by looking at phagocytosed Synapsin-1 puncta in combination with lysosomal marker LAMP1 to determine whether these puncta were co-localized within lysosomal compartments (Figure 8a, b). The synaptic uptake was further confirmed using 3D rendering of the phagocyte cells (Figure 8d). Both microglia and infiltrating phagocytes showed an increased engulfment of pre-synaptic punctae within and outside of the lysosomal compartment at c-MS day 3 compared to controls (Figure 8c, e). In the same manner, increased post-synaptic punctae, labelled through PSD95 and Homer1 in combination with LAMP1, could be observed both within and outside the lysosomal compartment in microglia (Figure 8f) and infiltrating phagocytes (Figure 8g) at the peak of acute inflammation compared to controls. Interestingly, infiltrating phagocyte cells displayed similar amounts of uptake of pre- and post-synaptic markers as microglia,

indicating a possible collaborative effect between infiltrating immune cells and microglia in synaptic uptake during inflammation of the grey matter.

All of these results suggest that our c-MS mouse model is an appropriate tool to study grey matter pathology of the CNS in neuroinflammatory conditions. Moreover, subsequent studies into mechanisms and processes taking place during neuroinflammation can be carried out in this model to help further understanding of the processes leading to synapse loss, the calcium changes taking place within dendritic spines, and the cues that lead to synaptic engulfment by phagocytes.

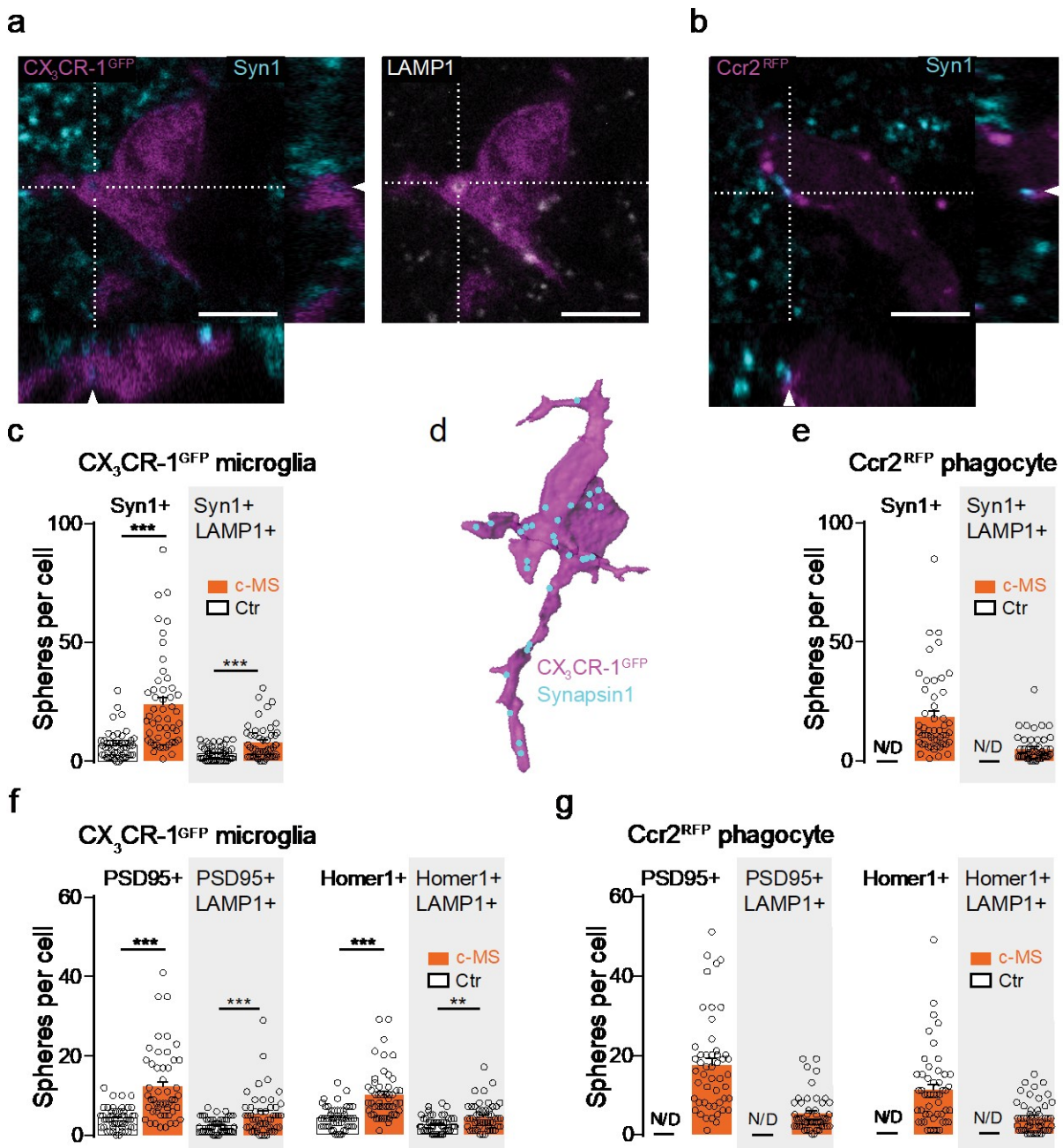


Figure 8: Microglia and infiltrating phagocytes engulf synapses in a cortical MS model. **a)** Orthogonal view of a CX3CR1^{GFP} cell (magenta) showing a Synapsin-1 (cyan) inclusion (left), which colocalizes with LAMP1 staining (white, right). **b)** Orthogonal view of a Ccr2^{RFP} cell (magenta) showing a Synapsin-1 (cyan) inclusion. **c)** Quantification of Synapsin-1 positive spheres and Synapsin-1/LAMP1 double positive spheres, reconstructed, within CX3CR1^{GFP} cells in the c-MS model and healthy controls (n=50 Ctr, n= 50 c-MS d3 cells from n=4 Ctr and n=5 c-MS d3 mice; mean ± SEM; unpaired t-test). **d)** 3D Imaris software reconstruction of a CX3CR1^{GFP} cell (magenta) and its Synapsin-1 (cyan) inclusions. **e)** Quantification of Synapsin-1 positive spheres and Synapsin-1/LAMP1 double positive spheres, reconstructed, within Ccr2^{RFP} cells in the c-MS model (n=50 c-MS d3 cells from n=5 mice; mean ± SEM). **f)** Quantification of postsynaptic marker positive spheres and their co-localization with LAMP1 within CX3CR1^{GFP} cells in the c-MS model and healthy controls. Left: PSD95 sphere quantification; right: Homer1 sphere quantification (n=50 Ctr and n=50 c-MS cells from n=5 Ctr and n=5 c-MS d3 vehicle treated animals; mean ± SEM; unpaired t-test). **g)** Quantification of postsynaptic marker positive spheres and their co-localization with LAMP1 within Ccr2^{RFP} cells in the c-MS model (n=50 c-MS cells from n=4 c-MS d3 vehicle treated animals; mean ± SEM). Scale bars in a, b: 5 µm. Abbreviations: Ctr: control; c-MS: cortical MS model; d3: perfused at day 3; Syn1: Synapsin-1; ND: No data. ***p<0.001, ** p<0.01. Figure modified from Figure 5 of Jafari et al., Nature Neuroscience 2021 paper.

IV.2 A mouse model of chronic grey matter inflammation

As introduced above, ageing is one of the biggest risk factors for neurodegeneration (Ganz et al., 2018, Hou et al., 2019, Wyss-Coray, 2016). Furthermore, age of MS onset plays a role in MS progression, where individuals with middle-age MS onset are more likely to reach progressive MS phases (Scalfari et al., 2011, Zeydan and Kantarci, 2020). As such we wanted to test the effect ageing would have in our c-MS mouse model and whether age would have an effect on the resolution of inflammation. For this purpose, we used middle-aged mice (10-12 months) of the *BiozziABH/ C57BL6J* background and induced our c-MS model (Figure 9a). We then investigated the same time points that we investigated for c-MS younger mice (Figure 5a), but also longer time points up to c-MS day 84 (Figure 9a). We subsequently characterized this middle-aged model in terms of spine pathology (Figure 9b, c), demyelination (Figure 9d, e), and inflammation (Figure 9f-h, Figure 10). This part of my thesis was performed in collaboration with Dr. Aleksandra Mezydło, Nils Treiber, and Virag Kocsis-Jutka. Dr. Mezydło and I designed the experiments. Dr. Mezydło, Nils Treiber, Virag Kocsis-Jutka, and I generated the c-MS mice for all the different time points. Virag Kocsis-Jutka collected data related to spine pathology. Dr. Mezydło and Nils Treiber analyzed data related to demyelination and inflammation. I analyzed data related to spine pathology and inflammation.

In terms of spine loss, Virag Kocsis-Jutka and I once again reconstructed the dendrites of sparsely labelled cortical projection neurons from layer V of *Thy1-GFP-M x BiozziABH* mice (Figure 9b). We observed that there was a significant loss of spines in layer V neurons (Figure 9c), at c-MS day 3, which was maintained up until c-MS day 84, point at which no recovery could be noted (Figure 9d) when compared to younger animals (Figure 5h).

To study demyelination, Dr. Mezydło and Nils Treiber stained *C57BL6J x BiozziABH* mice with MBP and quantified length of myelin sheaths (Figure 9d). Myelin length was largely reduced at c-MS day 3 and this myelin length reduction persisted past c-MS day 14. At

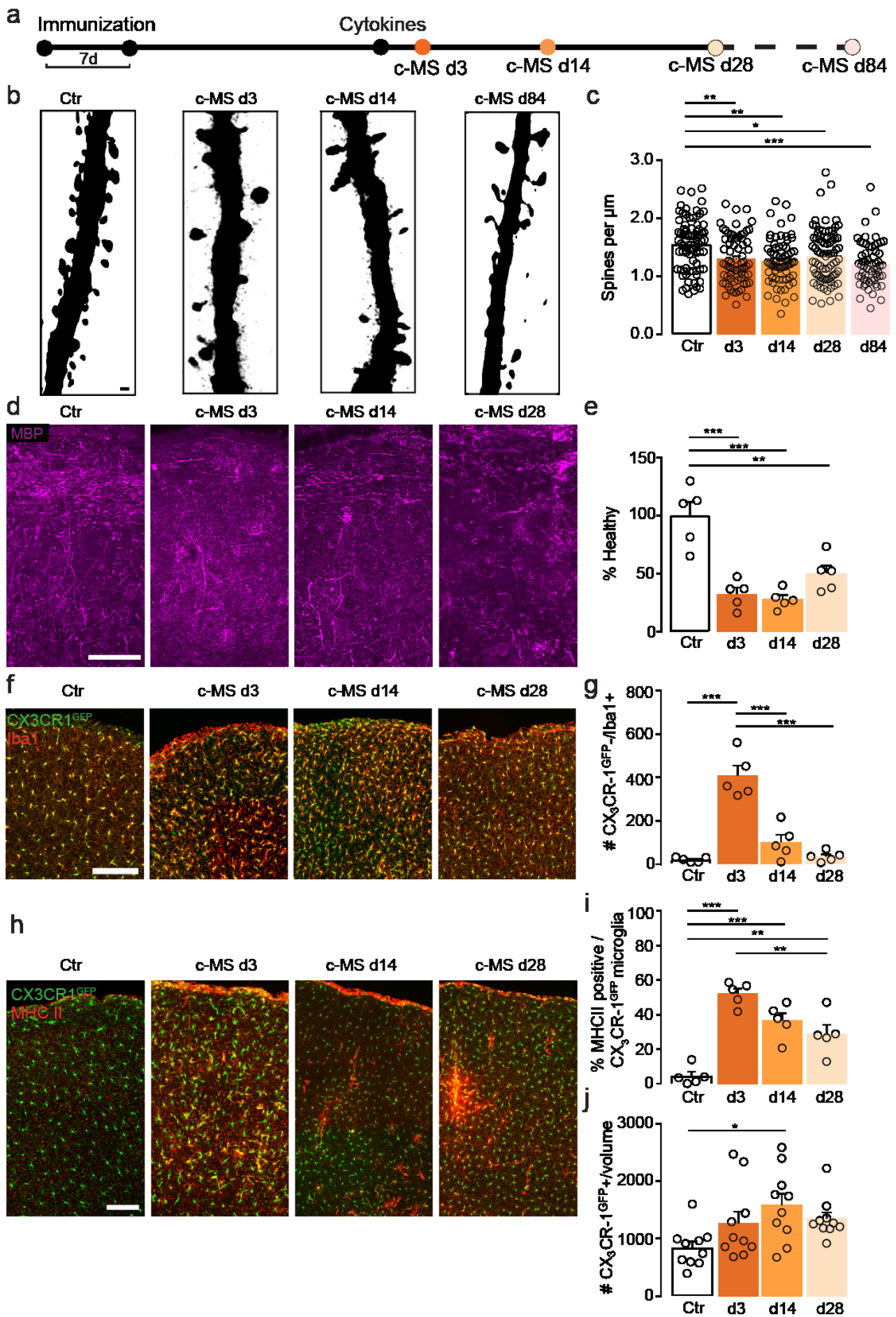


Figure 9: Histopathological characterization in a middle-aged mouse model of cortical Multiple Sclerosis. **a)** Schematic of experimental design to measure spine density, myelin internode density, and inflammation in our c-MS model at c-MS day 3 (perfusion 3 days following cytokine injection), c-MS day 14 (perfusion 14 days following cytokine injection), c-MS day 28 (perfusion 28 days following cytokine injection) and c-MS day 84 (perfusion 84 days following cytokine injection). **b)** Apical dendrite segments following deconvolution in control and c-MS mice layer V neurons. From left to right: Ctrl, c-MS d3, c-MS d14 and c-MS d84. **c)** Spine density of layer V contralateral dendrites over c-MS course (n=80 Ctrl, n=70 c-MS d3 and n=70 c-MS d14, n=80 c-MS d28 and n=60 c-MS d84 dendritic stretches from n=8 Ctrl, n=7 c-MS d3, n=7 c-MS d14, n=8 c-MS d28 and n=6 c-MS d84 mice; mean \pm SEM; Kruskal-Wallis test followed by Dunn's multiple comparisons test). **d)** Confocal representative images of internodes (MBP, magenta) in the somatosensory cortex of c-MS mice following cytokine injection. From left to right: Ctrl, c-MS d3, c-MS d14 and c-MS d28. **e)** Internode density of cortex lesion sites along c-MS course (n=5 Ctrl, n=5 c-MS d3, n=5 c-MS d14, and n=5 c-MS d28 mice; mean \pm SEM; one-way ANOVA followed by Tukey's multiple comparisons test). **f)** Confocal representative images of infiltrating phagocytes based on Iba1 (red) expression in CX3CR1^{GFP} (green) negative cells. From left to right: Ctrl, c-MS d3, c-MS d14 and c-MS d28. **g)** Number of infiltrating positive phagocytes based on Iba1 expression in CX3CR1^{GFP} negative cells along c-MS course (n=5 Ctrl, n=5 c-MS d3, n=5 c-MS d14, n=5 c-MS d28 mice; mean \pm SEM; one-way ANOVA followed by Tukey's multiple comparisons test) **h)** Confocal representative images of microglial cells (CX3CR1^{GFP}, green) activation based on MHCII (red) expression. From left to right: Ctrl, c-MS d3, c-MS d14 and c-MS d28. **i)** Percentages of activated microglia (% MHCII positive/ all CX₃CR-1^{GFP} cells) along c-MS course (n=5 Ctrl, n=5 c-MS d3, n=5 c-MS d14, n=5 c-MS d28 mice; mean \pm SEM; one-way ANOVA followed by Tukey's multiple comparisons test). **j)** Number of infiltrating CX₃CR-1^{GFP} cells per volume along c-MS course (n=10 Ctrl, n=10 c-MS d3, n=10 c-MS d14, n=10 c-MS d28 volumes from n=5 Ctrl, n=5 c-MS d3, n=5 c-MS d14, n=5 c-MS d28 mice; mean \pm SEM; one-way ANOVA followed by Tukey's multiple comparisons test). Deconvoluted images are used in panel b. Scale bars in b: 1 μ m, c, f, h: 100 μ m. Abbreviations: Ctrl: control; c-MS: cortical MS model; dX: perfused at day X. ***p<0.001, ** p<0.01, *p<0.05. Figure created by Emily Melisa Ullrich Gavilanes, includes data of Dr. Aleksandra Mezydło, Nils Treiber, Virag Kocsis-Jutka.

c-MS day 28 a small recovery could be observed, however the level of myelin length was still significantly lower (50.3% of healthy myelin length) than in the healthy control mice (Figure 9e).

Furthermore, together with Dr. Mezydło and Nils Treiber, we investigated the inflammatory phenotypes by quantifying the density of infiltrating myeloid cells and local microglia. We analyzed the number of infiltrating phagocytes by using CX₃CR-1^{GFP} x BiozziABH and staining them with Iba1. Infiltrating cells would be those that were Iba1 positive but CX₃CR-1^{GFP} negative (Figure 9f). The number of Iba1 positive, GFP-negative cells was largely increased at c-MS day 3, decreased at c-MS day 14 and reached almost control levels by c-MS day 28 (Figure 9g). To study microglia numbers, we used CX₃CR-1^{GFP} x BiozziABH mice and quantified microglia, while to study microglia activation we stained these mice with MHCII and colocalized it with microglia cells (Figure 9h). We could observe that microglia activation is at its highest at c-MS day 3 and that it slowly decreases over time. However, unlike in the younger mice, microglia have a sustained activation until c-MS day 28 and do not return to control levels (Figure 9i). Microglia number although increased at c-MS day 3 compared to

control, reaches its peak at c-MS day 14 and then decreases slowly again until c-MS day 28 but does not reach healthy control levels again (Figure 9j).

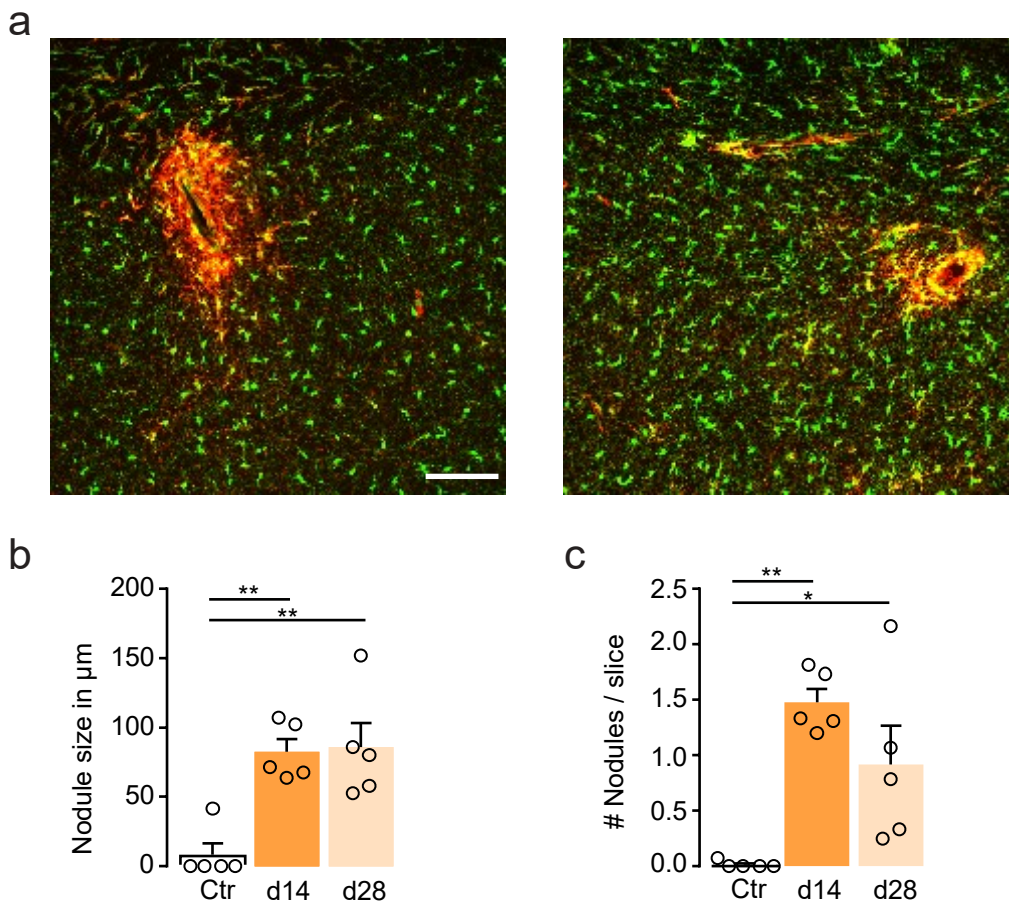


Figure 10: Microglia nodules are observed in a middle-aged mouse model of cortical Multiple Sclerosis. **a)** Confocal representative images of microglia nodules containing activated microglia. Microglia determined based on CX3CR1^{GFP} expression (green) activation based on MHCII (red) expression. **b)** Quantification of microglial nodule size based on criteria of a minimum of 4 MHCII/ CX3CR1^{GFP} double positive cells with soma no further than 15 µm from one another (n=5 Ctr, n=5 c-MS d14, n=5 c-MS d28 mice; mean ± SEM; one-way ANOVA followed by Tukey’s multiple comparisons test). **c)** Number of microglial nodules based on criteria of a minimum of 4 MHCII/ CX3CR1^{GFP} double positive cells with soma no further than 15 µm from one another (n=5 Ctr, n=5 c-MS d14, n=5 c-MS d28 mice; mean ± SEM; one-way ANOVA followed by Tukey’s multiple comparisons test). Scale bars in a: 100 µm. Abbreviations: Ctr: control; c-MS: cortical MS model; dX: perfused at day X. ** p<0.01, *p<0.05. Figure created by Emily Melissa Ullrich Gavilanes, includes data of Nils Treiber.

While analyzing the microglia activation, with CX₃CR-1^{GFP} x BiozziABH mice stained for MHCII, we also observed the formation of microglia nodules (Figure 10). Microglia nodules have been previously described as part of MS pathology in the normal appearing white matter. Moreover, they have been defined as clusters of activated microglia identified in the absence of leukocyte infiltration, astrogliosis or demyelination. These nodules may be representations of early MS lesion formation (Sato et al., 2015, Singh et al., 2013, van der Valk and Amor, 2009). The microglia nodules observed in our c-MS model were located

within or at the border of the cortex surrounding the lesion site and could vary in size and number (Figure 10a). A microglia nodule was defined as a cluster of at least 4 MHCII positive *CX3CR-1^{GFP}* positive cells with no more than 15 μm distance between cells. These nodules were first encountered at c-MS day 14, and their average size was maintained in c-MS day 28 (Figure 10b). The number of nodules found was the highest at c-MS day 14 and decreased for c-MS day 28 samples, nevertheless, it did not reach healthy control levels (Figure 10c).

All in all, age was observed to play a role in the neuroinflammatory grey matter response in our mouse model of cortical EAE. In terms of synaptic pathology, demyelination and inflammation, c-MS induction in middle-aged animals resulted in sustained reduction of spine density, decreased myelin length and increased activation and number of immune cells. This suggests that age plays a role in prolonging inflammatory resolution and can lead to the induction of chronic inflammation. This model of middle-aged mice would thereby be valuable when evaluating chronic pathology of MS or in testing therapies aimed for patients with more prolonged and chronic disease courses.

IV.3 Understanding neuronal pathology in MS: transcriptomics changes in the cMS model mapped together with MS patients

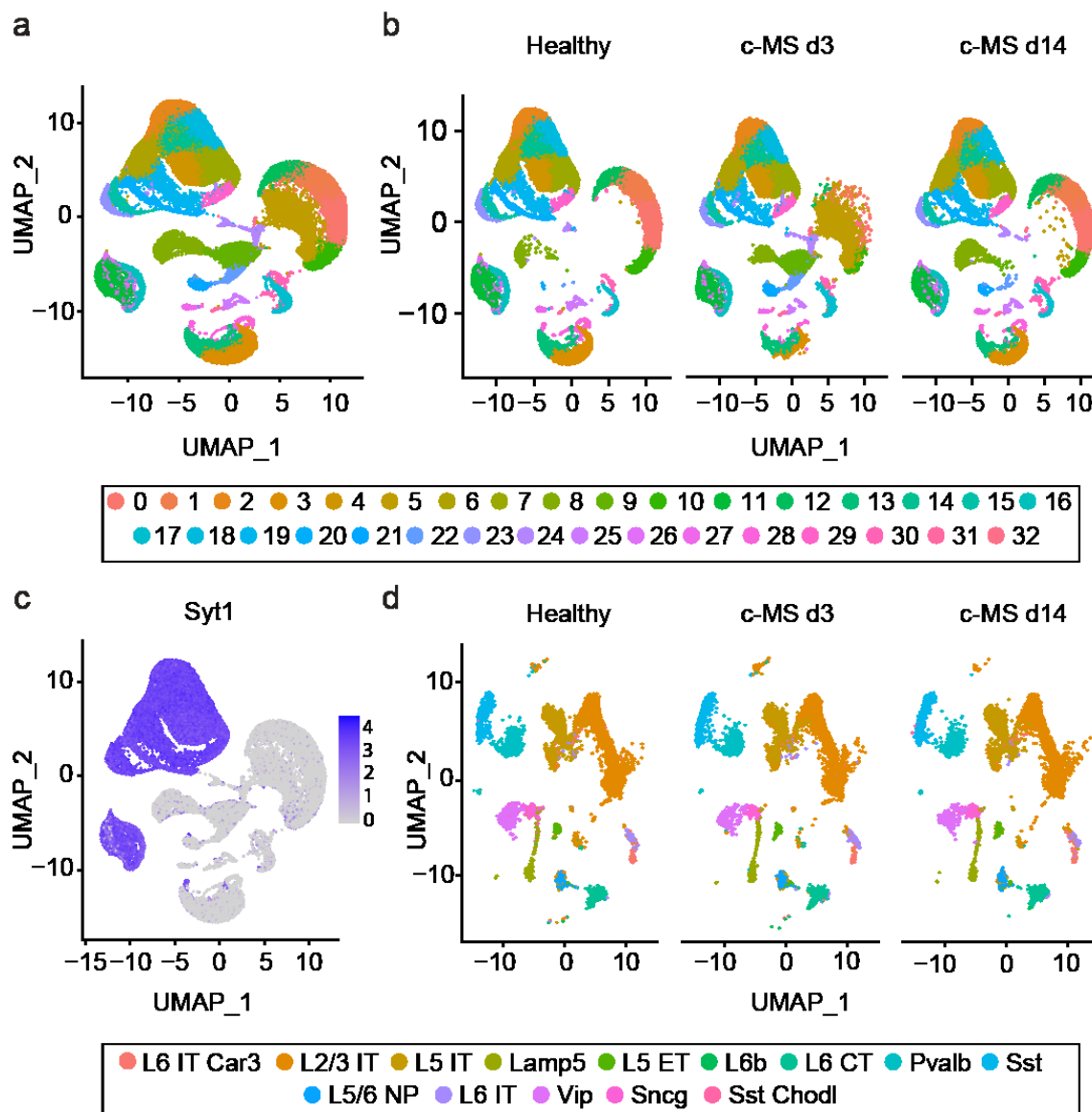


Figure 11: Single-nucleus RNA-seq profiling and characterization in a mouse model of cortical Multiple Sclerosis. **a)** Two-dimensional UMAP projection of all nuclei isolated and sequenced shows formation 32 clusters (n=5 Ctr, n=4 c-MS d3 and n= 4 mice). **b)** UMAP separation into control (left), c-MS d3 (middle) and c-MS d14 (right) shows expression of 32 clusters in all conditions with diverse nuclei number per cluster across conditions. **c)** Feature plot of *Syt1* expression for determination of neuronal clusters based on marker gene (*Syt1*) expression levels (violet intensity defines higher gene expression in cluster). **d)** UMAP of subset of neuronal nuclei obtained based on *Syt1* expression in c, and separated into shows control (left), c-MS d3 (middle) and c-MS d14 (right) 14 neuronal clusters, which can be further attributed to neuronal subtypes based on the Allen Brain Atlas nomenclature, with similar nuclei numbers in all clusters across all conditions. Abbreviations: Ctr: control; c-MS: cortical MS model; dX: perfused at day X. Figure created by Emily Melisa Ullrich Gavilanes, includes data from Dr. Aleksandra Mezydło, Veronika Pfaffenstaller.

In the next part of my project, we aimed to better understand the mechanisms involved in neuronal pathology observed in MS patients. In our c-MS model, we could observe signs of neuronal pathology in the form of reduced spine density (Figure 5) and increased calcium within dendritic spines (Figure 7). Thus, our aim was to use snRNA-seq to understand which transcriptomic changes could be driving neuronal pathology and lead to the neuronal phenotypes we could observe. This part was performed in collaboration with Dr. Aleksandra Mezydło, Dr. Eduardo Beltrán, Kristof Egervari Levente, Klara Eglseer, and Veronika Pfaffenstaller. Dr. Mezydło and I designed the experiments generated the c-MS animals and processed tissue for nuclei isolation. Dr. Beltrán FACS sorted the nuclei, generated the library for sorting and performed the initial data analysis. Kristof Egervari Levente generated the Merkler MS patient data set that was kindly provided to us. Klara Eglseer performed the mapping of data sets together. Veronika Pfaffenstaller performed analysis of mapped data sets under supervision of Clara de la Rosa del Val.

Dr. Mezydło and I isolated nuclei from the cortex of our young c-MS mice at day 3 and day 14 and used it for 10x snRNA-seq analysis. Following sequencing, together with Eduardo Beltrán, we performed analysis with the Seurat R package (Butler et al., 2018, Hao et al., 2021, Satija et al., 2015, Stuart et al., 2019) where we observed 32 clusters in the uniform manifold approximation and projection (UMAP) plot of our cortical nuclei belonging to different cell types (Figure 11a). Most clusters were similarly represented among healthy, c-MS day 3 and c-MS day 14 conditions, while cluster 5 seemed to be mostly related to the c-MS day 3 acute inflammation condition (Figure 11b). We then analyzed which clusters represented neurons by filtering the clusters for expression of neuronal marker *Syt1* (Figure 11c) and created a subset to take a further look only into the neurons of our data set. The neuron specific UMAP plot then had 14 clusters, that could be mapped using the Symphony package (Kang et al., 2021) into specific neuronal subtypes based on the Allen Motor cortex 10x single-cell reference data set (Bakken et al., 2021) and thus labelled. This mapping was performed by Klara Eglseer. The clusters were similarly represented in healthy, c-MS day 3 and c-MS day 14 conditions (Figure 11d).

In order to make our analysis more clinically translatable and patient relevant, we wanted to investigate mechanisms and signatures that were not only present in our c-MS model, but

also in MS patients. For this reason, Klara Eglseer mapped our c-MS model snRNA-seq data

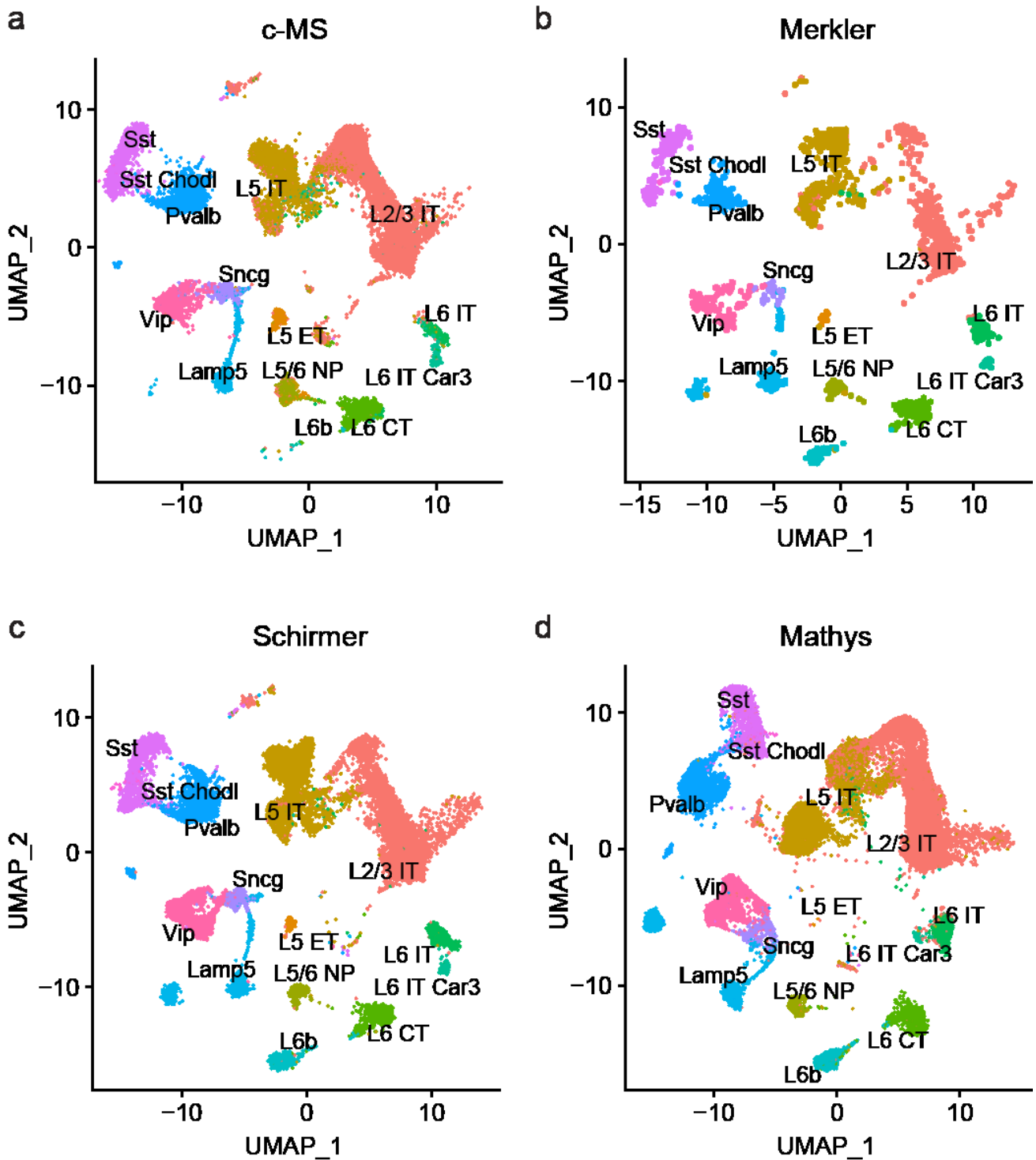


Figure 12: Mapping of snRNA-seq from c-MS mice, two MS patient data sets and an Alzheimer’s disease data set shows same neuronal subtypes. Two-dimensional UMAP projection of nuclei from (a) c-MS mice snRNA-seq data set mapped together with the (b) Merkler MS patient data set, the (c) Schirmer et al., MS patient data set; and the (d) Mathys et al., AD patient data set to the Allen Institute Brain Motor Cortex Atlas show the same neuronal subtypes as the atlas, with diverse nuclei number per cluster between data sets. Abbreviations: Ctr: control; c-MS: cortical MS model; MS: Multiple Sclerosis; AD: Alzheimer’s Disease. Figure created by Emily Melisa Ullrich Gavilanes, includes data from Klara Eglseer.

set together with two MS patient snRNA-seq data sets, one from our collaborator Prof. Doron Merkler where SMART-seq for single nuclei was used, and the online available Schirmer et al., 2019 10x snRNA-seq data set. To define if our genes and signatures were MS specific, she also mapped these data sets to the Mathys et al., 2019 10x snRNA-seq ROSMAP AD data set. Mapping was performed to the Allen Motor cortex 10x reference data set (Bakken et al., 2021) using the Symphony R-package (Kang et al., 2021). The c-MS model data set (Figure 12a), Merkler data set (Figure 12b), Schirmer data set (Figure 12c), and Mathys data set (Figure 12d) all showed the same neuron subtype expression and while the number of nuclei per neuronal subtype varied between data sets, the mapping seemed to be successful and could be used for further analysis of neuronal inflammatory signals and their prevalence in different neuronal subtypes.

When looking for MS specific genes and signatures of neuropathology, Veronika Pfaffenstaller and I focused on inflammatory signals, which means we used the comparison between our c-MS day 3 model and healthy controls in mice (referred to from now on as c-MS model day 3), between MS patients and healthy controls in the Merkler (Merkler MS) and Schirmer data sets (Schirmer MS), and between AD patients and controls in the Mathys data set (Mathys AD). Veronika Pfaffenstaller subsequently plotted the genes from these diseased vs healthy comparisons in correlation plots, filtering genes by using only those that were differentially expressed genes (DEGs) from the cMS model day 3 as a basis, between the c-MS model and the different patient data sets (Figure 13). To define up- and down-regulated genes, we a cutoff was set at 3 times the standard deviation of the log 2-fold change (FC) and an adjusted p-value of less than 0.05. In the c-MS model day 3 vs Merkler MS correlation, we observed 17 up-regulated and 11 down-regulated genes with a larger data spread in the c-MS data set and a slightly positive correlation between the two data sets (Figure 13a). In the c-MS model day 3 vs Schirmer MS data set, we found 31 up-regulated and 15 down-regulated genes this time with a similar spread in both data sets and once again a slight positive correlation (Figure 13b). Several genes could be observed to be conserved between the c-MS model day 3 vs Merkler MS and the c-MS model day 3 vs Schirmer MS up-regulated genes, these being: B2M, PSAP, ATP1B1, SERINC1, ACTB, PRNP, THY1, ITM2B, CKB (Figure 13a, b). Correlation between c-MS model day 3 and the Mathys AD data set showed 5 up-regulated and 11 down-regulated genes with a larger data spread in the c-MS model day 3 data set and a slightly positive correlation (Figure 13c). When comparing the overlapping genes from the MS patients and c-MS model day 3 data set with those that were differentially expressed (defined as genes over 3x standard deviation of mean and adjusted p-value of <0.05) in the Mathys AD data set, we observed 4 genes that were also differentially expressed in AD: ITM2B, ATP1B1, CKB, PRNP. These genes were therefore removed from our MS specific gene set. The correlations observed were maintained throughout different neuronal subtypes, meaning a single neuronal subtype was not responsible for biasing the correlations observed between the c-MS model day 3 vs Merkler MS data sets (Suppl Figure 1), the c-MS model day 3 vs Schirmer MS data sets (Suppl Figure 2) and the c-MS model day 3 vs Mathys AD data sets (Suppl Figure 3).

Overall, we could perform snRNA-seq of our c-MS mice and specifically select neuronal clusters. In a next step, we could integrate and map this neuronal data set together with two MS patient data sets and a control AD data set. From these data sets we could determine MS specific genes that were maintained between mice and humans. Our highestly

differentiated MS specific genes overlapping between our c-MS model and the MS patients were of B2M, PSAP, SERINC1, ACTB and THY1. From these genes we could select candidates and perform follow up studies to further understand the role these genes could play in the neuronal pathology of MS and whether these genes could be good therapeutic targets.

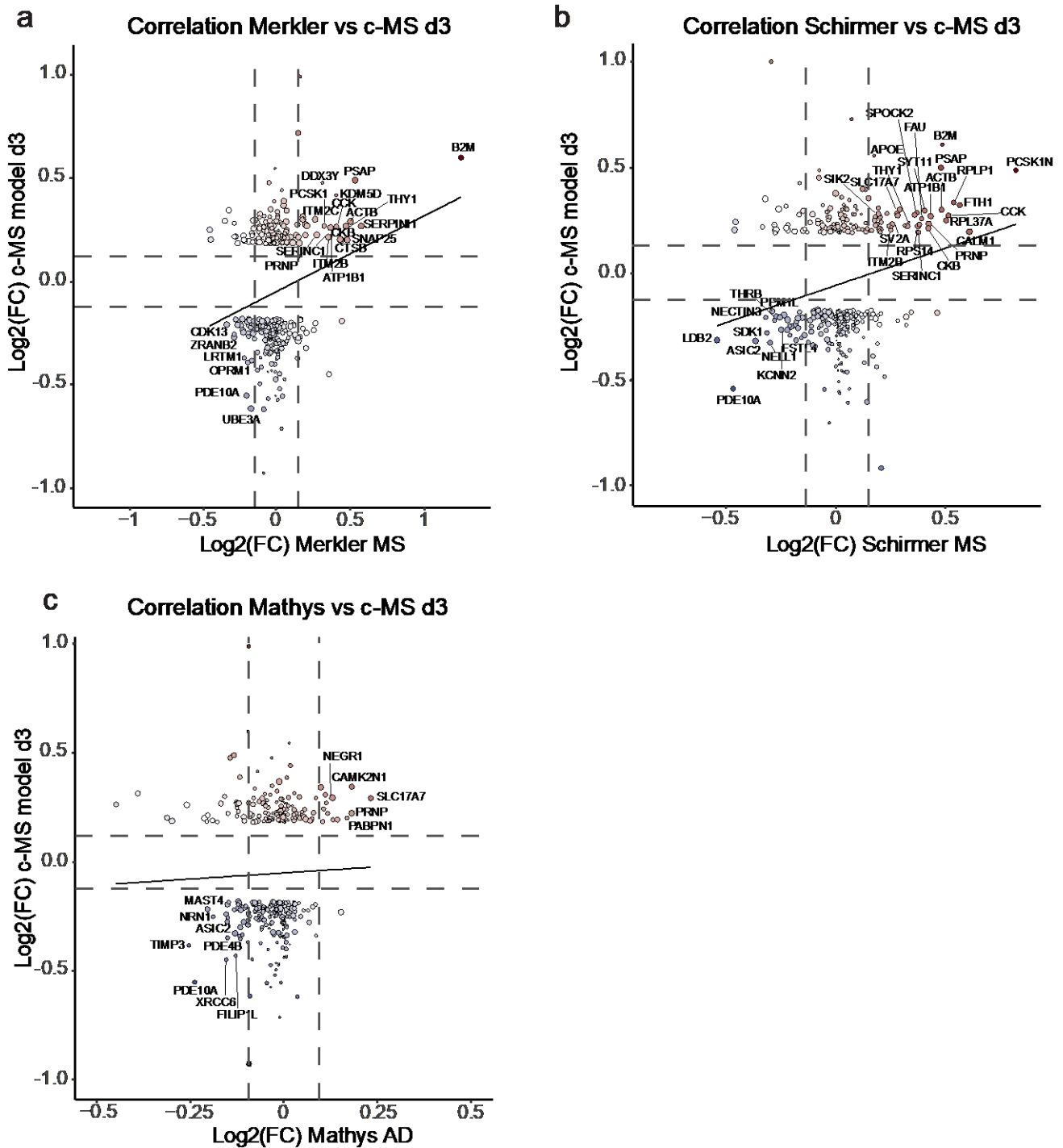


Figure 13: Correlation analysis between genes of c-MS mice and patient data sets presents MS-specific genes conserved across species. **a)** Correlation analysis of genes expressed in the c-MS d3 vs healthy mouse comparison and the Merkler MS patient vs healthy control comparison. Genes shown are filtered for DEGs in c-MS model day 3 data set. Positively correlated DEGs are shown in red. Negatively correlated DEGs are shown in blue. The stronger the correlation of a gene in both data sets the stronger the color towards red or blue. White colored genes are not strongly correlated. Dotted lines show threshold for consideration of DEGs at 3x SD of log2FC for each data set. **b)** Correlation analysis of genes expressed in the c-MS d3 vs Healthy mouse comparison and the Schirmer MS patient vs healthy control comparison. Genes shown are filtered for DEGs in c-MS model day 3 data set. Positively correlated DEGs are shown in red. Negatively correlated DEGs are shown in blue. The stronger the correlation of a gene in both data sets the stronger the color towards red or blue. White colored genes are not strongly correlated. Dotted lines show threshold for consideration of DEGs at 3x SD of log2FC for each data set. **c)** Correlation analysis of genes expressed in the c-MS d3 vs Healthy mouse comparison and the Mathys AD patient vs healthy control comparison. Genes shown are filtered for DEGs in c-MS model day 3 data set. Positively correlated DEGs are shown in red. Negatively correlated DEGs are shown in blue. The stronger the correlation of a gene in both data sets the stronger the color towards red or blue. White colored genes are not strongly correlated. Dotted lines show threshold for consideration of DEGs at 3x SD of log2FC for each data set. Size of data point shows percentage of nuclei expressing a gene in human disease vs control data set. Abbreviations: Ctr: control; c-MS: cortical MS model; MS: Multiple Sclerosis; AD: Alzheimer's Disease; DEG: differentially expressed gene; FC: fold change; SD: Standard deviation. Figure created by Emily Melisa Ullrich Gavilanes, includes data from Veronika Pfaffenstaller

IV.4 Mechanistic dissection and therapeutic targeting of neuronal pathology in the cMS model

Therapeutic options for progressive MS, where grey matter pathology is more prominent, are still limited nowadays. One of the possible reasons why, is the fact that the mechanisms leading to grey matter pathology and subsequent neuron pathology have yet to be elucidated. In this part of my thesis, we focused on targeting candidate genes obtained from the integrative snRNA-seq analysis of c-MS model and MS patients (Figure 14-17, Suppl Figure 4, 5). We aimed to affect these genes via knock out of these genes or related genes through the CRISPR/Cas9 system to further identify the role they play in neuronal pathology and to determine whether they can function as therapeutic targets. This part was performed in collaboration with Adinda Wens, Veronika Pfaffenstaller, Dr. Arek Kendirli, Clara de la Rosa del Val and Almir Aljovic. Dr. Arek Kendirli and Clara de la Rosa del Val established the *in vitro* sgRNA testing pipeline and Dr. Kendirli aided in the design and cloning of vectors used for in vivo CRISPR/Cas9 experiments as well as with FACS sorting of nuclei and mRNA library preparation. Adinda Wens and I established the in vivo and in vitro pipeline used for NeuN knockout. Almir Aljovic generated and kindly provided me with the AAV9 used for NeuN CRISPR/Cas9 knockout verification. Veronika Pfaffenstaller and I generated PSAP knockout mice and isolated nuclei, in addition Veronika Pfaffenstaller prepared the mRNA library for mRNA sequencing and performed bioinformatics analysis of PSAP knockouts. I performed gDNA and protein verification for all knockouts as well as generated, processed and analyzed tissue for the *lfngr1* knockout as well as performed the initial bioinformatics steps of PSAP knockout mRNA sequencing analysis.

Subsequently, we tested whether previously tested therapies targeting microglial activation (Figure 18, 19) could ameliorate the neuronal pathology that we observed in our c-MS model. For this part I collaborated with Dr. Adrian-Minh Schumacher, Dr. Mehrnoosh Jafari, Dr. Nellwyn Hagan, Dr. Dimitry Ofengeim, Josef Gans and Dr. Ross Gruber. Dr. Jafari, Dr. Schumacher and I generated the c-MS mice, collected, and analyzed the data for the CSF1R-inhibitor experiments. Dr. Hagan, Dr. Ofengeim and Joseph Gans provided us with the CSF1R-inhibitor. Dr. Gruber provided us with the BTK-inhibitor. I generated c-MS mice, treated them, collected data, and analyzed data for the BTK-inhibitor treatment.

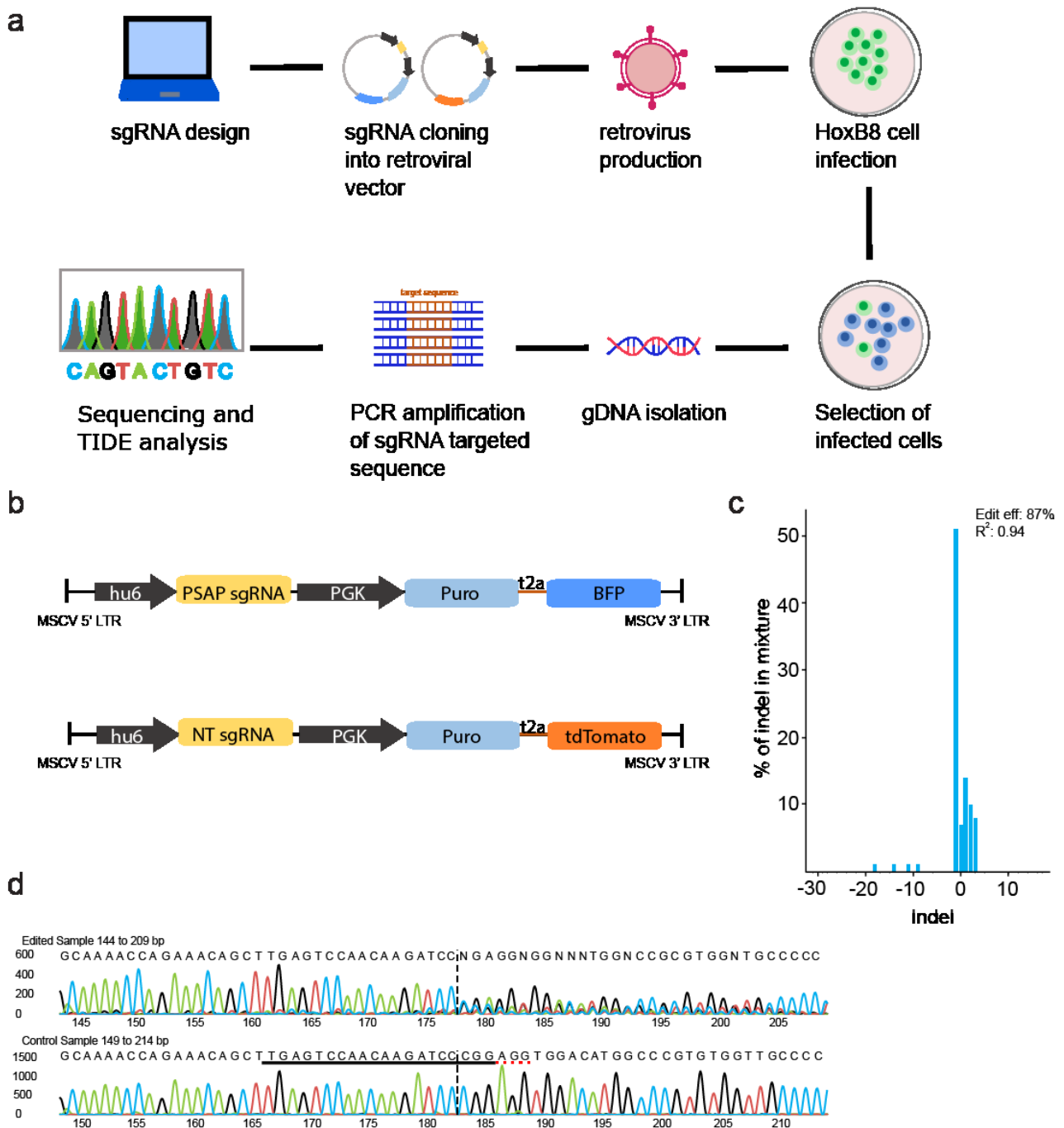


Figure 14: *In vitro* CRISPR/Cas9 KO pipeline for selection of sgRNA was applied for PSAP KO. **a)** Schematic of experimental pipeline used for selection of sgRNA *in vitro*. sgRNA testing was performed with retroviral vectors in Cas9-expressing HoxB8 cells followed by genomic DNA isolation, PCR amplification of target region, sequencing and TIDE- indel analysis. **b)** Retroviral sgRNA expression and selection cassette for PSAP sgRNA (top) and NT sgRNA (bottom). **c)** Percentage of indel distribution for PSAP sgRNA6 in genomic DNA of Cas9-expressing HoxB8 cells. Top values are the total editing efficiency and the R^2 value obtained from indel editing score. **d)** DNA sequencing trace of PSAP sgRNA6 edited sample (top) and NT sgRNA sample (bottom) showing the interference window for the sgRNA (solid line), PAM sequence (red dotted line) and the Cas9 cleavage site (dotted line). Abbreviations: sgRNA: single guide RNA; gDNA: genomic DNA; Puro: Puromycin resistance cassette; NT: non-targeted; TIDE: tracking of indels by decomposition. Figure created by Emily Melisa Ullrich Gavilanes, includes data from the Inference of CRISPR Editing v2 (ICE) webtool.

IV.4.1 CRISPR/Cas9 KO of candidates obtained from transcriptomic analysis

In order to better understand the underlying mechanisms leading to neuronal pathology observed in MS, we aimed to use the CRISPR/Cas9 system to target some of the candidate genes we could previously define through our snRNA-seq data sets (chapter IV part 3). Veronika Pfaffenstaller and I set to knock out PSAP, the gene for prosaposin, a lysosomal pre-protein that upon cleavage by Cathepsin D leads to the formation of saposin A-E molecules. Saposins act as activators in glycosphingolipid degradation in the lysosome. Furthermore, PSAP has been previously described to play a role in promoting cell survival and a protective role against ferroptosis, oxidative stress and lipid peroxidation (Sandhoff and Harzer, 2013, Tian et al., 2021, Meyer et al., 2014).

As a way to target PSAP, Adinda Wens and I first set to establish a CRISPR/Cas9 KO system based on the one described by Platt et al., 2014. The established system would provide versatility and allow for adaptability to test different gene KOs. This system consisted of an sgRNA selection and testing step *in vitro* in Cas9-expressing HoxB8 cells through tracking of indels by decomposition (TIDE) analysis in genomic DNA (Figure 14a), followed by *in vivo* specific cell targeting in *Rosa26-Cas9 x BiozziABH* mice (Figure 15a). The *in vitro* selection was adapted from the system used in our lab by Dr. Kendirli and Clara de la Rosa del Val.

In an initial step, Adinda Wens and I tested our system by using an already established and previously described sgRNA for NeuN (Platt et al., 2014) (Suppl Figure 4). NeuN is a highly expressed neuronal-specific splicing factor (Platt et al., 2014). We conducted initial sgRNA *in vitro* testing by TIDE sequencing of genomic DNA followed by *in vivo* analysis of TIDE at the genomic DNA level. Testing of knockout at the protein level through staining of nuclei for NeuN was performed as well as verification by *in situ* studies in fixed tissue (Suppl Figure 4a). *In vitro* testing of NeuN sgRNA in HoxB8 cells infected with retrovirus (Figure 14b top, NeuN sgRNA replaced PSAP) showed an editing efficiency of 79.6% with the highest indel proportion (around 50%) being a deletion of one nucleotide (Suppl Figure 4b). *In vivo* analysis of NeuN KO at the protein level was first observed during nuclei isolation and fluorescence activated cell sorting (FACS) analysis of neurons infected with the php.eb AAV enhanced green fluorescent protein (eGFP)-KASH virus (Figure 15b, bottom, NeuN sgRNA replaced NT). Nuclei of both NeuN infected samples, showed a marked reduction in APC-NeuN staining compared to samples infected with non-targeted (NT) sgRNA (Suppl Figure 4c).

Genomic DNA isolation from these FACS sorted nuclei, and subsequent analysis by TIDE sequencing, demonstrated a higher edit efficiency in infected cells of 86.5% in cortex samples with about 80% of the edits being a one nucleotide deletion (Suppl Figure 4d), similarly to what was observed in vitro (Suppl Figure 4b). As a following step, we used an AAV.9 produced virus with the NeuN sgRNA, producing mCherry labelling in infected cells (Suppl Figure 4e), to test whether we could also detect the KO in situ. Three weeks after virus

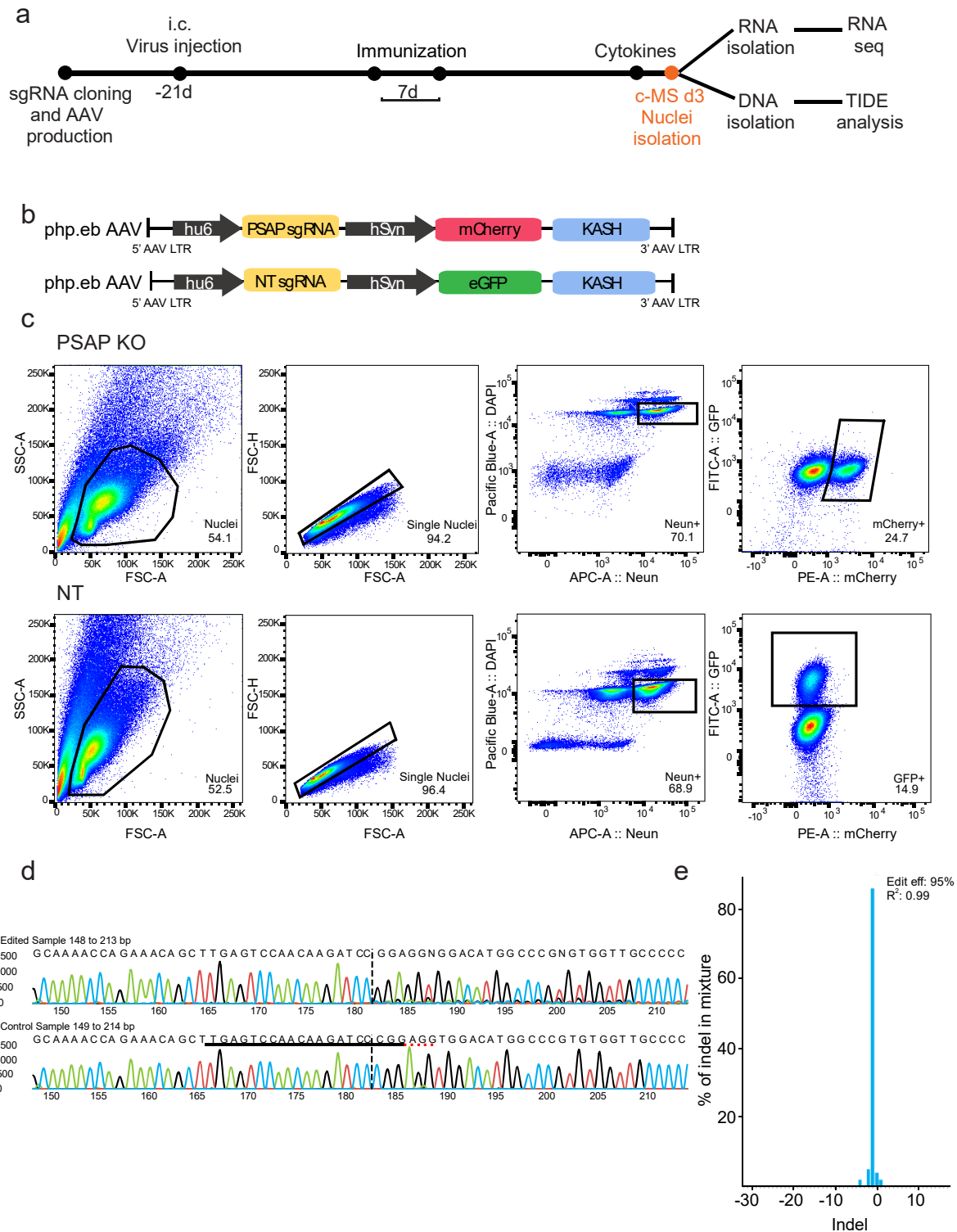


Figure 15: CRISPR/Cas9 PSAP KO in c-MS neurons *in vivo* can be verified at the genomic DNA level following AAV-mediated sgRNA targeting. **a)** Schematic of experimental design for *in vivo* verification and RNA-seq from nuclei of AAV-mediated CRISPR/Cas9 KO of PSAP in *R26-Cas9x BiozziABH* mice in c-MS. **b)** php.eb AAV expression cassette for PSAP sgRNA (top) and NT sgRNA (bottom) used for labeling of infected neuronal nuclear envelope. **c)** Representative FACS plots of neuronal nuclei transduced with AAV sgRNA vector targeting PSAP (with mCherry-KASH backbone, top) or NT control (eGFP-KASH backbone, bottom) in the cortex used for gating and selection of targeted neurons for further gDNA and RNA analysis. **d)** DNA sequencing trace of AAV-mediated *in vivo* CRISPR/Cas9 KO of PSAP sgRNA6 edited sample (top) and NT sgRNA sample (bottom) showing the interference window for the sgRNA (solid line), PAM sequence (red dotted line) and the Cas9 cleavage site (dotted line). **e)** Percentage of indel distribution for PSAP sgRNA6 in genomic DNA of nuclei isolated from PSAP sgRNA AAV- infected c-MS mice compared to NT. Top values are the total editing efficiency and the R^2 value obtained from indel editing score. Abbreviations: sgRNA: single guide RNA; gDNA: genomic DNA; NT: non-targeted; TIDE: tracking of indels by decomposition. Figure created by Emily Melisa Ullrich Gavilanes, includes data from the Inference of CRISPR Editing v2 (ICE) webtool.

injection, a mCherry positive area was detected around the injection site in the cortex of *Rosa26-Cas9 x BiozziABH* mice. When the tissue was stained with NeuN, it could be noted that the virus infected neurons displayed no NeuN staining, consistent with a NeuN KO (Suppl Figure 4F).

Following the verification of our CRISPR/Cas9 system *in vitro* and *in vivo* with NeuN, Veronika Pfaffenstaller and I used this system for the KO of PSAP. Once again, we started by designing sgRNAs for PSAP through the Broad Institute GPP sgRNA Designer (<https://portals.broadinstitute.org/gpp/public/analysis-tools/sgrna-design>) and tested them *in vitro* by cloning them into a retroviral vector (Figure 14b) that could then be used for infection of Cas9-expressing HoxB8 cells. Following genomic DNA isolation from our infected cells, we amplified the sequence targeted by the sgRNA and sent this for sequencing and TIDE analysis (Figure 14a). Five different sgRNAs were tested for PSAP, based on indel percentage and knockout score obtained from TIDE analysis, sgRNA6 was selected (Suppl Table 1). PSAP sgRNA6 had an 87% knockout efficiency with about 50% of the edits being a one nucleotide deletion (Figure 14c). Further observation of the trace obtained from sequencing and comparing the edit window between the KO and NT sample, showed that effective editing is taking place in samples infected with the PSAP sgRNA (Figure 14d). PSAP sgRNA6 was therefore used for further *in vivo* analysis of PSAP KO.

For *in vivo* CRISPR/Cas9 KO of PSAP, we used an AAV vector based on Platt et al., 2014. This vector has a KASH sequence linked to the fluorophore under a human Synapsin promoter which would label the nuclear envelope of neurons and upon nuclei isolation would allow us to distinguish between infected and uninfected cells as well as between different sgRNAs (Figure 15b). We then packaged this vector in a php.eb AAV capsid, which was designed to increase transduction efficiency in the CNS (Chan et al., 2017), and injected it intracortically into the mice 3 weeks before c-MS induction. At c-MS day 3 we isolated nuclei, which we FACS sorted, and from these isolated genomic DNA for KO verification at the genome level as well as RNA which was used for bulk RNA sequencing to determine transcriptional changes that could occur as a result of PSAP KO (Figure 15a). Isolated nuclei

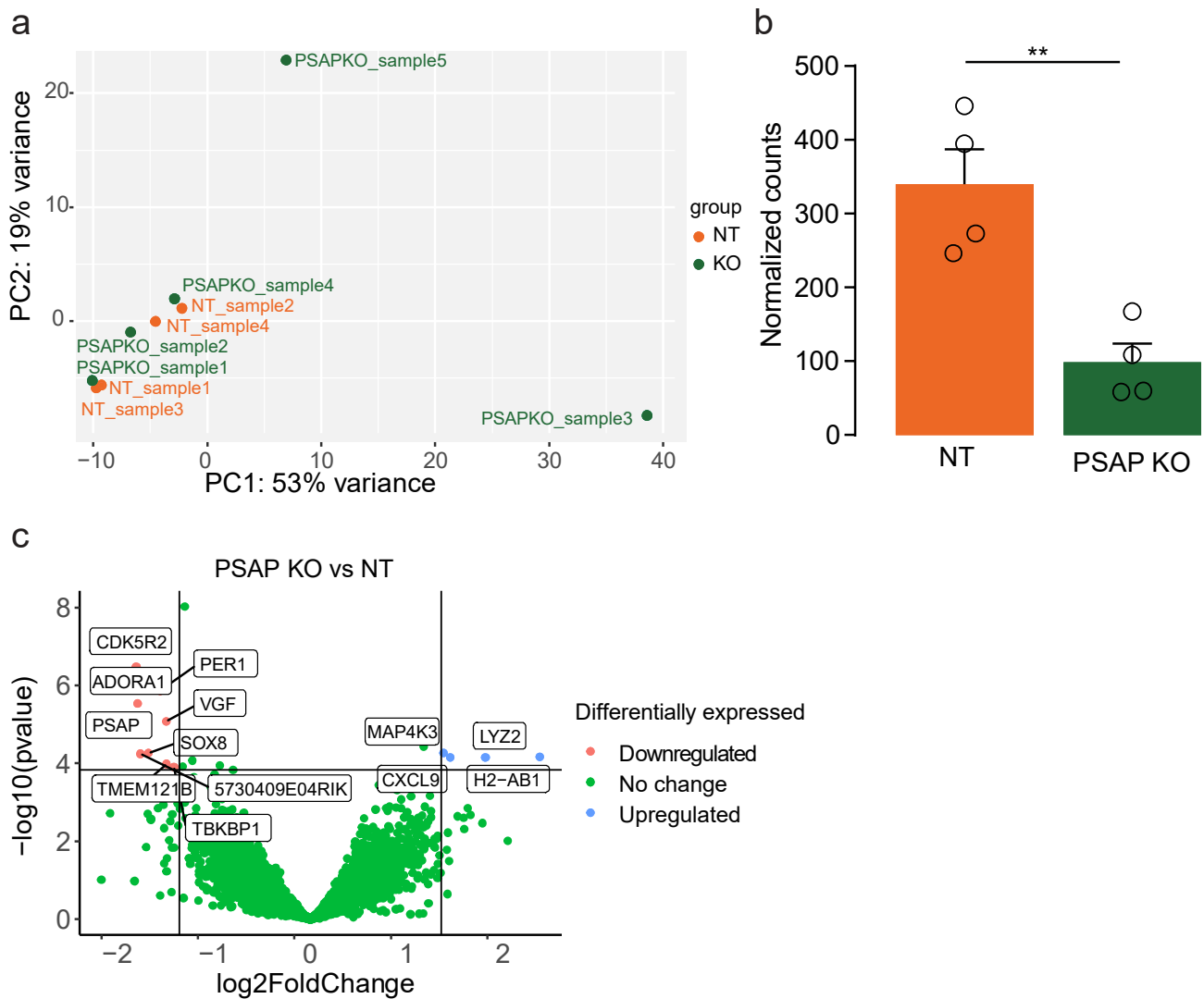


Figure 16: RNA-seq of AAV-mediated CRISPR/Cas9 PSAP KO in c-MS can be verified at the mRNA level. a) Two-dimensional principal component analysis for samples belonging to PSAP KO mice (green) and NT control samples (orange), shows clustering of most NT and PSAP samples, except for PSAP KO sample 3 which diverges in PC1 representing 53% variance. PSAP KO sample 3 was subsequently excluded from further analyses. b) mRNA normalized count quantification of PSAP KO and NT control mice in c-MS (n=4 NT, n=4 PSAP KO mice; mean \pm SEM; unpaired t-test). c) Volcano plot of PSAP KO vs NT comparison in c-MS mice showing DEGs upon PSAP KO. Significantly upregulated DEGs are shown in blue, significantly upregulated DEGs are shown in red. Lines indicate threshold for consideration of DEGs defined at 3x SD of $\log_2\text{FC}$ and adjusted p-value of ≤ 0.05 . Abbreviations: NT: non-targeted, PC: Principal component; FC: Fold change; SD: standard deviation. ** $p < 0.01$. Figure created by Emily Melisa Ullrich Gavilanes, includes data from Veronika Pfaffenstaller.

from cortex of infected cells were first gated based on granularity and size to obtain the nuclei and remove debris. Then, based on size of the samples single nuclei were selected removing doublets. DAPI and NeuN staining allowed for selection of neuronal specific nuclei, and from there, infected cells with PSAP sgRNA (mCherry positive) or NT sgRNA infected cells (eGFP

positive) could be selected for sorting (Figure 15c). Genomic DNA was subsequently isolated from some samples which was next used for amplification of the targeted sequence and TIDE analysis. The trace obtained from the TIDE analysis showed an effective deletion of a single nucleotide at bp 183 of the editing site of the PSAP KO sample (Figure 15d), which was further confirmed in the indel plot where an editing efficiency of 95% could be observed with over 80% of edits being the observed single nucleotide deletion (Figure 15e). Validation of KO at the genomic level *in vivo* allowed for further analysis of RNA sequencing of PSAP KO samples.

PSAP KO sorted nuclei were also used for RNA isolation and bulk sequencing. Five PSAP KO samples and four NT samples, each sample belonging to one mouse injected with the virus containing the PSAP sgRNA vector or the NT sgRNA vector, were sent for sequencing. Following sequencing trimming, counting and alignment through the Galaxy platform (Galaxy, 2022), samples were run through the DESeq2 analysis (Love et al., 2014) where PSAP KO samples were compared to NT samples. Principal component analysis (PCA) showed that most PSAP KO and NT samples cluster together, however PSAP KO sample 3 diverged from the remaining samples as can be noted by the large variance being described in PC1 (Figure 16a). Thus, PSAP KO sample 3 was removed from further analysis. Our next step was to determine if the KO we validated at the genomic level was also observed at the RNA level. For this, we looked at the normalized counts for PSAP in NT and PSAP KO samples and plotted the counts per group. PSAP KO samples had a significantly lower PSAP normalized count number than NT samples (Figure 16b). We further attempted to validate the knockout at RNA level by looking at the log₂ FC and the p-value to determine if PSAP was significantly downregulated. We could see that PSAP was significantly downregulated in our PSAP KO samples compared to NT, and that eight further genes were down regulated while four genes were significantly upregulated when comparing PSAP KO and NT samples (Figure 16c). Some of the genes that we could observe as upregulated in the PSAP KO samples were surprising to be found. For example, *Ly22* has been described as a myeloid marker (Guerrero-Juarez et al., 2019). This was interesting considering our nuclei sorting previous to RNA isolation was considered to be specific for neuronal nuclei (Figure 15c) and might indicate the presence of at least a minor contamination with myeloid cells.

Despite this potential limitation of our analysis, and with the consideration that PSAP is not a transcriptional regulator, we decided to use our PSAP KO vs NT data set to determine if specific processes previously related to PSAP could be observed to be transcriptomically modified upon PSAP KO. We first investigated whether the five genes previously found as our MS specific highly regulated genes in snRNA-seq data sets (Figure 13) were changed upon PSAP KO. Besides PSAP being downregulated, the other genes were not significantly changed between PSAP KO and NT (Figure 17a). We then looked at whether ferroptosis associated genes were changed upon PSAP KO. PSAP has been previously described as a protective factor regarding ferroptosis (Tian et al., 2021). Veronika Pfaffenstaller probed our data for ferroptosis genes obtained from FerrDb database version 2 (Zhou et al., 2023) and selected those that have been previously tested on mouse models or human cells. When she probed the expression of these genes in our PSAP KO vs NT data set we could observe that once again no genes were significantly changed upon PSAP KO, suggesting a PSAP KO might not directly affect ferroptosis at least on the level of gene expression in our c-MS model (Figure 17b). Interestingly, when Veronika Pfaffenstaller probed our snRNA-seq data sets for

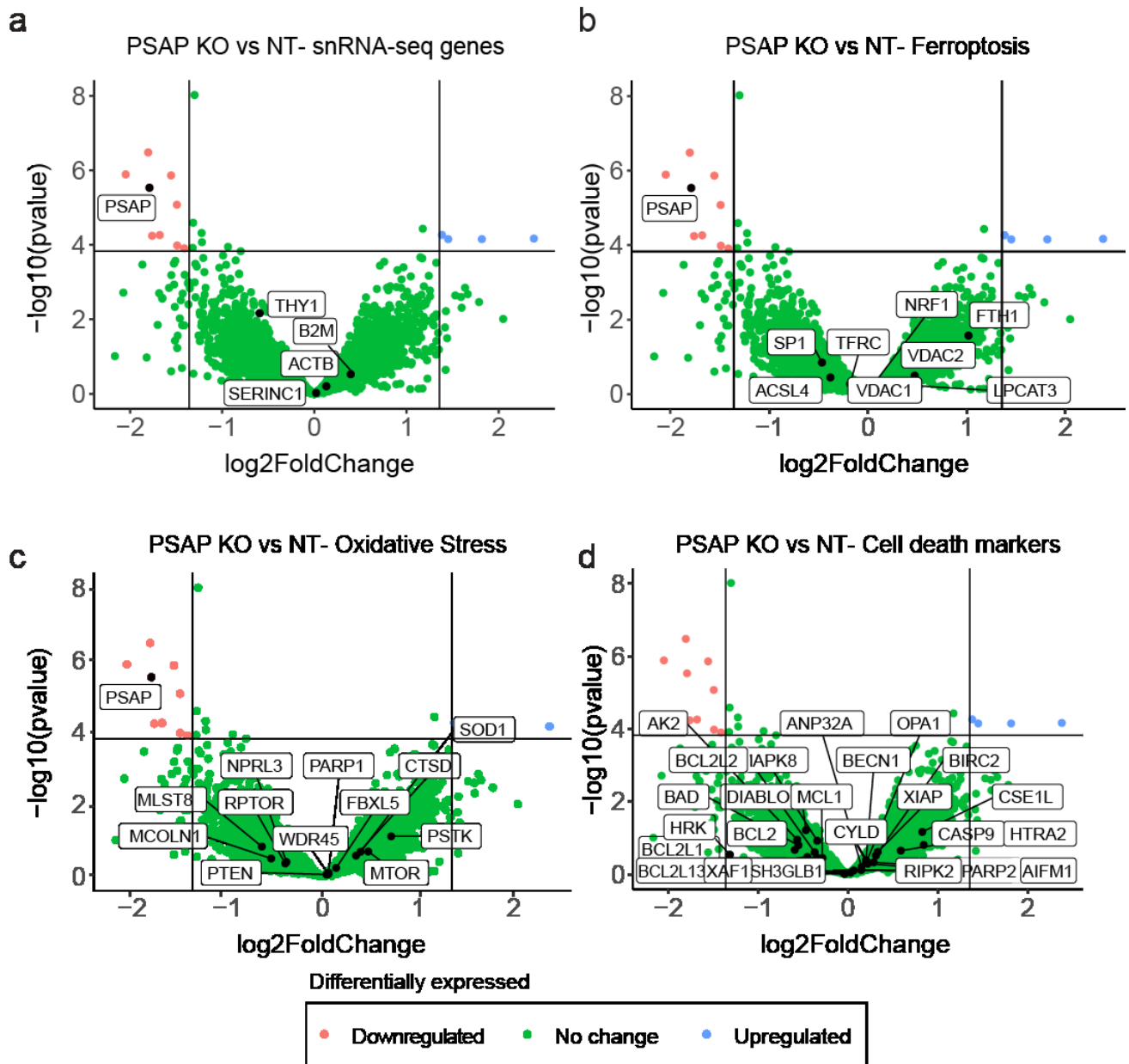


Figure 17: AAV-mediated CRISPR/Cas9 KO of PSAP in c-MS shows no effect in pathways PSAP has been described to be involved in. Volcano plots of PSAP KO vs NT comparison in c-MS mice were probed for effect in genes signatures defined (a) in this thesis for highly upregulated genes in snRNA-seq and previously described pathways where PSAP has been observed to play a role in Tian et al., 2021. PSAP has been described to play a role in (b) Ferroptosis, (c) Oxidative stress and (d) Cell death, however no DEGs besides PSAP could be observed in these pathways upon PSAP KO in c-MS. Significantly upregulated DEGs are shown in blue, significantly upregulated DEGs are shown in red. Lines indicate threshold for consideration of DEGs defined at 3x SD of log2FC and adjusted p-value of ≤ 0.05 . Abbreviations: NT: non-targeted, FC: Fold change; SD: standard deviation. Figure adapted by Emily Melisa Ullrich Gavilanes from figure in Veronika Pfaffenstaller’s master’s thesis.

these ferroptosis genes through a module score, she could detect a significantly higher expression of the ferroptosis signature in c-MS model day 3 mice (Suppl Figure 5a), MS

patients of the Merkler data set (Suppl Figure 5b), and MS patients both with active and inactive lesions of the Schirmer data set (Suppl Figure 5c) when compared to controls. Furthermore, these ferroptosis genes had significantly lower expression in AD patients compared to controls in the Mathys data (Suppl Figure 5d).

Based on previous studies that describe PSAP as a protective factor against oxidative stress (Tian et al., 2021), we decided to look at genes associated with this process that have been previously described and Veronika Pfaffenstaller manually curated them from different publications (Suppl Table 2). Upon probing of these genes in our PSAP KO vs NT data set we once again observed that none of these were significantly changed upon PSAP KO (Figure 17c). Finally, as PSAP was described as a protective factor to neuronal stress pathways usually leading to cell death and as a neuroprotective factor promoting cell survival (Meyer et al., 2014, Tian et al., 2021), we wanted to test whether cell death associated genes would be up or downregulated upon PSAP KO. Veronika Pfaffenstaller, therefore, selected genes involved in mouse and human studies found in the database Deathbase, which includes genes involved in apoptosis, necroptosis, and immune related cell death (Diez et al., 2010). Once she probed these genes in our PSAP KO data set, we saw that no genes were significantly changed in PSAP KO when compared to NT (Figure 17d). These results suggest that PSAP does not drive transcription of genes involved in ferroptosis, oxidative stress or cell death responses in our c-MS model.

I further wanted to test our CRISPR/Cas9 system with other candidate genes identified in our MS specific signature. B2M was highly expressed in the MS snRNA-seq data sets and in our c-MS mouse model but not in AD, which made it a strong candidate. B2M, the gene for beta 2 microglobulin, has been described to be activated by IFN γ signaling (Hunt and Wood, 1986). Due to the induction of our cortical lesions by Interferon gamma cytokine injection, I decided to target the Interferon gamma receptor 1 (Ifngr1) and in this way indirectly target B2M. I therefore used our CRISPR/ Cas9 pipeline and tested sgRNAs *in vitro* in Cas9-expressing HoxB8 cells, determined sgRNA efficiency through TIDE analysis (Figure 14a), and using the php.eb AAV virus containing the fluorophore-KASH sequence (Figure 15b) I was able to verify the sgRNA efficiency *in vivo* at the genomic level by TIDE analysis (Suppl Figure 6a). The Ifngr1 sgRNA3, had an *in vitro* editing efficiency of 68% with most of the indels being a one nucleotide insertion (Suppl Figure 6b) and an *in vivo* efficiency of 93% with once again most indels being a single nucleotide insertion (Suppl Figure 6c). For Ifngr1 KO, I wanted to test whether the gene KO would cause an amelioration of the observed synaptic phenotype of our c-MS model (Figure 5). I therefore performed an *in vivo* Ifngr1 sgRNA CRISPR/Cas9 knockout in *Rosa26-Cas9 x BiozziABH* mice (Suppl Figure 6d) with php.eb AAV viruses containing vectors with sgRNA and two fluorophores under the human Synapsin promoter. Both viruses had an eGFP fluorophore to make spine density analysis more consistent and in addition a second fluorophore, a Kusabira Orange fluorescent protein (KOFP) for the Ifngr1 sgRNA vector and an enhanced cyan fluorescent protein (eCFP) for the NT sgRNA containing vector to be able to differentiate with which sgRNA a specific neuron was infected (Suppl Figure 6e). Both viruses were co-injected in the right somatosensory cortex on the day of first immunization (day 0), and spine density analysis was performed at c-MS day 3 (Suppl Figure 6d). KOFP and eCFP expression allowed to select and differentiate single infected neurons with the Ifngr1 KO and those infected with NT in the cortex of c-MS mice (Suppl Figure 6f). The eGFP signal was widely expressed and

consistent throughout the tissue with both viruses allowing for accurate and comparable spine density quantification (Suppl Figure 6f, h). Spine density quantification showed that *Ifngr1* KO rescued the synaptic loss that was observed in c-MS day3 and in NT sgRNA samples (Suppl Figure 6g). Unfortunately, healthy control spine density levels both in animals infected with NT and with *Ifngr1* sgRNA were quite low and comparable to those of NT sgRNA infected c-MS day 3 mice which might be due to an inflammatory reaction being elicited by the AAV injection (Suppl Figure 6g). All in all, CRISPR/Cas9 KO of *Ifngr1* was verified at the genomic level and seems to be protective of synaptic loss in our c-MS model.

By using the CRISPR/Cas9 system we established, we were able to test the effect PSAP and *Ifngr1* KO has on our c-MS model. We could determine that upon PSAP knockout ferroptosis,

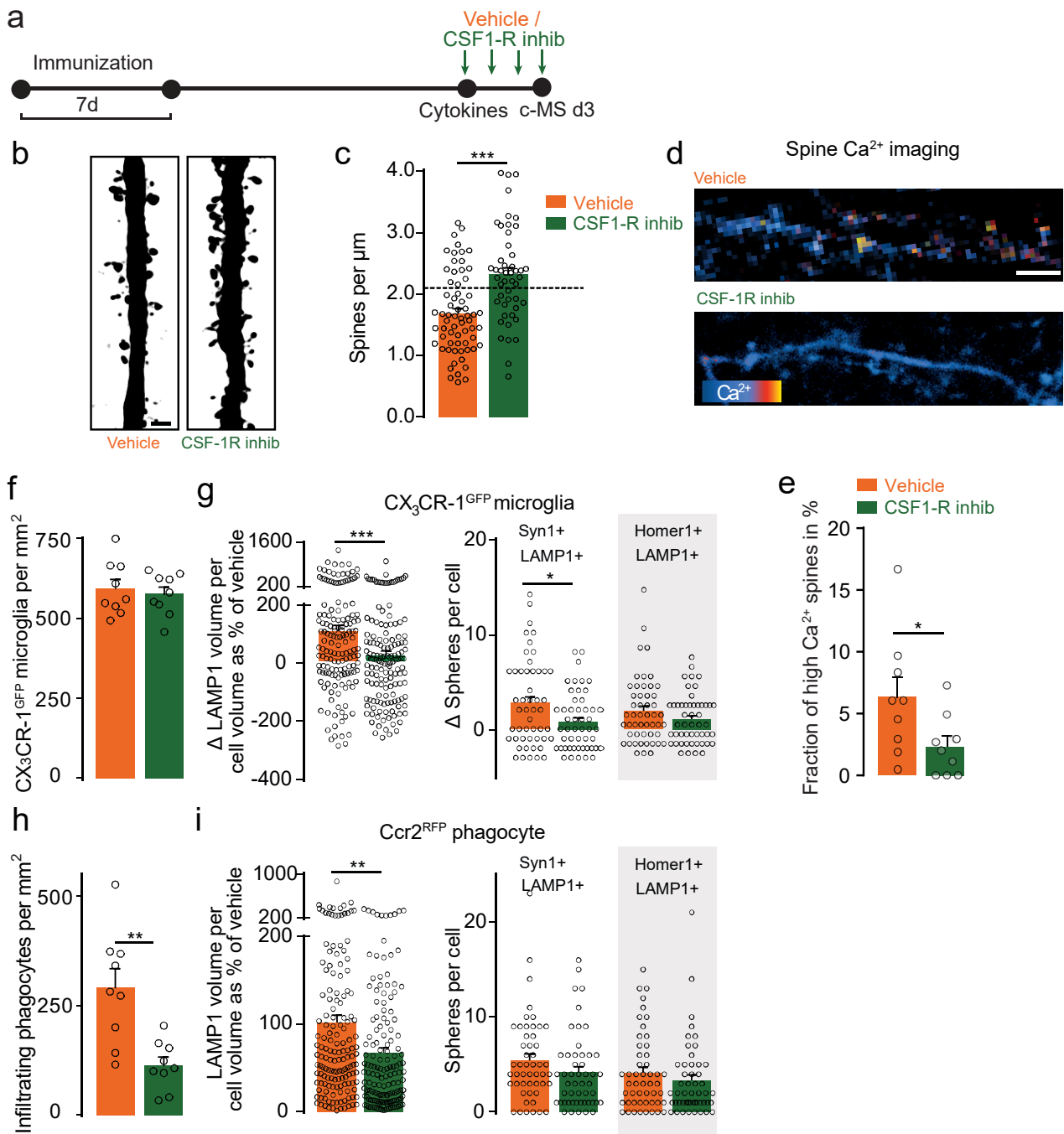


Figure 18: Blocking phagocyte entry and activation via CSF1R inhibitor treatment prevents synaptic loss in c-MS. **a)** Schematic timeline of treatment with vehicle or CSF1R-inhibitor in the c-MS model. **b)** Apical dendrite segments following deconvolution in vehicle and CSF1R-inhibitor treated c-MS mice layer V neurons. Left: vehicle treated, right: CSF1R-inhibitor treated. **c)** Spine density of layer V contralateral dendrites in c-MS d3 mice treated with vehicle or CSF1R-inhibitor (n=65 Vehicle, n=48 CSF1R-inhibitor dendritic stretches from n=8 Vehicle, n=7 CSF1R-inhibitor treated mice; mean \pm SEM; unpaired t-test). **d)** Representative *in vivo* ratiometric projection images of dendrites and spines color-coded for cytoplasmic Ca^{2+} levels of vehicle (top) and CSF1R-inhibitor (right) treated mice. **e)** Percentage of high Ca^{2+} spines in c-MS mice after treatment with vehicle or CSF1R-inhibitor (n=9 Vehicle, n=9 CSF1R-inhibitor treated c-MS mice; mean \pm SEM; unpaired t-test). **f)** Quantification of CX₃CR-1^{GFP} cell number in cortical sections of c-MS mice treated with vehicle or CSF1R-inhibitor (n=9 Vehicle and n=9 CSF1R-inhibitor treated mice; mean \pm SEM; unpaired t-test). **g)** Effects of synapse removal by CX₃CR-1^{GFP} cells in vehicle and CSF1R-inhibitor treated c-MS d3 mice. Left panel shows delta (Δ) of LAMP1 positive volume within CX₃CR-1^{GFP} cells as percentage of vehicle treated group. Delta refers to subtraction of volume of healthy controls (derived from Ctr group in Figure 8c, f) from vehicle or CSF1R-treated c-MS mice (n=150 Vehicle, n=150 CSF1R-inhibitor cells from n=5 vehicle and n=5 CSF1R-inhibitor treated c-MS mice; mean \pm SEM; unpaired t-test). Right panel shows delta (Δ) of the number of Synapsin-1/LAMP1 and Homer1/LAMP1 double positive spheres within CX₃CR-1^{GFP} cells in c-MS d3 mice treated with vehicle or CSF1R-inhibitor. Delta refers to subtraction of number of spheres of healthy controls (derived from Ctr group in Figure 8c, f) from vehicle or CSF1R-treated c-MS mice (n=50 Vehicle, n=50 CSF1R-inhibitor cells from n=5 Vehicle and n=5 CSF1R-inhibitor treated mice; mean \pm SEM; unpaired t-test; data for Homer1/LAMP1 vehicle treated group was replotted from Figure 8f). **h)** Quantification of infiltrating phagocytes defined by Iba1 positive CX₃CR-1^{GFP} cells in c-MS d3 mice treated with vehicle or CSF1R-inhibitor (n=9 vehicle and n=9 CSF1R-inhibitor treated mice; mean \pm SEM; unpaired t-test). **i)** Effects of synapse removal by Ccr2^{RFP} cells in vehicle and CSF1R-inhibitor treated c-MS d3 mice. Left panel shows LAMP1 volume within Ccr2^{RFP} cells as percentage of vehicle treated group (n=150 Vehicle and n=150 CSF1R-inhibitor cells from n=4 Vehicle and n=5 CSF1R-inhibitor treated mice; mean \pm SEM; unpaired t-test). Right panel shows number of Synapsin-1/LAMP1 and Homer1/LAMP1 double positive spheres within Ccr2^{RFP} cells in c-MS d3 mice treated with vehicle or CSF1R-inhibitor (n=50 Vehicle and n=50 CSF1R-inhibitor cells from n=4 vehicle and n=5 CSF1R-inhibitor treated c-MS d3 mice; mean \pm SEM; unpaired t-test; data for Homer1/LAMP1 vehicle treated group was replotted from Figure 8g). Deconvoluted images are used in panel b. Scale bar in b: 2 μ m, d: 5 μ m. Abbreviations: c-MS: cortical MS model; dX: perfused at day X. ***p<0.001, ** p<0.01, *p<0.05. Figure modified from Figure 6 of Jafari et al., Nature Neuroscience 2021 paper.

oxidative stress and cell death pathways were unchanged compared to control, while *Ifngr1* KO ameliorated the synaptic phenotype that was previously observed in the peak acute inflammatory time point in c-MS mice. This suggests that *Ifngr1* could be a potential therapeutic target for MS cortical grey matter pathology.

IV.4.2 Inhibiting microglial activation to prevent synapse loss in the cMS model

Based on the previous observation that microglia engulf synapses at the peak of CNS inflammation at c-MS day 3 in our c-MS model (Figure 8), Dr. Jafari, Dr. Schumacher and I wanted to test if interfering with microglial activation could help rescue this phenotype. For this purpose, we relied on small molecule therapy that target microglial functions. In a first

step, we used a colony stimulating factor 1 receptor (CSF1R) inhibitor. These inhibitors

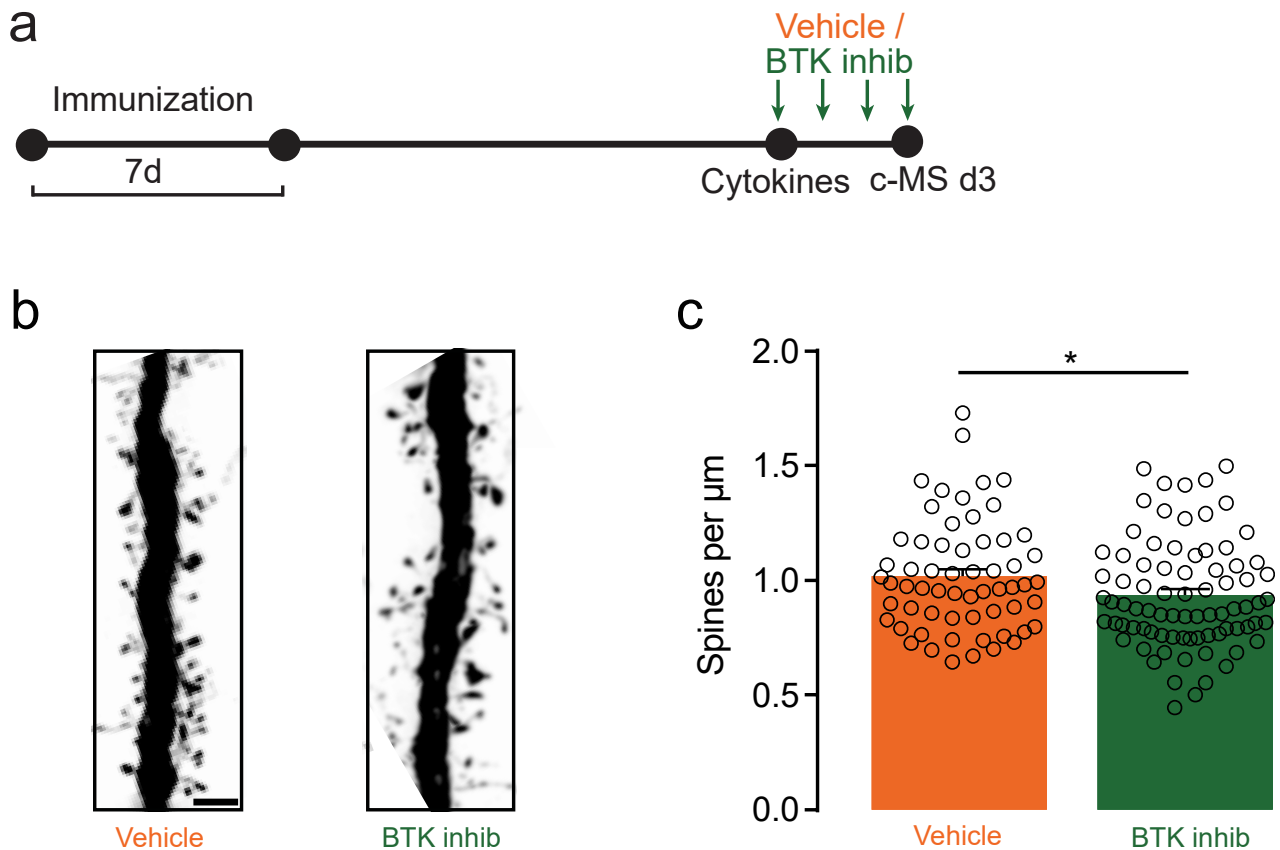


Figure 19: Inhibition of microglial phagocytosis via BTK inhibitor treatment does not ameliorate synaptic pathology in c-MS. **a)** Schematic timeline of treatment with vehicle or BTK-inhibitor in the c-MS model. **b)** Apical dendrite segments following deconvolution in vehicle and BTK-inhibitor treated c-MS mice layer V neurons. Left: vehicle treated, right: BTK-inhibitor treated. **c)** Spine density of layer V contralateral dendrites in c-MS d3 mice treated with vehicle or BTK-inhibitor (n=60 Vehicle, n=80 BTK-inhibitor dendritic stretches from n=6 Vehicle, n=8 BTK-inhibitor treated mice; mean \pm SEM; Mann-Whitney U test). Deconvoluted images are used in panel b. Scale bar in b: 2.5 μm . Abbreviations: c-MS: cortical MS model; dX: perfused at day X. *p<0.05. Figure created by Emily Melisa Ullrich Gavilanes.

deplete microglia cells when used at high concentrations. However, at the lower concentration used here, they inhibit microglial proliferation and attenuate some of their damage associated phenotypes (Hagan et al., 2020, Nissen et al., 2018, Olmos-Alonso et al., 2016). We applied the CSF1R inhibitor intraperitoneally to c-MS mice from day of cytokine injection daily until c-MS day 3 (Figure 18a). We could see that treatment with CSF1R inhibitor did rescue synapse pathology (Figure 5) in our c-MS model at day 3 compared to vehicle treated mice (Figure 18b, c). Furthermore, the increased calcium we observed in spines of our c-MS mice at day 3 (Figure 7) was significantly reduced in mice treated with the CSF1R inhibitor compared to vehicle treated mice (Figure 18d, e). When we looked at phagocytes, we could observe that the number of infiltrating phagocytes was reduced in c-MS mice treated with CSF1R inhibitor (Figure 18h), while microglia cell number remained unchanged (Figure

18f). A further characterization of microglia and infiltrating phagocytes showed a reduction in lysosomal content measured by LAMP1 volume in both microglia and infiltrating phagocytes (Figure 18g, 18i). A decrease in presynaptic material uptake was further observed in microglia cells as well as a trend for decreased postsynaptic material uptake (Figure 18g). Infiltrating phagocytes also showed a trend for slightly decreased uptake of pre and post synaptic material which, however, was not significant (Figure 18i). Taking these data together we could observe that CSF1R inhibition at low concentrations leads to a rescue of the phenotypes we observed and characterized in our c-MS model by reducing microglial phagocytosis of synapses and decreasing the recruitment of infiltrating phagocytes.

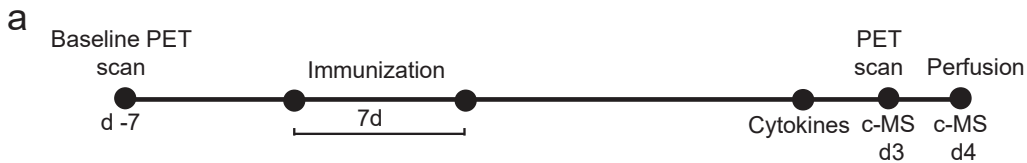
I further wanted to test whether a second small molecule, Bruton's tyrosine kinase (BTK) inhibitor, would play a role in ameliorating synaptic pathology in our c-MS model. BTK has been identified as a key regulator of microglial phagocytosis and inhibition of its activity has shown decreased microglial uptake of synaptosomes in AD (Keaney et al., 2019). As such, I treated our c-MS mice with BTK inhibitor through oral gavage, daily, from the day of the cytokine injection until our c-MS day 3 (Figure 19a). Unlike the CSF-1R inhibitor, the BTK-inhibitor did not ameliorate the spine density loss observed in our c-MS model (Figure 5), but rather it was observed to exacerbate it to some extent (Figure 19b, c). For this reason, the analysis of therapeutic treatment of BTK-inhibitor in our c-MS model was stopped.

Small molecules targeting microglia activation and functions in our c-MS model showed mixed results. Although, CSF1R inhibitor showed promising results in ameliorating synaptic pathology, a different microglia modulator, the BTK-inhibitor, did not show any rescue of the pathology. Using microglial targeting therapeutic strategies can therefore be a promising option for MS if the right target is selected.

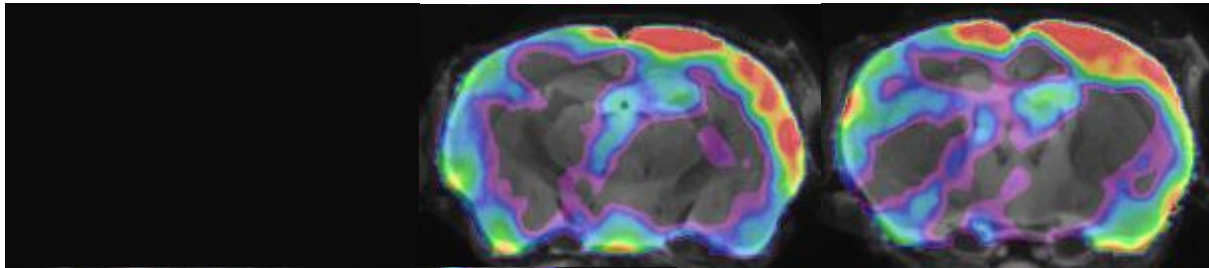
IV.5 PET/CT tracing of synapse loss

As it was previously described in this thesis, neuronal pathology and neurodegeneration are crucial processes taking place during MS progression and should be important steps targeted through therapeutic strategies. Despite the relevance of neuronal pathology in MS, our ability to distinguish when this is taking place in patients is very limited. Most MS patients undergo MRI scans to follow MS progression and lesion formation. However, MRI scans distinguish grey matter lesions based on demyelination and are unable to distinguish underlying neuronal pathology (Lublin et al., 2014). For this reason, we collaborated with the group of Dr. Matthias Brendel (Department of Nuclear Medicine, LMU), to test a PET tracer targeting synaptic vesicle glycoprotein 2a (SV2a). [18F] UCB-H is a SV2a specific tracer developed as a non-invasive method to measure synapse density in vivo (Warnock et al., 2014). SV2a is the most ubiquitously expressed of the SV2 proteins and has been shown to be expressed in excitatory and inhibitory synapses, thus, its use in tracking synaptic density (Bajjalieh et al., 1994). In our experiment, we did a baseline scan a week prior to the first immunization and following c-MS induction, we performed a second PET scan at c-MS day 3. Sham control animals were EAE induced and PBS injected (Figure 20a). This part was performed in collaboration with Lea Kunze, Laura Bartos and Carla Ares Carral. Lea Kunze and Laura Bartos performed the PET scans for the c-MS mice generated by me. Laura Bartos analyzed the PET scans. Carla Ares Carral analyzed the synaptic pathology of the c-MS mice histopathologically.

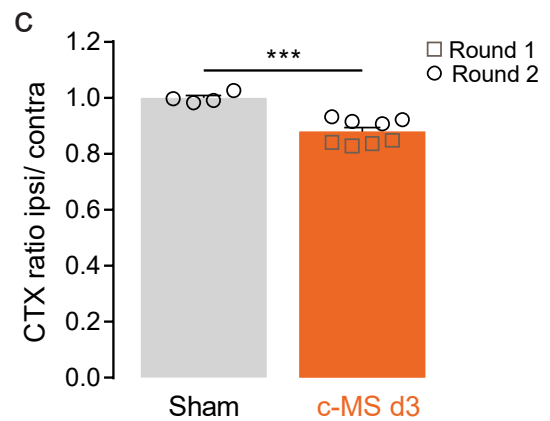
PET scan results obtained by Laura Bartos, in c-MS mice, showed a quantitative reduction of the SV2A PET signal at the cortical lesion site (SUV: 0.718 ± 0.047) when compared to sham injected controls (SUV: 0.841 ± 0.047 , $p = 0.0017$). The mirrored region of interest in the



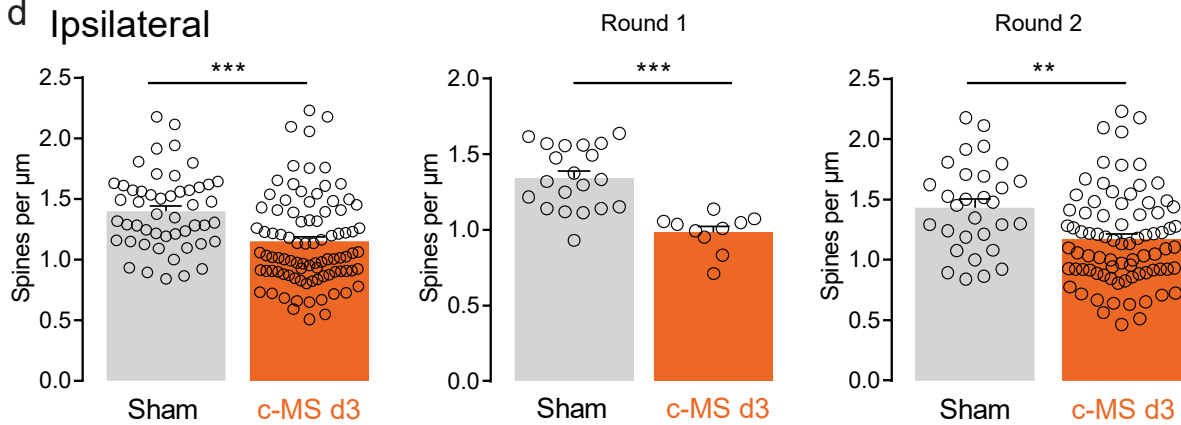
b



cortical MS vs. SHAM



d Ipsilateral



e Contralateral

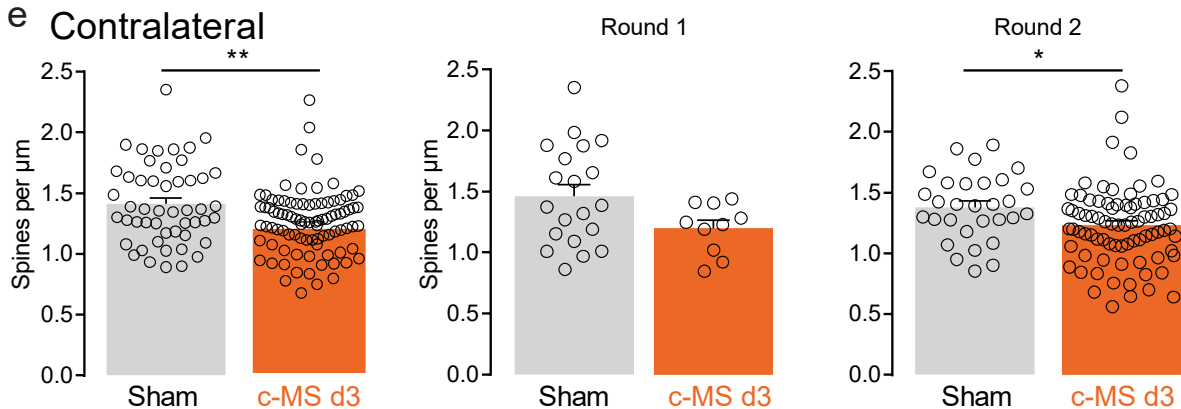


Figure 20: PET imaging with [18F] UCB-H SV2a specific tracer can distinguish synapse loss *in vivo* reminiscent of the one observed *in situ* in the c-MS model. **a)** Schematic timeline of PET imaging in the c-MS model. **b)** [18F] UCB-H uptake subtraction image showing a decrease in SUVr values in c-MS mice ipsilateral to cytokine injection compared to sham control (EAE with PBS injection) mice. Δ SUVr refers to the difference between c-MS and sham mice. **c)** Ratio between cortex ipsilateral and contralateral uptake values in c-MS d3 and sham control mice. Brown datapoints in c-MS d3 column represent round1 animals, while black data points represent round 2 animals (1:2 diluted cytokine concentration). (n=4 sham and n=8 c-MS d3 mice; mean \pm SEM; unpaired t-test). **d)** Spine density of layer V ipsilateral dendrites in c-MS d3 mice following PET imaging compared to sham control mice. Left panel shows spines from combined round 1 and round 2 mice (n=50 sham control, n=90 c-MS d3 dendritic stretches from n=5 sham control, n=9 c-MS d3 mice; mean \pm SEM; Mann-Whitney U test). Middle panel shows spines from round 1 mice (n=20 sham control, n=10 c-MS d3 dendritic stretches from n=2 sham control, n=1 c-MS d3 mice; mean \pm SEM; unpaired t-test). Right panel shows spines from round 2 mice (n=30 sham control, n=80 c-MS d3 dendritic stretches from n=3 sham control, n=8 c-MS d3 mice; mean \pm SEM; Mann-Whitney U test). **e)** Spine density of layer V contralateral dendrites in c-MS d3 mice following PET imaging compared to sham control mice. Left panel shows spines from combined round 1 and round 2 mice (n=50 sham control, n=90 c-MS d3 dendritic stretches from n=5 sham control, n=9 c-MS d3 mice; mean \pm SEM; Mann-Whitney U test). Middle panel shows spines from round 1 mice (n=20 sham control, n=10 c-MS d3 dendritic stretches from n=2 sham control, n=1 c-MS d3 mice; mean \pm SEM; unpaired t-test). Right panel shows spines from round 2 mice (n=30 sham control, n=80 c-MS d3 dendritic stretches from n=3 sham control, n=8 c-MS d3 mice; mean \pm SEM; Mann-Whitney U test). Abbreviations: c-MS: cortical MS model; dX: perfused at day X; SUVr: Standardized uptake value ratio. ***p<0.001, ** p<0.01, *p<0.05. Figure created by Emily Melisa Ullrich Gavilanes, includes data from Laura Bartos and Carla Ares Carral.

contralateral hemisphere did not show an alteration of the SV2A PET signal when comparing c-MS mice (SUV: 0.817 ± 0.030) and sham injected controls (SUV: 0.841 ± 0.049 ; p = 0.300). Importantly, the reduction of the SV2A PET signal in c-MS mice was cytokine dose dependent, showing a more pronounced signal decrease after administration of undiluted cytokine dose (SUV: 0.685 ± 0.027 , Figure 20c round 1) compared to administration of 1:2 diluted cytokines (SUV: 0.751 ± 0.039 , Figure 20c round 2). Use of the contralateral SUV for normalization of the tracer uptake at the cortical lesion site yielded higher effect sizes for the contrast of c-MS mice and sham injected controls (Figure 20b, c, p = 0.0004; Cohens d = 11.1) compared to the aforementioned SUV comparison (Cohens d = 9.0). The increase of the effect size was even higher for the comparison of cytokine doses (ratio Cohens d = 23.8 for round 1 mice vs SUV Cohens d = 5.6 for round 2 mice), speaking for improved statistical power by use of contralateral normalization. Visualization of ratio differences between c-MS and sham injected control mice at the voxel level showed a widespread reduction of SV2A PET signals in the ipsilateral cortex of the c-MS model (Figure 20b).

PET scanned mice were subsequently perfused with PBS and tissue was overnight post-fixed in 4% PFA (Figure 20a) for *in situ* spine density analysis. As animals used for the PET scan experiment were *GFP-M x BiozziABH* mice, we could reconstruct the dendrites of sparsely labelled layer V neurons as previously described (Figure 5). Spine density analysis was performed ipsilaterally (Figure 20d) as well as contralaterally (Figure 20e) to cytokine injection, presenting decreased spine density in c-MS mice compared to sham mice and was further separated in the two experimental rounds. Round 1 mice, as described above, were c-MS induced with the normal cytokine dose and presented a lower spine density ipsilaterally

than sham mice (Figure 20d). Contralaterally, round 1 mice showed a tendency to have a reduced spine density compared to sham mice, however these were non-significant (Figure 20e). A second round of the experiment was carried out with a 1:2 diluted cytokine dose. These animals presented a decreased synaptic density in PET scanning (Figure 20c), and in fixed tissue analysis (Figure 20d, e) compared to sham mice, however as expected the effect observed was less prominent than the one observed in the mice in the previous round (Figure 20e, right panel). In conclusion, the results of our PET scanning experiment with a new synapse tracer are very promising and indicate the capacity of the PET tracer to track synaptic loss to a similar magnitude than what we observed in fixed tissue analysis. This tracer could thereby become a valuable tool to track synaptic pathology in MS patients.

Chapter V: Discussion

V.1 Disease modeling of cortical MS pathology, advances and challenges

Grey matter pathology is a key process that takes place in MS, which not only drives cognitive symptoms, but also helps predict disability progression (Calabrese et al., 2012, Kutzelnigg and Lassmann, 2006). Despite grey matter pathology being such a critical process, most animal models of MS, particularly the rodent EAE models, focus mainly on the spinal cord white matter tracts (Lassmann and Bradl, 2017). Modelling of grey matter pathology has therefore required the development of new models, one of them induced through T-cell transfer of T-cells specific to β -synuclein (Lodygin et al., 2019), while most are induced by the injection of pro-inflammatory cytokines directly into the cortex of rodents, after peripheral EAE immunization (Gardner et al., 2013, Lagumersindez-Denis et al., 2017, Merkler et al., 2006). This is precisely the type of model that we adapted into mice and used throughout studies in this thesis in Figures 5-10 (Jafari et al., 2021).

We used a F1 background of *C57Bl6J* and *BiozziABH* mice due to *BiozziABH* high antibody response, and their capacity to develop a relapsing-remitting disease course (Baker et al., 1990). These mice further proved to develop cortical lesions upon i.c. injection of TNF α and IFN γ , which allowed us to model cortical grey matter pathology observed in MS patients (Haider et al., 2016, Jurgens et al., 2016, Kutzelnigg and Lassmann, 2006, Lucchinetti et al., 2011). The use of this model, in two age variants, was successful in mimicking synaptic loss (Figure 5, Figure 9b, c), demyelinating cortical lesions (Figure 6a, b, Figure 9d, e), microglial activation (Figure 6c, d, Figure 9h, j) and peripheral phagocyte infiltration in cortical lesions (Figure 6e, f, Figure 9f, g). Moreover, the two age variations of the model could prove valuable to help us further explore different disease components and interesting characteristics of the model itself.

The model induced in 8–14-week-old mice allowed us to further understand processes taking place in cortical grey matter pathology. We could observe calcium changes occurring within dendrites and spines which might prime these for removal (Figure 7). Furthermore, we could determine synaptic engulfment carried out by microglia and infiltrating phagocytes happening under neuroinflammatory conditions (Figure 8). These processes are quite interesting and should be further studied and specifically targeted due to their relation to the pathological changes taking place in the grey matter. Additionally, in our young c-MS model, we had a remarkable spontaneous resolution of inflammation (Figure 6d, f) and recovery of synaptic and demyelinating phenotypes (Figure 5h, Figure 6b, respectively) were observed to occur 2 weeks after cortical lesion induction (c-MS d14). This phenomenon might be useful to study potential recovery cues or transcriptomic signatures that are present in the mouse model at the recovery stage but not in MS patients at least at the progressive stage of the disease. Since our transcriptomics data set (Figure 11) includes mice of the c-MS d14 stage, it would be interesting to explore which pathways are being activated in our c-MS model but are not induced in the MS patient data sets (Figure 12). We could further try to boost these pathways and see if they can help rescue MS phenotypes. Thus, studying the recovery pathways in our model might be an interesting focus to consider in the future.

The model induced in middle-aged mice (10-12 months), was also appealing in its own manner. Unlike our young model, these mice presented a phenotype more consistent with chronic inflammation (Figure 9f-j), with sustained spine loss up to 84 days following lesion

induction (Figure 9b, c), and persisting demyelination (Figure 9d, e). This model can therefore be noted to more closely resemble the pathology observed in MS patients with a more progressive disease course (Kamm et al., 2014, Lucchinetti et al., 2011, Ontaneda et al., 2017). This model could thus be used to test therapies to rescue grey matter phenotypes such as remyelination boosting or neuron replacement. Additionally, this model presented an interesting phenotype that we had not previously observed in our young model, which was the formation of microglia nodules (Figure 10). Microglia nodules have been previously observed in MS patients and are thought to be early signs of lesion formation (Sato et al., 2015, Singh et al., 2013, van der Valk and Amor, 2009). We could observe that these nodules first appeared 2 weeks after lesion induction and were maintained up to day 28 following lesion induction (Figure 10b, c). Although the number of nodules decreased (Figure 10c), the size of them was maintained or even slightly increased (Figure 10b) between c-MS day 14 and c-MS day 28 which might be due to smaller nodules merging with each other, forming larger nodules over time. These nodules contain activated microglia and, due to the sustained pathology observed in our model could be hypothesized to be the source of damage that leads to the persisting demyelination and spine density decrease. This hypothesis should still be verified, of course, but could have important implications when using this model to study MS pathology or to test potential recovery therapeutic strategies.

While being a promising model that mimics different aspects of cortical grey matter neuroinflammation very well and allows further study into mechanisms and pathways (Figure 5, 6, 9, 10), limitations for our tested models also exist. For instance, the injection of cytokines directly into the brain may bias the responses and drive pathology in a specific manner. Although TNF α and IFN γ are known to be involved in MS pathology signalling and can drive inflammatory responses (Arellano et al., 2015, Fresegna et al., 2020), they are not the only signalling molecules that have been identified to play a role in MS pathogenesis (Wang et al., 2018). Therefore, responses observed in our model particularly in terms of transcriptomics analysis (Figure 10-13) might be biased towards signalling evoked by these cytokines, observed for example in the high expression of B2M and STAT1 molecules (Figure 13) known to play a role in IFN γ signalling (Hu and Ivashkiv, 2009, Hunt and Wood, 1986). These molecules might be relevant in MS but might not be able to describe the full extent of observed patient pathology, while they might describe to a large extent pathology in our c-MS model. It is therefore not surprising that we see a rescue of the synaptic phenotype upon the knockout of the *Ifngr1* through our CRISPR/Cas9 system (Suppl Figure 6g).

Further limitations exist in our model in terms of the stage of the disease that is being modelled. Patients' samples that are analyzed for pathology, omics, and *in situ* studies are generally post-mortem tissue, thus belonging to patients who most likely died due to arising complications during the advanced stage of the disease (Harding et al., 2020). Our initial c-MS induction in young animals, while being able to model lesion pathology, happens to recover spontaneously (Figure 5, 6), thereby making it hard for us to truly model the chronic inflammation and the pathways which take place in progressive MS. On the other hand, our middle-aged model (Figure 9, 10), has still not been fully characterized, and although more likely to resemble chronic MS pathology, might still not be able to fully resemble pathological events taking place in MS. On top of that, our c-MS model in middle-aged mice also presents challenges that arise from the age of the mice: first in terms of time until experimental induction (10-12 months), and second in terms of age playing a role in animals' recovery from

surgical procedures, both for c-MS induction, and in potential therapeutic testing. Surgical procedures, on their own might lead to an increased neuroinflammatory response evoked (Rosczyk et al., 2008). Furthermore, upon ageing, even healthy individuals have been observed to express markers of pathological conditions, such as brain atrophy (Elobeid et al., 2016), making our results harder to interpret as the neuroinflammatory signatures we observed might not be fully attributed to our c-MS model induction, but perhaps also to the role of ageing in these mice. While progressive MS does occur more in ageing patients (Papadopoulos et al., 2020), separating the pathological mechanisms of MS and ageing might be a complicated task when looking to target MS pathology itself.

Modelling of complex diseases such as MS has proved to be a challenging task (Williams et al., 2004). Ideally a disease model would be able to recreate the whole disease range including disease stages and the full pathology of the disease. However, this has been ineffective in MS and has been proven to be even more challenging when it comes to translating animal studies into patients (Mix et al., 2010, Williams et al., 2004). Mouse models however have still shown to be beneficial in understanding the pathology of MS as the EAE model has helped to elucidate many of the processes taking place in different MS stages (Mix et al., 2010, Steinman et al., 2023). Thus, our cortical MS model can be a valuable tool in further studies into cortical grey matter pathology taking place during neuroinflammatory conditions. Although not perfect, it can accurately mimic cortical lesion pathology of MS and can thereby be very helpful in elucidating and understanding mechanisms leading to said pathology. Using new tools that allow better translation of studies between humans and mice such as integration and mapping of omics data sets, we could further improve the insight into MS pathology and allow our model to be used as a better tool for preclinical understanding of mechanisms, and testing of therapeutic approaches.

V.2 Mapping of patients' data sets and models as a potential bridge for better mechanistic understanding and therapeutic targeting

Translation of insights from animal models to patients is one of the greatest challenges scientists encounter when investigating diseases and pathologies. Despite large number of publications on disease mechanisms based on observations in animal models, translation of these into therapies for patients has been relatively slow. One of the reasons why translation is difficult might be related to the heterogeneity that exists in human diseases which may not be fully recapitulated in the animal models (Frangogiannis, 2022). This is at least partly due to the fact that animals used for disease modelling generally have a controlled genetic background, while patients of the disease have varying genetic backgrounds which increases variability when trying to translate observations from mice to humans (Williams et al., 2004).

In order to bridge the translational gap from animals to patients, new techniques have been developed to allow more direct comparison and accessibility to data sets belonging to these groups. In the past years, omics analyses have gained popularity, and thus, there have been increasing numbers of open-source data sets available from different sources. For instance, single-cell and single nuclear RNA data sets for patients of various diseases such as MS and AD can now be easily accessed and used for further research purposes (Kaufmann et al., 2021, Mathys et al., 2019, Schirmer et al., 2019). In the same way, atlases describing single-cell sequencing for different species are continuously getting updated and made available (Bakken et al., 2021).

Leveraging the development of new technologies that have recently emerged to map data sets upon one another and to reference atlases (Kang et al., 2021), we hypothesized that mapping our c-MS data together with patient data sets would help control for the variability between them and further allow us to define candidates that have a higher translational probability. In this study we were able to successfully map our cMS data set (Figure 11), two MS patient data sets: from a collaborator (Merkler data set) and from the publicly available Schirmer et al., data set; as well as the AD ROSMAP data set from Mathys et al., to the publicly available Allen brain atlas single-cell human motor cortex data set (Bakken et al., 2021), in order to obtain overlapping neuronal clusters (Figure 12). The mapping of these data sets together allowed us to focus on conserved MS-specific genes across species, with higher potential to play a role in MS pathology. We could therefore study these genes in our model, and if they played an important role in the pathology of c-MS model, we could further use them as possible targets for MS therapy.

The mapping of the data sets worked out well in the sense that all data sets showed the same clusters containing neuronal subtypes (Figure 12), despite the size and heterogeneity that might have existed in the way data was acquired. This mapped data set then allowed us to investigate the relationships between the different data sets within it. Mapping four data sets together offered a multitude of possibilities for data analysis, but we focused on our c-MS data and its shared properties with patient data sets (Figure 13). As our model could be manipulated and further studies could be performed in it, it became our focus to analyze to which extent it was related to patient data sets and what data we could obtain from it. Indeed, we could successfully identify five differentially regulated genes that were similarly regulated between both MS patient data sets and the c-MS model, but not with our control AD data set (Figure 13). Moreover, we could show that these genes were differentially regulated in most neuronal populations rather than being specific to single neuron clusters (Suppl Figure 1-3). Higher numbers of differentially regulated genes could be identified from the single correlations; however, it was important to us to obtain a robust signature of genes that would be correlated to different patient data sets. These genes then became our basis for further analyses that we could perform to investigate mechanisms and pathways that might be involved in grey matter pathogenesis.

Even though our mapping was successful, and we accomplished our goal of finding an MS specific signature, different challenges had to be addressed throughout the different steps that were taken to get there. The first step to consider was that when mapping data sets from different species to a specific atlas, we need to convert the gene orthologs from one species into the other so they can be comparable. We converted mouse genes into their human orthologs to be able to map all subsequent data sets to the Allen brain atlas single-cell of the human motor cortex (Bakken et al., 2021). This however can bring challenges as our conversion is based on transferring names of mouse genes into those in humans. However, the overlap between gene orthologs across species is not always perfect and although genes can have the same names they do not necessarily share a conserved function (Gharib and Robinson-Rechavi, 2011). Furthermore, even if genes might have a conserved function, genes can differ in terms of temporal trajectories between species, meaning that the function they perform during specific time points in one organism might not be conserved in another (Cardoso-Moreira et al., 2020). In the next step, we mapped our data sets together to the expression in the Allen brain atlas (Bakken et al., 2021), which allowed us to compare

different neuronal subtypes. However, it is important to consider that during the mapping procedure cells or nuclei are assigned to their most closely related expression cluster based on the brain atlas specification and using these labels as a default. This labelling strategy can then lead to the exclusion of smaller neuronal subpopulations since they will be mapped to their most transcriptionally similar reference cluster (Kang et al., 2021). We further faced challenges when it came to comparing the data sets. Most data sets used for the integration are based on 10x-snrRNA-seq (c-MS model, Schirmer, Mathys), while the Merkler data set was produced through SMART-seq. Thus, the different data sets contain different sequencing depth, with the Merkler data set having less cells, however with more identified genes (Ding et al., 2020). Due to the lower sequencing depth in other data sets, compared to the Merkler one, some important genes could have been lost during our analysis, those that could only be discovered with a higher sequencing depth. In the same way, the lower number of cells used in the Merkler data set can lead to us missing subtype population effects in this data set when comparing data sets.

All things considered, mapping of data sets across species and models can be an extremely valuable tool to help scientists bridge the gap that exists when it comes to translation of studies in mouse models to patients. The ability to integrate diverse data sets coming from different sources, sequencing techniques and even species by mapping them to a reference data set is novel but will probably be more consistently used in the future due to its great potential. Up until now, researchers have focused on studying model relevant pathways and then seeing whether they played a role in disease. Tools such as single-cell reference atlas mapping allow better translatability of studies, as researchers can focus on genes and pathways that overlap between patients and disease models. Progress is still to be made in mapping systems to address concerns when it comes to orthologs, sequencing depth and the loss of small cell subtypes, however, these systems are continuously being improved and further developed.

V.3 CRISPR/Cas9 KO as a method to understand candidates, mechanisms and determine therapeutic potential of candidate genes

Since its discovery in 2012, the CRISPR/Cas9 technology has initiated a new era of gene editing research. The CRISPR/Cas9 system allows for versatility, adaptability and robustness of gene editing research and has thus been extensively utilized in recent years (Khurana et al., 2022). As such, in this thesis we aimed to establish a CRISPR/Cas9 system for neuron specific gene editing. Once established, we could utilize this system to test out previously obtained candidate genes and determine their role in grey matter pathology. To establish our system, we recreated the knockout of NeuN which was performed by Platt et al., using their sgRNA sequence (Suppl Figure 4). We were able to verify this knockout at the genomic and at the protein level (Suppl Figure 4). While knockout in neurons for NeuN was successful and could be verified in multiple levels by us but also in previous studies (Platt et al., 2014), the use of CRISPR/Cas9 has shown mixed results when targeting CNS cells. Diverse CRISPR/Cas9 studies showing success in targeting neurons have been performed in culture or at prenatal stages (Incontro et al., 2014, Straub et al., 2014). However, targeting of neurons *in vivo* at adult stages has proved to be a bigger challenge. In order to truly “validate” a knockout, validation has to be performed at the protein level. This in turn relies in the availability of good antibodies which are not available for all proteins (Nishizono et al., 2020). It is therefore to be expected that few papers have been published with successful

CRISPR/Cas9 *in vivo* in adult mice, and that they have been reliant on nuclei expressed proteins with good antibodies available (Platt et al., 2014, Swiech et al., 2015). Due to the validation problems at the protein level, in our system, we aimed to validate our knockouts at the genome (DNA) level via indel tracking and to subsequently look at the knockout in terms of RNA expression (Figures 14-17) or in terms of phenotype rescue (Suppl Figure 6).

Our CRISPR/Cas9 system was made up of two main components. The initial component was testing the sgRNA *in vitro* to analyze the efficiency of various sgRNAs in order to select the one which was more effective in generating indels (Figure 14). For this purpose, we used retroviral infection, with our sgRNA, of Cas9 expressing HoxB8 cells as our method of choice. From these cells, we could subsequently isolate genomic DNA and, following amplification of the target sequence and sequencing of this fragment, could determine indel efficiency (Figure 14). The second component of our system was the *in vivo* use of our selected sgRNA. Here we used AAV mediated targeting of neurons through the use of the php.eb capsid (Chan et al., 2017) and local injection directly into the cortex of *R26-Cas9 x BiozziABH* animals constitutively expressing Cas9 (Platt et al., 2014). We subsequently performed nuclei isolation of cortical neurons, selected those infected with our sgRNA and used them for knockout validation through genomic DNA isolation and indel efficiency analysis (Figure 15a). Once we validated knockouts at the *in vivo* level, we used the sgRNA for further evaluation purposes such as knockout RNA seq or phenotype studies.

The main purpose of our CRISPR/Cas9 system was, as previously mentioned, to test our MS specific candidates that we obtained from our snRNA-seq data sets. Knocking out these genes would allow us to understand the role they played in our c-MS pathology and to perhaps understand the mechanisms by which they acted. We first selected PSAP as a candidate and hypothesized that if we knock out this protein, thought to be neuroprotective against ferroptosis and oxidative stress (Meyer et al., 2014, Tian et al., 2021), we would be able to observe changes towards a more inflammatory or neurodegenerative signature in RNA-seq analyses. We generated sgRNA candidates, tested them *in vitro* (Figure 14), *in vivo* (Figure 15) and subsequently did RNA-seq from nuclei isolated from neurons infected with PSAP sgRNA (Figure 15-16). We could determine that our knockout was effective at the RNA level as we saw a downregulation of PSAP expression (Figure 16b, c). However, we could not detect any specific upregulated or downregulated genes that would offer us a clue to the role PSAP plays in our c-MS model or to the mechanisms that it may be involved in (Figure 16c). Next, we tried to determine whether the protective role observed for PSAP in ferroptosis, oxidative stress or against neuron death (Meyer et al., 2014, Tian et al., 2021), would be absent upon our knockout. Unfortunately, we saw neither up- nor downregulation of genes that are associated with those pathways upon PSAP KO (Figure 17). We were especially surprised by the lack of regulation of ferroptosis, as this pathway had been observed to be significantly upregulated in our c-MS mice compared to control in a module score ran in our snRNA-seq data set (Suppl Figure 5). Thus, at least based on these experiments we were unable to find evidence supporting the hypothesis that PSAP KO would exacerbate neuronal stress and damage signatures. However, it is important to consider that we have not been able to validate a PSAP KO at protein level, therefore if PSAP protein was still present at the day of nuclei isolation, any RNA signature related to it might not yet have been regulated. As neurons in our mice are at the postmitotic state, it is possible that proteins have a slow turnover, especially if like PSAP, they might be secreted and can remain in the extracellular

space for longer periods of time (Meyer et al., 2014). Furthermore, we cannot be entirely sure if PSAP would induce transcriptional regulation in itself or perhaps its absence would activate regulation pathways at the protein level only. Additionally, we might not be able to detect a PSAP KO signature as this might have been diluted by a possible contamination of our PSAP KO samples. One of the most unexpected parts of our RNA-seq results was that some of the upregulated genes in our PSAP KO were genes that have been previously linked to non-neuronal cells (Guerrero-Juarez et al., 2019). We observed gene upregulation and a high expression of genes like *Lyz2*, a marker for myeloid cells, in our PSAP KO (Figure 16c). The presence of RNA coming from a different cell type, especially when we observe them at higher counts (data not shown), provides us with the possibility that RNA from contaminating cells could dilute our PSAP KO signature and miss potential interesting transcriptomic pathways. It is thus important in the future to repeat the transcriptomic analysis for PSAP KO, reducing contamination by possibly introducing more washing steps during nuclei isolation to ensure no RNA could bind to isolated nuclei. Moreover, investigating PSAP KO on a phenotype level might provide further answers to the role PSAP plays in the c-MS model and the mechanisms it might be involved on. Finally, it would be important to verify a KO at the protein level to make sure that we are observing PSAP KO in the right timeline. In the future we plan to confirm results obtained through the CRISPR/ Cas9 mediated PSAP KO as well as to further investigate PSAP role in our c-MS model by using a F1 background of conventional *PSAP fl/fl*, recently generated (He et al., 2022), and *Biozzi ABH mice*. Altogether, this information would provide us the ability to discern whether PSAP would be a promising therapeutic target for MS grey matter pathology.

Our second target from the snRNA-seq data set for targeting was B2M. Due to the induction of B2M as a response to IFN γ (Hunt and Wood, 1986), we aimed to target this protein indirectly by instead targeting the *Ifngr1*. With an *Ifngr1* KO, we further wanted to explore whether we could see changes in phenotypes observed in our c-MS model such as spine loss (Figure 5). We once again tested our knockout *in vitro* and *in vivo* (Suppl Figure 6a-c) and then used a system to generate a *Ifngr1* knockout in neurons of the somatosensory cortex, while having an endogenous control within the same animal and slightly lateral location, with an NT sgRNA co-injection (Suppl Figure 6d-h). Our system worked well in c-MS mice where we saw an increase in spine density in our *Ifngr1* KO mice compared to the NT mice (Suppl Figure 6g). However, our healthy control mice presented a reduced spine density comparable to the NT mice (Suppl Figure 6g). We believe that the virus injection in the healthy mice induced an inflammatory reaction, probably due to the virus production method, where other low kDA proteins and messengers released into the media of packaging cells could have been carried on. This problem was probably not observed in the c-MS mice due to the inflammation induced there by the model and probable resolution with the help of the more active immune system. A cleaner virus purification method would therefore solve this problem and allow us to verify whether the phenotype rescue indeed occurs. However, the phenotype rescue would be expected due to the induction of the model by intracortical injection of IFN γ and the effects of this knockout should therefore be analyzed more carefully.

Throughout this thesis, we established and used a CRISPR/Cas9 system in neurons to attempt to determine mechanisms playing role in grey matter pathology. Although the system was shown to work at the genomic level via successful indel induction, which was shown to be a good precursor for protein level knockout (Swiech et al., 2015), we had a hard time

validating it at the protein level besides NeuN. Both of our selected candidate genes for KO (PSAP and *lfng1*) did not have good antibodies for immunohistochemistry analyses, and while there has been good *lfng1* FACS antibodies, neuron isolation, due to their morphology, is a complicated process to obtain single cells for FACS (Grindberg et al., 2013, Swiech et al., 2015). We therefore relied in phenotype observations and RNA-seq analysis from nuclei to determine whether our KO worked. However, we are not fully aware if any remaining protein might still exist in neurons and would influence our results. Furthermore, by using nuclei only for our analysis, we lose any signals from mRNA regulations that are occurring elsewhere on neurons. Neurons can induce translation in dendrites, which requires transport of mRNA to these compartments (Eberwine et al., 2001). Regulation at these compartments would not be noticed through our analysis of nuclei-based mRNA. We also need to consider that many pathways in neurons are regulated by signals released by glial cells (Tasker et al., 2012). Our *php.eb* capsid has been described to also target astrocytes (Chan et al., 2017), and due to the use of an RNA promoter for the sgRNA expression, it is likely that some astrocytes have also been infected and could suffer the protein knockout. These could also influence the results obtained via our knockout experiments and should be properly addressed in further control experiments.

The use of CRISPR/Cas9 in neuronal populations is a process that requires continuous work to address all potential problems that may arise when using it. Despite potential complications that stem while setting up this method, we are convinced that once proven to work it will play a big role in understanding gene function in the brain as it is has in other tissues (Tschaharganeh et al., 2016). The CRISPR/Cas9 system can thenceforth play a role in understanding genes and their respective function, as well as in determining whether these genes can be used as therapeutic targets.

V.4 Microglia phagocytosis blocking and its potentials in neuroinflammation

Compared to the large number of treatments approved for RRMS, few, if any, effective therapeutic options are available for progressive MS therapy. Emerging therapies tested nowadays therefore aim to target neuroprotection and repair promoting strategies rather than anti-inflammatory targeting (Chataway et al., 2014, Ontaneda et al., 2017). In our c-MS model, we could observe that the immune system plays an important role in pathogenesis of grey matter pathology as an increased activation of microglia and number of infiltrating immune cells (Figure 6) was found. These immune cells further play a role in the uptake of synaptic components (Figure 8). It thus became interesting for us to test whether treatment of our c-MS mice with small molecules designed to modulate microglia activation would help prevent phenotypes observed during grey matter neuroinflammation. We used two main treatments for this purpose, a CSF1R inhibitor and a BTK inhibitor.

CSF1R is the receptor that modulates CSF1 signaling, necessary for microglia viability (Elmore et al., 2014). CSF1R inhibitors have different roles depending on their concentration. At higher concentrations the inhibitor depletes microglia cells, while at lower concentrations it inhibits microglial proliferation and attenuate some of their damage associated phenotypes (Dagher et al., 2015, Hagan et al., 2020, Nissen et al., 2018, Olmos-Alonso et al., 2016). CSF1R inhibition has previously been shown to be effective in reducing microglia proliferation and association with A β plaques in AD mouse models, thereby improving their performance in cognition, memory tasks and preventing synaptic degeneration (Dagher et al., 2015,

Olmos-Alonso et al., 2016). Thus, we tested a CSF1R inhibitor in our c-MS model as a potential method to ameliorate the grey matter pathology (Figure 5-8). The inhibition of CSF1R showed very promising results as a rescue of spine density and calcium accumulation in spines was observed (Figure 18b-e). Furthermore, we saw a decrease in infiltrating cells, decreased uptake of synaptic components from phagocytic cells and a decreased lysosomal volume within phagocytes (Figure 18f-i). Moreover, we did not observe changes in microglia number, which was previously described in AD models (Olmos-Alonso et al., 2016). However, this might be a result of the inhibitor concentration used in our c-MS model or on the inhibitor that was used itself. CSF1R inhibitor, in our c-MS model, was shown to ameliorate c-MS grey matter pathology compared to vehicle and could be a good therapeutic strategy in MS.

We further explored a second treatment that modulates microglial properties, the BTK inhibitor. BTK is an enzyme that helps regulate microglial phagocytic activity. Just like with the CSF1R inhibitor, inhibition of BTK has demonstrated a decrease synapse uptake in AD (Keaney et al., 2019). Based on this observation, we tested whether the BTK inhibitor would lead to an amelioration of the synaptic spine phenotype in c-MS. Treatment with BTK inhibitor, however, proved unsuccessful as treated mice showed no protection against spine loss compared to vehicle-treated controls (Figure 19). It is possible that our treatment strategy was unsuccessful with the BTK inhibitor being applied the day of lesion induction and earlier treatment might be able to rescue the phenotype. On the other hand, it is also probable that the application of BTK would not have an effect in the c-MS model itself due to the way the model is induced, or the way pathology is formed. Even though we did not see any results with our c-MS model, BTK inhibitors have made progress in MS treatment with multiple variations having reached late-stage clinical trials. BTK inhibitors, in the way that they are used in clinical trials, act as a drug that blocks B-cell maturation while also modulating macrophage and microglia activity (Dolgin, 2021).

Therapeutic strategies to modulate the immune system could be crucial in targeting progressive MS and grey matter pathology. CSF1R inhibitor treatment of our c-MS mice showed promise in rescuing the neuronal pathology that was observed upon lesion induction (Figure 18). Therefore, we suggest that CSF1R inhibition at lower doses could be a potential therapy targeting grey matter pathology of MS, due to its effect in the peripheral and CNS-resident response of phagocytic cells. Based on our results, we propose that progressive MS grey matter pathology could benefit from immunomodulatory therapies focused on the CNS as a mechanism to prevent its progression.

V.5 PET tracing as means to track MS progression but also to define good therapeutic administration time points

Synapse loss is a widespread process that has been described in various CNS regions in multiple studies conducted on post-mortem tissue of MS patients (Dutta et al., 2011, Jurgens et al., 2016, Michailidou et al., 2015, Papadopoulos et al., 2009, Petrova et al., 2020, Vercellino et al., 2022, Wegner et al., 2006, Werneburg et al., 2020, Zoupi et al., 2021). In other neuroinflammatory conditions, it is estimated that the extent of synapse loss predicts the extent of patient disability (DeKosky et al., 1996, Hasbani, 2000, Terry et al., 1991). Thus, synapse loss should be considered an important component in progressive MS disability accrual.

Diagnosis of MS is usually performed through a combination of clinical symptoms with input from imaging studies, usually MRI confirmation of demyelinating lesions (Filippi et al., 2018, Lublin et al., 2014, Ontaneda et al., 2017). MRI imaging is then subsequently carried on continuously in MS patients due to its high-sensitivity for detection of demyelinating lesions, and consequently for its ability to track disease progression based on lesion formation (Filippi et al., 2018, Lublin et al., 2014, Traboulsee and Li, 2006). However, while MRI can help predict stages of the disease, it is not able to fully recapitulate the pathological features that are taking place at a particular moment in time for a patient. PET imaging can help tackle this problem through the use of radiotracers that can bind to diverse biologically active compounds in different cells, such as glial cells, and thus provide a snapshot of different components of the pathology unravelling at a specific time (Debruyne et al., 2003, Oh et al., 2011). Since the spatial resolution of PET has been improved by the use of PET-CT (Beyer et al., 2000, Vaquero and Kinahan, 2015) or PET-MRI methods (Al-Nabhani et al., 2014, Vaquero and Kinahan, 2015), it has become an even more valuable tool based on the versatility that comes with various tracer development. Hence, we propose the utilization of PET tracer [18F] UCB-H, a SV2a specific tracer, as a new method to track synaptic pathology in MS patients.

In order to examine the accuracy of [18F] UCB-H, we tested this tracer in our c-MS model, which exhibits a decrease in spine density in the peak of acute inflammation (c-MS day 3) following lesion induction (Figure 5). We compared the ipsilateral side (cytokine injection side) to the contralateral side as means of normalization for PET scanning (Figure 20). As a control, we used sham mice which were EAE induced and PBS-injected on the same day as c-MS mice were cytokine injected. We effectively saw a decrease in synapses, measured both through PET and through our *in situ* analysis of tissue fixed following the PET scan, in c-MS mice compared to sham mice (Figure 20). This in turn, is consistent with the view that the [18F] UCB-H tracer has a high specificity for SV2a binding and recreated our previous observations. Furthermore, we performed this experiment in two rounds, round one with normal induction of our c-MS model and round two where the c-MS model was induced with a lower cytokine concentration (1:2 diluted), which could be clearly differentiated in c-MS mice but not in sham mice through PET imaging (Figure 20c) and immunohistochemistry analysis (Figure 20d-e). Additional studies *in situ* to stain and correlate SV2a expression to the one observed *in vivo* should provide added support to the results obtained, since synaptic loss quantification between both methods cannot be directly correlated. Despite drawbacks that could ensue due to the limitation of spatial resolution or sensitivity in small animal PET studies (Du and Jones, 2023), we were still able to notice a significant change in PET imaging, reflecting of synaptic pathology observed *in situ*; further substantiating the high sensitivity of the SV2a tracer. The [18F] UCB-H tracer results observed were therefore very promising within our c-MS mice and suggest that this tracer can be used in MS patients to determine their extent of synaptic loss. The availability of a tracer such as the [18F] UCB-H SV2a specific tracer, could have a substantial impact for MS patients, as doctors would not only be able to distinguish the extent of synaptic loss that is taking place, but also could use the Sv2a PET as a read out parameter in clinical trials targeting progressive MS. Timing has been determined as a crucial component in therapy determining the long-term outcomes of patients in MS (Merkel et al., 2017). Thus, utilization of [18F] UCB-H could provide benefits for patients in multiple fronts: disease tracking, determination of time points for therapeutic intervention and follow up of the impact of therapeutic treatment. Based on our results, we

propose that the [18F] UCB-H SV2a tracer should be further explored in clinical studies as MS patients would benefit greatly from imaging that could determine the extent of grey matter pathology.

V.6 Concluding remarks

Taken together, the results of this thesis provided a characterization of two mouse models for cortical grey matter pathology of MS and subsequent use of these models for further understanding of underlying neuropathology as well as for testing of treatments and of PET tracers. Both mouse models with different aged animals, were able to mimic MS pathology in terms of demyelination, inflammation and spine loss. Further analysis showed a potential connection between increased calcium, synapse loss and immune cell phagocytosis of synapses. These observations were used as a basis for further studies into neuron pathology and the aim to understand processes taking place in neurons via transcriptomic analysis. While performing transcriptomic analysis, we aimed to investigate translatable processes relevant to our model and to MS pathology and therefore we mapped MS patient data sets and our c-MS model data set to a common reference data set derived from the healthy human cortex. We further defined MS specificity of our selected genes by using an AD data set and excluding genes that would be differentially expressed in both diseases. The identification of MS specific highly regulated genes that overlapped with our model then aided in our selection of candidates that could be used to further investigate grey matter pathology. Using CRISPR/Cas9 mediated knockout, we targeted two of our candidate genes and attempted to understand their role through transcriptomic and phenotypic analyses. Although, we could not pinpoint the particular role these genes play, we hypothesize that they do play a role in cortical grey matter pathology and that further analysis at perhaps different time points could be better to elucidate their mechanisms. PSAP has been described to play a role as a neuroprotective molecule against oxidative stress, ferroptosis and cell death (Meyer et al., 2014, Tian et al., 2021). As such, it could have a potential protective role in our c-MS model which might start at the peak of inflammation but might have a higher impact later on when the grey matter pathology starts to recover. CRISPR/Cas9 mediated KO can be a very valuable tool for understanding mechanisms and determining therapeutic candidates for MS.

Further therapeutic strategies tested in our model included targeting microglial activation and phagocytosis. Targeting of microglial activation and phagocytosis through a CSF1R-inhibitor proved to be successful in preventing or rescuing pathology. All together the strategies tested could be used to target different components of progressive MS pathology and prevent disease progression.

The work on this thesis was highly focused on translatable approaches to study and treat MS. While early results in this thesis focus on trying to understand the grey matter pathology of MS and treat it, the approach with the most immediate potential for translation was the testing of the SV2a [18F] UCB-H PET tracer. This tracer showed high sensitivity in detecting synaptic changes in our model and could therefore be employed to observe synaptic pathology in MS patients.

Results obtained throughout my PhD work and shown in this thesis could thus be an important step in understanding MS pathology and both models characterized could in turn be valuable for assessing novel treatments or diagnostic strategies.

Chapter VI: References

1993. Interferon beta-1b is effective in relapsing-remitting multiple sclerosis. I. Clinical results of a multicenter, randomized, double-blind, placebo-controlled trial. The IFNB Multiple Sclerosis Study Group. *Neurology*, 43, 655-61.
1998. Placebo-controlled multicentre randomised trial of interferon beta-1b in treatment of secondary progressive multiple sclerosis. European Study Group on interferon beta-1b in secondary progressive MS. *Lancet*, 352, 1491-7.
- ABUDAYYEH, O. O., GOOTENBERG, J. S., ESSLETZBICHLER, P., HAN, S., JOUNG, J., BELANTO, J. J., VERDINE, V., COX, D. B. T., KELLNER, M. J., REGEV, A., LANDER, E. S., VOYTAS, D. F., TING, A. Y. & ZHANG, F. 2017. RNA targeting with CRISPR-Cas13. *Nature*, 550, 280-284.
- AL-NABHANI, K. Z., SYED, R., MICHOPPOULOU, S., ALKALBANI, J., AFAQ, A., PANAGIOTIDIS, E., O'MEARA, C., GROVES, A., ELL, P. & BOMANJI, J. 2014. Qualitative and quantitative comparison of PET/CT and PET/MR imaging in clinical practice. *J Nucl Med*, 55, 88-94.
- ALAWIEH, A. M., LANGLEY, E. F., FENG, W., SPIOTTA, A. M. & TOMLINSON, S. 2020. Complement-Dependent Synaptic Uptake and Cognitive Decline after Stroke and Reperfusion Therapy. *J Neurosci*, 40, 4042-4058.
- ALBERT, M., BARRANTES-FREER, A., LOHRBERG, M., ANTEL, J. P., PRINEAS, J. W., PALKOVITS, M., WOLFF, J. R., BRUCK, W. & STADELMANN, C. 2017. Synaptic pathology in the cerebellar dentate nucleus in chronic multiple sclerosis. *Brain Pathol*, 27, 737-747.
- ALTER, M., LEIBOWITZ, U. & SPEER, J. 1966. Risk of multiple sclerosis related to age at immigration to Israel. *Arch Neurol*, 15, 234-7.
- ANDERS, S., PYL, P. T. & HUBER, W. 2015. HTSeq--a Python framework to work with high-throughput sequencing data. *Bioinformatics*, 31, 166-9.
- ANDERSEN, O., ELOVAARA, I., FARKKILA, M., HANSEN, H. J., MELLGREN, S. I., MYHR, K. M., SANDBERG-WOLLHEIM, M. & SOELBERG SORENSEN, P. 2004. Multicentre, randomised, double blind, placebo controlled, phase III study of weekly, low dose, subcutaneous interferon beta-1a in secondary progressive multiple sclerosis. *J Neurol Neurosurg Psychiatry*, 75, 706-10.
- ANTONIOU, P., MICCIO, A. & BRUSSON, M. 2021. Base and Prime Editing Technologies for Blood Disorders. *Front Genome Ed*, 3, 618406.
- ARELLANO, G., OTTUM, P. A., REYES, L. I., BURGOS, P. I. & NAVES, R. 2015. Stage-Specific Role of Interferon-Gamma in Experimental Autoimmune Encephalomyelitis and Multiple Sclerosis. *Front Immunol*, 6, 492.
- BAJJALIEH, S. M., FRANTZ, G. D., WEIMANN, J. M., MCCONNELL, S. K. & SCHELLER, R. H. 1994. Differential expression of synaptic vesicle protein 2 (SV2) isoforms. *J Neurosci*, 14, 5223-35.
- BAKER, D., O'NEILL, J. K., GSCHMEISSNER, S. E., WILCOX, C. E., BUTTER, C. & TURK, J. L. 1990. Induction of chronic relapsing experimental allergic encephalomyelitis in Biozzi mice. *J Neuroimmunol*, 28, 261-70.
- BAKKEN, T. E., HODGE, R. D., MILLER, J. A., YAO, Z., NGUYEN, T. N., AEVERMANN, B., BARKAN, E., BERTAGNOLLI, D., CASPER, T., DEE, N., GARREN, E., GOLDY, J., GRAYBUCK, L. T., KROLL, M., LASKEN, R. S., LATHIA, K., PARRY, S., RIMORIN, C., SCHEUERMANN, R. H., SCHORK, N. J., SHEHATA, S. I., TIEU, M., PHILLIPS, J. W., BERNARD, A., SMITH, K. A., ZENG, H., LEIN, E. S. & TASIC, B. 2018. Single-nucleus and single-cell transcriptomes compared in matched cortical cell types. *PLoS One*, 13, e0209648.
- BAKKEN, T. E., JORSTAD, N. L., HU, Q., LAKE, B. B., TIAN, W., KALMBACH, B. E., CROW, M., HODGE, R. D., KRIENEN, F. M., SORENSEN, S. A., EGGERMONT, J., YAO, Z., AEVERMANN, B. D., ALDRIDGE, A. I., BARTLETT, A., BERTAGNOLLI, D., CASPER, T., CASTANON, R. G., CRICHTON, K., DAIGLE, T. L., DALLEY, R., DEE, N., DEMBROW, N., DIEP, D., DING, S. L., DONG, W., FANG, R., FISCHER, S., GOLDMAN, M., GOLDY, J., GRAYBUCK, L. T., HERB, B. R., HOU, X., KANCHERLA, J., KROLL, M., LATHIA, K., VAN LEW, B., LI, Y. E., LIU, C. S., LIU, H., LUCERO, J. D., MAHURKAR, A., MCMILLEN, D., MILLER, J. A., MOUSSA, M., NERY, J. R., NICOVICH, P. R., NIU, S. Y., ORVIS, J., OSTEEEN, J. K., OWEN, S., PALMER, C. R., PHAM, T., PLONGTHONGKUM, N., POIRION, O., REED, N. M., RIMORIN, C., RIVKIN, A., ROMANOW, W. J.,

- SEDENO-CORTES, A. E., SILETTI, K., SOMASUNDARAM, S., SULC, J., TIEU, M., TORKELESON, A., TUNG, H., WANG, X., XIE, F., YANNY, A. M., ZHANG, R., AMENT, S. A., BEHRENS, M. M., BRAVO, H. C., CHUN, J., DOBIN, A., GILLIS, J., HERTZANO, R., HOF, P. R., HOLLT, T., HORWITZ, G. D., KEENE, C. D., KHARCHENKO, P. V., KO, A. L., LELIEVELDT, B. P., LUO, C., MUKAMEL, E. A., PINTO-DUARTE, A., PREISSEL, S., REGEV, A., REN, B., SCHEUERMANN, R. H., SMITH, K., SPAIN, W. J., WHITE, O. R., KOCH, C., HAWRYLYCZ, M., TASIC, B., MACOSKO, E. Z., MCCARROLL, S. A., TING, J. T., et al. 2021. Comparative cellular analysis of motor cortex in human, marmoset and mouse. *Nature*, 598, 111-119.
- BARANZINI, S. E. & OKSENBERG, J. R. 2017. The Genetics of Multiple Sclerosis: From 0 to 200 in 50 Years. *Trends Genet*, 33, 960-970.
- BATRA, R., NELLES, D. A., PIRIE, E., BLUE, S. M., MARINA, R. J., WANG, H., CHAIM, I. A., THOMAS, J. D., ZHANG, N., NGUYEN, V., AIGNER, S., MARKMILLER, S., XIA, G., CORBETT, K. D., SWANSON, M. S. & YEO, G. W. 2017. Elimination of Toxic Microsatellite Repeat Expansion RNA by RNA-Targeting Cas9. *Cell*, 170, 899-912 e10.
- BELLIZZI, M. J., GEATHERS, J. S., ALLAN, K. C. & GELBARD, H. A. 2016. Platelet-Activating Factor Receptors Mediate Excitatory Postsynaptic Hippocampal Injury in Experimental Autoimmune Encephalomyelitis. *J Neurosci*, 36, 1336-46.
- BEN-NUN, A., WEKERLE, H. & COHEN, I. R. 1981. The rapid isolation of clonable antigen-specific T lymphocyte lines capable of mediating autoimmune encephalomyelitis. *Eur J Immunol*, 11, 195-9.
- BEYER, T., TOWNSEND, D. W., BRUN, T., KINAHAN, P. E., CHARRON, M., RODDY, R., JERIN, J., YOUNG, J., BYARS, L. & NUTT, R. 2000. A combined PET/CT scanner for clinical oncology. *J Nucl Med*, 41, 1369-79.
- BJORNEVIK, K., CORTESE, M., HEALY, B. C., KUHLE, J., MINA, M. J., LENG, Y., ELLEDGE, S. J., NIEBUHR, D. W., SCHER, A. I., MUNGER, K. L. & ASCHERIO, A. 2022. Longitudinal analysis reveals high prevalence of Epstein-Barr virus associated with multiple sclerosis. *Science*, 375, 296-301.
- BOVE, R. & CHITNIS, T. 2013. Sexual disparities in the incidence and course of MS. *Clin Immunol*, 149, 201-10.
- BOVE, R. & CHITNIS, T. 2014. The role of gender and sex hormones in determining the onset and outcome of multiple sclerosis. *Mult Scler*, 20, 520-6.
- BRENDEL, M., PROBST, F., JAWORSKA, A., OVERHOFF, F., KORZHOVA, V., ALBERT, N. L., BECK, R., LINDNER, S., GILDEHAUS, F. J., BAUMANN, K., BARTENSTEIN, P., KLEINBERGER, G., HAASS, C., HERMS, J. & ROMINGER, A. 2016. Glial Activation and Glucose Metabolism in a Transgenic Amyloid Mouse Model: A Triple-Tracer PET Study. *J Nucl Med*, 57, 954-60.
- BRINKMAN, E. K., CHEN, T., AMENDOLA, M. & VAN STEENSEL, B. 2014. Easy quantitative assessment of genome editing by sequence trace decomposition. *Nucleic Acids Res*, 42, e168.
- BRONNUM-HANSEN, H., KOCH-HENRIKSEN, N. & STENAGER, E. 2004. Trends in survival and cause of death in Danish patients with multiple sclerosis. *Brain*, 127, 844-50.
- BURROWS, D. J., MCGOWN, A., JAIN, S. A., DE FELICE, M., RAMESH, T. M., SHARRACK, B. & MAJID, A. 2019. Animal models of multiple sclerosis: From rodents to zebrafish. *Mult Scler*, 25, 306-324.
- BUTLER, A., HOFFMAN, P., SMIBERT, P., PAPALEXI, E. & SATIJA, R. 2018. Integrating single-cell transcriptomic data across different conditions, technologies, and species. *Nat Biotechnol*, 36, 411-420.
- CAGNOLI, P. C., SUNDGREN, P. C., KAIRYS, A., GRAFT, C. C., CLAUW, D. J., GEBARSKI, S., MCCUNE, W. J. & SCHMIDT-WILCKE, T. 2012. Changes in regional brain morphology in neuropsychiatric systemic lupus erythematosus. *J Rheumatol*, 39, 959-67.
- CALABRESE, M., PORETTO, V., FAVARETTO, A., ALESSIO, S., BERNARDI, V., ROMUALDI, C., RINALDI, F., PERINI, P. & GALLO, P. 2012. Cortical lesion load associates with progression of disability in multiple sclerosis. *Brain*, 135, 2952-61.
- CARDOSO-MOREIRA, M., SARROPOULOS, I., VELTEN, B., MORT, M., COOPER, D. N., HUBER, W. & KAESMANN, H. 2020. Developmental Gene Expression Differences between Humans and Mammalian Models. *Cell Rep*, 33, 108308.
- CARDOZO, P. L., DE LIMA, I. B. Q., MACIEL, E. M. A., SILVA, N. C., DOBRANSKY, T. & RIBEIRO, F. M. 2019. Synaptic Elimination in Neurological Disorders. *Curr Neuropharmacol*, 17, 1071-1095.

- CARLTON, W. W. 1966. Response of mice to the chelating agents sodium diethyldithiocarbamate, alpha-benzoinoxime, and biscyclohexanone oxaldihydrazone. *Toxicol Appl Pharmacol*, 8, 512-21.
- CARSWELL, R. 1838. *Pathological anatomy: illustrations of the elementary forms of disease*, London, Longman, Orme, Brown, Green and Longman.
- CHAN, K. Y., JANG, M. J., YOO, B. B., GREENBAUM, A., RAVI, N., WU, W. L., SANCHEZ-GUARDADO, L., LOIS, C., MAZMANIAN, S. K., DEVERMAN, B. E. & GRADINARU, V. 2017. Engineered AAVs for efficient noninvasive gene delivery to the central and peripheral nervous systems. *Nat Neurosci*, 20, 1172-1179.
- CHANGEUX, J. P. & DANCHIN, A. 1976. Selective stabilisation of developing synapses as a mechanism for the specification of neuronal networks. *Nature*, 264, 705-12.
- CHATAWAY, J., SCHUERER, N., ALSANOUSI, A., CHAN, D., MACMANUS, D., HUNTER, K., ANDERSON, V., BANGHAM, C. R., CLEGG, S., NIELSEN, C., FOX, N. C., WILKIE, D., NICHOLAS, J. M., CALDER, V. L., GREENWOOD, J., FROST, C. & NICHOLAS, R. 2014. Effect of high-dose simvastatin on brain atrophy and disability in secondary progressive multiple sclerosis (MS-STAT): a randomised, placebo-controlled, phase 2 trial. *Lancet*, 383, 2213-21.
- COHEN, J. A., CUTTER, G. R., FISCHER, J. S., GOODMAN, A. D., HEIDENREICH, F. R., KOOIJMANS, M. F., SANDROCK, A. W., RUDICK, R. A., SIMON, J. H., SIMONIAN, N. A., TSAO, E. C., WHITAKER, J. N. & INVESTIGATORS, I. 2002. Benefit of interferon beta-1a on MSFC progression in secondary progressive MS. *Neurology*, 59, 679-87.
- CONANT, D., HSIAU, T., ROSSI, N., OKI, J., MAURES, T., WAITE, K., YANG, J., JOSHI, S., KELSO, R., HOLDEN, K., ENZMANN, B. L. & STONER, R. 2022. Inference of CRISPR Edits from Sanger Trace Data. *CRISPR J*, 5, 123-130.
- CONFAVREUX, C., VUKUSIC, S. & ADELEINE, P. 2003. Early clinical predictors and progression of irreversible disability in multiple sclerosis: an amnesic process. *Brain*, 126, 770-82.
- CONSTANTINESCU, C. S., FAROOQI, N., O'BRIEN, K. & GRAN, B. 2011. Experimental autoimmune encephalomyelitis (EAE) as a model for multiple sclerosis (MS). *Br J Pharmacol*, 164, 1079-106.
- COULOUME, L., BARBIN, L., LERAY, E., WIERTLEWSKI, S., LE PAGE, E., KERBRAT, A., ORY, S., LE PORT, D., EDAN, G., LAPLAUD, D. A. & MICHEL, L. 2020. High-dose biotin in progressive multiple sclerosis: A prospective study of 178 patients in routine clinical practice. *Mult Scler*, 26, 1898-1906.
- COX, D. B., PLATT, R. J. & ZHANG, F. 2015. Therapeutic genome editing: prospects and challenges. *Nat Med*, 21, 121-31.
- CRADDOCK, J. & MARKOVIC-PLESE, S. 2015. Immunomodulatory therapies for relapsing-remitting multiple sclerosis: monoclonal antibodies, currently approved and in testing. *Expert Rev Clin Pharmacol*, 8, 283-96.
- CRAMER, S. P., SIMONSEN, H., FREDERIKSEN, J. L., ROSTRUP, E. & LARSSON, H. B. 2014. Abnormal blood-brain barrier permeability in normal appearing white matter in multiple sclerosis investigated by MRI. *Neuroimage Clin*, 4, 182-9.
- DAGHER, N. N., NAJAFI, A. R., KAYALA, K. M., ELMORE, M. R., WHITE, T. E., MEDEIROS, R., WEST, B. L. & GREEN, K. N. 2015. Colony-stimulating factor 1 receptor inhibition prevents microglial plaque association and improves cognition in 3xTg-AD mice. *J Neuroinflammation*, 12, 139.
- DAUER, W. & PRZEDBORSKI, S. 2003. Parkinson's disease: mechanisms and models. *Neuron*, 39, 889-909.
- DEAN, G. & KURTZKE, J. F. 1971. On the risk of multiple sclerosis according to age at immigration to South Africa. *Br Med J*, 3, 725-9.
- DEBRUYNE, J. C., VERSIJPT, J., VAN LAERE, K. J., DE VOS, F., KEPPENS, J., STRIJCKMANS, K., ACHTEN, E., SLEGGERS, G., DIERCKX, R. A., KORF, J. & DE REUCK, J. L. 2003. PET visualization of microglia in multiple sclerosis patients using [11C]PK11195. *Eur J Neurol*, 10, 257-64.
- DEKOSKY, S. T., SCHEFF, S. W. & STYREN, S. D. 1996. Structural correlates of cognition in dementia: quantification and assessment of synapse change. *Neurodegeneration*, 5, 417-21.
- DELTCHEVA, E., CHYLINSKI, K., SHARMA, C. M., GONZALES, K., CHAO, Y., PIRZADA, Z. A., ECKERT, M. R., VOGEL, J. & CHARPENTIER, E. 2011. CRISPR RNA maturation by trans-encoded small RNA and host factor RNase III. *Nature*, 471, 602-7.

- DI LIBERTO, G., PANTELYUSHIN, S., KREUTZFELDT, M., PAGE, N., MUSARDO, S., CORAS, R., STEINBACH, K., VINCENTI, I., KLIMEK, B., LINGNER, T., SALINAS, G., LIN-MARQ, N., STASZEWSKI, O., COSTA JORDAO, M. J., WAGNER, I., EGERVARI, K., MACK, M., BELLONE, C., BLUMCKE, I., PRINZ, M., PINSCHER, D. D. & MERKLER, D. 2018. Neurons under T Cell Attack Coordinate Phagocyte-Mediated Synaptic Stripping. *Cell*, 175, 458-471 e19.
- DIEZ, J., WALTER, D., MUNOZ-PINEDO, C. & GABALDON, T. 2010. DeathBase: a database on structure, evolution and function of proteins involved in apoptosis and other forms of cell death. *Cell Death Differ*, 17, 735-6.
- DING, J., ADICONIS, X., SIMMONS, S. K., KOWALCZYK, M. S., HESSION, C. C., MARJANOVIC, N. D., HUGHES, T. K., WADSWORTH, M. H., BURKS, T., NGUYEN, L. T., KWON, J. Y. H., BARAK, B., GE, W., KEDAIGLE, A. J., CARROLL, S., LI, S., HACOEN, N., ROZENBLATT-ROSEN, O., SHALEK, A. K., VILLANI, A. C., REGEV, A. & LEVIN, J. Z. 2020. Systematic comparison of single-cell and single-nucleus RNA-sequencing methods. *Nat Biotechnol*, 38, 737-746.
- DOBIN, A., DAVIS, C. A., SCHLESINGER, F., DRENKOW, J., ZALESKI, C., JHA, S., BATUT, P., CHAISSON, M. & GINGERAS, T. R. 2013. STAR: ultrafast universal RNA-seq aligner. *Bioinformatics*, 29, 15-21.
- DOLGIN, E. 2021. BTK blockers make headway in multiple sclerosis. *Nat Biotechnol*, 39, 3-5.
- DU, J. & JONES, T. 2023. Technical opportunities and challenges in developing total-body PET scanners for mice and rats. *EJNMMI Phys*, 10, 2.
- DURINCK, S., SPELLMAN, P. T., BIRNEY, E. & HUBER, W. 2009. Mapping identifiers for the integration of genomic datasets with the R/Bioconductor package biomaRt. *Nat Protoc*, 4, 1184-91.
- DUTTA, R., CHANG, A., DOUD, M. K., KIDD, G. J., RIBAUDO, M. V., YOUNG, E. A., FOX, R. J., STAUGAITIS, S. M. & TRAPP, B. D. 2011. Demyelination causes synaptic alterations in hippocampi from multiple sclerosis patients. *Ann Neurol*, 69, 445-54.
- DUTTA, R. & TRAPP, B. D. 2007. Pathogenesis of axonal and neuronal damage in multiple sclerosis. *Neurology*, 68, S22-31; discussion S43-54.
- EBERWINE, J., MIYASHIRO, K., KACHARMINA, J. E. & JOB, C. 2001. Local translation of classes of mRNAs that are targeted to neuronal dendrites. *Proc Natl Acad Sci U S A*, 98, 7080-5.
- ECCLES, R. M., LOYNING, Y. & OSHIMA, T. 1966. Effects of hypoxia on the monosynaptic reflex pathway in the cat spinal cord. *J Neurophysiol*, 29, 315-31.
- EISENER-DORMAN, A. F., LAWRENCE, D. A. & BOLIVAR, V. J. 2009. Cautionary insights on knockout mouse studies: the gene or not the gene? *Brain Behav Immun*, 23, 318-24.
- ELMORE, M. R., NAJAFI, A. R., KOIKE, M. A., DAGHER, N. N., SPANGENBERG, E. E., RICE, R. A., KITAZAWA, M., MATUSOW, B., NGUYEN, H., WEST, B. L. & GREEN, K. N. 2014. Colony-stimulating factor 1 receptor signaling is necessary for microglia viability, unmasking a microglia progenitor cell in the adult brain. *Neuron*, 82, 380-97.
- ELOBEID, A., LIBARD, S., LEINO, M., POPOVA, S. N. & ALAFUZOFF, I. 2016. Altered Proteins in the Aging Brain. *J Neuropathol Exp Neurol*, 75, 316-25.
- FEINBERG, I. 1982. Schizophrenia: caused by a fault in programmed synaptic elimination during adolescence? *J Psychiatr Res*, 17, 319-34.
- FERREIRA, N. S., ENGELSBY, H., NEESS, D., KELLY, S. L., VOLPERT, G., MERRILL, A. H., FUTERMAN, A. H. & FAERGEMAN, N. J. 2017. Regulation of very-long acyl chain ceramide synthesis by acyl-CoA-binding protein. *J Biol Chem*, 292, 7588-7597.
- FILIPPI, M., BAR-OR, A., PIEHL, F., PREZIOSA, P., SOLARI, A., VUKUSIC, S. & ROCCA, M. A. 2018. Multiple sclerosis. *Nat Rev Dis Primers*, 4, 43.
- FISCHER, M. T., WIMMER, I., HOFTBERGER, R., GERLACH, S., HAIDER, L., ZRZAVY, T., HAMETNER, S., MAHAD, D., BINDER, C. J., KRUMBHOLZ, M., BAUER, J., BRADL, M. & LASSMANN, H. 2013. Disease-specific molecular events in cortical multiple sclerosis lesions. *Brain*, 136, 1799-815.
- FLEISCHER, V., KOLB, R., GROPPA, S., ZIPP, F., KLOSE, U. & GROGER, A. 2016. Metabolic Patterns in Chronic Multiple Sclerosis Lesions and Normal-appearing White Matter: Intraindividual Comparison by Using 2D MR Spectroscopic Imaging. *Radiology*, 281, 536-543.

- FONSECA, M. I., ZHOU, J., BOTTO, M. & TENNER, A. J. 2004. Absence of C1q leads to less neuropathology in transgenic mouse models of Alzheimer's disease. *J Neurosci*, 24, 6457-65.
- FORSLIN, Y., BERGENDAL, A., HASHIM, F., MARTOLA, J., SHAMS, S., WIBERG, M. K., FREDRIKSON, S. & GRANBERG, T. 2018. Detection of Leukocortical Lesions in Multiple Sclerosis and Their Association with Physical and Cognitive Impairment: A Comparison of Conventional and Synthetic Phase-Sensitive Inversion Recovery MRI. *AJNR Am J Neuroradiol*, 39, 1995-2000.
- FRANGOIANNIS, N. G. 2022. Why animal model studies are lost in translation. *J Cardiovasc Aging*, 2.
- FREEDMAN, M. S., KAPLAN, J. M. & MARKOVIC-PLESE, S. 2013. Insights into the Mechanisms of the Therapeutic Efficacy of Alemtuzumab in Multiple Sclerosis. *J Clin Cell Immunol*, 4.
- FRESEGNA, D., BULLITTA, S., MUSELLA, A., RIZZO, F. R., DE VITO, F., GUADALUPI, L., CAIOLI, S., BALLETTA, S., SANNA, K., DOLCETTI, E., VANNI, V., BRUNO, A., BUTTARI, F., STAMPANONI BASSI, M., MANDOLESI, G., CENTONZE, D. & GENTILE, A. 2020. Re-Examining the Role of TNF in MS Pathogenesis and Therapy. *Cells*, 9.
- FRISCHER, J. M., BRAMOW, S., DAL-BIANCO, A., LUCCHINETTI, C. F., RAUSCHKA, H., SCHMIDBAUER, M., LAURSEN, H., SORENSEN, P. S. & LASSMANN, H. 2009. The relation between inflammation and neurodegeneration in multiple sclerosis brains. *Brain*, 132, 1175-89.
- FRISCHER, J. M., WEIGAND, S. D., GUO, Y., KALE, N., PARISI, J. E., PIRKO, I., MANDREKAR, J., BRAMOW, S., METZ, I., BRUCK, W., LASSMANN, H. & LUCCHINETTI, C. F. 2015. Clinical and pathological insights into the dynamic nature of the white matter multiple sclerosis plaque. *Ann Neurol*, 78, 710-21.
- GALAXY, C. 2022. The Galaxy platform for accessible, reproducible and collaborative biomedical analyses: 2022 update. *Nucleic Acids Res*, 50, W345-51.
- GANZ, A. B., BEKER, N., HULSMAN, M., SIKKES, S., NETHERLANDS BRAIN, B., SCHELTENS, P., SMIT, A. B., ROZEMULLER, A. J. M., HOOZEMANS, J. J. M. & HOLSTEGE, H. 2018. Neuropathology and cognitive performance in self-reported cognitively healthy centenarians. *Acta Neuropathol Commun*, 6, 64.
- GARDNER, C., MAGLIOZZI, R., DURRENBERGER, P. F., HOWELL, O. W., RUNDLE, J. & REYNOLDS, R. 2013. Cortical grey matter demyelination can be induced by elevated pro-inflammatory cytokines in the subarachnoid space of MOG-immunized rats. *Brain*, 136, 3596-608.
- GEINISMAN, Y., DE TOLEDO-MORRELL, L. & MORRELL, F. 1986. Loss of perforated synapses in the dentate gyrus: morphological substrate of memory deficit in aged rats. *Proc Natl Acad Sci U S A*, 83, 3027-31.
- GEURTS, J. J., BO, L., ROOSEDAAL, S. D., HAZES, T., DANIELS, R., BARKHOF, F., WITTER, M. P., HUITINGA, I. & VAN DER VALK, P. 2007. Extensive hippocampal demyelination in multiple sclerosis. *J Neuropathol Exp Neurol*, 66, 819-27.
- GHARIB, W. H. & ROBINSON-RECHAVI, M. 2011. When orthologs diverge between human and mouse. *Brief Bioinform*, 12, 436-41.
- GHOLAMZAD, M., EBTEKAR, M., ARDESTANI, M. S., AZIMI, M., MAHMUDI, Z., MOUSAVI, M. J. & ASLANI, S. 2019. A comprehensive review on the treatment approaches of multiple sclerosis: currently and in the future. *Inflamm Res*, 68, 25-38.
- GLANTZ, L. A. & LEWIS, D. A. 2000. Decreased dendritic spine density on prefrontal cortical pyramidal neurons in schizophrenia. *Arch Gen Psychiatry*, 57, 65-73.
- GOLD, R., KAPPOS, L., ARNOLD, D. L., BAR-OR, A., GIOVANNONI, G., SELMAJ, K., TORNATORE, C., SWEETSER, M. T., YANG, M., SHEIKH, S. I., DAWSON, K. T. & INVESTIGATORS, D. S. 2012. Placebo-controlled phase 3 study of oral BG-12 for relapsing multiple sclerosis. *N Engl J Med*, 367, 1098-107.
- GONZALEZ, R. G. 2012. Clinical MRI of acute ischemic stroke. *J Magn Reson Imaging*, 36, 259-71.
- GRINDBERG, R. V., YEE-GREENBAUM, J. L., MCCONNELL, M. J., NOVOTNY, M., O'SHAUGHNESSY, A. L., LAMBERT, G. M., ARAUZO-BRAVO, M. J., LEE, J., FISHMAN, M., ROBBINS, G. E., LIN, X., VENEPALLY, P., BADGER, J. H., GALBRAITH, D. W., GAGE, F. H. & LASKEN, R. S. 2013. RNA-sequencing from single nuclei. *Proc Natl Acad Sci U S A*, 110, 19802-7.
- GROVER, V. P., TOGNARELLI, J. M., CROSSEY, M. M., COX, I. J., TAYLOR-ROBINSON, S. D. & MCPHAIL, M. J. 2015. Magnetic Resonance Imaging: Principles and Techniques: Lessons for Clinicians. *J Clin Exp Hepatol*, 5, 246-55.

- GUERRERO-JUAREZ, C. F., DEDHIA, P. H., JIN, S., RUIZ-VEGA, R., MA, D., LIU, Y., YAMAGA, K., SHESTOVA, O., GAY, D. L., YANG, Z., KESSENBROCK, K., NIE, Q., PEAR, W. S., COTSARELIS, G. & PLIKUS, M. V. 2019. Single-cell analysis reveals fibroblast heterogeneity and myeloid-derived adipocyte progenitors in murine skin wounds. *Nat Commun*, 10, 650.
- HAGAN, N., KANE, J. L., GROVER, D., WOODWORTH, L., MADORE, C., SALEH, J., SANCHO, J., LIU, J., LI, Y., PROTO, J., ZELIC, M., MAHAN, A., KOTHE, M., SCHOLTE, A. A., FITZGERALD, M., GISEVIUS, B., HAGHIKIA, A., BUTOVSKY, O. & OFENGEIM, D. 2020. CSF1R signaling is a regulator of pathogenesis in progressive MS. *Cell Death Dis*, 11, 904.
- HAIDER, L., ZRZAVY, T., HAMETNER, S., HOFTBERGER, R., BAGNATO, F., GRABNER, G., TRATTNIG, S., PFEIFENBRING, S., BRUCK, W. & LASSMANN, H. 2016. The topography of demyelination and neurodegeneration in the multiple sclerosis brain. *Brain*, 139, 807-15.
- HALL, S. M. 1972. The effect of injections of lysophosphatidyl choline into white matter of the adult mouse spinal cord. *J Cell Sci*, 10, 535-46.
- HAMMOND, S. R., ENGLISH, D. R. & MCLEOD, J. G. 2000. The age-range of risk of developing multiple sclerosis: evidence from a migrant population in Australia. *Brain*, 123 (Pt 5), 968-74.
- HAMPEL, H., CARACI, F., CUELLO, A. C., CARUSO, G., NISTICO, R., CORBO, M., BALDACCI, F., TOSCHI, N., GARACI, F., CHIESA, P. A., VERDOONER, S. R., AKMAN-ANDERSON, L., HERNANDEZ, F., AVILA, J., EMANUELE, E., VALENZUELA, P. L., LUCIA, A., WATLING, M., IMBIMBO, B. P., VERGALLO, A. & LISTA, S. 2020. A Path Toward Precision Medicine for Neuroinflammatory Mechanisms in Alzheimer's Disease. *Front Immunol*, 11, 456.
- HAO, Y., HAO, S., ANDERSEN-NISSEN, E., MAUCK, W. M., 3RD, ZHENG, S., BUTLER, A., LEE, M. J., WILK, A. J., DARBY, C., ZAGER, M., HOFFMAN, P., STOECKIUS, M., PAPALEXI, E., MIMITOU, E. P., JAIN, J., SRIVASTAVA, A., STUART, T., FLEMING, L. M., YEUNG, B., ROGERS, A. J., MCEL RATH, J. M., BLISH, C. A., GOTTARDO, R., SMIBERT, P. & SATIJA, R. 2021. Integrated analysis of multimodal single-cell data. *Cell*, 184, 3573-3587 e29.
- HARDING, K., ZHU, F., ALOTAIBI, M., DUGGAN, T., TREMLETT, H. & KINGWELL, E. 2020. Multiple cause of death analysis in multiple sclerosis: A population-based study. *Neurology*, 94, e820-e829.
- HARTUNG, H. P., GONSETTE, R., KONIG, N., KWIECINSKI, H., GUSEO, A., MORRISSEY, S. P., KRAPF, H., ZWINGERS, T. & MITOXANTRONE IN MULTIPLE SCLEROSIS STUDY, G. 2002. Mitoxantrone in progressive multiple sclerosis: a placebo-controlled, double-blind, randomised, multicentre trial. *Lancet*, 360, 2018-25.
- HASBANI, M., UNDERHILL SM, DE ERAUSQUIN F, GOLDBERG M 2000. Synapse Loss and Regeneration: A Mechanism for Functional Decline and Recovery after Cerebral Ischemia? *Neuroscientist*, 6, 110-119.
- HAUSER, S. L., WAUBANT, E., ARNOLD, D. L., VOLLMER, T., ANTEL, J., FOX, R. J., BAR-OR, A., PANZARA, M., SARKAR, N., AGARWAL, S., LANGER-GOULD, A., SMITH, C. H. & GROUP, H. T. 2008. B-cell depletion with rituximab in relapsing-remitting multiple sclerosis. *N Engl J Med*, 358, 676-88.
- HAWKER, K., O'CONNOR, P., FREEDMAN, M. S., CALABRESI, P. A., ANTEL, J., SIMON, J., HAUSER, S., WAUBANT, E., VOLLMER, T., PANITCH, H., ZHANG, J., CHIN, P., SMITH, C. H. & GROUP, O. T. 2009. Rituximab in patients with primary progressive multiple sclerosis: results of a randomized double-blind placebo-controlled multicenter trial. *Ann Neurol*, 66, 460-71.
- HE, Y., ZHANG, X., FLAIS, I. & SVENNINGSSON, P. 2022. Decreased Prosaposin and Progranulin in the Cingulate Cortex Are Associated with Schizophrenia Pathophysiology. *Int J Mol Sci*, 23.
- HEMOND, C. C. & BAKSHI, R. 2018. Magnetic Resonance Imaging in Multiple Sclerosis. *Cold Spring Harb Perspect Med*, 8.
- HOLTMAAT, A., BONHOEFFER, T., CHOW, D. K., CHUCKOWREE, J., DE PAOLA, V., HOFER, S. B., HUBENER, M., KECK, T., KNOTT, G., LEE, W. C., MOSTANY, R., MRSIC-FLOGEL, T. D., NEDIVI, E., PORTERA-CAILLIAU, C., SVOBODA, K., TRACHTENBERG, J. T. & WILBRECHT, L. 2009. Long-term, high-resolution imaging in the mouse neocortex through a chronic cranial window. *Nat Protoc*, 4, 1128-44.
- HONG, S., BEJA-GLASSER, V. F., NFOYOYIM, B. M., FROUIN, A., LI, S., RAMAKRISHNAN, S., MERRY, K. M., SHI, Q., ROSENTHAL, A., BARRES, B. A., LEMERE, C. A., SELKOE, D. J. & STEVENS, B. 2016. Complement and microglia mediate early synapse loss in Alzheimer mouse models. *Science*, 352, 712-716.

- HOU, Y., DAN, X., BABBAR, M., WEI, Y., HASSELBALCH, S. G., CROTEAU, D. L. & BOHR, V. A. 2019. Ageing as a risk factor for neurodegenerative disease. *Nat Rev Neurol*, 15, 565-581.
- HU, X. & IVASHKIV, L. B. 2009. Cross-regulation of signaling pathways by interferon-gamma: implications for immune responses and autoimmune diseases. *Immunity*, 31, 539-50.
- HUNT, J. S. & WOOD, G. W. 1986. Interferon-gamma induces class I HLA and beta 2-microglobulin expression by human amnion cells. *J Immunol*, 136, 364-7.
- HUTTENLOCHER, P. R. 1979. Synaptic density in human frontal cortex - developmental changes and effects of aging. *Brain Res*, 163, 195-205.
- INCONTRO, S., ASENSIO, C. S., EDWARDS, R. H. & NICOLL, R. A. 2014. Efficient, complete deletion of synaptic proteins using CRISPR. *Neuron*, 83, 1051-7.
- INGELFINGER, F., BELTRAN, E., GERDES, L. A. & BECHER, B. 2022. Single-cell multiomics in neuroinflammation. *Curr Opin Immunol*, 76, 102180.
- INNOVATIVE GENOMICS INSTITUTE, H. H. 2022. *CRISPR Clinical Trials: A 2022 Update* [Online]. Available: CRISPR Clinical Trials: A 2022 Update - Innovative Genomics Institute (IGI) [Accessed 05.02.2023].
- INVESTIGATORS, C. T., COLES, A. J., COMPSTON, D. A., SELMAJ, K. W., LAKE, S. L., MORAN, S., MARGOLIN, D. H., NORRIS, K. & TANDON, P. K. 2008. Alemtuzumab vs. interferon beta-1a in early multiple sclerosis. *N Engl J Med*, 359, 1786-801.
- JAFARI, M., SCHUMACHER, A. M., SNAIDERO, N., ULLRICH GAVILANES, E. M., NEZIRAJ, T., KOCSIS-JUTKA, V., ENGELS, D., JURGENS, T., WAGNER, I., WEIDINGER, J. D. F., SCHMIDT, S. S., BELTRAN, E., HAGAN, N., WOODWORTH, L., OFENGEIM, D., GANS, J., WOLF, F., KREUTZFELDT, M., PORTUGUES, R., MERKLER, D., MISGELD, T. & KERSCHENSTEINER, M. 2021. Phagocyte-mediated synapse removal in cortical neuroinflammation is promoted by local calcium accumulation. *Nat Neurosci*, 24, 355-367.
- JEFFERY, N. D. & BLAKEMORE, W. F. 1995. Remyelination of mouse spinal cord axons demyelinated by local injection of lysolecithin. *J Neurocytol*, 24, 775-81.
- JINEK, M., CHYLINSKI, K., FONFARA, I., HAUER, M., DOUDNA, J. A. & CHARPENTIER, E. 2012. A programmable dual-RNA-guided DNA endonuclease in adaptive bacterial immunity. *Science*, 337, 816-21.
- JINEK, M., EAST, A., CHENG, A., LIN, S., MA, E. & DOUDNA, J. 2013. RNA-programmed genome editing in human cells. *Elife*, 2, e00471.
- JOHNSON, K. A., FOX, N. C., SPERLING, R. A. & KLUNK, W. E. 2012. Brain imaging in Alzheimer disease. *Cold Spring Harb Perspect Med*, 2, a006213.
- JOHNSON, K. P., BROOKS, B. R., COHEN, J. A., FORD, C. C., GOLDSTEIN, J., LISAK, R. P., MYERS, L. W., PANITCH, H. S., ROSE, J. W. & SCHIFFER, R. B. 1995. Copolymer 1 reduces relapse rate and improves disability in relapsing-remitting multiple sclerosis: results of a phase III multicenter, double-blind placebo-controlled trial. The Copolymer 1 Multiple Sclerosis Study Group. *Neurology*, 45, 1268-76.
- JOHNSON, K. P., BROOKS, B. R., COHEN, J. A., FORD, C. C., GOLDSTEIN, J., LISAK, R. P., MYERS, L. W., PANITCH, H. S., ROSE, J. W., SCHIFFER, R. B., VOLLMER, T., WEINER, L. P. & WOLINSKY, J. S. 1998. Extended use of glatiramer acetate (Copaxone) is well tolerated and maintains its clinical effect on multiple sclerosis relapse rate and degree of disability. Copolymer 1 Multiple Sclerosis Study Group. *Neurology*, 50, 701-8.
- JOHNSON, T. A., JIRIK, F. R. & FOURNIER, S. 2010. Exploring the roles of CD8(+) T lymphocytes in the pathogenesis of autoimmune demyelination. *Semin Immunopathol*, 32, 197-209.
- JURGENS, T., JAFARI, M., KREUTZFELDT, M., BAHN, E., BRUCK, W., KERSCHENSTEINER, M. & MERKLER, D. 2016. Reconstruction of single cortical projection neurons reveals primary spine loss in multiple sclerosis. *Brain*, 139, 39-46.
- KAMM, C. P., UITDEHAAG, B. M. & POLMAN, C. H. 2014. Multiple sclerosis: current knowledge and future outlook. *Eur Neurol*, 72, 132-41.
- KANG, C. & BLAIR, H. A. 2022. Correction to: Ofatumumab: A Review in Relapsing Forms of Multiple Sclerosis. *Drugs*, 82, 63.
- KANG, J. B., NATHAN, A., WEINAND, K., ZHANG, F., MILLARD, N., RUMKER, L., MOODY, D. B., KORSUNSKY, I. & RAYCHAUDHURI, S. 2021. Efficient and precise single-cell reference atlas mapping with Symphony. *Nat Commun*, 12, 5890.

- KAPOOR, R., HO, P. R., CAMPBELL, N., CHANG, I., DEYKIN, A., FORRESTAL, F., LUCAS, N., YU, B., ARNOLD, D. L., FREEDMAN, M. S., GOLDMAN, M. D., HARTUNG, H. P., HAVRDOVA, E. K., JEFFERY, D., MILLER, A., SELLEBJERG, F., CADAVID, D., MIKOL, D., STEINER, D. & INVESTIGATORS, A. 2018. Effect of natalizumab on disease progression in secondary progressive multiple sclerosis (ASCEND): a phase 3, randomised, double-blind, placebo-controlled trial with an open-label extension. *Lancet Neurol*, 17, 405-415.
- KAPPOS, L., LI, D., CALABRESI, P. A., O'CONNOR, P., BAR-OR, A., BARKHOF, F., YIN, M., LEPPERT, D., GLANZMAN, R., TINBERGEN, J. & HAUSER, S. L. 2011. Ocrelizumab in relapsing-remitting multiple sclerosis: a phase 2, randomised, placebo-controlled, multicentre trial. *Lancet*, 378, 1779-87.
- KAPPOS, L., RADUE, E. W., O'CONNOR, P., POLMAN, C., HOHLFELD, R., CALABRESI, P., SELMAJ, K., AGOROPOULOU, C., LEYK, M., ZHANG-AUBERSON, L., BURTIN, P. & GROUP, F. S. 2010. A placebo-controlled trial of oral fingolimod in relapsing multiple sclerosis. *N Engl J Med*, 362, 387-401.
- KAUFMANN, M., EVANS, H., SCHAUPP, A. L., ENGLER, J. B., KAUR, G., WILLING, A., KURSAWE, N., SCHUBERT, C., ATTFIELD, K. E., FUGGER, L. & FRIESE, M. A. 2021. Identifying CNS-colonizing T cells as potential therapeutic targets to prevent progression of multiple sclerosis. *Med (N Y)*, 2, 296-312 e8.
- KAWAKAMI, N., LASSMANN, S., LI, Z., ODOARDI, F., RITTER, T., ZIEMSEN, T., KLINKERT, W. E., ELLWART, J. W., BRADL, M., KRIVACIC, K., LASSMANN, H., RANSOHOFF, R. M., VOLK, H. D., WEKERLE, H., LININGTON, C. & FLUGEL, A. 2004. The activation status of neuroantigen-specific T cells in the target organ determines the clinical outcome of autoimmune encephalomyelitis. *J Exp Med*, 199, 185-97.
- KEANEY, J., GASSER, J., GILLET, G., SCHOLZ, D. & KADIU, I. 2019. Inhibition of Bruton's Tyrosine Kinase Modulates Microglial Phagocytosis: Therapeutic Implications for Alzheimer's Disease. *J Neuroimmune Pharmacol*, 14, 448-461.
- KHURANA, A., SAYED, N., SINGH, V., KHURANA, I., ALLAWADHI, P., RAWAT, P. S., NAVIK, U., PASUMARTHI, S. K., BHARANI, K. K. & WEISKIRCHEN, R. 2022. A comprehensive overview of CRISPR/Cas 9 technology and application thereof in drug discovery. *J Cell Biochem*, 123, 1674-1698.
- KIESEIER, B. C. 2011. The mechanism of action of interferon-beta in relapsing multiple sclerosis. *CNS Drugs*, 25, 491-502.
- KLEIN, B., MROWETZ, H., BARKER, C. M., LANGE, S., RIVERA, F. J. & AIGNER, L. 2018. Age Influences Microglial Activation After Cuprizone-Induced Demyelination. *Front Aging Neurosci*, 10, 278.
- KLUYVER, T., RAGAN-KELLEY, B. P., F., GRANGER, B. B., M. FREDERIC, J., KELLEY, K., HAMRICK, J., GROUT, J., CORLAY, S., IVANOV, P., AVILA, D. & ABDALLA, S. W., C. 2016. *Jupyter Notebooks – a publishing format for reproducible computational workflows*.
- KOMOR, A. C., KIM, Y. B., PACKER, M. S., ZURIS, J. A. & LIU, D. R. 2016. Programmable editing of a target base in genomic DNA without double-stranded DNA cleavage. *Nature*, 533, 420-4.
- KRIEGER, S. C., COOK, K., DE NINO, S. & FLETCHER, M. 2016. The topographical model of multiple sclerosis: A dynamic visualization of disease course. *Neurol Neuroimmunol Neuroinflamm*, 3, e279.
- KUTZELNIGG, A. & LASSMANN, H. 2006. Cortical demyelination in multiple sclerosis: a substrate for cognitive deficits? *J Neurol Sci*, 245, 123-6.
- KUTZELNIGG, A., LUCCHINETTI, C. F., STADELMANN, C., BRUCK, W., RAUSCHKA, H., BERGMANN, M., SCHMIDBAUER, M., PARISI, J. E. & LASSMANN, H. 2005. Cortical demyelination and diffuse white matter injury in multiple sclerosis. *Brain*, 128, 2705-12.
- LACAR, B., LINKER, S. B., JAEGER, B. N., KRISHNASWAMI, S. R., BARRON, J. J., KELDER, M. J. E., PARYLAK, S. L., PAQUOLA, A. C. M., VENEPALLY, P., NOVOTNY, M., O'CONNOR, C., FITZPATRICK, C., ERWIN, J. A., HSU, J. Y., HUSBAND, D., MCCONNELL, M. J., LASKEN, R. & GAGE, F. H. 2016. Nuclear RNA-seq of single neurons reveals molecular signatures of activation. *Nat Commun*, 7, 11022.
- LAGUMERSINDEZ-DENIS, N., WRZOS, C., MACK, M., WINKLER, A., VAN DER MEER, F., REINERT, M. C., HOLLASCH, H., FLACH, A., BRUHL, H., CULLEN, E., SCHLUMBOHM, C., FUCHS, E., LININGTON, C., BARRANTES-FREER, A., METZ, I., WEGNER, C., LIEBETANZ, D., PRINZ, M., BRUCK, W., STADELMANN, C. & NESSLER, S. 2017. Differential contribution of immune effector mechanisms to cortical demyelination in multiple sclerosis. *Acta Neuropathol*, 134, 15-34.

- LASSMANN, H. & BRADL, M. 2017. Multiple sclerosis: experimental models and reality. *Acta Neuropathol*, 133, 223-244.
- LASSMANN, H., BRUCK, W. & LUCCHINETTI, C. 2001. Heterogeneity of multiple sclerosis pathogenesis: implications for diagnosis and therapy. *Trends Mol Med*, 7, 115-21.
- LEE, C. M., CRADICK, T. J., FINE, E. J. & BAO, G. 2016. Nuclease Target Site Selection for Maximizing On-target Activity and Minimizing Off-target Effects in Genome Editing. *Mol Ther*, 24, 475-87.
- LEES, J. R., GOLUMBEK, P. T., SIM, J., DORSEY, D. & RUSSELL, J. H. 2008. Regional CNS responses to IFN-gamma determine lesion localization patterns during EAE pathogenesis. *J Exp Med*, 205, 2633-42.
- LERAY, E., MOREAU, T., FROMONT, A. & EDAN, G. 2016. Epidemiology of multiple sclerosis. *Rev Neurol (Paris)*, 172, 3-13.
- LINTHICUM, D. S., MUNOZ, J. J. & BLASKETT, A. 1982. Acute experimental autoimmune encephalomyelitis in mice. I. Adjuvant action of Bordetella pertussis is due to vasoactive amine sensitization and increased vascular permeability of the central nervous system. *Cell Immunol*, 73, 299-310.
- LIU, J., SUPNET, C., SUN, S., ZHANG, H., GOOD, L., POPUGAEVA, E. & BEZPROZVANNY, I. 2014. The role of ryanodine receptor type 3 in a mouse model of Alzheimer disease. *Channels (Austin)*, 8, 230-42.
- LIU, X. S., WU, H., KRZISCH, M., WU, X., GRAEF, J., MUFFAT, J., HNISZ, D., LI, C. H., YUAN, B., XU, C., LI, Y., VERSHKOV, D., CACACE, A., YOUNG, R. A. & JAENISCH, R. 2018. Rescue of Fragile X Syndrome Neurons by DNA Methylation Editing of the FMR1 Gene. *Cell*, 172, 979-992 e6.
- LODYGIN, D., HERMANN, M., SCHWEINGRUBER, N., FLUGEL-KOCH, C., WATANABE, T., SCHLOSSER, C., MERLINI, A., KORNER, H., CHANG, H. F., FISCHER, H. J., REICHARDT, H. M., ZAGREBELSKY, M., MOLLENHAUER, B., KUGLER, S., FITZNER, D., FRAHM, J., STADELMANN, C., HABERL, M., ODOARDI, F. & FLUGEL, A. 2019. beta-Synuclein-reactive T cells induce autoimmune CNS grey matter degeneration. *Nature*, 566, 503-508.
- LOHSE, A. W., MOR, F., KARIN, N. & COHEN, I. R. 1989. Control of experimental autoimmune encephalomyelitis by T cells responding to activated T cells. *Science*, 244, 820-2.
- LOVE, M. I., HUBER, W. & ANDERS, S. 2014. Moderated estimation of fold change and dispersion for RNA-seq data with DESeq2. *Genome Biol*, 15, 550.
- LUBLIN, F., MILLER, D. H., FREEDMAN, M. S., CREE, B. A. C., WOLINSKY, J. S., WEINER, H., LUBETZKI, C., HARTUNG, H. P., MONTALBAN, X., UITDEHAAG, B. M. J., MERSCHHEMKE, M., LI, B., PUTZKI, N., LIU, F. C., HARING, D. A., KAPPOS, L. & INVESTIGATORS, I. S. 2016. Oral fingolimod in primary progressive multiple sclerosis (INFORMS): a phase 3, randomised, double-blind, placebo-controlled trial. *Lancet*, 387, 1075-1084.
- LUBLIN, F. D., REINGOLD, S. C., COHEN, J. A., CUTTER, G. R., SORENSEN, P. S., THOMPSON, A. J., WOLINSKY, J. S., BALCER, L. J., BANWELL, B., BARKHOF, F., BEBO, B., JR., CALABRESI, P. A., CLANET, M., COMI, G., FOX, R. J., FREEDMAN, M. S., GOODMAN, A. D., INGLESE, M., KAPPOS, L., KIESEIER, B. C., LINCOLN, J. A., LUBETZKI, C., MILLER, A. E., MONTALBAN, X., O'CONNOR, P. W., PETKAU, J., POZZILLI, C., RUDICK, R. A., SORMANI, M. P., STUVE, O., WAUBANT, E. & POLMAN, C. H. 2014. Defining the clinical course of multiple sclerosis: the 2013 revisions. *Neurology*, 83, 278-86.
- LUCCHINETTI, C. F., POPESCU, B. F., BUNYAN, R. F., MOLL, N. M., ROEMER, S. F., LASSMANN, H., BRUCK, W., PARISI, J. E., SCHEITHAUER, B. W., GIANNINI, C., WEIGAND, S. D., MANDREKAR, J. & RANSOHOFF, R. M. 2011. Inflammatory cortical demyelination in early multiple sclerosis. *N Engl J Med*, 365, 2188-97.
- LUI, H., ZHANG, J., MAKINSON, S. R., CAHILL, M. K., KELLEY, K. W., HUANG, H. Y., SHANG, Y., OLDHAM, M. C., MARTENS, L. H., GAO, F., COPPOLA, G., SLOAN, S. A., HSIEH, C. L., KIM, C. C., BIGIO, E. H., WEINTRAUB, S., MESULAM, M. M., RADEMAKERS, R., MACKENZIE, I. R., SEELEY, W. W., KARYDAS, A., MILLER, B. L., BORRONI, B., GHIDONI, R., FARESE, R. V., JR., PAZ, J. T., BARRES, B. A. & HUANG, E. J. 2016. Progranulin Deficiency Promotes Circuit-Specific Synaptic Pruning by Microglia via Complement Activation. *Cell*, 165, 921-35.
- LUO, J., PADHI, P., JIN, H., ANANTHARAM, V., ZENITSKY, G., WANG, Q., WILLETTE, A. A., KANTHASAMY, A. & KANTHASAMY, A. G. 2019. Utilization of the CRISPR-Cas9 Gene Editing System to Dissect Neuroinflammatory and Neuropharmacological Mechanisms in Parkinson's Disease. *J Neuroimmune Pharmacol*, 14, 595-607.

- LYU, X., TOYONAGA, T., DENG, G., HUANG, Y., CARSON, R., ZHOU, J. & CAI, Z. 2020. Monitoring synaptic loss in a rat model of stroke: a PET imaging study with [18F]SynVesT-2, radiotracer for the synaptic vesicle protein 2A (SV2A). *Journal of Nuclear Medicine*, 61, 84.
- MALECKA, I., PRZYBEK-SKRZYPECKA, J., KUROWSKA, K., MIROWSKA-GUZEL, D. & CZLONKOWSKA, A. 2021. Clinical and laboratory parameters by age for patients diagnosed with multiple sclerosis between 2000 and 2015. *Neurol Neurochir Pol*, 55, 387-393.
- MATHYS, H., DAVILA-VELDERRAIN, J., PENG, Z., GAO, F., MOHAMMADI, S., YOUNG, J. Z., MENON, M., HE, L., ABDURROB, F., JIANG, X., MARTORELL, A. J., RANSOHOFF, R. M., HAFLER, B. P., BENNETT, D. A., KELLIS, M. & TSAI, L. H. 2019. Single-cell transcriptomic analysis of Alzheimer's disease. *Nature*, 570, 332-337.
- MCDONALD, W. I., COMPSTON, A., EDAN, G., GOODKIN, D., HARTUNG, H. P., LUBLIN, F. D., MCFARLAND, H. F., PATY, D. W., POLMAN, C. H., REINGOLD, S. C., SANDBERG-WOLLHEIM, M., SIBLEY, W., THOMPSON, A., VAN DEN NOORT, S., WEINSHENKER, B. Y. & WOLINSKY, J. S. 2001. Recommended diagnostic criteria for multiple sclerosis: guidelines from the International Panel on the diagnosis of multiple sclerosis. *Ann Neurol*, 50, 121-7.
- MCWILLIAMS, J. R. & LYNCH, G. 1984. Synaptic density and axonal sprouting in rat hippocampus: stability in adulthood and decline in late adulthood. *Brain Res*, 294, 152-6.
- MERKEL, B., BUTZKUEVEN, H., TRABOULSEE, A. L., HAVRDOVA, E. & KALINCIK, T. 2017. Timing of high-efficacy therapy in relapsing-remitting multiple sclerosis: A systematic review. *Autoimmun Rev*, 16, 658-665.
- MERKLER, D., ERNSTING, T., KERSCHENSTEINER, M., BRUCK, W. & STADELMANN, C. 2006. A new focal EAE model of cortical demyelination: multiple sclerosis-like lesions with rapid resolution of inflammation and extensive remyelination. *Brain*, 129, 1972-83.
- MERLINI, M., RAFALSKI, V. A., RIOS CORONADO, P. E., GILL, T. M., ELLISMAN, M., MUTHUKUMAR, G., SUBRAMANIAN, K. S., RYU, J. K., SYME, C. A., DAVALOS, D., SEELEY, W. W., MUCKE, L., NELSON, R. B. & AKASSOGLU, K. 2019. Fibrinogen Induces Microglia-Mediated Spine Elimination and Cognitive Impairment in an Alzheimer's Disease Model. *Neuron*, 101, 1099-1108 e6.
- MEYER, R. C., GIDDENS, M. M., COLEMAN, B. M. & HALL, R. A. 2014. The protective role of prosaposin and its receptors in the nervous system. *Brain Res*, 1585, 1-12.
- MICHAILIDOU, I., WILLEMS, J. G., KOOI, E. J., VAN EDEN, C., GOLD, S. M., GEURTS, J. J., BAAS, F., HUITINGA, I. & RAMAGLIA, V. 2015. Complement C1q-C3-associated synaptic changes in multiple sclerosis hippocampus. *Ann Neurol*, 77, 1007-26.
- MIX, E., MEYER-RIENECKER, H., HARTUNG, H. P. & ZETTL, U. K. 2010. Animal models of multiple sclerosis--potentials and limitations. *Prog Neurobiol*, 92, 386-404.
- MOCK, E. E. A., HONKONEN, E. & AIRAS, L. 2021. Synaptic Loss in Multiple Sclerosis: A Systematic Review of Human Post-mortem Studies. *Front Neurol*, 12, 782599.
- MONTALBAN, X., GOLD, R., THOMPSON, A. J., OTERO-ROMERO, S., AMATO, M. P., CHANDRARATNA, D., CLANET, M., COMI, G., DERFUSS, T., FAZEKAS, F., HARTUNG, H. P., HAVRDOVA, E., HEMMER, B., KAPPOS, L., LIBLAU, R., LUBETZKI, C., MARCUS, E., MILLER, D. H., OLSSON, T., PILLING, S., SELMAJ, K., SIVA, A., SORENSEN, P. S., SORMANI, M. P., THALHEIM, C., WIENDL, H. & ZIPP, F. 2018.ECTRIMS/EAN guideline on the pharmacological treatment of people with multiple sclerosis. *Eur J Neurol*, 25, 215-237.
- MONTALBAN, X., HAUSER, S. L., KAPPOS, L., ARNOLD, D. L., BAR-OR, A., COMI, G., DE SEZE, J., GIOVANNONI, G., HARTUNG, H. P., HEMMER, B., LUBLIN, F., RAMMOHAN, K. W., SELMAJ, K., TRABOULSEE, A., SAUTER, A., MASTERMAN, D., FONTOURA, P., BELACHEW, S., GARREN, H., MAIRON, N., CHIN, P., WOLINSKY, J. S. & INVESTIGATORS, O. C. 2017. Ocrelizumab versus Placebo in Primary Progressive Multiple Sclerosis. *N Engl J Med*, 376, 209-220.
- MORIZAWA, Y. M., HIRAYAMA, Y., OHNO, N., SHIBATA, S., SHIGETOMI, E., SUI, Y., NABEKURA, J., SATO, K., OKAJIMA, F., TAKEBAYASHI, H., OKANO, H. & KOIZUMI, S. 2017. Reactive astrocytes function as phagocytes after brain ischemia via ABCA1-mediated pathway. *Nat Commun*, 8, 28.

- MURMU, R. P., LI, W., SZEPESI, Z. & LI, J. Y. 2015. Altered sensory experience exacerbates stable dendritic spine and synapse loss in a mouse model of Huntington's disease. *J Neurosci*, 35, 287-98.
- NAKAMURA, T., OH, C. K., LIAO, L., ZHANG, X., LOPEZ, K. M., GIBBS, D., DEAL, A. K., SCOTT, H. R., SPENCER, B., MASLIAH, E., RISSMAN, R. A., YATES, J. R., 3RD & LIPTON, S. A. 2021. Noncanonical transnitrosylation network contributes to synapse loss in Alzheimer's disease. *Science*, 371.
- NISHIZONO, H., YASUDA, R. & LAVIV, T. 2020. Methodologies and Challenges for CRISPR/Cas9 Mediated Genome Editing of the Mammalian Brain. *Front Genome Ed*, 2, 602970.
- NISSEN, J. C., THOMPSON, K. K., WEST, B. L. & TSIRKA, S. E. 2018. Csf1R inhibition attenuates experimental autoimmune encephalomyelitis and promotes recovery. *Exp Neurol*, 307, 24-36.
- NOSEWORTHY, J. H., LUCCHINETTI, C., RODRIGUEZ, M. & WEINSHENKER, B. G. 2000. Multiple sclerosis. *N Engl J Med*, 343, 938-52.
- NOVGORODOV, S. A., RILEY, C. L., KEFFLER, J. A., YU, J., KINDY, M. S., MACKLIN, W. B., LOMBARD, D. B. & GUDZ, T. I. 2016. SIRT3 Deacetylates Ceramide Synthases: IMPLICATIONS FOR MITOCHONDRIAL DYSFUNCTION AND BRAIN INJURY. *J Biol Chem*, 291, 1957-1973.
- O'CONNOR, P., WOLINSKY, J. S., CONFAVREUX, C., COMI, G., KAPPOS, L., OLSSON, T. P., BENZERDJEB, H., TRUFFINET, P., WANG, L., MILLER, A., FREEDMAN, M. S. & GROUP, T. T. 2011. Randomized trial of oral teriflunomide for relapsing multiple sclerosis. *N Engl J Med*, 365, 1293-303.
- OH, U., FUJITA, M., IKONOMIDOU, V. N., EVANGELOU, I. E., MATSUURA, E., HARBERTS, E., FUJIMURA, Y., RICHERT, N. D., OHAYON, J., PIKE, V. W., ZHANG, Y., ZOGHBI, S. S., INNIS, R. B. & JACOBSON, S. 2011. Translocator protein PET imaging for glial activation in multiple sclerosis. *J Neuroimmune Pharmacol*, 6, 354-61.
- OLMOS-ALONSO, A., SCHETTERS, S. T., SRI, S., ASKEW, K., MANCUSO, R., VARGAS-CABALLERO, M., HOLSCHER, C., PERRY, V. H. & GOMEZ-NICOLA, D. 2016. Pharmacological targeting of CSF1R inhibits microglial proliferation and prevents the progression of Alzheimer's-like pathology. *Brain*, 139, 891-907.
- OLSSON, T., BARCELLOS, L. F. & ALFREDSSON, L. 2017. Interactions between genetic, lifestyle and environmental risk factors for multiple sclerosis. *Nat Rev Neurol*, 13, 25-36.
- ONTANEDA, D., THOMPSON, A. J., FOX, R. J. & COHEN, J. A. 2017. Progressive multiple sclerosis: prospects for disease therapy, repair, and restoration of function. *Lancet*, 389, 1357-1366.
- OVERHOFF, F., BRENDEL, M., JAWORSKA, A., KORZHOVA, V., DELKER, A., PROBST, F., FOCKE, C., GILDEHAUS, F. J., CARLSEN, J., BAUMANN, K., HAASS, C., BARTENSTEIN, P., HERMS, J. & ROMINGER, A. 2016. Automated Spatial Brain Normalization and Hindbrain White Matter Reference Tissue Give Improved [(18)F]-Florbetaben PET Quantitation in Alzheimer's Model Mice. *Front Neurosci*, 10, 45.
- PACHTER, J. S., DE VRIES, H. E. & FABRY, Z. 2003. The blood-brain barrier and its role in immune privilege in the central nervous system. *J Neuropathol Exp Neurol*, 62, 593-604.
- PANITCH, H., MILLER, A., PATY, D., WEINSHENKER, B. & NORTH AMERICAN STUDY GROUP ON INTERFERON BETA-1B IN SECONDARY PROGRESSIVE, M. S. 2004. Interferon beta-1b in secondary progressive MS: results from a 3-year controlled study. *Neurology*, 63, 1788-95.
- PAPADOPOULOS, D., DUKES, S., PATEL, R., NICHOLAS, R., VORA, A. & REYNOLDS, R. 2009. Substantial archaeocortical atrophy and neuronal loss in multiple sclerosis. *Brain Pathol*, 19, 238-53.
- PAPADOPOULOS, D., MAGLIOZZI, R., MITSIKOSTAS, D. D., GORGOULIS, V. G. & NICHOLAS, R. S. 2020. Aging, Cellular Senescence, and Progressive Multiple Sclerosis. *Front Cell Neurosci*, 14, 178.
- PATY, D. W. & LI, D. K. 1993. Interferon beta-1b is effective in relapsing-remitting multiple sclerosis. II. MRI analysis results of a multicenter, randomized, double-blind, placebo-controlled trial. UBC MS/MRI Study Group and the IFNB Multiple Sclerosis Study Group. *Neurology*, 43, 662-7.
- PEARCE, J. M. 2005. Historical descriptions of multiple sclerosis. *Eur Neurol*, 54, 49-53.
- PETANJEK, Z., JUDAS, M., SIMIC, G., RASIN, M. R., UYLINGS, H. B., RAKIC, P. & KOSTOVIC, I. 2011. Extraordinary neoteny of synaptic spines in the human prefrontal cortex. *Proc Natl Acad Sci U S A*, 108, 13281-6.
- PETROVA, N., NUTMA, E., CARASSITI, D., RS NEWMAN, J., AMOR, S., ALTMANN, D. R., BAKER, D. & SCHMIERER, K. 2020. Synaptic Loss in Multiple Sclerosis Spinal Cord. *Ann Neurol*, 88, 619-625.

- PICELLI, S., BJORKLUND, A. K., FARIDANI, O. R., SAGASSER, S., WINBERG, G. & SANDBERG, R. 2013. Smart-seq2 for sensitive full-length transcriptome profiling in single cells. *Nat Methods*, 10, 1096-8.
- PLATT, R. J., CHEN, S., ZHOU, Y., YIM, M. J., SWIECH, L., KEMPTON, H. R., DAHLMAN, J. E., PARNAS, O., EISENHAURE, T. M., JOVANOVIĆ, M., GRAHAM, D. B., JHUNJHUNWALA, S., HEIDENREICH, M., XAVIER, R. J., LANGER, R., ANDERSON, D. G., HACOEN, N., REGEV, A., FENG, G., SHARP, P. A. & ZHANG, F. 2014. CRISPR-Cas9 knockin mice for genome editing and cancer modeling. *Cell*, 159, 440-55.
- POLMAN, C. H., O'CONNOR, P. W., HAVRDOVA, E., HUTCHINSON, M., KAPPOS, L., MILLER, D. H., PHILLIPS, J. T., LUBLIN, F. D., GIOVANNONI, G., WAJGT, A., TOAL, M., LYNN, F., PANZARA, M. A., SANDROCK, A. W. & INVESTIGATORS, A. 2006. A randomized, placebo-controlled trial of natalizumab for relapsing multiple sclerosis. *N Engl J Med*, 354, 899-910.
- PROCACCINI, C., DE ROSA, V., PUCINO, V., FORMISANO, L. & MATARESE, G. 2015. Animal models of Multiple Sclerosis. *Eur J Pharmacol*, 759, 182-91.
- PULECIO, J., VERMA, N., MEJIA-RAMIREZ, E., HUANGFU, D. & RAYA, A. 2017. CRISPR/Cas9-Based Engineering of the Epigenome. *Cell Stem Cell*, 21, 431-447.
- RAE-GRANT, A., DAY, G. S., MARRIE, R. A., RABINSTEIN, A., CREE, B. A. C., GRONSETH, G. S., HABOUBI, M., HALPER, J., HOSEY, J. P., JONES, D. E., LISAK, R., PELLETIER, D., POTREBIC, S., SITCOV, C., SOMMERS, R., STACHOWIAK, J., GETCHIUS, T. S. D., MERRILLAT, S. A. & PRINGSHEIM, T. 2018. Practice guideline recommendations summary: Disease-modifying therapies for adults with multiple sclerosis: Report of the Guideline Development, Dissemination, and Implementation Subcommittee of the American Academy of Neurology. *Neurology*, 90, 777-788.
- REBOLDI, A., COISNE, C., BAUMJOHANN, D., BENVENUTO, F., BOTTINELLI, D., LIRA, S., UCCELLI, A., LANZAVECCHIA, A., ENGELHARDT, B. & SALLUSTO, F. 2009. C-C chemokine receptor 6-regulated entry of TH-17 cells into the CNS through the choroid plexus is required for the initiation of EAE. *Nat Immunol*, 10, 514-23.
- RODRIGUEZ, A., EHLENBERGER, D., KELLIHER, K., EINSTEIN, M., HENDERSON, S. C., MORRISON, J. H., HOF, P. R. & WEARNE, S. L. 2003. Automated reconstruction of three-dimensional neuronal morphology from laser scanning microscopy images. *Methods*, 30, 94-105.
- ROSCZYK, H. A., SPARKMAN, N. L. & JOHNSON, R. W. 2008. Neuroinflammation and cognitive function in aged mice following minor surgery. *Exp Gerontol*, 43, 840-6.
- ROTSTEIN, D. L., MARRIE, R. A., MAXWELL, C., GANDHI, S., SCHULTZ, S. E., FUNG, K. & TU, K. 2019. MS risk in immigrants in the McDonald era: A population-based study in Ontario, Canada. *Neurology*, 93, e2203-e2215.
- SANDHOFF, K. & HARZER, K. 2013. Gangliosides and gangliosidoses: principles of molecular and metabolic pathogenesis. *J Neurosci*, 33, 10195-208.
- SATIJA, R., FARRELL, J. A., GENNERT, D., SCHIER, A. F. & REGEV, A. 2015. Spatial reconstruction of single-cell gene expression data. *Nat Biotechnol*, 33, 495-502.
- SATO, F., MARTINEZ, N. E., STEWART, E. C., OMURA, S., ALEXANDER, J. S. & TSUNODA, I. 2015. "Microglial nodules" and "newly forming lesions" may be a Janus face of early MS lesions; implications from virus-induced demyelination, the Inside-Out model. *BMC Neurol*, 15, 219.
- SCALFARI, A., NEUHAUS, A., DAUMER, M., EBERS, G. C. & MURARO, P. A. 2011. Age and disability accumulation in multiple sclerosis. *Neurology*, 77, 1246-52.
- SCHIRMER, L., VELMESHEV, D., HOLMQVIST, S., KAUFMANN, M., WERNEBURG, S., JUNG, D., VISTNES, S., STOCKLEY, J. H., YOUNG, A., STEINDEL, M., TUNG, B., GOYAL, N., BHADURI, A., MAYER, S., ENGLER, J. B., BAYRAKTAR, O. A., FRANKLIN, R. J. M., HAEUSSLER, M., REYNOLDS, R., SCHAFFER, D. P., FRIESE, M. A., SHIOW, L. R., KRIEGSTEIN, A. R. & ROWITCH, D. H. 2019. Neuronal vulnerability and multilineage diversity in multiple sclerosis. *Nature*, 573, 75-82.
- SCHNEIDER, C. A., RASBAND, W. S. & ELICEIRI, K. W. 2012. NIH Image to ImageJ: 25 years of image analysis. *Nat Methods*, 9, 671-5.
- SCHUMACHER, A. M. M., C. KERSCHENSTEINER, M. 2017. Pathology and Pathogenesis of Progressive Multiple Sclerosis: Concepts and Controversies. *Neurology International Open*, 01, E171-E181.

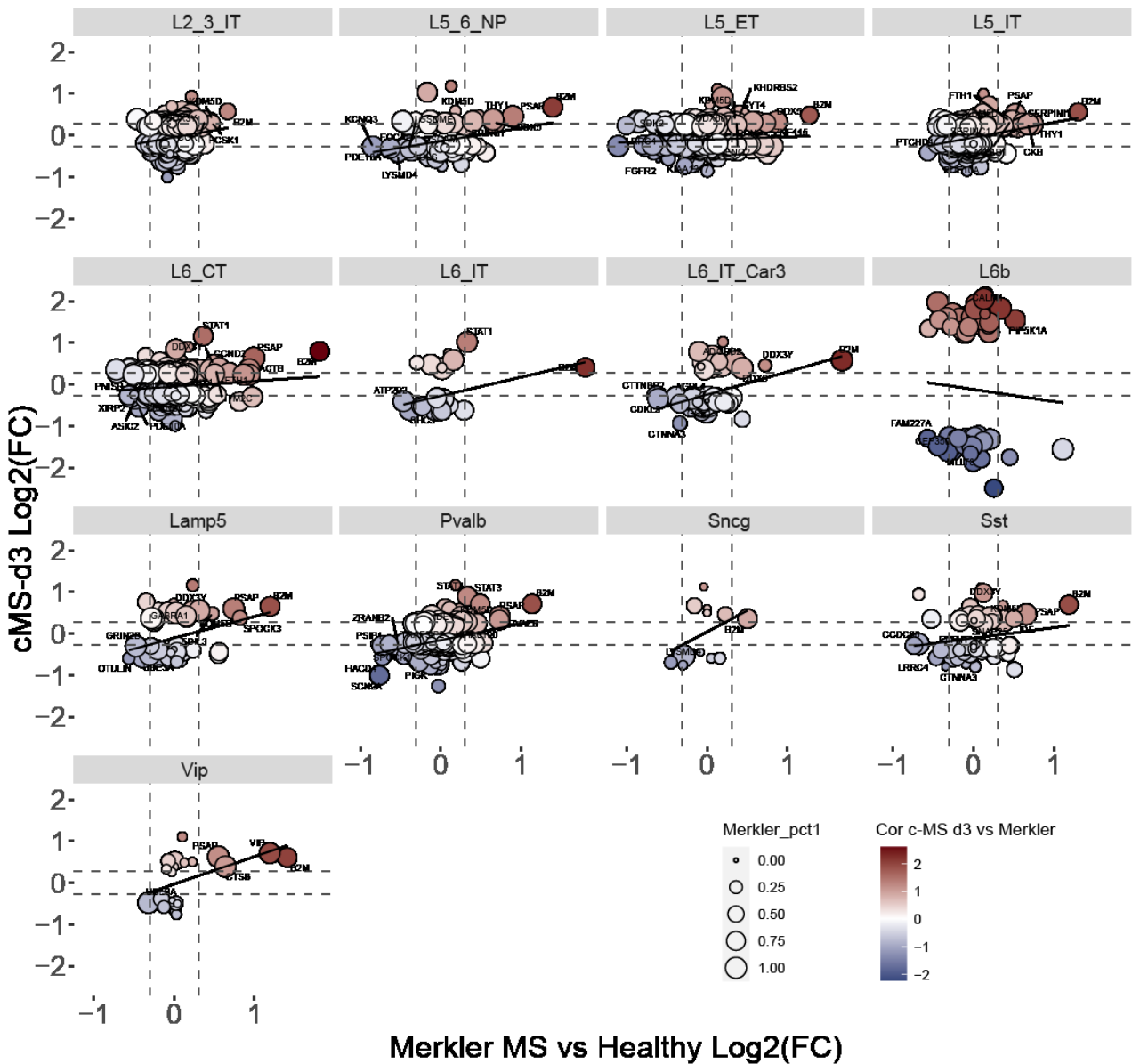
- SEDEL, F., BERNARD, D., MOCK, D. M. & TOURBAH, A. 2016. Targeting demyelination and virtual hypoxia with high-dose biotin as a treatment for progressive multiple sclerosis. *Neuropharmacology*, 110, 644-653.
- SELLGREN, C. M., GRACIAS, J., WATMUFF, B., BIAG, J. D., THANOS, J. M., WHITTREDGE, P. B., FU, T., WORRINGER, K., BROWN, H. E., WANG, J., KAYKAS, A., KARMACHARYA, R., GOOLD, C. P., SHERIDAN, S. D. & PERLIS, R. H. 2019. Increased synapse elimination by microglia in schizophrenia patient-derived models of synaptic pruning. *Nat Neurosci*, 22, 374-385.
- SENKAL, C. E., SALAMA, M. F., SNIDER, A. J., ALLOPENNA, J. J., RANA, N. A., KOLLER, A., HANNUN, Y. A. & OBEID, L. M. 2017. Ceramide Is Metabolized to Acylceramide and Stored in Lipid Droplets. *Cell Metab*, 25, 686-697.
- SHI, Q., CHOWDHURY, S., MA, R., LE, K. X., HONG, S., CALDARONE, B. J., STEVENS, B. & LEMERE, C. A. 2017. Complement C3 deficiency protects against neurodegeneration in aged plaque-rich APP/PS1 mice. *Sci Transl Med*, 9.
- SHI, X., LUO, L., WANG, J., SHEN, H., LI, Y., MAMTILAHUN, M., LIU, C., SHI, R., LEE, J. H., TIAN, H., ZHANG, Z., WANG, Y., CHUNG, W. S., TANG, Y. & YANG, G. Y. 2021. Stroke subtype-dependent synapse elimination by reactive gliosis in mice. *Nat Commun*, 12, 6943.
- SINGH, S., METZ, I., AMOR, S., VAN DER VALK, P., STADELMANN, C. & BRUCK, W. 2013. Microglial nodules in early multiple sclerosis white matter are associated with degenerating axons. *Acta Neuropathol*, 125, 595-608.
- SORENSEN, P. S., BERTOLOTTO, A., EDAN, G., GIOVANNONI, G., GOLD, R., HAVRDOVA, E., KAPPOS, L., KIESEIER, B. C., MONTALBAN, X. & OLSSON, T. 2012. Risk stratification for progressive multifocal leukoencephalopathy in patients treated with natalizumab. *Mult Scler*, 18, 143-52.
- SORENSEN, P. S., LISBY, S., GROVE, R., DEROSIER, F., SHACKELFORD, S., HAVRDOVA, E., DRULOVIC, J. & FILIPPI, M. 2014. Safety and efficacy of ofatumumab in relapsing-remitting multiple sclerosis: a phase 2 study. *Neurology*, 82, 573-81.
- STEINMAN, L., FOX, E., HARTUNG, H. P., ALVAREZ, E., QIAN, P., WRAY, S., ROBERTSON, D., HUANG, D., SELMAJ, K., WYNN, D., CUTTER, G., MOK, K., HSU, Y., XU, Y., WEISS, M. S., BOSCO, J. A., POWER, S. A., LEE, L., MISKIN, H. P., CREE, B. A. C., ULTIMATE, I. & INVESTIGATORS, U. I. 2022. Ublituximab versus Teriflunomide in Relapsing Multiple Sclerosis. *N Engl J Med*, 387, 704-714.
- STEINMAN, L., PATARCA, R. & HASELTINE, W. 2023. Experimental encephalomyelitis at age 90, still relevant and elucidating how viruses trigger disease. *J Exp Med*, 220.
- STEWART, A., BIEL, D., BRENDDEL, M., DEWENTER, A., ROEMER, S., RUBINSKI, A., LUAN, Y., DICHGANS, M., EWERS, M., FRANZMEIER, N. & ALZHEIMER'S DISEASE NEUROIMAGING, I. 2022. Functional network segregation is associated with attenuated tau spreading in Alzheimer's disease. *Alzheimers Dement*.
- STIDWORTHY, M. F., GENOUD, S., SUTER, U., MANTEI, N. & FRANKLIN, R. J. 2003. Quantifying the early stages of remyelination following cuprizone-induced demyelination. *Brain Pathol*, 13, 329-39.
- STOJA, E., KONSTANDIN, S., PHILIPP, D., WILKE, R. N., BETANCOURT, D., BERTUCH, T., JENNE, J., UMATHUM, R. & GUNTHER, M. 2021. Improving magnetic resonance imaging with smart and thin metasurfaces. *Sci Rep*, 11, 16179.
- STRAUB, C., GRANGER, A. J., SAULNIER, J. L. & SABATINI, B. L. 2014. CRISPR/Cas9-mediated gene knock-down in post-mitotic neurons. *PLoS One*, 9, e105584.
- STUART, T., BUTLER, A., HOFFMAN, P., HAFEMEISTER, C., PAPALEXI, E., MAUCK, W. M., 3RD, HAO, Y., STOECKIUS, M., SMIBERT, P. & SATIJA, R. 2019. Comprehensive Integration of Single-Cell Data. *Cell*, 177, 1888-1902 e21.
- SWANSON, E., LORD, C., READING, J., HEUBECK, A. T., GENGE, P. C., THOMSON, Z., WEISS, M. D., LI, X. J., SAVAGE, A. K., GREEN, R. R., TORGERSON, T. R., BUMOL, T. F., GRAYBUCK, L. T. & SKENE, P. J. 2021. Simultaneous trimodal single-cell measurement of transcripts, epitopes, and chromatin accessibility using TEA-seq. *Elife*, 10.
- SWIECH, L., HEIDENREICH, M., BANERJEE, A., HABIB, N., LI, Y., TROMBETTA, J., SUR, M. & ZHANG, F. 2015. In vivo interrogation of gene function in the mammalian brain using CRISPR-Cas9. *Nat Biotechnol*, 33, 102-6.

- T HART, B. A., VAN MEURS, M., BROK, H. P., MASSACESI, L., BAUER, J., BOON, L., BONTROP, R. E. & LAMAN, J. D. 2000. A new primate model for multiple sclerosis in the common marmoset. *Immunol Today*, 21, 290-7.
- TASKER, J. G., OLIET, S. H., BAINS, J. S., BROWN, C. H. & STERN, J. E. 2012. Glial regulation of neuronal function: from synapse to systems physiology. *J Neuroendocrinol*, 24, 566-76.
- TERRY, R. D., MASLIAH, E., SALMON, D. P., BUTTERS, N., DETERESA, R., HILL, R., HANSEN, L. A. & KATZMAN, R. 1991. Physical basis of cognitive alterations in Alzheimer's disease: synapse loss is the major correlate of cognitive impairment. *Ann Neurol*, 30, 572-80.
- THESTRUP, T., LITZLBAUER, J., BARTHOLOMAUS, I., MUES, M., RUSSO, L., DANA, H., KOVALCHUK, Y., LIANG, Y., KALAMAKIS, G., LAUKAT, Y., BECKER, S., WITTE, G., GEIGER, A., ALLEN, T., ROME, L. C., CHEN, T. W., KIM, D. S., GARASCHUK, O., GRIESINGER, C. & GRIESBECK, O. 2014. Optimized ratiometric calcium sensors for functional in vivo imaging of neurons and T lymphocytes. *Nat Methods*, 11, 175-82.
- THYAGARAJAN, T., TOTEY, S., DANTON, M. J. & KULKARNI, A. B. 2003. Genetically altered mouse models: the good, the bad, and the ugly. *Crit Rev Oral Biol Med*, 14, 154-74.
- TIAN, R., ABARIENTOS, A., HONG, J., HASHEMI, S. H., YAN, R., DRAGER, N., LENG, K., NALLS, M. A., SINGLETON, A. B., XU, K., FAGHRI, F. & KAMPMANN, M. 2021. Genome-wide CRISPRi/a screens in human neurons link lysosomal failure to ferroptosis. *Nat Neurosci*, 24, 1020-1034.
- TOMMASIN, S., GIANNI, C., DE GIGLIO, L. & PANTANO, P. 2019. Neuroimaging Techniques to Assess Inflammation in Multiple Sclerosis. *Neuroscience*, 403, 4-16.
- TOURBAH, A., LEBRUN-FRENAY, C., EDAN, G., CLANET, M., PAPEIX, C., VUKUSIC, S., DE SEZE, J., DEBOUVERIE, M., GOUT, O., CLAVELOU, P., DEFER, G., LAPLAUD, D. A., MOREAU, T., LABAUGE, P., BROCHET, B., SEDEL, F., PELLETIER, J. & GROUP, M.-S. S. 2016. MD1003 (high-dose biotin) for the treatment of progressive multiple sclerosis: A randomised, double-blind, placebo-controlled study. *Mult Scler*, 22, 1719-1731.
- TRABOULSEE, A. L. & LI, D. K. 2006. The role of MRI in the diagnosis of multiple sclerosis. *Adv Neurol*, 98, 125-46.
- TRAPP, B. D., VIGNOS, M., DUDMAN, J., CHANG, A., FISHER, E., STAUGAITIS, S. M., BATTAPADY, H., MORK, S., ONTANEDA, D., JONES, S. E., FOX, R. J., CHEN, J., NAKAMURA, K. & RUDICK, R. A. 2018. Cortical neuronal densities and cerebral white matter demyelination in multiple sclerosis: a retrospective study. *Lancet Neurol*, 17, 870-884.
- TSCHAHARGANEH, D. F., LOWE, S. W., GARIPPA, R. J. & LIVSHITS, G. 2016. Using CRISPR/Cas to study gene function and model disease in vivo. *FEBS J*, 283, 3194-203.
- TSELIS, A., KHAN, O. & LISAK, R. P. 2007. Glatiramer acetate in the treatment of multiple sclerosis. *Neuropsychiatr Dis Treat*, 3, 259-67.
- TUTUNCU, M., TANG, J., ZEID, N. A., KALE, N., CRUSAN, D. J., ATKINSON, E. J., SIVA, A., PITTOCK, S. J., PIRKO, I., KEEGAN, B. M., LUCCHINETTI, C. F., NOSEWORTHY, J. H., RODRIGUEZ, M., WEINSHENKER, B. G. & KANTARCI, O. H. 2013. Onset of progressive phase is an age-dependent clinical milestone in multiple sclerosis. *Mult Scler*, 19, 188-98.
- VAN DER VALK, P. & AMOR, S. 2009. Preactive lesions in multiple sclerosis. *Curr Opin Neurol*, 22, 207-13.
- VAQUERO, J. J. & KINAHAN, P. 2015. Positron Emission Tomography: Current Challenges and Opportunities for Technological Advances in Clinical and Preclinical Imaging Systems. *Annu Rev Biomed Eng*, 17, 385-414.
- VERCELLINO, M., MARASCIULO, S., GRIFONI, S., VALLINO-COSTASSA, E., BOSA, C., PASANISI, M. B., CROCIARA, P., CASALONE, C., CHIO, A., GIORDANA, M. T., CORONA, C. & CAVALLA, P. 2022. Acute and chronic synaptic pathology in multiple sclerosis gray matter. *Mult Scler*, 28, 369-382.
- WAKASHIMA, T., ABE, K. & KIHARA, A. 2014. Dual functions of the trans-2-enoyl-CoA reductase TER in the sphingosine 1-phosphate metabolic pathway and in fatty acid elongation. *J Biol Chem*, 289, 24736-48.

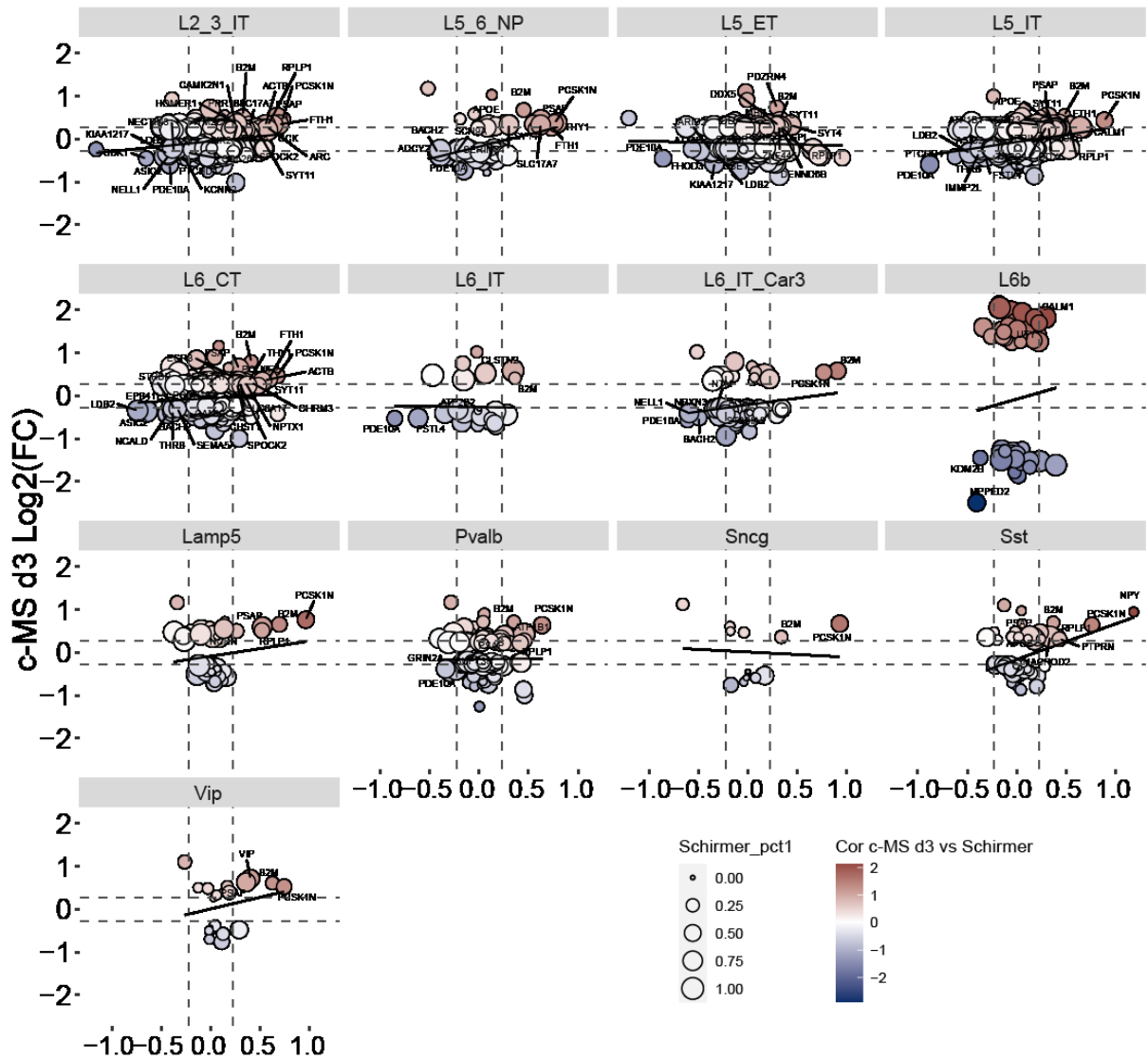
- WAKE, H., MOORHOUSE, A. J., JINNO, S., KOHSAKA, S. & NABEKURA, J. 2009. Resting microglia directly monitor the functional state of synapses in vivo and determine the fate of ischemic terminals. *J Neurosci*, 29, 3974-80.
- WANG, K., SONG, F., FERNANDEZ-ESCOBAR, A., LUO, G., WANG, J. H. & SUN, Y. 2018. The Properties of Cytokines in Multiple Sclerosis: Pros and Cons. *Am J Med Sci*, 356, 552-560.
- WARNOCK, G. I., AERTS, J., BAHRI, M. A., BRETIN, F., LEMAIRE, C., GIACOMELLI, F., MIEVIS, F., MESTDAGH, N., BUCHANAN, T., VALADE, A., MERCIER, J., WOOD, M., GILLARD, M., SERET, A., LUXEN, A., SALMON, E. & PLENEVAUX, A. 2014. Evaluation of 18F-UCB-H as a novel PET tracer for synaptic vesicle protein 2A in the brain. *J Nucl Med*, 55, 1336-41.
- WEARNE, S. L., RODRIGUEZ, A., EHLENBERGER, D. B., ROCHER, A. B., HENDERSON, S. C. & HOF, P. R. 2005. New techniques for imaging, digitization and analysis of three-dimensional neural morphology on multiple scales. *Neuroscience*, 136, 661-80.
- WEGNER, C., ESIRI, M. M., CHANCE, S. A., PALACE, J. & MATTHEWS, P. M. 2006. Neocortical neuronal, synaptic, and glial loss in multiple sclerosis. *Neurology*, 67, 960-7.
- WEINSHENKER, B. G., BASS, B., RICE, G. P., NOSEWORTHY, J., CARRIERE, W., BASKERVILLE, J. & EBERS, G. C. 1989. The natural history of multiple sclerosis: a geographically based study. I. Clinical course and disability. *Brain*, 112 (Pt 1), 133-46.
- WERNEBURG, S., JUNG, J., KUNJAMMA, R. B., HA, S. K., LUCIANO, N. J., WILLIS, C. M., GAO, G., BISCOLA, N. P., HAVTON, L. A., CROCKER, S. J., POPKO, B., REICH, D. S. & SCHAFFER, D. P. 2020. Targeted Complement Inhibition at Synapses Prevents Microglial Synaptic Engulfment and Synapse Loss in Demyelinating Disease. *Immunity*, 52, 167-182 e7.
- WILLIAMS, S. M., HAINES, J. L. & MOORE, J. H. 2004. The use of animal models in the study of complex disease: all else is never equal or why do so many human studies fail to replicate animal findings? *Bioessays*, 26, 170-9.
- WOLINSKY, J. S., NARAYANA, P. A., O'CONNOR, P., COYLE, P. K., FORD, C., JOHNSON, K., MILLER, A., PARDO, L., KADOSH, S., LADKANI, D. & GROUP, P. R. T. S. 2007. Glatiramer acetate in primary progressive multiple sclerosis: results of a multinational, multicenter, double-blind, placebo-controlled trial. *Ann Neurol*, 61, 14-24.
- WU, H. Y., HUDRY, E., HASHIMOTO, T., KUCHIBHOTLA, K., ROZKALNE, A., FAN, Z., SPIRES-JONES, T., XIE, H., ARBEL-ORNATH, M., GROSSKREUTZ, C. L., BACSKAI, B. J. & HYMAN, B. T. 2010. Amyloid beta induces the morphological neurodegenerative triad of spine loss, dendritic simplification, and neuritic dystrophies through calcineurin activation. *J Neurosci*, 30, 2636-49.
- WYSS-CORAY, T. 2016. Ageing, neurodegeneration and brain rejuvenation. *Nature*, 539, 180-186.
- YANG, W. S., SRIRAMARATNAM, R., WELSCH, M. E., SHIMADA, K., SKOUTA, R., VISWANATHAN, V. S., CHEAH, J. H., CLEMONS, P. A., SHAMJI, A. F., CLISH, C. B., BROWN, L. M., GIROTTI, A. W., CORNISH, V. W., SCHREIBER, S. L. & STOCKWELL, B. R. 2014. Regulation of ferroptotic cancer cell death by GPX4. *Cell*, 156, 317-331.
- YESHOKUMAR, A. K., NARULA, S. & BANWELL, B. 2017. Pediatric multiple sclerosis. *Curr Opin Neurol*, 30, 216-221.
- ZEYDAN, B. & KANTARCI, O. H. 2020. Impact of Age on Multiple Sclerosis Disease Activity and Progression. *Curr Neurol Neurosci Rep*, 20, 24.
- ZHENG, G. X., TERRY, J. M., BELGRADER, P., RYVKIN, P., BENT, Z. W., WILSON, R., ZIRALDO, S. B., WHEELER, T. D., MCDERMOTT, G. P., ZHU, J., GREGORY, M. T., SHUGA, J., MONTESCLAROS, L., UNDERWOOD, J. G., MASQUELIER, D. A., NISHIMURA, S. Y., SCHNALL-LEVIN, M., WYATT, P. W., HINDSON, C. M., BHARADWAJ, R., WONG, A., NESS, K. D., BEPPU, L. W., DEEG, H. J., MCFARLAND, C., LOEB, K. R., VALENTE, W. J., ERICSON, N. G., STEVENS, E. A., RADICH, J. P., MIKKELSEN, T. S., HINDSON, B. J. & BIELAS, J. H. 2017. Massively parallel digital transcriptional profiling of single cells. *Nat Commun*, 8, 14049.
- ZHOU, N., YUAN, X., DU, Q., ZHANG, Z., SHI, X., BAO, J., NING, Y. & PENG, L. 2023. FerrDb V2: update of the manually curated database of ferroptosis regulators and ferroptosis-disease associations. *Nucleic Acids Res*, 51, D571-D582.

- ZIEHN, M. O., AVEDISIAN, A. A., TIWARI-WOODRUFF, S. & VOSKUHL, R. R. 2010. Hippocampal CA1 atrophy and synaptic loss during experimental autoimmune encephalomyelitis, EAE. *Lab Invest*, 90, 774-86.
- ZOUP, L., BOOKER, S. A., EIGEL, D., WERNER, C., KIND, P. C., SPIRES-JONES, T. L., NEWLAND, B. & WILLIAMS, A. C. 2021. Selective vulnerability of inhibitory networks in multiple sclerosis. *Acta Neuropathol*, 141, 415-429.

Supplementary Data

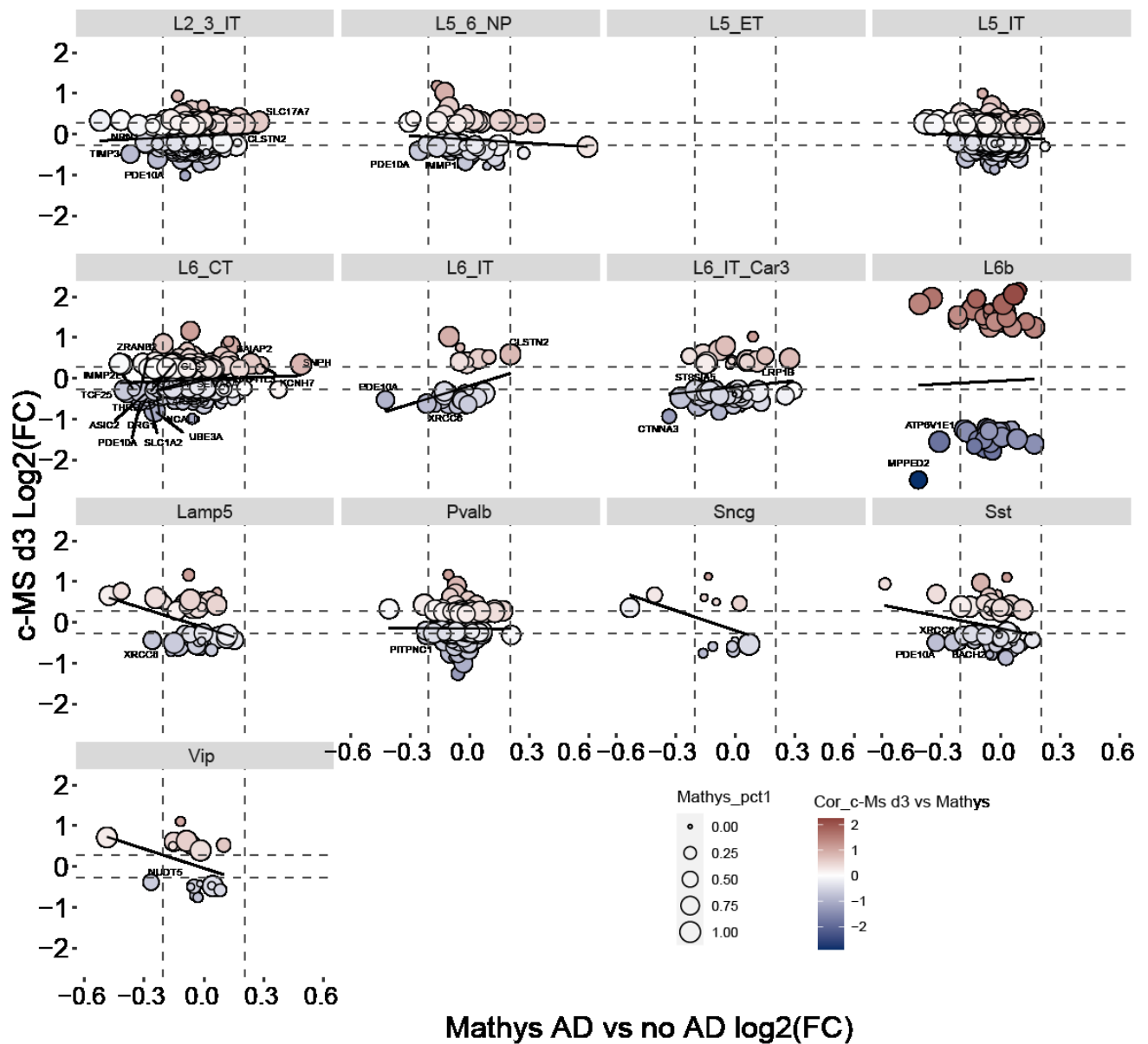


Suppl Figure 1: Correlation analysis between genes of c-MS model mice and Doron MS patient data set shows no cluster specificity. Correlation analysis of all genes expressed in the c-MS model d3 vs Healthy mouse comparison and the Merkler MS patient vs healthy control comparison separated by neuronal clusters. Positively correlated and significantly DEGs are shown in red. Negatively correlated and significantly DEGs are shown in blue, size of the dots shows percent of expression in Merkler data set cells. Dotted lines show threshold for consideration of DEGs at 3x SD of log2FC for each data set.

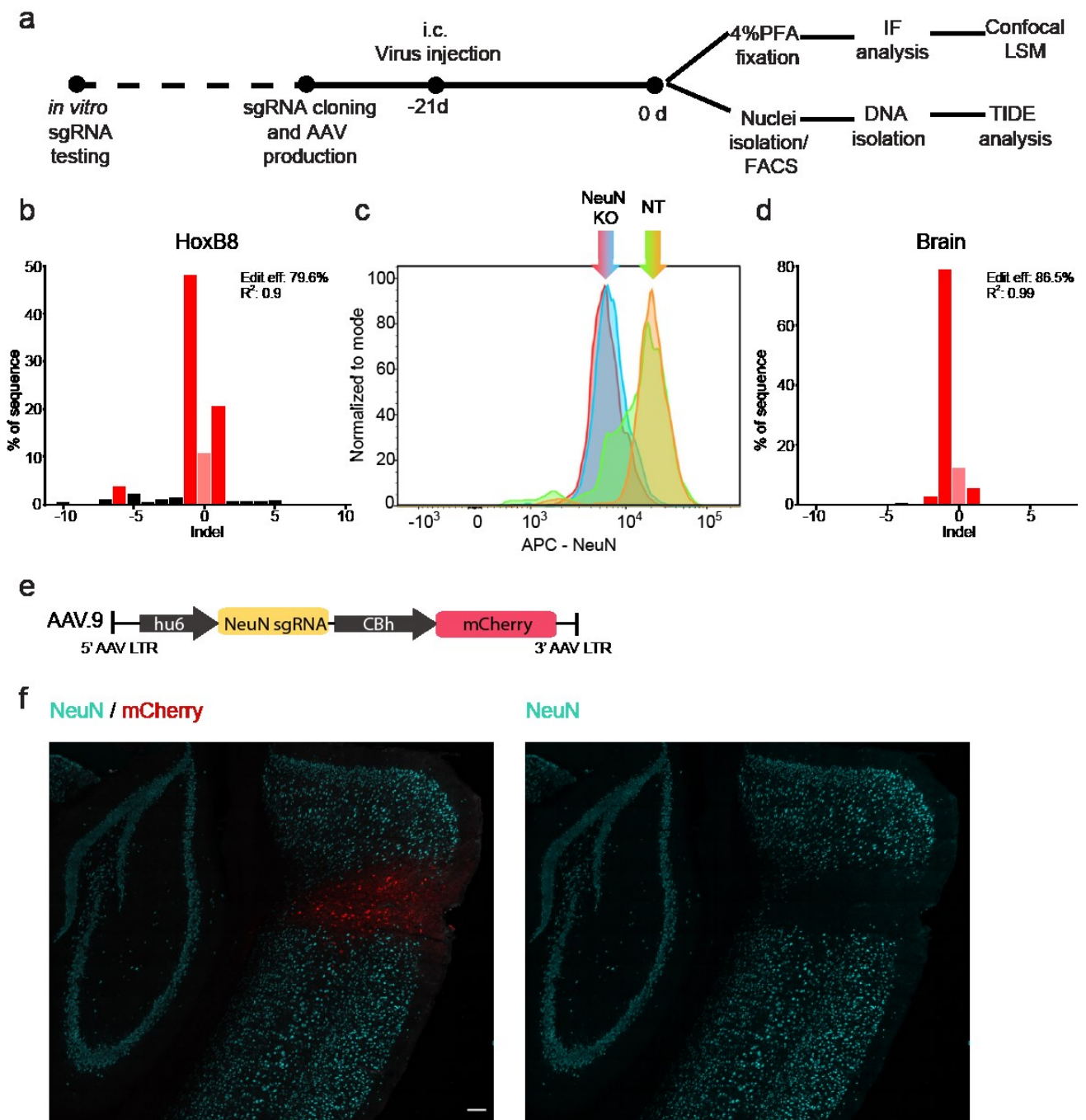


Schirmer MS vs Healthy Log2(FC)

Suppl Figure 2: Correlation analysis between genes of c-MS mice and Schirmer MS patient data set shows no cluster specificity. Correlation analysis of all genes expressed in the c-MS d3 vs Healthy mouse comparison and the Schirmer MS patient vs healthy control comparison separated by neuronal clusters. Positively correlated and significantly DEGs are shown in red. Negatively correlated and significantly DEGs are shown in blue, size of the dots shows percent of expression in Schirmer cells. Dotted lines show threshold for consideration of DEGs at 3x SD of log2FC for each data set.

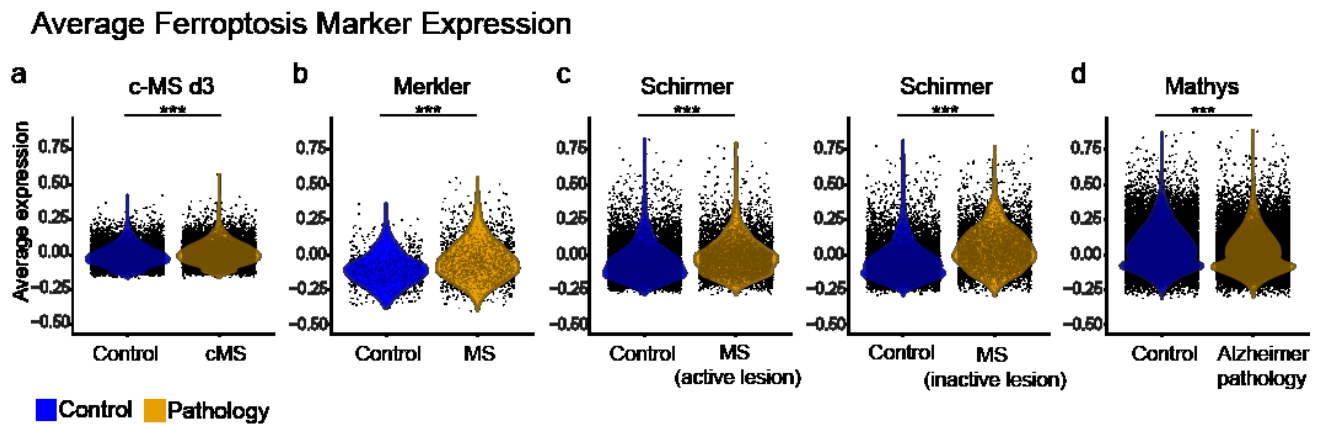


Suppl Figure 3: Correlation analysis between genes of c-MS mice and Mathys AD patient data set shows no cluster specificity. Correlation analysis of all genes expressed in the c-MS d3 vs Healthy mouse comparison and the Mathys AD patient vs healthy control comparison separated by neuronal clusters. Positively correlated and significantly DEGs are shown in red. Negatively correlated and significantly DEGs are shown in blue, size of the dots shows percent of expression in Mathys cells. Dotted lines show threshold for consideration of DEGs at 3x SD of log2FC for each data set.

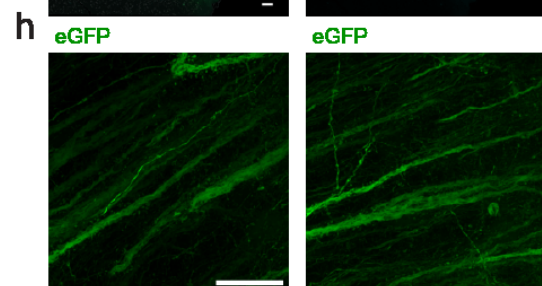
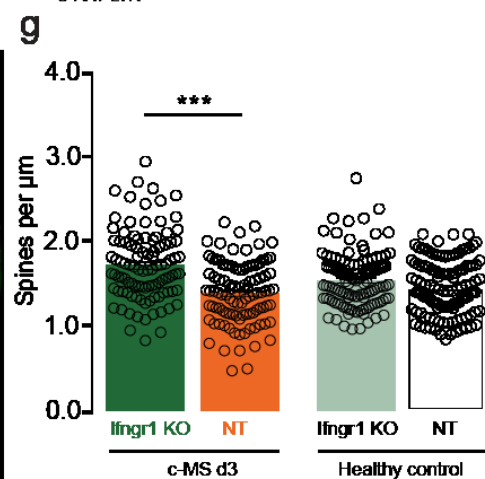
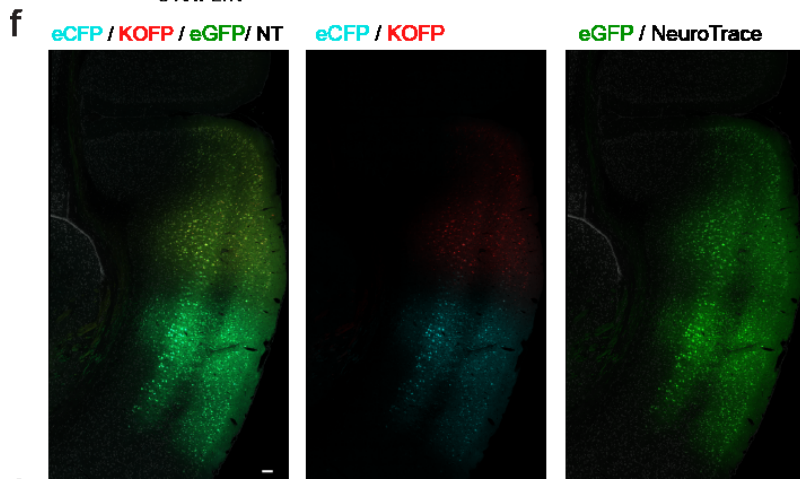
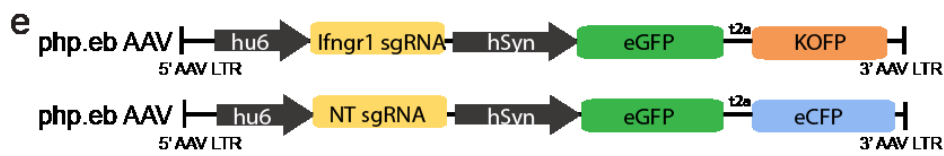
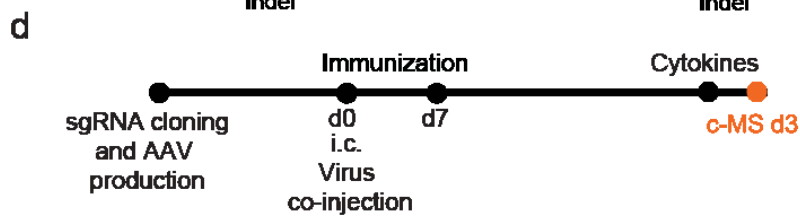
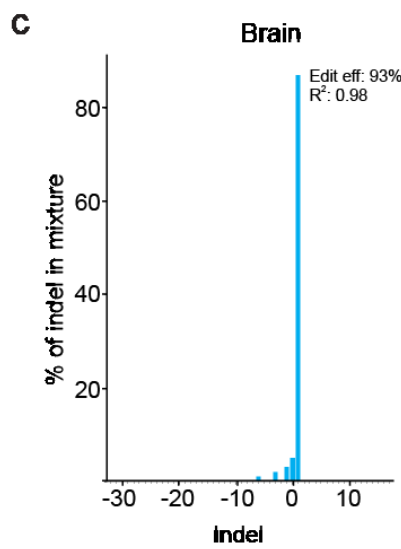
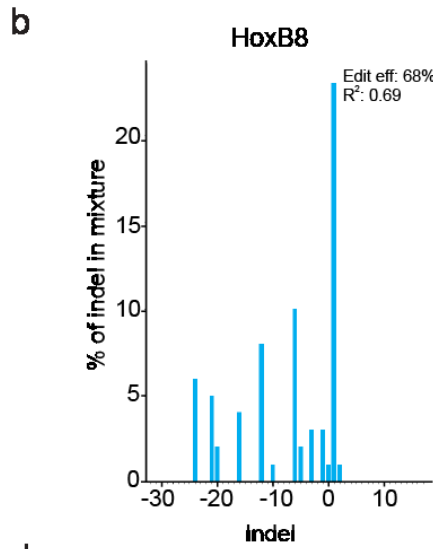
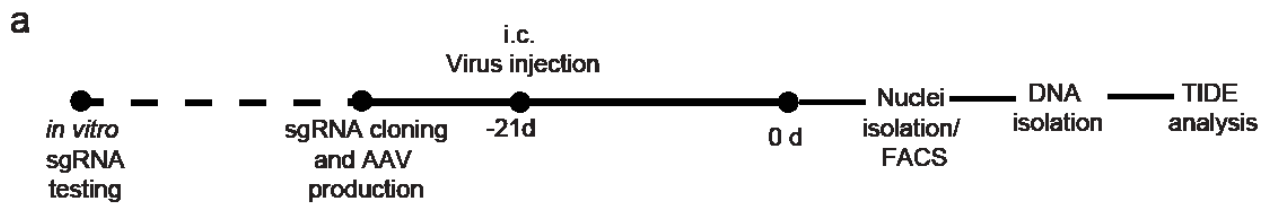


Suppl Figure 4: AAV-mediated CRISPR/Cas9 KO of NeuN can be validated at the gDNA and protein level *in vivo*. **a)** Schematic of experimental design for *in vivo* verification from nuclei and *in situ* of AAV-mediated CRISPR/Cas9 KO of PSAP in *R26-Cas9x BiozziABH* mice. **b)** Percentage of indel distribution for NeuN sgRNA in genomic DNA of Cas9-expressing HoxB8 cells. Top values are the total editing efficiency and the R^2 value obtained from indel editing score. **c)** Representative FACS histogram of nuclei transduced with NeuN sgRNA (blue, red) compared to NT sgRNA (green, orange) in the cortex based their NeuN expression level. Each histogram color represents nuclei belonging to one mouse infected with NeuN sgRNA or NT sgRNA. **d)** Percentage of indel distribution for NeuN sgRNA in genomic DNA of nuclei isolated from NeuN sgRNA AAV- infected mice compared to NT. Top values are the total editing efficiency and the R^2 value obtained from indel editing score. **e)** AAV9 AAV expression cassette for NeuN sgRNA used for labeling of infected neurons. **f)** Confocal representative overview images of NeuN sgRNA infected neurons in the NeuN stained somatosensory cortex of *R26-Cas9x BiozziABH* mice. Left panel shows merged NeuN (cyan) staining

and mCherry infected neurons (red). Right panel shows NeuN (cyan) staining only. Scale bar f 100 μ m. Figure created by Emily Melisa Ullrich Gavilanes, includes data from Adinda Wens.



Suppl Figure 5: Average expression of Ferroptosis in snRNA-seq studies shows MS specificity. Violin plots showing single nuclei average expression of manually and database curated ferroptosis markers in (a) c-MS d3 and healthy control mice; (b) Merkler data set MS patients and healthy controls; (c) Schirmer data set MS patients with active lesions (left), inactive lesions (right) and healthy controls; and (d) Mathys data set AD pathology and no pathology controls. Calculation between pathology and non-pathology or disease and healthy control groups was performed using the Seurat module function. All comparisons were made using a students t-test to determine statistical significance. Abbreviations: c-MS: cortical MS model; d3: perfused at day 3. ***p < 0.001. Figure adapted by Emily Melisa Ullrich Gavilanes from Veronika Pfaffenstaller's Master's thesis.



Suppl Figure 6: AAV-mediated CRISPR/Cas9 KO of *Ifngr1* can be validated at the gDNA level and ameliorates c-MS synaptic loss. **a)** Schematic of experimental design for *in vivo* verification from nuclei of AAV-mediated CRISPR/Cas9 KO of *Ifngr1* in *R26-Cas9x BiozziABH* mice at the genomic DNA level. **b)** Percentage of indel distribution for *Ifngr1* sgRNA3 in genomic DNA of Cas9-expressing *HoxB8* cells. Top values are the total editing efficiency and the R^2 value obtained from indel editing score. **c)** Percentage of indel distribution for *Ifngr1* sgRNA in genomic DNA of nuclei isolated from *Ifngr1* sgRNA AAV- infected mice compared to NT. Top values are the total editing efficiency and the R^2 value obtained from indel editing score. **d)** Schematic of experimental design for *in vivo* synapse phenotype evaluation of AAV-mediated CRISPR/Cas9 KO of *Ifngr1* in *R26-Cas9x BiozziABH* mice. **e)** php.eb AAV expression cassette for *Ifngr1* sgRNA (top) and NT sgRNA (bottom) used for labeling of infected neurons. eGFP expression is meant for quantification while Kusabira Orange FP (KOF, in *Ifngr1* sgRNA vector) and eCFP (in NT sgRNA vector) are meant for differentiation of experimental and control sgRNA infected dendrites. **f)** Confocal representative overview images of *Ifngr1* sgRNA infected and NT sgRNA infected neurons in the somatosensory cortex of c-MS d3 *R26-Cas9x BiozziABH* mice, ipsilateral to cytokine injection. Left panel shows merged *Ifngr1* sgRNA infected cells (eGFP and KOF positive), NT sgRNA infected cells (eCFP and eGFP positive) and NeuroTrace Nissl staining. Middle panel shows only the channels used for differentiating experimental from control cells: *Ifngr1* KO express KOF (red) while NT control express eCFP (cyan). Right panel shows widespread eGFP (green) signal from both viruses and NeuroTrace Nissl staining (grey). **g)** Spine density of layer V ipsilateral dendrites in c-MS d3 (left) and healthy control (right) mice infected with *Ifngr1* sgRNA or NT sgRNA (n=100 *Ifngr1* sgRNA infected, n=100 NT sgRNA infected dendritic stretches from n=10 c-MS d3 mice; n=120 *Ifngr1* sgRNA infected, n=120 NT sgRNA infected dendritic stretches from n=12 healthy control mice; mean \pm SEM; Kruskal-Wallis test followed by Dunn's multiple comparisons test). **h)** Confocal representative images of dendritic stretches of *Ifngr1* sgRNA infected (left) and NT sgRNA infected (right) layer V neurons in the somatosensory cortex of c-MS d3 *R26-Cas9x BiozziABH* mice, ipsilateral to cytokine injection. Scale bar in f: 100 μ m, in h: 20 μ m. Abbreviations: c-MS: cortical MS model; d3: perfused at day 3; KOF: Kusabira Orange Fluorescent protein. ***p<0.001. Figure created by Emily Melissa Ullrich Gavilanes.

Suppl Table 1: In vitro CRISPR/Cas9 indel efficiency, knockout score and model fit of PSAP targeting sgRNAs

PSAP sgRNA number	Sequence	Indel %	KO score	R^2 model fit
1	CTACGTGGACCAGTATTCCG	40	40	0.98
2	TCTGGCATAAAATCACATTG	19	15	0.99
3	AAACTGTTGTCACCGAAGCT	30	26	0.98
4	TCAACCACCTCCTTGACAG	15	14	0.99
6	TGAGTCCAACAAGATCCCGG	93	87	0.97

Suppl Table 2: Manually curated oxidative stress gene signature

Tested Gene	Association	Publication
GPX4	Incorporates selenocysteine into proteins, essential for neuronal survival under oxidative stress, ferroptosis prevention through peroxidized lipid reduction	(Yang et al., 2014)
PSTK	Incorporates selenocysteine into proteins, essential for neuronal survival under oxidative stress	(Tian et al., 2021)
SEPHS2	Incorporates selenocysteine into proteins, essential for neuronal survival under oxidative stress	(Tian et al., 2021)
SEPSECS	Incorporates selenocysteine into proteins, essential for neuronal survival under oxidative stress	(Tian et al., 2021)
MTOR, RPTOR, MLST8	mTORC1 complex component	(Tian et al., 2021)
RHEB	mTOR pathway activator	(Tian et al., 2021)
NPRL3	mTORC1 inhibitor	(Tian et al., 2021)
PARP1, SAT1, NOX5	Positive ROS regulator	(Tian et al., 2021)
PTEN, FH	Negative ROS regulator	(Tian et al., 2021)
ACSL1-3, 5 and 6	Enzymes involved in metabolism of fatty aldehyde products of sphingolipid clearance	(Wakashima et al., 2014)
FBXL5	Negative regulation of iron levels	(Tian et al., 2021)
NFU1, NUBPL, MCOLN1	Encode endolysosomal iron release channel	(Tian et al., 2021)
CTSD, GM2A	Activator for glycosphingolipid degradation	(Tian et al., 2021)
WDR45	Involved in lysosomal degradation, associated with Neurodegeneration with Brain Iron Accumulation	(Tian et al., 2021)
DGAT	Ceramide acyl transferase	(Senkal et al., 2017)
CERS2	Interact with fatty acyl binding protein to channel long fatty acids for ceramide synthesis	(Ferreira et al., 2017)
SIRT3	Regulated ceramide biosynthesis through deacetylation	(Novgorodov et al., 2016)
SOD1	superoxide dismutase	(Tian et al., 2021)

Acknowledgements

First and foremost, I would like to thank my supervisor and adviser Prof. Martin Kerschensteiner. He has been an amazing supervisor and mentor who has gone above and beyond when it comes to providing advice for both my project and my career. Thank you for trusting me with this project, lab responsibilities, and for all the guidance and support throughout the last years. The great atmosphere of the lab is a good representation of Martin and his decision-making abilities. I would also like to thank you Dr. Adrian-Minh Schumacher and Dr. Aleksandra Mezydło for all their help and lessons they taught me at the beginning of my PhD as well as for being available for questions from me when I needed them. Thank you to Dr. Eduardo Beltrán for all his assistance when it came to the single nuclei RNA seq analysis and to Elma Bambur, Jutta Marks, Berni Fiedler and Anja Schmalz for their help within the lab and with all paperwork and official matters.

I wanted to profusely thank Prof. Thomas Misgeld and Prof. Veit Rothhammer who as members of my thesis advisory committee provided me with encouragement, advice and time during all our meetings. Their constructive comments and knowledge helped in multiple ways to move my project forward.

I would like to thank PD Dr. Steffan Dietzel, Dr. Andreas Thomae and Mariano Gonzalez Pisfil for their constant help and assistance with the microscopes in the bioimaging facility and in the same way wanted to acknowledge the core facility bioimaging of the Biomedical Center for part of the microscopy in this thesis. In the same way I would like to thank Dr. Lisa Richter and Parvis Khosravani for their assistance with the flow cytometry machines in the Core Facility Flow Cytometry of the LMU. A further thank you goes to Stefan Krebs from LAFUGA for all his help with NGS sequencing of my CRISPR/Cas9 samples, as well as to Gisela Brinkmann from the Sanger sequencing service team at the faculty of biology for running what seemed to be an endless number of samples from all my cloning for me.

I wanted to thank Kristof Egervari Levente and Prof. Doron Merkler for kindly providing us with their MS patient and control data set as well as their advice when analyzing snRNA-seq data.

Furthermore, I wanted to thank Dr. Nellwyn Hagan, Dr. Ross Gruber and Dimitry Ofengeim in Sanofi for providing us with their novel small molecule phagocyte treatment and their support throughout these experiments.

Additionally, I wanted to thank Laura Bartos, Lea Kunze and Giovanna Palumbo for all their support and help with the PET experiments and in the Nuklearmedizin facility.

I want to thank Adinda Wens for being the first long-term person in the small lab with me and for collaborating with me in the wild ride that was establishing the CRISPR/Cas9 system. Her ideas and contributions were always extremely helpful, and I am very lucky to have worked closely with her.

I would further like to thank Dr. Arek Kendirli for always being willing to help with plasmid design but most of all for always being willing to listen to the different parts of my project and to jump with many helpful ideas. I truly want to thank Clara de la Rosa del Val for all her help and supervision when it came to the bioinformatics data but also for sharing her knowledge with me and giving me extremely helpful scientific advice.

I want to say a very big thank you to Daniela Beckman, Ioanna Emmanouilidis and all the current and past members of the small lab for making every day better at work and supporting me in the good days but most of all for pushing me to continue in the bad days. Going to work was a pleasure always knowing that you would be around. I want to further thank Yves Carpentier-Solano who has been an amazing addition to the small lab. Since he has arrived, he has been willing to help me in many ways and I wanted to further express my appreciation for the effort he put in making this thesis better.

Thank you to Paula Sánchez, Daniel Engels and Yi-Heng Tai who were always willing to help with my project and provide advice for me. A very big thank you also goes to all other present and former members of the Kerschensteiner and Bareyre labs who made the lab be an amazing place and for always letting me come to the big lab to get some of their amazing snacks.

I would like to give the biggest of 'thanks' to Virag Kocsis-Jutka, Veronika Pfaffenstaller, Nils Treiber, Carla Ares Carral and Diego Ruiz who as my students probably taught me as much or more than I taught them. They made me look forward to go to the lab even when I was exhausted, and I am extremely lucky to have been able to work with such a wonderful group of people. Without their help the projects in this thesis would not be where they are. I am lucky to call them my friends and to have found people who were so eager to help in every way. Thank you truly and from the bottom of my heart for the days when you were my hands because I could not use mine.

I am lucky to have an amazingly supportive family, so thank you to my sister for always being there for me throughout the years. Thank you to my parents who were always supportive of my choices. Thank you for being there for me every step of the way and for taking the time to listen to every single one of my presentations so I could practice them. I would never be where I am without you- I love you. Thank you to my grandparents and my aunts and cousins for their support throughout the years.

Finally, I would like to say a very important thank you to David, you made it so easy for me to put as much work as I needed into my work. You made my bad days good and my good days better. I would never be able to thank you enough for all your support and help.

List of publications

Mezydło A*, Treiber N*, **Ullrich Gavilanes EM**, Eichenseer K, Ancău M, Wens A, Ares Carral C, Schifferer M, Snaidero N, Misgeld T* & Kerschensteiner M*. *Remyelination by surviving oligodendrocytes is inefficient in the inflamed mammalian cortex*. Neuron. 2023.

Jafari M*, Schumacher AM*, Snaidero N*, **Ullrich Gavilanes EM**, Neziraj T, Kocsis-Jutka V, Engels D, Jürgens T, Wagner I, Flórez Weldinger JD, Schmidt SS, Beltrán E, Hagan N, Woodworth L, Ofengein D, Gans J, Wolf F, Kreutzfeld M, Portugues R, Merkler D*, Misgeld T* & Kerschensteiner M*. *Phagocyte-mediated synapse removal in cortical neuroinflammation is promoted by local calcium accumulation*. Nature Neuroscience. 2021

Uhlmann RE*, Rother C*, Rasmussen J, Schelle J, Bergmann C, **Ullrich Gavilanes EM**, Fritschi SK, Buehler A, Baumnn F, Skodras A, Al-Shaana R, Beschorner N, Ye L, Kaeser SA, Obermüller U, Christensen S, Kartberg F, Stavenhagen JB, Rahfeld JU, Cynis H, Qian F, Weinreb PH, Bussiere T, Walker LC, Staufienbiel M, Jucker M. *Acute targeting of preamyloidseeds in transgenic mice reduces Alzheimer-like pathology later in life*. Nature Neuroscience. 2020

München, den (Munich, date)

Unterschrift (Signature)

EM. Ullrich Gavilanes

München, den (Munich, date)

Unterschrift (Signature), Supervisor

Prof. Dr. Markin Kerschensteiner

Curriculum vitae

Personal Data: **Emily Melisa Ullrich Gavilanes**

Place of Birth: Quito, Ecuador

Nationality: Ecuadorian, German

Date of Birth: 30th of June 1995

Education

10/2019-Present **Graduate School of Systemic Neurosciences, LMU, Munich, DE**

PhD student

10/2016-09/2018 **Eberhard Karls Universität, Tübingen, DE**

Master of Science, Cellular and Molecular Neuroscience

08/2013-06/2016 **Jacobs University Bremen, Bremen, DE**

Bachelor of Science, Biochemistry and Cell Biology

Research Experience

11/2018-Present **University Hospital Munich and Biomedical Center, Munich, DE**

PhD at the AG Kerschensteiner in the Institute of Clinical Neuroimmunology

02/2018-09/2018 **Hertie Institute for Clinical Brain Research, Tübingen, DE**

Master's thesis at the AG Jucker, department of Cell biology of neurological diseases

11/2017-02/2018 **Hertie Institute for Clinical Brain Research, Tübingen, DE**

Laboratory rotation at the AG Neher, department of Cell biology of neurological diseases

09/2017-11/1017 **DZNE, Tübingen, DE**

Laboratory rotation at the AG Rizzu, department of Applied Genomics for Neurodegenerative Diseases

09/2015-06/2016 **Jacobs University Bremen, Bremen, DE**

Bachelor's thesis at the AG Brix, department of Life Sciences and Chemistry

Publications

Mezydło A*, Treiber N*, **Ullrich Gavilanes EM**, Eichenseer K, Ancău M, Wens A, Ares Carral C, Schifferer M, Snaidero N, Misgeld T* & Kerschensteiner M*. *Remyelination by surviving oligodendrocytes is inefficient in the inflamed mammalian cortex*. Neuron. 2023.

Jafari M*, Schumacher AM*, Snaidero N*, **Ullrich Gavilanes EM**, Neziraj T, Kocsis-Jutka V, Engels D, Jürgens T, Wagner I, Flórez Weldinger JD, Schmidt SS, Beltrán E, Hagan N,

Woodworth L, Ofengein D, Gans J, Wolf F, Kreutzfeld M, Portugues R, Merkler D*, Misgeld T* & Kerschensteiner M*. *Phagocyte-mediated synapse removal in cortical neuroinflammation is promoted by local calcium accumulation*. Nature Neuroscience. 2021

Uhlmann RE*, Rother C*, Rasmussen J, Schelle J, Bergmann C, **Ullrich Gavilanes EM**, Fritschi SK, Buehler A, Baumnn F, Skodras A, Al-Shaana R, Beschorner N, Ye L, Kaeser SA, Obermüller U, Christensen S, Kartberg F, Stavenhagen JB, Rahfeld JU, Cynis H, Qian F, Weinreb PH, Bussiere T, Walker LC, Staufenbiel M, Jucker M. *Acute targeting of preamyloidseeds in transgenic mice reduces Alzheimer-like pathology later in life*. Nature Neuroscience. 2020

Abstracts

Ullrich Gavilanes EM, Mezydlo A, de la Rosa del Val C, Treiber N, Kocsis-Jutka V, Kerschensteiner M. "An animal model of cortical grey matter inflammation resembling progressive MS pathology". 10th International Conference on Autoimmunity: Mechanisms and Novel Treatments, Crete, 2022.

Eidesstatliche Versicherung / Affidavit

Emily Melisa Ullrich Gavilanes

(Studierende/Student)

Hiermit versichere ich an Eides statt, dass ich die vorliegende Dissertation

Mechanisms of Neuronal Pathology in a model of Grey Matter Inflammation

selbstständig angefertigt habe, mich außer der angegebenen keiner weiteren Hilfsmittel bedient und alle Erkenntnisse, die aus dem Schrifttum ganz oder annähernd übernommen sind, als solche kenntlich gemacht und nach ihrer Herkunft unter Bezeichnung der Fundstelle einzeln nachgewiesen habe.

I hereby confirm that the dissertation Mechanisms of Neuronal Pathology in a model of Grey Matter Inflammation is the result of my own work and that I have only used sources or materials listed and specified in the dissertation.

München/ Munich

25.10.2023

(Datum/date)

Emily Melisa Ullrich Gavilanes

(Unterschrift/ Signature)

Author contributions

The results from Figures 5-8 and 18 from this thesis are modified from the paper: *Phagocyte-mediated synapse removal in cortical neuroinflammation is promoted by local calcium accumulation*. [Jafari M, Schumacher AM, Snaidero N, **Ullrich Gavilanes EM**, Neziraj T, Kocsis-Jutka V, Engels D, Jürgens T, Wagner I, Flórez Weidinger JD, Schmidt SS, Beltrán E, Hagan N, Woodworth L, Ofengeim D, Gans J, Wolf F, Kreutzfeld M, Portugues R, Merkler D, Misgeld T & Kerschensteiner M]. 2021. Nature Neuroscience.

- Prof. Thomas Misgeld and Prof. Martin Kerschensteiner helped to design experiments and wrote the paper.
- Dr. Mehrnoosh Jafari designed experiments, generated c-MS animals, processed the tissue at all time points, treated animals, collected and analyzed the data for Figures 5, 6, 8 and 18
- Dr. Adrian-Minh Schumacher designed experiments, generated c-MS animals, treated animals, performed *in vivo* two-photon microscopy, collected, processed and analyzed data for Figures 6, 7, 8 and 18
- Tradite Neziraj collected and analyzed data for Figure 6
- Virag Kocsis-Jutka analyzed data for Figure 7
- Emily Melisa Ullrich Gavilanes generated c-MS animals, processed tissue at c-MS d3 time point, treated animals, performed *in vivo* two-photon microscopy, collected, processed and analyzed data for figures 7, 8, and 18.
- Dr. Nellwyn Hagan, Dr. Dimitry Ofengeim and Josef Gans provided us with the CSF1R-inhibitor for Figure 18.

Furthermore, data for Figure 6 regarding demyelination was generated from c-MS induction to data analysis by Dr. Aleksandra Mezydło and is found in *Remyelination by surviving oligodendrocytes is inefficient in the inflamed mammalian cortex*. [Mezydło A, Treiber N, **Ullrich Gavilanes EM**, Eichenseer K, Ancău M, Wens A, Ares Carral C, Schifferer M, Snaidero N, Misgeld T & Kerschensteiner M] Neuron. 2023.

For middle-aged c-MS Figures 9 and 10, work was performed by Dr. Aleksandra Mezydło, Nils Treiber, Virag Kocsis-Jutka and Emily Melisa Ullrich Gavilanes

- Dr. Aleksandra Mezydło and Emily Melisa Ullrich Gavilanes designed experiments, generated c-MS animals, processed tissue at all time points, collected and analyzed data for Figures 9 and 10.
- Nils Treiber generated c-MS animals, processed tissue for all time points, and analyzed data for Figures 9 and 10.
- Virag Kocsis-Jutka generated c-MS animals, processed tissue for time points c-MS day 3, c-MS day 14 and c-MS day 28 of synaptic pathology (Figure 9 b, c).

For generation of c-MS snRNA-seq, mapping to the Merkler, Schirmer, and Mathys data set and analysis of mapped data sets in Figures 11-13 and Suppl Figure 5, work was performed by Dr. Aleksandra Mezydło, Dr. Eduardo Beltrán, Klara Eglseder, Kristof Egervari Levente, Clara de la Rosa del Val, Veronika Pfaffenstaller and Emily Melisa Ullrich Gavilanes.

- Dr. Aleksandra Mezydło and Emily Melisa Ullrich Gavilanes designed c-MS experiments, generated c-MS animals, processed tissue for nuclei isolation.

- Dr. Eduardo Beltrán FACS sorted nuclei and did initial c-MS data analysis observed in Figure 11 as well as provided guidance for mapping of data.
- Kristof Egervari Levente generated the Merkler MS patient data set and kindly provided it to us. This data is used in Figures 12-13 and Suppl Figure 5.
- Klara Eglseer mapped the data sets together as observed in Figure 12 and necessary for Figure 13 analysis.
- Veronika Pfaffenstaller performed analysis of mapped data sets for Figure 13 and Suppl Figure 5.
- Clara de la Rosa del Val provided support, advice and supervision when it come to data set mapping and analysis for Figures 12-13 and Suppl Figure 5.
- Emily Melisa Ullrich Gavilanes helped to design experiments and guide analysis of snRNA-seq data sets.

For CRISPR/Cas9 KO pipeline establishment and candidate KO verification and analysis in Figures 14-17, Suppl figures 4, 6, work was performed by Dr. Arek Kendirli, Clara de la Rosa del Val, Adinda Wens, Almir Aljovic, Veronika Pfaffenstaller and Emily Melisa Ullrich Gavilanes.

- Dr. Arek Kendirli and Clara de la Rosa del Val established the *in vitro* pipeline used for sgRNA testing in Cas9-expressing HoxB8 cells for Figure 14 and parts of Suppl Figures 4, 6. Furthermore Dr. Arek Kendirli helped with the design and cloning of AAV-vectors used for experiments in Figure 15 and necessary for generation of data in Figure 16-17 as well as those in Suppl Figure 6. He further helped with FACS sorting of gene edited nuclei and in the mRNA library generation of PSAP KO and NT mice. Clara de la Rosa del Val provided support, advice and supervision for RNA-seq analysis of PSAP KO in Figures 16, 17.
- Adinda Wens established the *in vitro* and *in vivo* pipeline continuously used in this thesis for neuronal specific markers in Figures 14-17, Suppl Figures 4, 6. Furthermore she generated the NeuN CRISPR/Cas9 KO and performed gDNA verification in Suppl Figure 4.
- Almir Aljovic generated and kindly provided the AAV9 necessary for NeuN CRISPR/Cas9 KO in Suppl Figure 4.
- Veronika Pfaffenstaller aided in generation of CRISPR/Cas9 edited c-MS mice for Figures 15 and Suppl Figure 6 a-c as well as isolated nuclei and prepared the mRNA library for PSAP KO. Furthermore, she performed the RNA-seq data analysis for PSAP KO in Figures 16-17.
- Emily Melisa Ullrich Gavilanes established the *in vitro* and *in vivo* pipeline continuously used in this thesis for neuronal specific markers in Figures 14-17, Suppl Figures 4, 6. Furthermore, I worked in the generation of the NeuN CRISPR/Cas9 KO and performed gDNA and protein verification in Suppl Figure 4. Additionally, I generated c-MS CRISPR/Cas9 KO of *lfng1* and PSAP as well as processed and analyzed tissue for the *lfng1* KO in Suppl Figure 6 as well as isolated nuclei for Figure 15-17 and Suppl Figure 4, 6. I performed the TIDE analysis for Figures 15, 16, Suppl Figures 4, 6. I performed the first analysis of PSAP KO in RNA seq in Figure 16 and provided guidance for the data in Figure 17.

For BTK-inhibitor treatment, Emily Melisa Ullrich Gavilanes generated c-MS mice, performed the treatment, collected the tissue and analyzed the data. The BTK-inhibitor was kindly provided by Dr. Ross Gruber in Sanofi who also provided guidance with the treatment.

For the PET imaging of SV2a in c-MS in Figure 20, work was performed by Laura Bartos, Lea Kunze, Carla Ares Carral and Emily Melisa Ullrich Gavilanes.

- Lea Kunze and Laura Bartos performed the PET scanning in c-MS mice. Furthermore, Laura Bartos performed the analysis and processing of *in vivo* images obtained from the scan observed in Figure 20 b, c.
- Carla Ares Carral performed the *in situ* tissue processing, imaging and analysis of tissue from PET imaged mice.
- Emily Melisa Ullrich Gavilanes designed the experiments, generated c-MS mice, performed the perfusions and provided support and guidance during the *in situ* tissue analysis.

München, den (Munich, date)

Unterschrift (Signature)
EM. Ullrich Gavilanes

München, den (Munich, date)

Unterschrift (Signature), Supervisor
Prof. Dr. Markin Kerschensteiner

Copyrights and Permissions

SPRINGER NATURE LICENSE TERMS AND CONDITIONS

Jun 22, 2023

This Agreement between Ms. Emily Ullrich Gavilanes ("You") and Springer Nature ("Springer Nature") consists of your license details and the terms and conditions provided by Springer Nature and Copyright Clearance Center.

License Number	5574120188693
License date	Jun 22, 2023
Licensed Content Publisher	Springer Nature
Licensed Content Publication	Nature Reviews Disease Primers
Licensed Content Title	Multiple sclerosis
Licensed Content Author	Massimo Filippi et al
Licensed Content Date	Nov 8, 2018
Type of Use	Thesis/Dissertation
Requestor type	non-commercial (non-profit)
Format	print and electronic
Portion	figures/tables/illustrations
Number of figures/tables/illustrations	1

Would you like a high resolution image with your order?	no
Will you be translating?	no
Circulation/distribution	1 - 29
Author of this Springer Nature content	no
Title	Mechanisms of Neuronal Pathology in a model of Grey Matter Inflammation
Institution name	LMU Munich